Low-Profile Magnetic Integration for High-Frequency Point-of-Load Converter

Qiang Li

Dissertation submitted to the Faculty of the
Virginia Polytechnic Institute and State University
in partial fulfillment of the requirements for the degree of

Doctor of Philosophy
in
Electrical Engineering

Fred C. Lee, Chair
Paolo Mattavelli
Guo-Quan Lu
Dong S. Ha
Michael S. Hsiao

August 11th, 2011
Blacksburg, Virginia

Keywords: Magnetic integration, Low temperature co-fired ceramics, planar inductor, high power density, high frequency, Point-of-Load converter

Low-Profile Magnetic Integration for High-Frequency Point-of-Load Converter

Qiang Li

(Abstract)

Today, every microprocessor is powered with a Voltage Regulator (VR), which is also known as a high current Point-of-Load converter (POL). These circuits are mostly constructed using discrete components, and populated on the motherboard. With this solution, the passive components such as inductors and capacitors are bulky. They occupy a considerable footprint on the motherboard. The problem is exacerbated with the current trend of reducing the size of all forms of portable computing equipment from laptop to netbook, increasing functionalities of PDA and smart phones. In order to solve this problem, a high power density POL needs to be developed. An integration solution was recently proposed to incorporate passive components, especially magnetic components, with active components in order to realize the needed power density for the POL. Today's discrete VR only has around 100W/in^3 power density. The 3D integration concept is widely used for low current integrated POL. With this solution, a very low profile planar inductor is built as a substrate for the active components of the POL. By doing so, the POL footprint can be dramatically saved, and the available space is also fully utilized. This 3D integrated POL can achieve 300-1000W/in^3 power density, however, with considerably less current. This might address the needs of small hand-held equipment such as PDA and Smart phone type of applications. It does not, however, meet the needs for such applications as netbook, laptop, desk-top and server applications where tens and hundreds of amperes are needed. So, although the high density integrated POL has been demonstrated at low current level, magnetic integration is still one of the toughest barriers for integration, especially for high current POL.

In order to alleviate the intense thirst from the computing and telecom industry for high power density POL, the 3D integration concept needs be extended from low current applications to high current applications. The key technology for 3D integration is the low-profile planar inductor design. Before this research, there was no general methodology to analyze and design a low-profile planar inductor due to its non-uniform flux distribution, which is totally different as a conventional bulky inductor. A Low Temperature Co-fired Ceramic (LTCC) inductor is one of the most promising candidates for 3D integration for high current applications. For the LTCC inductor, besides the non-uniform flux, it also has non-linear permeability, which makes this problem even more complicated. This research focuses on penetrating modeling and design barriers for planar magnetic to develop high current 3D integrated POL with a power density dramatically higher than today's industry products in the same current level.

In the beginning, a general analysis method is proposed to classify different low-profile inductor structures into two types according to their flux path pattern. One is a vertical flux type; another one is a lateral flux type. The vertical flux type means that the magnetic flux path plane is perpendicular with the substrate. The lateral flux type means that the magnetic flux path plane is parallel with the substrate. This analysis method allows us to compare different inductor structures in a more general way to reveal the essential difference between them. After a very thorough study, it shows that a lateral flux structure is superior to a vertical flux structure for low-profile high current inductor design from an inductance density point of view, which contradicts conventional thinking. This conclusion is not only valid for the LTCC planar inductor, which has very non-linear permeability, but is also valid for the planar inductor with other core material, which has constant permeability.

Next, some inductance and loss models for a planar lateral flux inductor with a non-uniform flux are also developed. With the help of these models, different LTCC lateral flux inductor structures (single-turn structure and multi-turn structures) are compared systematically. In this comparison, the inductance density, winding loss and core loss are all considered. The proposed modeling methodology is a valuable extension of previous uniform flux inductor modeling, and can be used to solve other modeling problems, such as non-uniform flux transformer modeling.

After that, a design method is proposed for the LTCC lateral flux inductor with non-uniform flux distribution. In this design method, inductor volume, core thickness, winding loss, core loss are all considered, which has not been achieved in previous conventional inductor design methods. With the help of this design method, the LTCC lateral flux inductor can be optimized to achieve small volume, small loss and low profile at the same time. Several LTCC inductor substrates are also designed and fabricated for the 3D integrated POL. Comparing the vertical flux inductor substrate with the lateral flux inductor substrate, we can see a savings of 30% on the footprint, and a much simpler fabrication process. A 1.5MHz, 5V to 1.2V, 15A 3D integrated POL converter with LTCC lateral flux inductor substrate is demonstrated with 300W/in^3 power density, which has a factor of 3 improvements when compared to today's industry products.

Furthermore, the LTCC lateral flux coupled inductor is proposed to further increase power density of the 3D integrated POL converter. Due to the DC flux cancelling effect, the size of LTCC planar coupled inductor can be dramatically reduced to only 50% of the LTCC planar non-coupled inductor. Compared to previous vertical flux coupled inductor prototypes, a lateral flux coupled inductor prototype is demonstrated to have a 50% core thickness reduction. A

1.5MHz, 5V to 1.2V, 40A 3D integrated POL converter with LTCC lateral flux coupled inductor substrate is demonstrated with 700W/in^3 power density, which has a factor of 7 improvements when compared to today's industry POL products in the same current level.

In conclusion, this research not only overcame some major academia problems about analysis and design for planar magnetic components, but also made significant contributions to the industry by successfully scaling the integrated POL from today's 1W-5W case to a 40W case. This level of integration would significantly save the cost, and valuable motherboard real estate for other critical functions, which may enable the next technological innovation for the whole computing and telecom industry.

To My Parents

Jilin Li

Yumei Xu

Acknowledgments

With sincere appreciation in my heart, I would like to express my gratitude and appreciation to the following people, without whom this dissertation would not have been possible.

In particular, I am very grateful to my advisor and mentor, Professor Fred C. Lee, for his advising and encouragement. His extensive knowledge, broad vision and creative thinking have been a source of inspiration for me throughout the years. It was an invaluable learning experience to be his student. From him I have learned not only the extensive knowledge, but also the research and working attitude. "Never stop challenging yourself", "Always go back to your first assumption" I will always keep these valuable words in my mind.

A lot of this work was a team effort. I am grateful to the whole Integrated Power Supply (IPS) group including Mr. David Gilham, who helped LTCC inductor and 3D integrated converter fabrication; Dr. Arthur Ball, who helped 3D integrated converter design; Dr. Michele Lim, Dr. Yan Dong, and Mr. Yipeng Su, who helped LTCC inductor design and testing; Mr. Mingkai Mu, and Dr. Feng Zheng, who helped LTCC inductor core loss testing and simulation. Without your help, I could not have completed this work in such a short amount of time.

I should give my special thanks to Dr. Ming Xu, for his teaching and support. I have learned a lot from him, not only from his research, but also from his daily life. Besides a professor, he is also a good friend and big brother to me.

I also want to acknowledge the other members of my advisory committee, Dr. Paolo Mattavelli, Dr. Guo-Quan Lu, Dr. Dong S. Ha, and Dr. Michael S. Hsiao, for their suggestions and encouragement throughout this entire process.

It has been a great pleasure to work with the talented and dedicated colleagues in the Center for Power Electronics Systems (CPES). I am especially want to thanks my colleagues in the Power Management Consortium (PMC) group: Dr. Shuo Wang, Dr. Yang Qiu, Dr. Juanjuan Sun, Dr. Kisun Lee, Dr. Julu Sun, Dr. Chuanyun Wang, Dr. Dianbo Fu, Dr. Yan Jiang, Dr. Jian Li, Mr. Doug Sterk, Mr. David Reusch, Mr. Yucheng Ying, Dr. Ke Jin, Mr. Bin Huang, Mr. Ya

Liu, Mr. Yi Sun, Dr. Pengju Kong, Mr. Pengjie Lai, Mr. Zijian Wang, Mr. Qian Li, Mr. Daocheng Huang, Dr. Xiaoyong Ren, Mr. Shu Ji, Dr. Xinke Wu, Mr. Feng Yu and Mr. Yingyi Yan, Mr. Weiyi Feng, Mr. Shuilin Tian, Mr. Haoran Wu, Mr. Wei Zhang, Mr. Li Jiang. It was a pleasure and my honor to work with such a talented and creative team. My thanks also go to all of the other students and visiting scholars I have met in CPES during my five-year study. Their friendships and help have made my stay at CPES pleasant and enjoyable.

I would also like to give special mention to the wonderful members of the CPES staffs who were always willing to help me out, Ms. Linda Gallagher, Ms. Teresa Shaw, Ms. Trish Rose, Mr. Robert Martin, Ms. Linda Long, Ms. Marianne Hawthorne, and Mr. Jamie Evans. I also owe a debt of the deepest gratitude to Ms. Keara Axelrod and Ms. Suzanne Farmer, who offered me a great help in polishing my writing.

My deepest appreciation goes toward my father Jilin Li and mother Yumei Xu, who has always been there with their love, support, understanding and encouragement for all my endeavors. Your love and encouragement has been the most valuable thing in my life.

This work was supported by the Power Management Consortium (Delta Electronics, Texas Instruments, Intel, Intersil, International Rectifier, Linear Technology, National Semiconductor, NXP Semiconductors, Emerson Network Power, Huawei Technologies, Hipro Electronics, Lite-On Technology, Monolithic Power Systems, Richtek Technology, Infineon, OSRAM Sylvania, FSP, Primarion, Renesas, and Maxim Integrated Products, Analog Devices), and the Engineering Research Center Shared Facilities supported by the National Science Foundation under NSF Award Number EEC- 9731677. This work was also conducted with the use of Maxwell software, donated in kind by Ansoft Corporation of the CPES Industrial Consortium.

Table of Contents

List of Figures

List of Tables

Chapter 1. Introduction

1.1 Background of High-Current POL for Computing Applications

Responding to Intel®'s request in 1997, CPES developed the multi-phase voltage regular module to power the new generation of microprocessors, which had a drastic increase in current demand and operated with a much lower voltage and a higher data processing rate than the previous generation of microprocessor [1]-[4]. Today every processor is powered with one of these multi-phase VR's. The design is scalable with each phase providing a 20-25A current. The number of phases (modules) has increased from 1 to 8-10 phases over the past decade. These circuits are mostly constructed using discrete components and attached to the motherboard. In order to achieve a circuit efficiency of around 85%, the circuit is operated at a lower frequency; around 200-600 kHz.

Passive components such as inductors and capacitors are bulky. They occupy a considerable foot-print on the motherboard, as shown in Figure 1.1. This problem is exacerbated by the current trend of reducing the size of all forms of portable computing equipment from notebooks to netbooks, increasing functionalities of smart phones, as well as the increasing use of cloud computing instead of a more traditional network-based computing. Recently, industry leaders such as IBM and Cisco have been promoting the idea of replacing these embedded VR solutions with plug-in modules, namely "power blocks" to save the motherboard real estate for other critical functions. With this concept, the power stage of the VR is built outside of the motherboard as an unregulated power block; only the control and output capacitor remain on the motherboard.

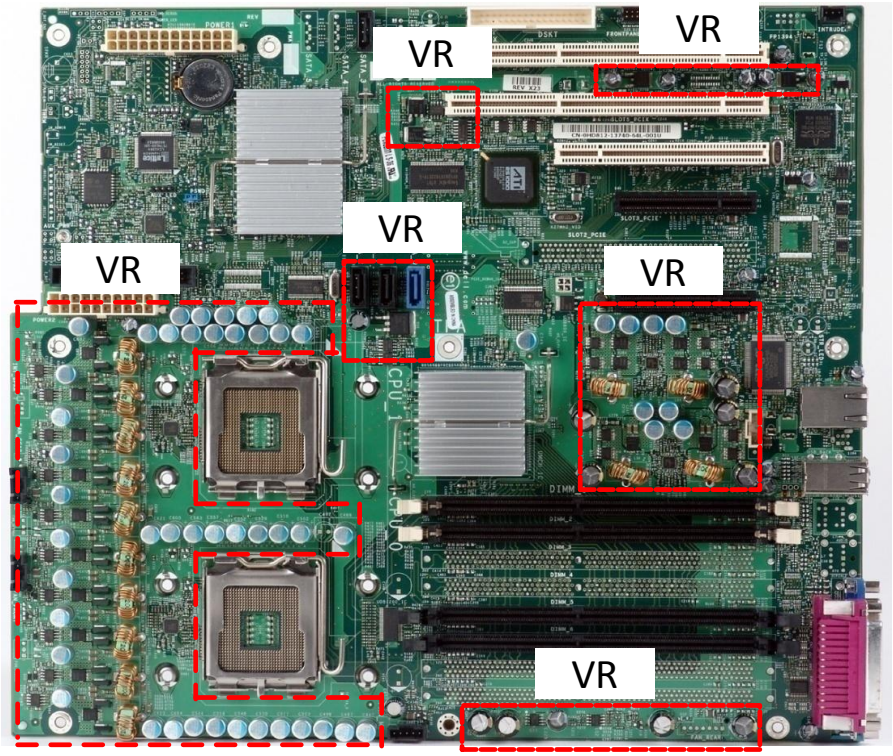

Figure 1.1 30% of the area of the motherboard is occupied by the VR

Figure 1.2 shows a 20A power block product from Delta Electronics [5]. In Figure 1.2, it can be seen that the magnetic component is the most bulky component of today's power block products. In order to dramatically save motherboard space, the magnetic components of the power block must be made significantly smaller than has been demonstrated to date. To achieve these goals two things have to happen simultaneously; one is a significant increase in the switching frequency to reduce the size and weight of magnetic components. The second is to integrate magnetic components with active components to realize the needed power density. Today, this concept has been demonstrated at a level less than 5A and a power density around 700W/in^3. This might address the need of small hand-held equipment such as PDAs and smart phones, but it is far from meeting the needs for such applications as netbooks, notebooks, desktop and server applications where tens and hundreds of amperes are needed. New integration technology should be developed to achieve an unprecedented 15-40A level integrated converter

with a power density greater than 700W/in^3 to free up significant motherboard space for other critical functions.

Figure 1.2 Power block module from Delta Electronics

1.2 The State of the Art of Integrated Converters

Figure 1.3 shows power density as a function of output current in today's POL products. The integrated POLs shown in Figure 1.3 can achieve 700-1000W/in^3 power density; however, with considerably less current (<5A) than previous POLs. The power density of the POL is reduced as the current increases. With a 5A-20A output current, most POL products are built as capsulated modules, and the power density is around 200-500W/in^3. With a large output current (>20A), POL products are built as discrete converters, and the power density is around 100W/in^3. Figure 1.4 shows two integrated POL commercial products with very low output current. Figure 1.4(a) is a 500mA micro DC-DC converter from Fuji Electric Device Technology Co., Ltd., which fully integrates a ferrite inductor with a silicon IC [6]. Figure 1.4(b) is National Semiconductor's 650mA DC-DC converter [7]. It can be seen that for low-output current application, the inductor can be made to be small enough to be placed on back of the IC die and serve as a substrate, which is defined as 3D integration.

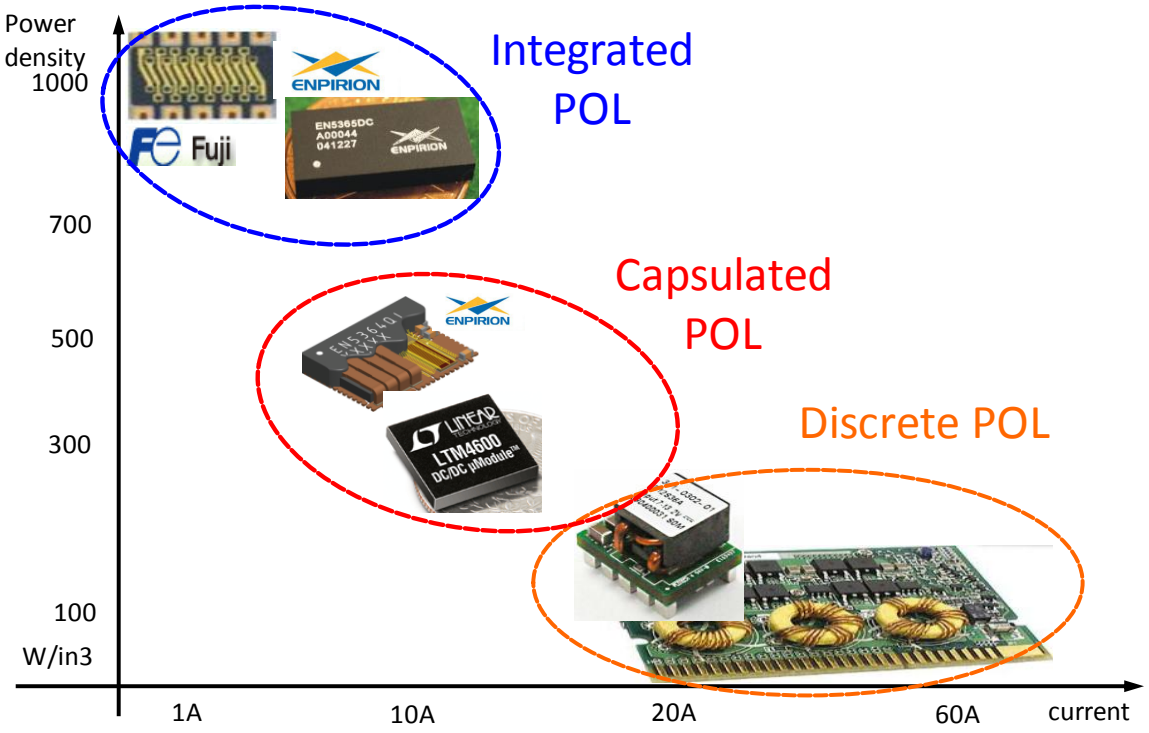

Figure 1.3 Power density of today's POL products

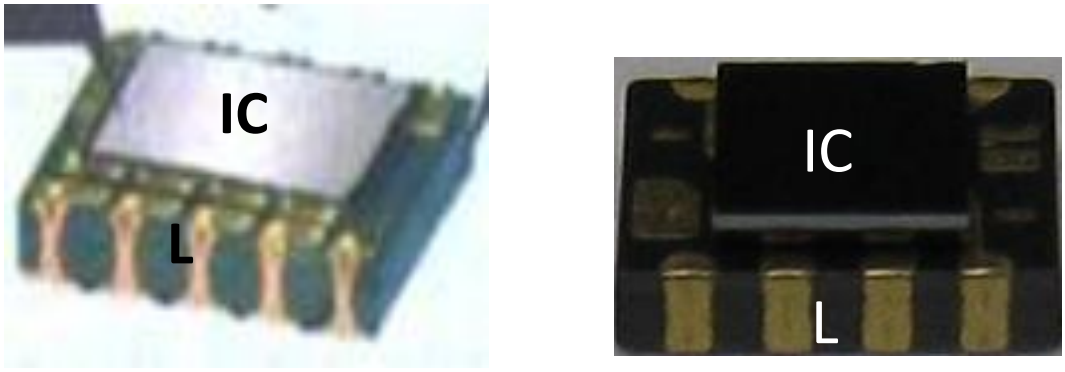

(a) (b)

Figure 1.4 Integrated POL commercial products with very low output current: (a) 500mA micro DC-DC converter from Fuji Electric Device Technology Co., Ltd., (b) National Semiconductor's 650mA DC-DC converter

Figure 1.5 shows an internal image of two capsulated POLs for higher-current applications. Figure 1.5(a) shows Enpirion's 9A POL converter EN5396 [8]. Figure 1.5(b) is Linear

Technology's 12A POL converter LT4601[9]. In this case, the inductor is located next to the IC die due to its large physical size, thus causing the power density to suffer. At a higher current level, the POL is usually manufactured using discrete components and operating at significantly lower switching frequencies (300kHz-600kHz), thus resulting in much larger passive components. A typical example is the voltage regulator modules currently used for powering the new generation of microprocessors. Normally, today's discrete VRM only have around 100W/in^3 power density.

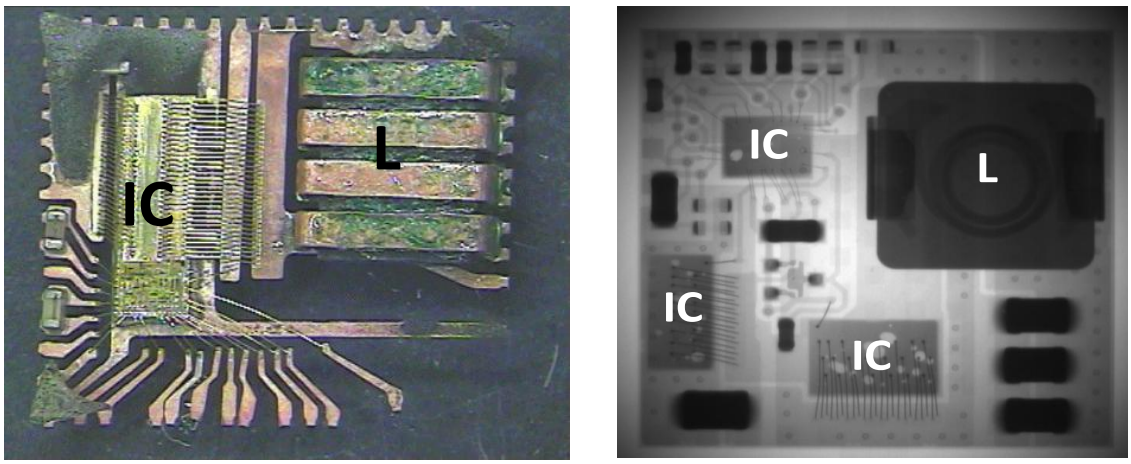

(a) (b)

Figure 1.5 Internal images of two capsulated POLs for higher current applications: (a) Enpirion's 9A POL converter EN5396, (b) Linear Technology's 12A POL converter LT4601

As a conclusion, with low current, today's industry can perform integration to achieve very high-density and compact POLs, but with high current, it is very difficult to integrate the inductor with a silicon IC by using state-of-the-art technology. Basically, the bulky and high-profile inductor is the bottleneck for high-current integration. For high-current applications, inductors need to store large amounts of energy, so the core size is normally very bulky. Furthermore, the large inductor current also requires large winding to reduce winding loss. Generally speaking, these two reasons make it much more difficult to integrate inductors for

high-current applications than for low-current applications. In order to reduce the size of these bulky inductors to make them easy to integrate, several technology barriers must be overcome. First, the switching frequencies of these high-current POLs need to be increased from several hundred kHz to several MHz to reduce the required inductance. Second, better packaging and integration methods should be developed for high-current applications. Third, a novel inductor structure needs be developed to achieve a low profile, high inductance density, and low loss for high-current inductors.

1.3 The State of the Art of Device Technologies for High-Frequency Applications

Over the years, power-MOSFETs have become the power device of choice for many applications. Through several decades, MOSFETs have continued to evolve. From planar HEXFETs to trench FETs and super-junction FETs, silicon-based MOSFETs have made dramatic improvement in figures of merit (FOMs) to effectively serve a variety of applications.

For low-voltage applications, Figure 1.6 shows that VDMOS is usually used with POL applications with a voltage greater than 30V. When the rated voltage is less than 30V, trench MOSFETs and lateral MOSFETs are widely used in today's POL applications. Generally speaking, a lateral device is used with low voltage (<20V) and low current (<10A), and it can be operated at a frequency above 1MHz. Today’s best 7V lateral MOSFET module is capable of running at 5MHz with a 1A current but with a buck conversion ratio of only 2-3. For a 30V application, the trench MOSFET is the most popular choice. However, today's best 30V trench MOSFET module usually operates at less than 600 kHz with 25A current.

Around 2008, the lateral trench MOSFET, which is best used with a voltage range from 15V to 25V and a current level similar to the trench MOSFET, was introduced by industry. Its FOM is almost half that of the trench MOSFET. This newcomer, the lateral-trench MOSFET, has some potential to fill this application gap between lateral and trench devices. To meet ever-increasing market needs in power MOSFETs, International Rectifier has developed GaNpowIR™, a gallium nitride (GaN) based power device technology platform that promises to deliver performance FOMs ten times better than the existing state-of-the-art silicon devices, and has very promising potential for high-frequency applications [10].

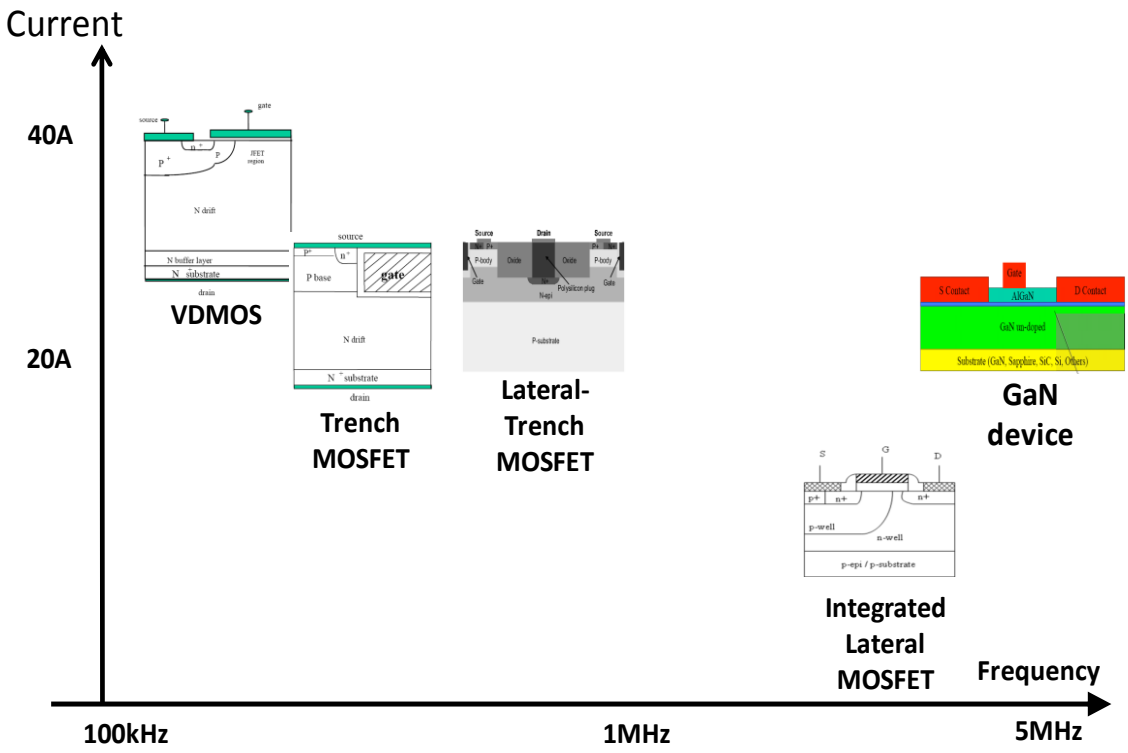

Figure 1.6 Operating frequency and current range for different power MOSFET

The different packaging methods used in different ways to connect the MOSFET die to the pins cause different packaging parasitic inductances, which also greatly impact device switching

loss [11]. Besides the FOM of the die, different packaging methods will also have a significant impact on device performance [12]. Figure 1.7 shows three major commercial packaging methods for a 30V MOSFET; the SO-8, the LFPAK and the DrMOS. The DrMOS packaging method integrates the MOSFET and the driver. By integrating these components, it is possible to locate the driver very close to the MOSFET, and minimize the gate-driving loop. Therefore, the common-source parasitic inductance (Ls) can be greatly reduced to 0.1nH.

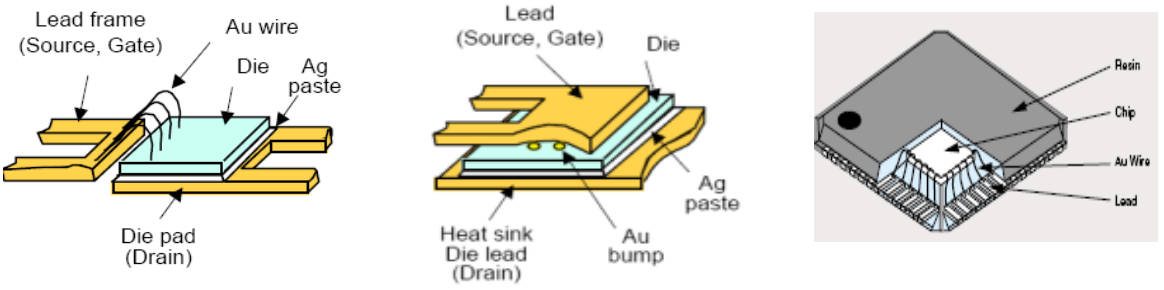

Figure 1.7 Commercial packaging methods and their parasitic inductances: (a) SO8 (b) LFPAK (c) DrMOS

In order to make a performance comparison between different packaging methods, [12] evaluated the device loss for a Renesas RJK0305DPB MOSFET die [13] with different packaging methods. Figure 1.8 shows the loss breakdown with the different packaging. The circuit conditions are: V_{in}=12V, V_o=1.2V, I_o=20A, and F_s=600kHz. In [12], the losses due to packaging parasitic inductances Ls and Ld are packaging-related; and the Qgs2 and Qgd-related loss, conduction loss, and gate driving loss are all silicon-die-related. From the loss breakdown, it can be seen that by changing from the SO-8 package to the LFPAK, the packaging-related loss can be greatly reduced due to the smaller parasitic inductance Ls. However, the Ls-related loss is still a dominant part of the total loss. The silicon-die-related loss and the packaging-related loss

are almost half and half. The DrMOS packaging method can further improve the performance by further reducing Ls. From Figure 1.8, it can be seen that the packaging-related loss of the DrMOS is no longer a dominant part of the total loss. In this case the silicon-die-related loss is more important than the packaging-related loss.

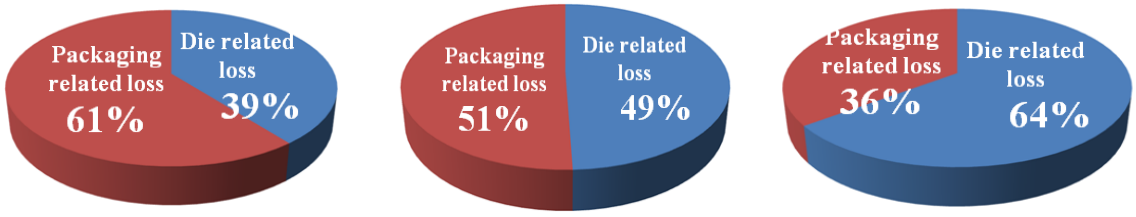

(a) (b) (c)

Figure 1.8 Loss Breakdown in terms of packaging and die related losses for Renesas RJK0305DPB MOSFET die with different packaging: (a) SO8, (b) LFPAK, (c) Dr.MOS

Figure 1.9 shows other packaging methods, IR DirectFET and Vishay PolarPak packaging, which also provide low losses. As a result, they also have potential for use in high-frequency operations. In order to reduce the parasitic inductance to reduce switching-related loss, an integrated POL has been introduced by many companies, such as TI, Maxim, Linear Tech, and National Semiconductor. These POLs integrate all the active components into one chip, which can not only reduce the parasitic inductance, but also make the converter more compact. The frequency of these integrated POLs has been pushed from several hundred kHz to several MHz. Figure 1.10 shows the working frequency and current range for today's power MOSFET products. It can be seen that today's trench MOSFET with advanced packaging, a lateral-trench MOSFET and a GaN device all can be used to build a high-current POL with several MHz switching frequency. Thus, generally speaking, the semiconductor devices are no longer a bottleneck for developing high-frequency, high-density integrated converters.

Ls=0.1nH Ls=0.1nH

(a) (b)

Figure 1.9 Other packaging methods with low Ls: (a) DirectFET from IR, (b) PolarPak from Vishay

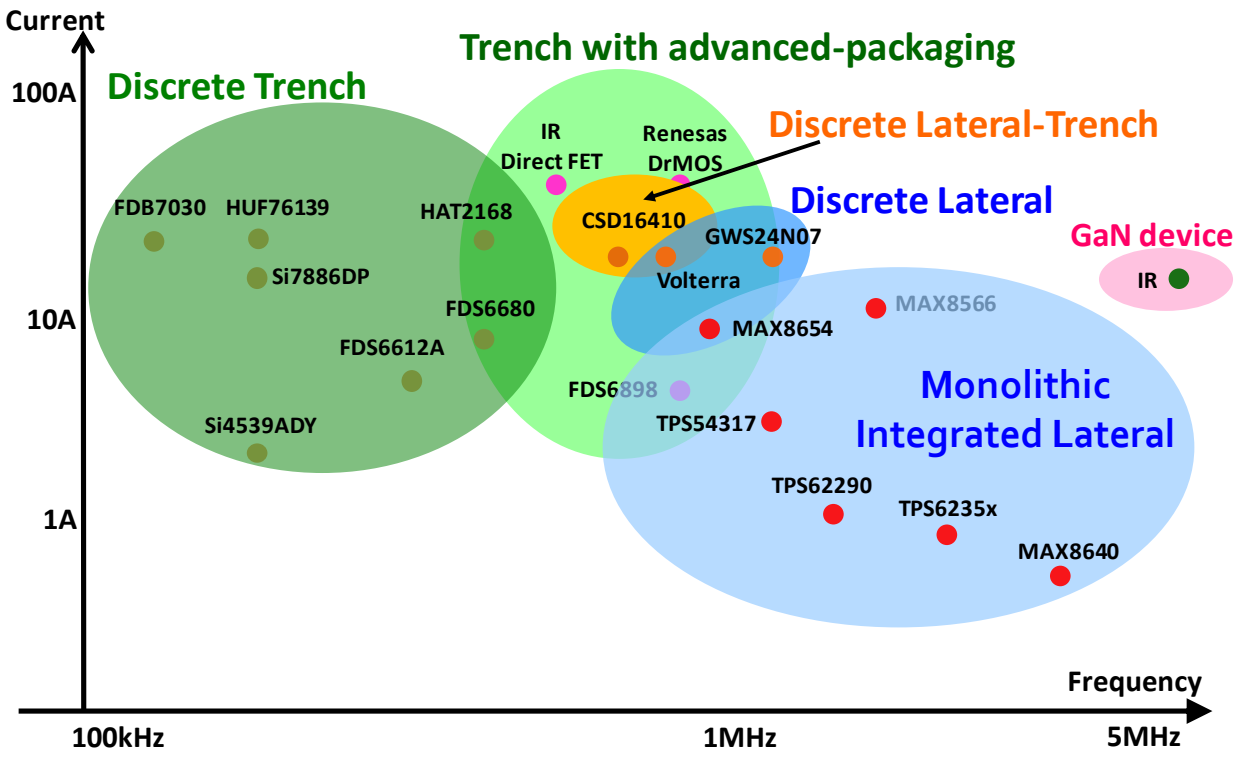

Figure 1.10 Operating frequency and current range for today's power MOSFET products

1.4 The State of the Art of High-Frequency Magnetic Material

As mentioned in the previous section, semiconductor devices have been prominent in the efforts towards improvements in power electronics systems. With miniaturization and improvements in device performance, the development of power electronics systems has progressed to a state where the active devices' impact on the system's size and cost has been taken over by the passive components. Magnetic components have been one of the bulkiest components, taking up significant circuit surface area. With further demands for miniaturization in power transformers and inductors, magnetic-core materials with low energy losses and high flux densities, permeability, and operating frequencies are in high demand.

Using detailed survey results of magnetic materials, this section identifies some magnetic materials that are promising for high-frequency integrated converter applications. Figure 1.11 is the possible working frequency range for different magnetic materials. Among the commercial products, Fe-based powders, including Kool Mu materials, typically operate below 1MHz; and the MnZn ferrite cannot be operated beyond 5 MHz; NiZn ferrite is almost the only material that can be used at frequencies as high as 10MHz. Besides these commercial magnetic materials, there is much ongoing research trying to develop some new magnetic materials for high-frequency and integration applications, such as granular film material CoZrO, polymer-bonded materials, thin film alloy such as CoNiFe, and low-temperature co-fired ceramics (LTCC) ferrite.

In granular films, magnetic particles are embedded in oxide insulating matrix phases, which results in high dc resistivity. CoZrO is one of the granular film materials. This material can have constant resistivity (590 μohm·cm) up to 20MHz [14].

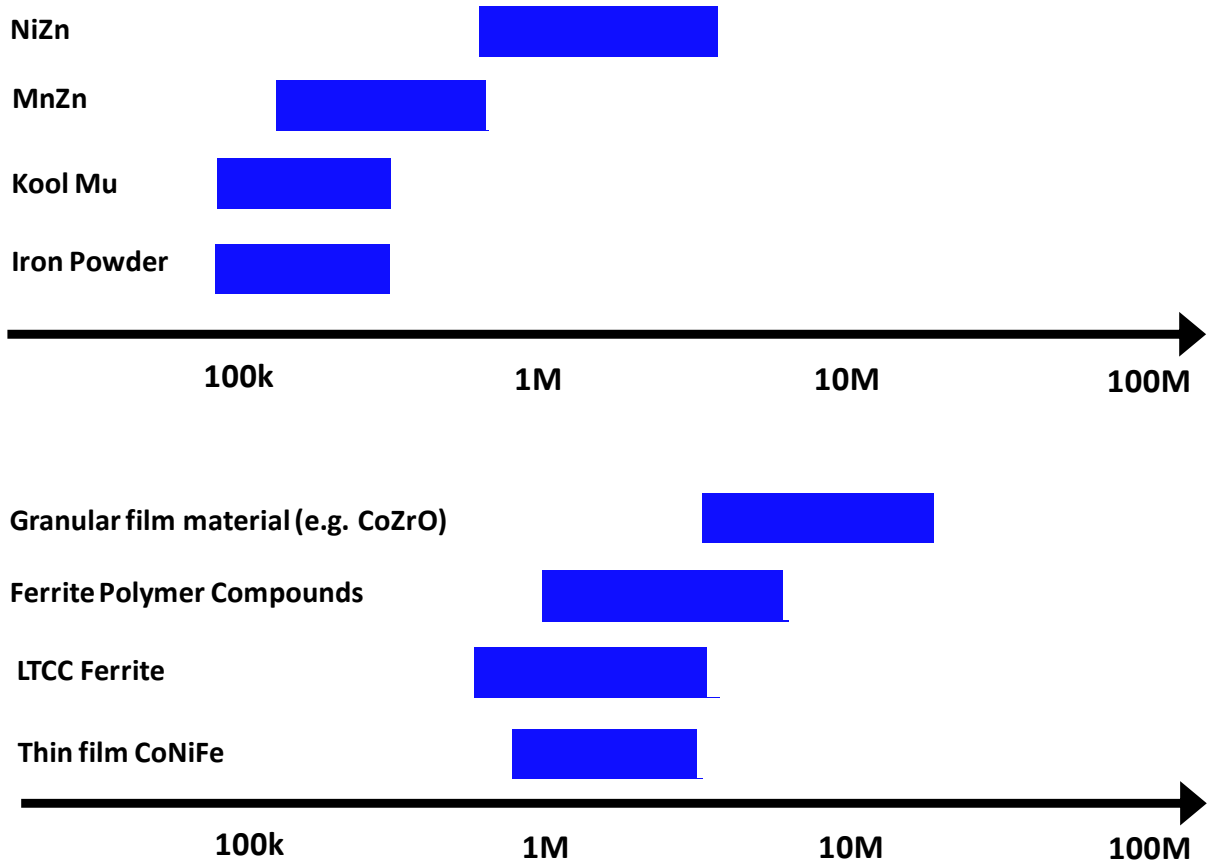

Figure 1.11 Possible working frequency ranges for different magnetic materials

The polymer-bonded magnetic material is composed of polymer matrices and magnetic powders which can be produced by traditional polymer processing methods. One of the important advantages of polymer-bonded magnetic material is the ease of molding, such as injection molding, which can save on manufacturing costs. Ferrite polymer is one promising polymer bonding material for high-frequency applications. Since it has a higher resistivity than other magnetic materials, eddy current losses are reduced [15]. The electroplated alloy CoNiFe was first introduced for magnetic recording applications. Later on it has been used for power conversion applications. In fact, because CoNiFe is a metal alloy magnetic material, it should be designed very carefully to reduce eddy current loss. According to [16], when the core thickness is reduced to 2.4μm, the CoNiFe can have core loss density as low as NiZn ferrite 4F1. The

LTCC ferrite material is actually ferrite particles mixed with a ceramic tape material. The thin, flexible LTCC tape layers can be stacked together in various shapes, pressed, and then fired in an oven to create a hard ferrite structure [17][18]. Compared with traditional ferrite material such as NiZn ferrite, LTCC ferrite can have almost the same permeability and core loss density, but it has much more flexibility for building integrated magnetic components [19].

Figure 1.12 shows the frequency dependence of initial permeability for different magnetic materials. It is clear that the emerging material developed by ongoing research can have constant permeability at higher frequencies than conventional materials. There are several magnetic materials that can even have constant permeability up to more than 20MHz, such as granular film CoZrO, and NiZn ferrite 4F1 from Ferrocube.

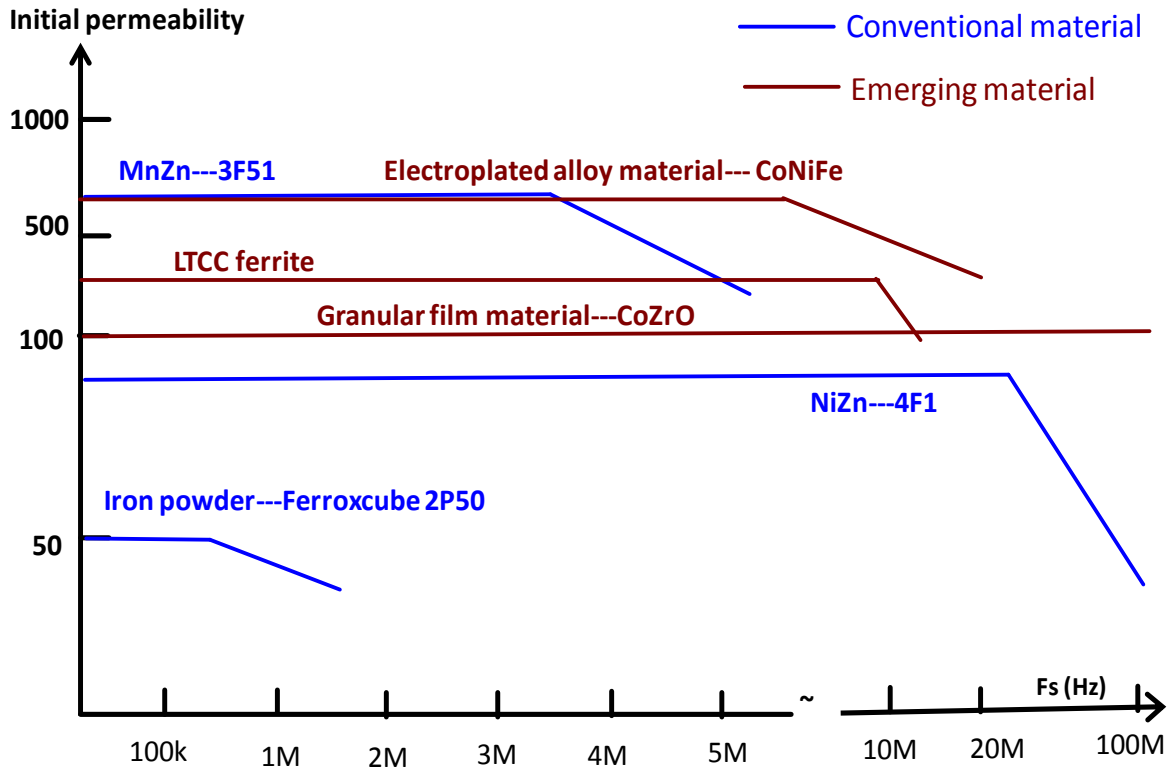

Figure 1.12 Frequency dependence of initial permeability for different magnetic materials

Figure 1.13 shows the core loss density of different magnetic materials. It can be seen that at high frequencies, the granular film CoZrO, NiZn ferrite 4F1 LTCC ferrite and thin film alloy CoNiFe have lower core loss densities than other materials. At higher frequencies, CoZrO granular films of less than 10μm thick have the lowest core loss; CoNiFe thin films also have acceptable losses. However, it is not economically viable to grow multilayered materials of mm thickness using vacuum deposition, making these materials unsuitable for high-power applications. Among above mentioned magnetic materials, the LTCC ferrite has already been demonstrated to be a good candidate for high-current, high-frequency and integration applications [18]. Thus, in this dissertation, LTCC ferrite is chosen as the magnetic material to develop advanced integrated magnetic components.

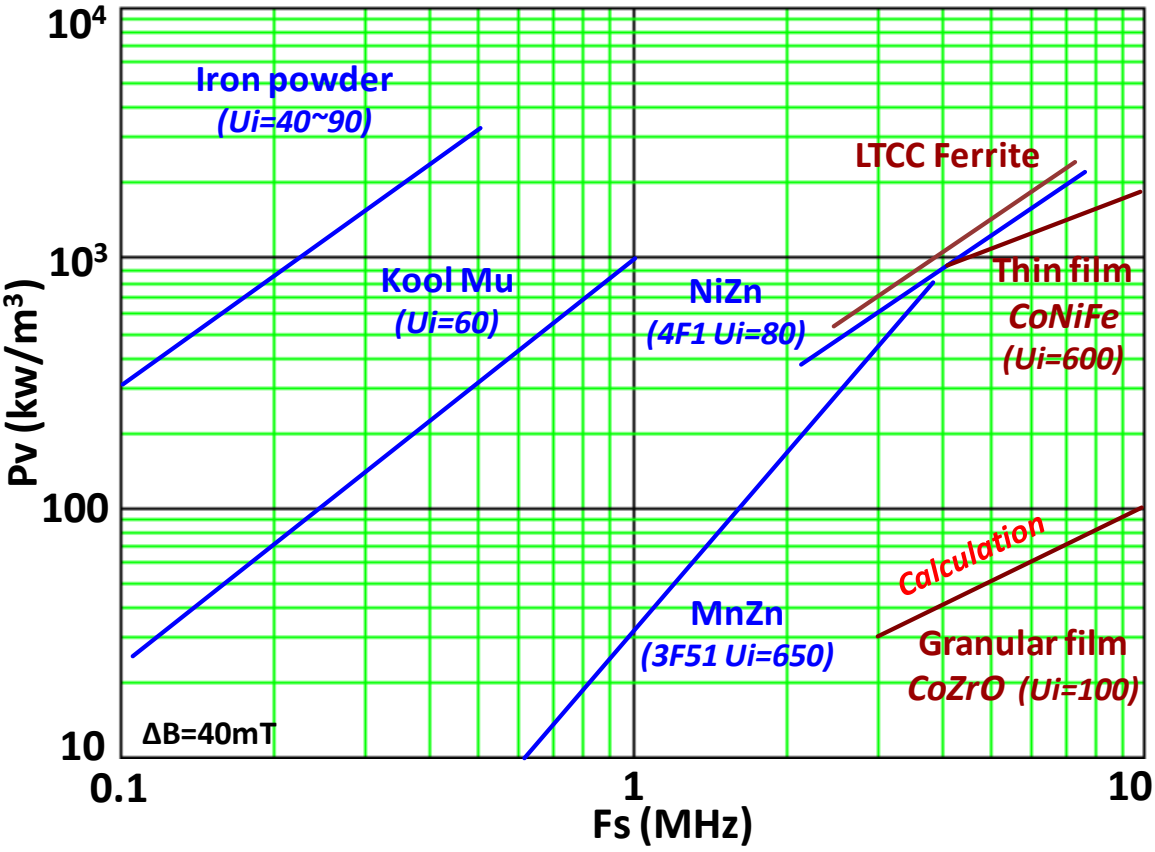

Figure 1.13 Core loss density of different magnetic materials

1.5 Available Technologies for Magnetics Integration

In view of the numerous techniques available for magnetic integration, the integration techniques can be classified into the following categories: 1) Wafer-level integration; 2) Package-level integration; and 3) Board-level integration. Figure 1.14 shows the total survey results of the integrated converter with different magnetic integration methods. Figure 1.14 shows that from low integration levels (board-level) to high integration levels (wafer-level), the output current is reduced and the frequency is increased.

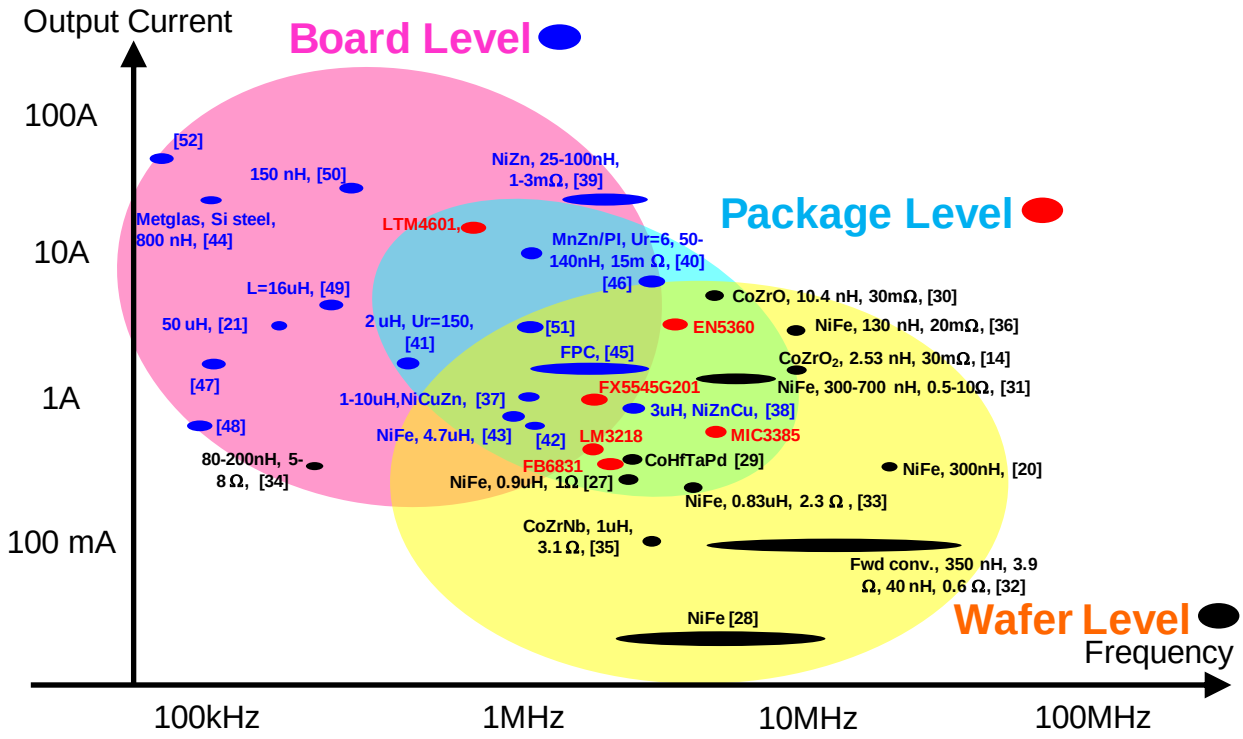

Figure 1.14 Output current and operating frequency of integrated converter with different magnetic integration methods

For wafer-level integration, the inductor or transformer is built in or on the silicon die. The processes are compatible with silicon processing. For magnetics built on the silicon die, the magnetics can be fabricated on top of the active circuitry, which reduces the footprint. For

magnetics fabricated in the silicon, the active circuit is built beside the magnetics on the same die. Figure 1.15 shows the survey results of an integrated converter with wafer-level integration. From Figure 1.15, it can be seen that the current level of magnetics on silicon is generally lower than the current level of magnetics in silicon. The current range using on-silicon magnetics is more suitable for operation at less than 1 A. The current capability of the magnetic component can be improved by forming conductors of larger cross-sectional areas in the silicon. For in-silicon magnetics, the current level can be increased to several amperes.

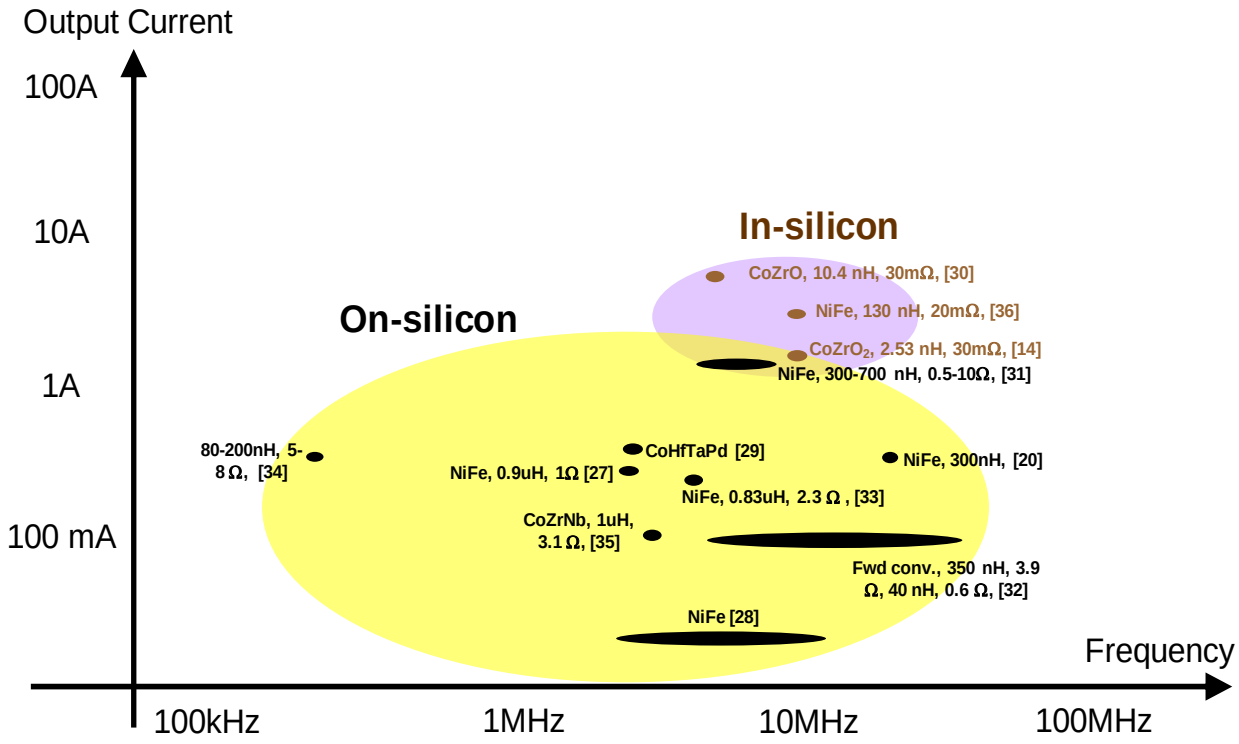

Figure 1.15 Output current and operating frequency of integrated converter with wafer-level integration

Figure 1.16 shows one example of magnetic integration on silicon demonstrated by the Tyndall National Institute [20]. The magnetic material is an alloy of nickel and iron that is deposited on the silicon surface by electroplating. The thickness of the layer of magnetic material is determined by the design, and is generally limited to less than 10 μm to limit the eddy current

loss. The entire process consists of 5 mask layers. The inductor coil consists of electroplated copper which can be deposited to a maximum thickness of 50 µm. Due to this coil thickness limitation, this inductor only can handle around 500mA of current. Figure 1.17 shows another example of magnetic integration in silicon demonstrated by Dartmouth University [14]. A V-shaped groove is etched into the silicon. The CoZrO granular films, magnetic material, insulator and conductor are deposited into the groove. The cross-sectional area of the conductor is determined by the cross-sectional area of the groove, which is relatively large. So, this inductor can handle around 7A current.

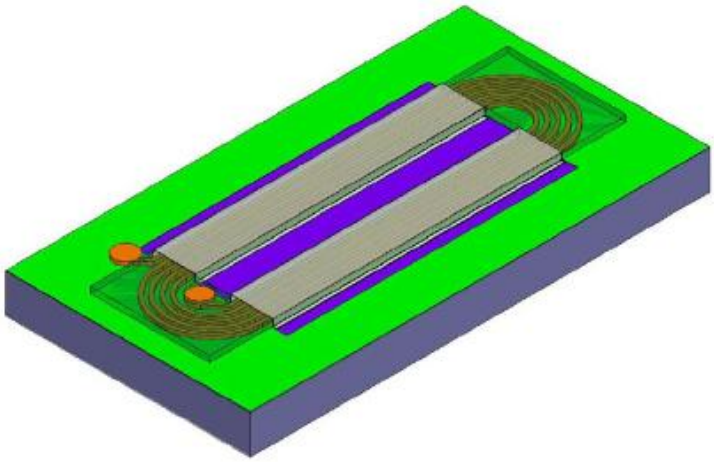

Figure 1.16 Integrated micro-inductor on a silicon substrate demonstrated by Tyndall National Institute [20]

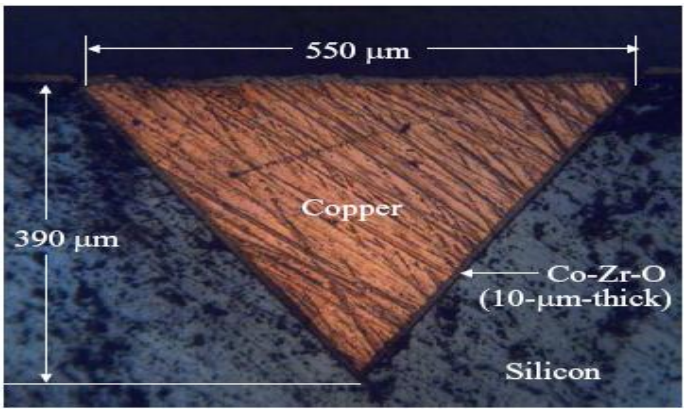

Figure 1.17 V-groove on chip inductor with large copper cross-sectional area to improve current capability of the on-chip inductor demonstrated by Dartmouth University [14]

The package-level integration also can be called capsulated integration. With this technology, the magnetic component is co-packaged side-by-side with the silicon die or used as a platform for the silicon device and connected internally within the package. There are currently many industry products with package-level integrated magnetics that come from different companies, such as Enprion, Linear Tech, National Semiconductor and Fuji. Almost all of these industry products belong to this kind of package-level integration. An example of these products can be seen Figure 1.5.

For board-level integration, the magnetic component is built on a substrate on which the active device can be mounted. Board-level integration can be classified into two categories. One is integrating the inductor / transformer in an organic-based substrate, such as PCB substrate, where the processing temperature is low (<200 °C). Another package-level integration method is integrating the component in a ceramic-based substrate where the processing temperature for the component is high (> 200 °C). The mechanical properties of the organic substrate are usually not compatible with the silicon die; for example, the PCB material FR4 has a coefficient of thermal expansion (CTE) of 17 ppm/°C, but the CTE of silicon material is only 4 ppm/°C. Thus, FR4 will have CTE mismatching problem if the silicon die is directly integrated with the PCB. For ceramic-based technology, the materials involved, such as LTCC, can support higher operating temperatures and have a CTE value around 5 ppm/°C, which is close to that of silicon.

Figure 1.18 shows the survey results of an integrated converter with board-level integration. It can be seen that there is currently a large overlap between organic-based and ceramic-based technology. However, the ceramic-based technology looks like it has more potential for higher-frequency applications because it can be compatible with a silicon die, which can achieve much closer interconnection to reduce parasitic inductance and resistance.

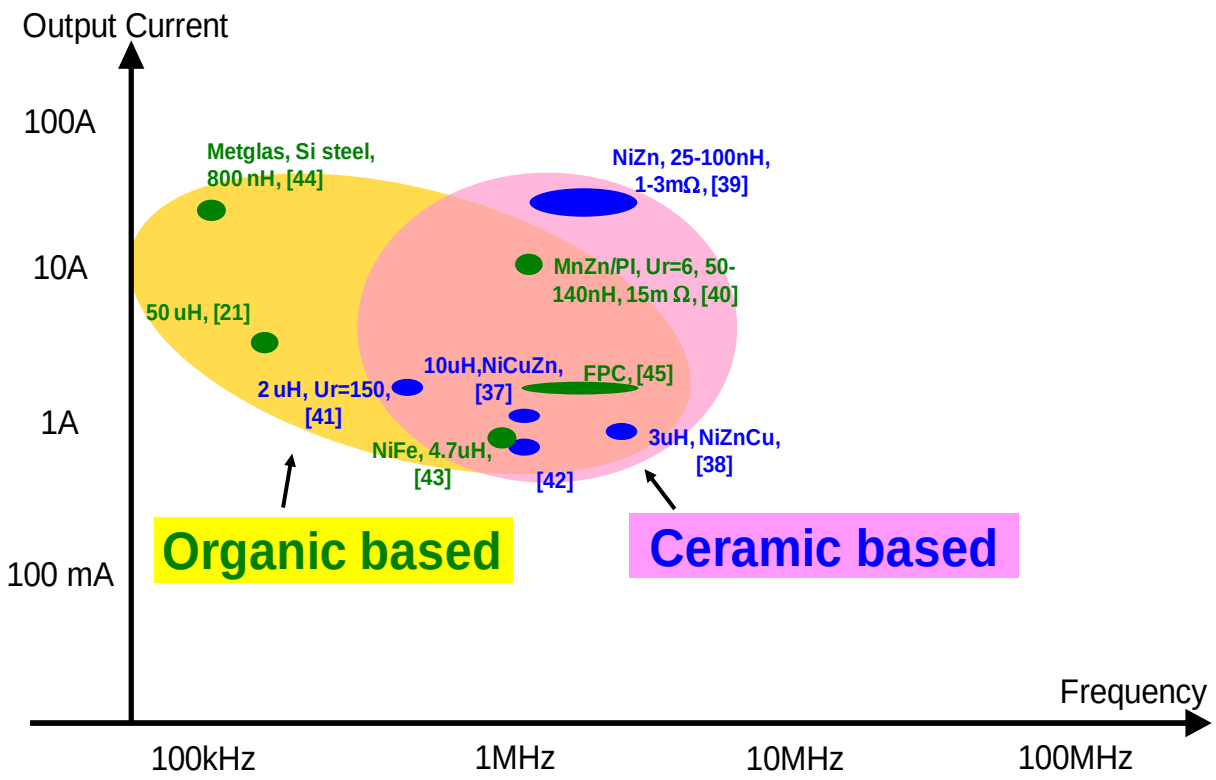

Figure 1.18 Output current and operating frequency of integrated converter with board-level integration

Figure 1.19 shows one example of an organic-based board-level integration developed by Philips [21]. In [21], a 60W PCB integrated converter was designed and fabricated. Its transformer is entirely integrated into the PCB. Standard PCB lamination processes are used for the layering of the integrated components, and the magnetic components are realized by using Maglam magnetic material for the core and PCB trace as winding. The Maglam material is a ferrite polymer compound that can be adapted for compatibility with the PCB laminating process.

Figure 1.20 shows another example of ceramic-based board-level integration developed by CPES Virginia Tech [22]. A 20W integrated POL converter was fabricated based on ceramic technology. The LTCC ferrite was used to build a very low-profile inductor, which is used as substrate for the whole converter. Direct-bonded copper (DBC) ceramics were used as active layer to carry the power device, driver and capacitors. As mentioned above, this ceramic-based

board-level integration is good for high-frequency and high-current applications: The switching frequency of this integrated POL is 1.5MHz, and the output current is 15-20A. Thus, in this dissertation, ceramic based board-level integration is used to develop high–density, high-frequency integrated POL converters.

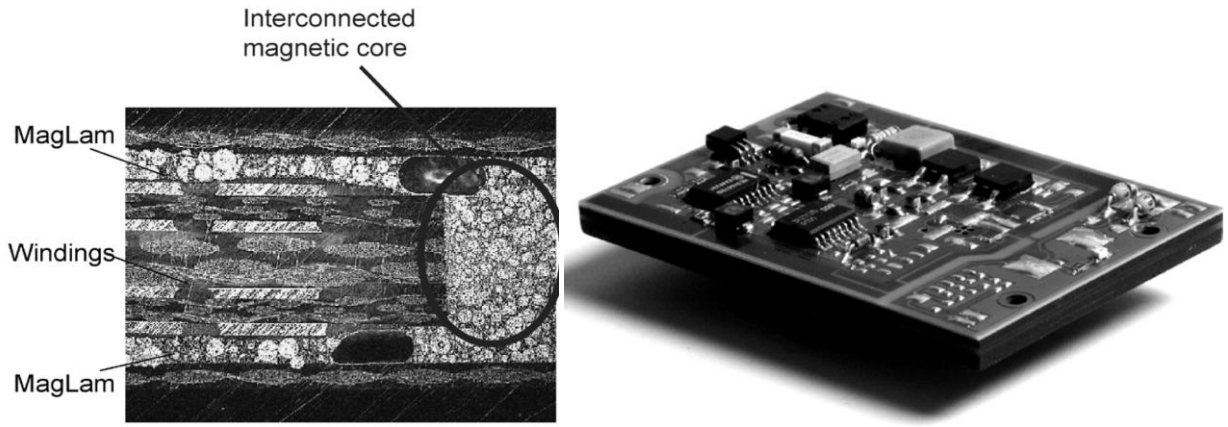

Figure 1.19 A 60W PCB integrated converter developed by Philips [21]

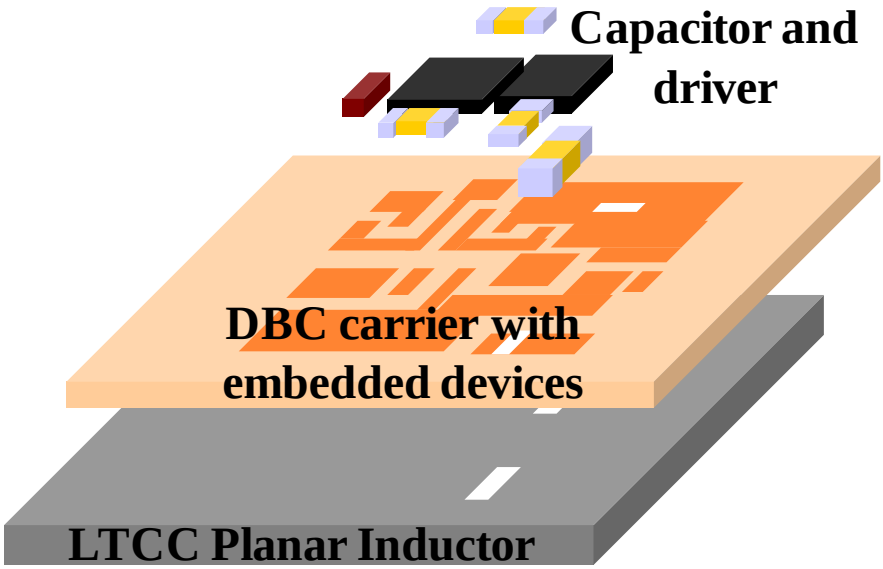

Figure 1.20 A 20W integrated POL converter fabricated based on ceramic technology developed by CPES Virginia Tech [22]

1.6 Strengths and Challenges for 3D Integration with DBC Carrier and LTCC Inductor Substrate

1.6.1 Basic Concept of 3D Integrated Converter

An example of the integrated converter with magnetic substrate shown in Figure 1.20, which shows a 3D integrated converter. The basic concept of 3D integration is to integrate the whole converter in a vertical way. First, very low profile passive layers are built as a substrate for the whole converter, and the active layers are built above the passive layers. Most active devices can be embedded into the active layer. A conceptual diagram of this 3D integration is shown in Figure 1.21. This vertical 3D integration allows for footprint saving and full space utilization, which greatly increases the converter's power density.

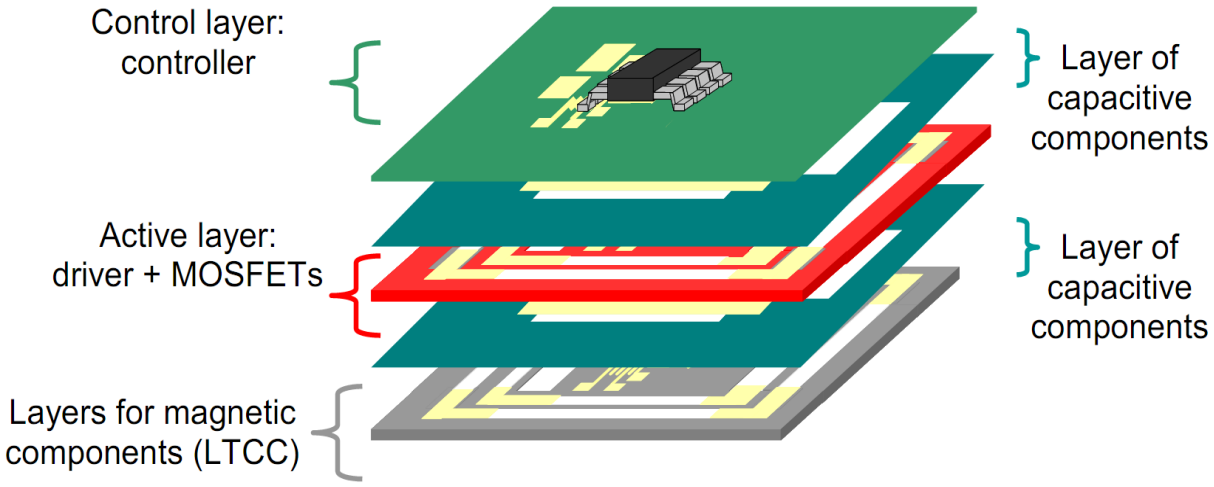

Figure 1.21 Conceptual diagram of this 3D integration

This integration concept has already been adopted by industry to build very high-density POL converters. Figure 1.4 shows two 3D integrated POL products. The first is from NSC, and the second is from Fuji. However, today's 3D integrated POL products can handle only very small amounts of current; usually below 5A. The fundamental technology barrier for extending

this 3D integration concept to high-current application is low-profile magnetic design. Reference [18] proposes the use of LTCC thick-film technology to build a low-profile inductor substrate for high-current 3D integration. Detailed information about this low-profile LTCC inductor substrate is introduced in the following section.

1.6.2 3D Integrated Converter with LTCC Inductor Substrate

The LTCC processing technique involves screen-printing conductive pastes on the surface of tapes to form conductive patterns. It is a relatively mature technology for radio-frequency (RF) applications. Many research works have been published on printing very thin conductive layers with fine pitch on LTCC tape for radio-frequency applications [23]-[25]. The LTCC processing technique has better thermo-mechanical performance than traditional PCB substrate.

Table 1.1 compares the thermo-mechanical properties of LTCC and PCB. The thermal conductivity of LTCC material is around 4, which is much better than traditional PCB material FR4. Thus, the LTCC substrate can have better thermal performance than PCB substrate. Another benefit of LTCC material is that its coefficient of thermal expansion is very close to that of silicon (CTE of silicon=3-4). Hence the mechanical stresses caused by temperature changes can be reduced when the LTCC components are integrated with silicon components, which can improve the reliability of the integrated module. Furthermore, as a thick film technology, it is very easy to use LTCC technology to fabricate a sufficiently thick magnetic core and winding for high-current applications. In summary, LTCC technology has thermo-mechanical properties suitable for integrating with silicon, and is a promising technique for low-profile electronics. It also has potential for use in low-profile magnetics integration for high-current applications. Therefore, there are many other researchers exploring LTCC for power electronics applications.

Table 1.1 Comparison of the thermo-mechanical properties of LTCC and FR4

	LTCC	FR4
Thermal conductivity (W/m°C)	2-5	0.3
CTE(ppm/°C)	4-8	17

Figure 1.22 shows the LTCC inductor developed by CPES. Figure 1.22 (a) shows a sectional drawing of this LTCC inductor. It can be seen that the winding is embedded in the LTCC core. Because this inductor needs to be sintered at 900°C, silver paste is used to build the inductor winding instead of copper.

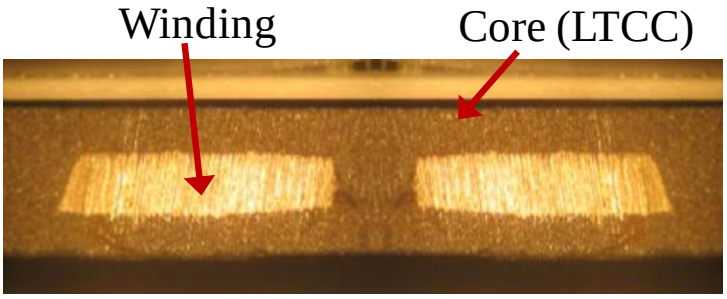

(a)

(b)

Figure 1.22 LTCC inductor substrate: (a) cross-section view, (b) top view

Figure 1.23 shows the first-generation prototype of CPES's 3D integrated converter with an LTCC inductor substrate. In this prototype, the silver traces were directly screen printed on the top of a very-low-profile LTCC inductor. Then other components were mounted on the surface of the inductor to build the whole converter. The integration method demonstrated by this prototype is a simple process and also can achieve very high power density. However, it is very difficult to use this method for high-frequency applications. Because the circuit trace is laid directly on top of the inductor substrate, the parasitic inductance of the active circuit is increased, which will cause larger ringing and switching loss.

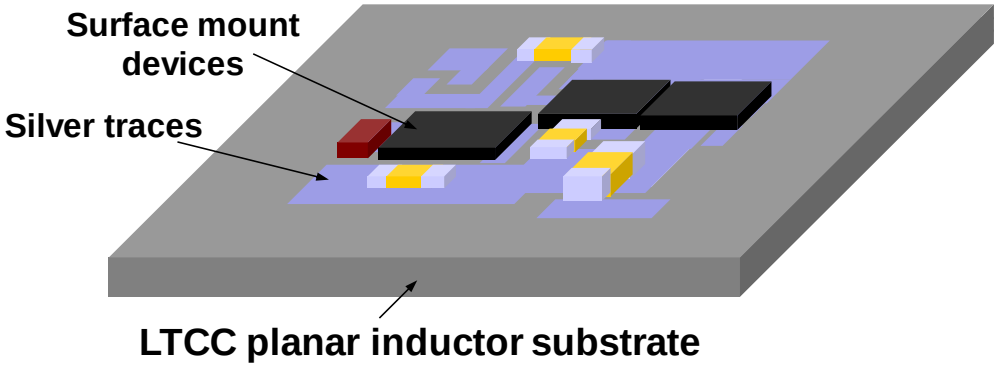

(a)

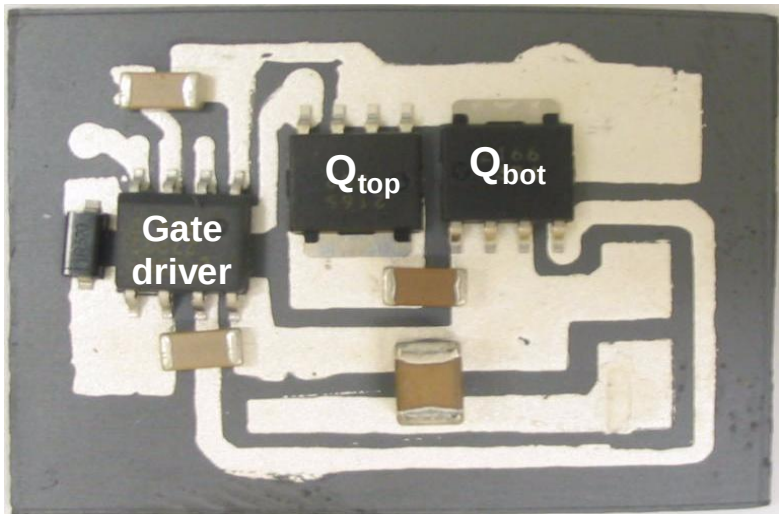

(b)

Figure 1.23 First-generation prototype of CPES's 3D integrated converter with LTCC inductor substrate: (a) concept drawing, (b) real prototype

As a result, the second-generation prototype was modified by using an additional active layer to carry the active device and to form a shield layer to reduce the parasitic inductance of the active circuit [18]. Figure 1.24 shows a concept drawing of this design.

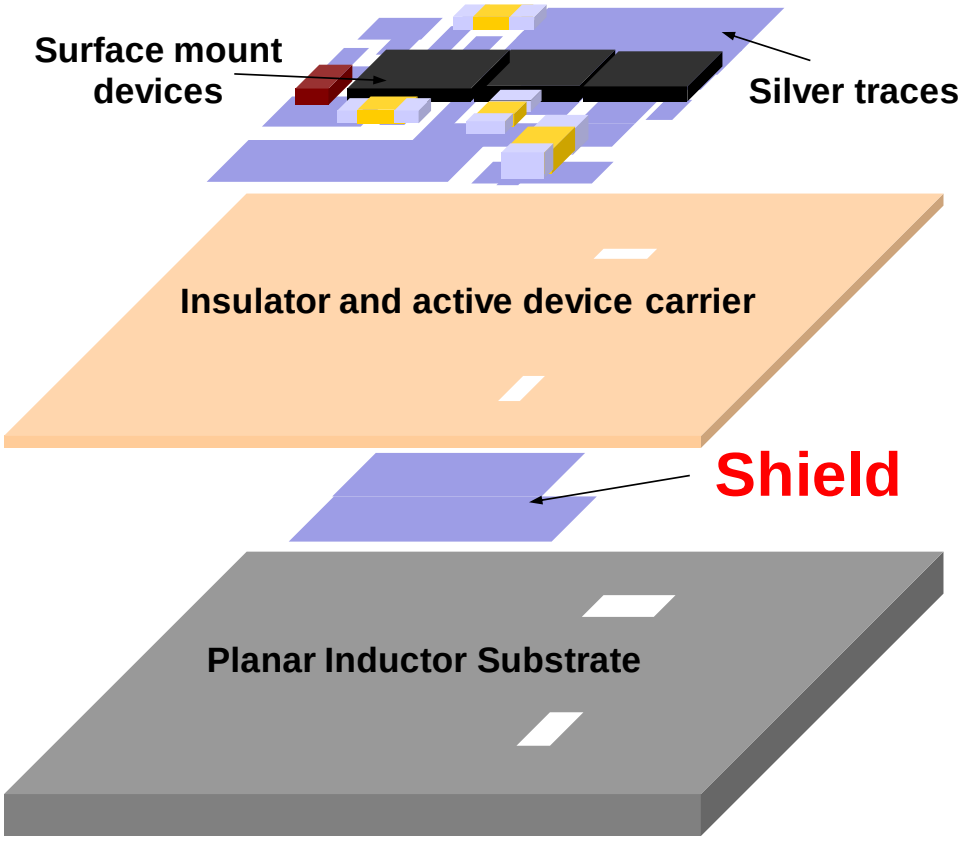

Figure 1.24 Concept drawing of second-generation prototype of CPES's 3D integrated converter with LTCC inductor substrate

Figure 1.25 shows the switching waveform of this integrated POL with and without the shield layer. It can be seen that the shield layer can dramatically reduce ringing, which is good for high-frequency operation. Figure 1.26 shows the results of testing for converter efficiency. The 3D integrated converter with a shield layer can have higher efficiency due to less switching loss caused by parasitic inductance.

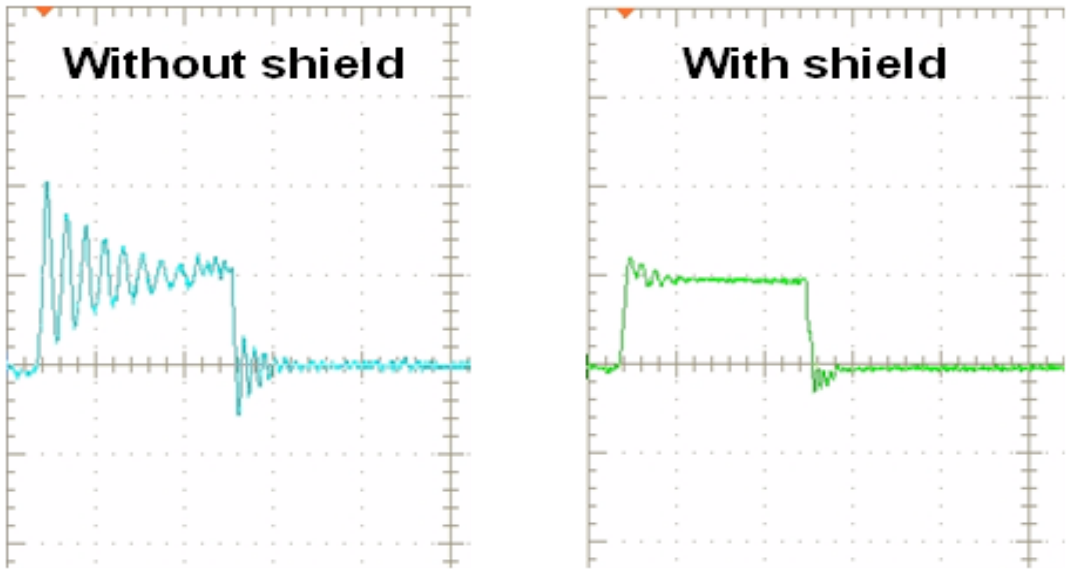

Figure 1.25 Switching waveform of CPES's second-generation 3D integrated converter with and without shield layer

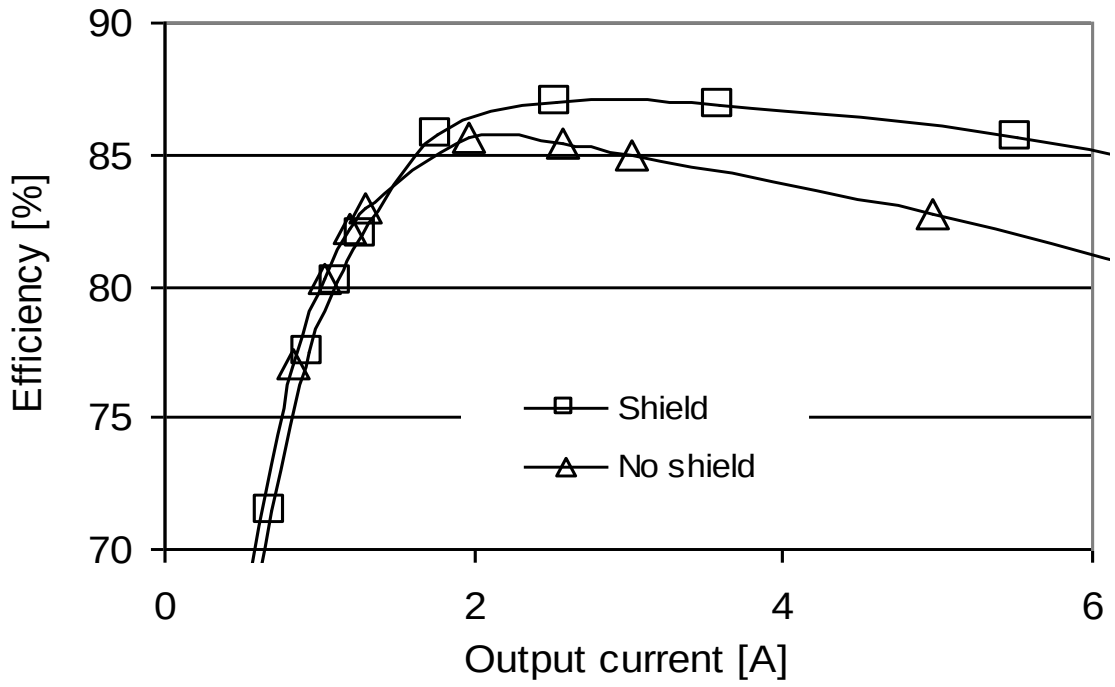

Figure 1.26 Test results of the efficiency of CPES's second-generation 3D integrated converter

1.6.3 DBC Carrier for 3D Integrated Converter

To further improve the performance of 3D integrated POL converter, [22] proposes to use AlN (aluminum-nitride) DBC (direct-bonded copper) ceramics as the device carrier to build active layer for CPES's third-generation 3D integrated POL. The active bare-die devices are embedded inside the AlN ceramic. This solution will allow the placement of the decoupling capacitor directly on top of the active device, which can minimize the parasitic loop inductance to increase circuit efficiency. Figure 1.27 shows a concept drawing of this embedded device solution. Using this method, [22] successfully reduced the parasitic loop inductance to 0.82nH.

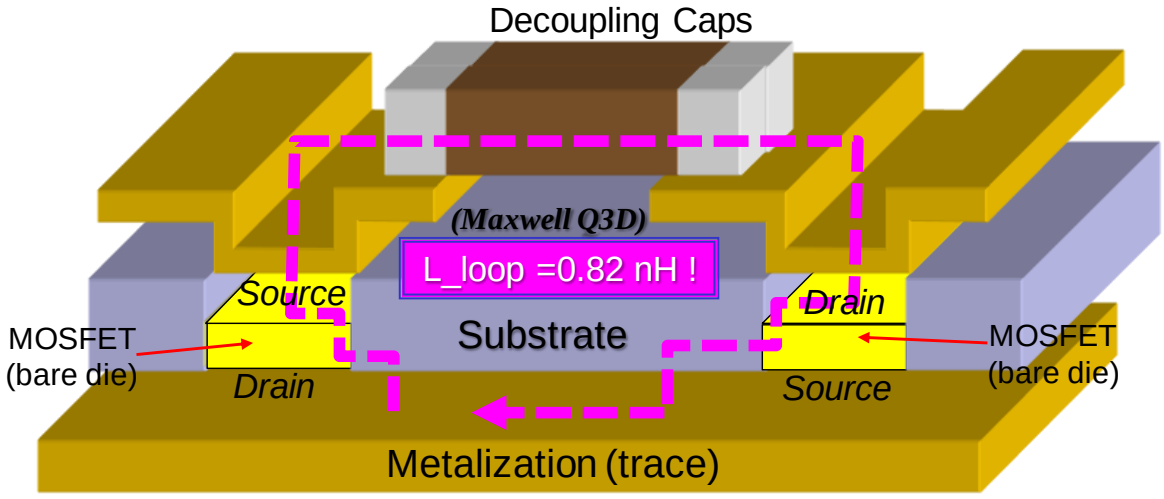

Figure 1.27 Concept drawing CPES's third-generation 3D integrated POL with AlN DBC carrier

Another benefit of using AlN DBC is its great heat-spreading effect. When using a substrate with a low thermal conductivity, such as FR4 PCB (thermal conductivity is about 4 W/m°K), the heat generated by the converter cannot spread out very quickly. This means there will be some hotspots around the main power dissipation devices – typically the power MOSFETs. This situation will be dramatically changed when using an AlN DBC substrate. The thermal conductivity of AlN DBC is about 150 W/m°K, which is 40 times better than the FR4

PCB material. Hence heat can quickly spread out into a large volume rather than be restricted in a small area. As a result, by using an AlN DBC substrate, the heat can be effectively spread over the entire substrate.

Figure 1.28 shows the thermal simulation results of heat distribution with the FR4 PCB substrate and the AlN DBC substrate. It can be seen that with the PCB substrate, the maximum temperature (158°C) is about 60°C higher than average temperature (96.8°C), which means there is a hot spot on the PCB. However, with the AlN DBC substrate, the maximum temperature is only 98.2°C. Compared with the average temperature (95.5°C), it is only 3°C higher, which means the AlN DBC substrate has very even heat distribution. This improvement directly translates into either higher current output or smaller package size.

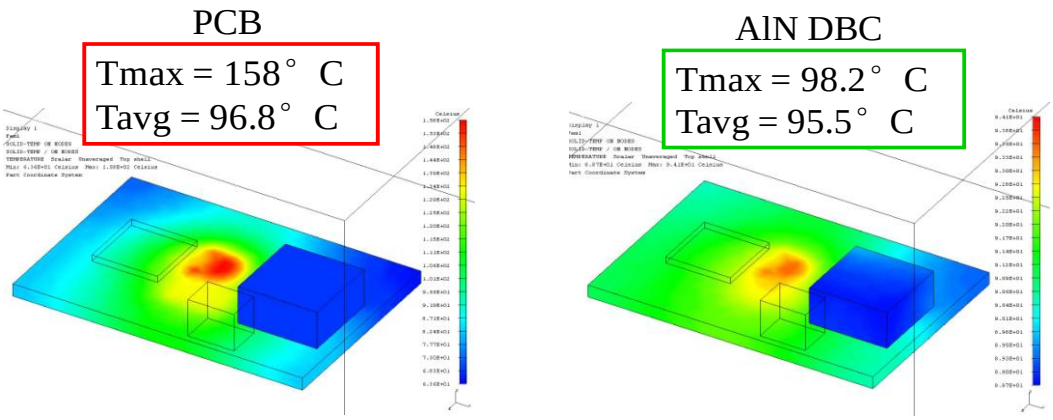

Figure 1.28 Thermal simulation results of heat distribution with FR4 PCB substrate and AlN DBC substrate

Besides the higher thermal conductivity of AlN DBC, the embedded device solution also can help heat dissipation. As shown in Figure 1.29, with the embedded device solution, the heat can be dissipated on both sides of the DBC substrate. However, there is only one side for cooling in a traditional surface-mounted solution. Therefore using an AlN DBC carrier and a cooling fan of moderate size, the heat sink can be eliminated, which will increase the power density, lower

the cost, and allow for a very low profile. [22] successfully demonstrated some ultra-high density 3D integrated POL converter with an AlN DBC carrier.

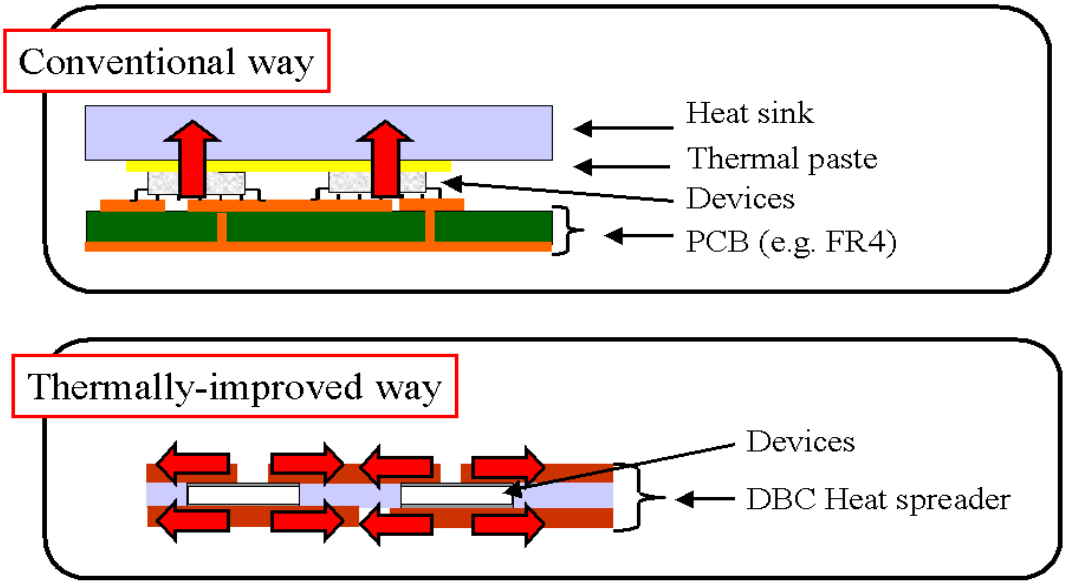

Figure 1.29 Concept drawing of heat dissipation method for FR4 PCB substrate with surface mounted device and AlN DBC substrate with embedded bare die device

1.6.4 Previous Achievement of 3D Integrated Converter with DBC Carrier and LTCC Inductor Substrate

In 2004, CPES demonstrated a 3D integrated high power POL converter, shown in Figure 1.30(a), that mimicked the converter in the low-power POL shown in Figure 1.4. The trench MOSFET switches were adopted to handle the high current. The drivers and controller IC were packaged together with the trench MOSFET switches to build the active stage of the POL converter module. The AlN DBC ceramics were employed as the die holder to improve the active stage thermal conductivity and performance. With the AlN DBC, double-sided cooling was achieved to further improve the thermal performance of the fully integrated POL converter module. The LTCC inductor with the silver paste winding, shown in Figure 1.22, was adopted

for the low-profile inductor. By controlling the winding cross-section and length, the low-inductance DCR was achieved to minimize the conduction loss. The power density for this first generation of 3D integrated POLs was demonstrated at 260W/in^3 for the first time.

In 2008, a further improvement in power density was realized by inverse coupling of two-phase inductors [22] and [26]. The inverse-coupled LTCC inductor can save 50% of the footprint comparing with a non-coupled inductor. The integrated LTCC vertical-flux-coupled inductor POL converter module achieves 500W/in^3 power density, as shown in Figure 1.30(b).

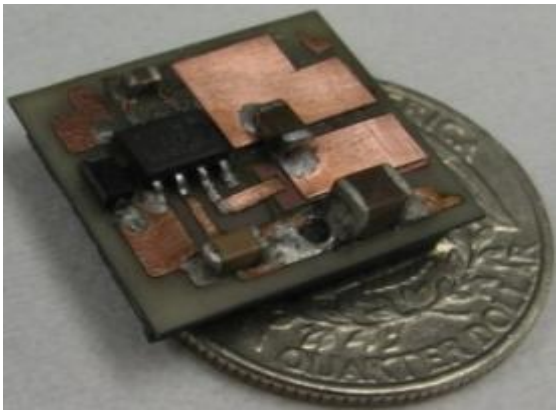

(a)

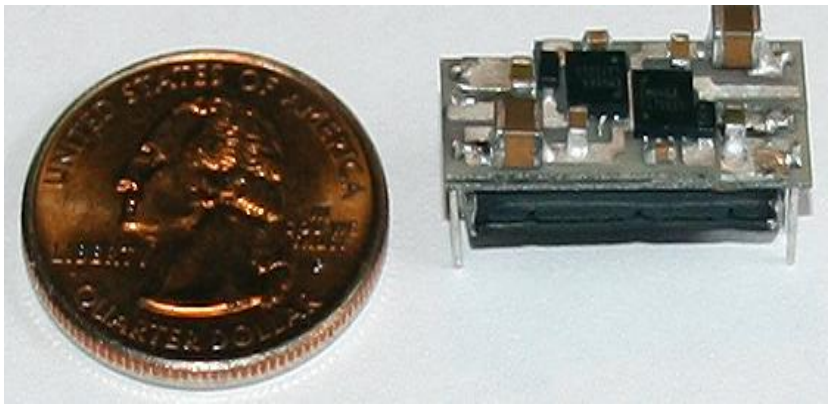

(b)

Figure 1.30 CPES 3D integrated high power POL converter: (a) Single–phase, 1.5MHz 20A POL, achieving 260W/in^3 power density (b) Two-phase 1.5MHz 40A POL with coupled inductor, achieving 500W/in^3 power density

1.6.5 Remaining Challenges for 3D Integrated Converter with DBC Carrier and LTCC Inductor Substrate

Although the use of a 3D integrated converter for high-frequency and high-current application has been researched for many years and the performance of prototypes has continually improved over several generations, there are still some unsolved issues and challenges remaining in this area. Previously, most research work was focused on improving the fabrication process and active-layer design for this 3D integrated converter. However, the LTCC inductor design was not improved very much from prototype generation one to prototype generation three. In fact, the LTCC inductor substrate has already become one of the bottlenecks for further improving the power density and efficiency for this integrated converter.

In Figure 1.30 (a), it can be seen that the active layer of the single-phase converter actually can be designed with a smaller footprint. However, the active layer was designed to match the inductor footprint. If the inductor footprint can be reduced, the footprint of this converter can be reduced as well. Although previous designs of the LTCC coupled inductor had a very small footprint, they had a very thick core. Because LTCC ferrite and silver paste have different shrinking coefficients, it is very difficult to fabricate a very thick LTCC inductor without cracking. In order to help avoid this cracking problem, [26] proposed to create many small holes on the LTCC core to relieve the stress. The LTCC inductor example shown in Figure 1.22 was fabricated with many small holes on the core. The figure shows that the LTCC core still has some small cracking when fabricated with this complicated process.

Besides low inductance density and difficulty of fabrication, previous LTCC planar inductors also didn't have very accurate models to optimize the design. Because flux distribution

is very non-uniform in these planar inductor structures, the traditional inductance calculation method for discrete inductors, which assumes the flux is uniform, cannot be used directly. This problem becomes even more unconventional and complicated when the planar inductor substrate is built using magnetic material with non-linear permeability, such as the inductor substrate built with low-temperature co-fired ceramic (LTCC) ferrite. As a result, some novel inductance models need to be developed for these LTCC inductors. Furthermore, the winding ACR loss and core loss both also need to be studied to help optimize the low-profile LTCC inductor design for high-frequency applications.

1.7 Dissertation Outline

This dissertation mainly focuses on modeling and inductor structure optimization for LTCC planar inductors, trying to penetrate the technological barriers of LTCC planar inductor substrate design to further improve the performance of the 3D integrated POL converter, especially its power density for high-current and high-frequency applications. This dissertation consists of six chapters, organized as follows:

Chapter 1 gives an introduction of the research background.

Chapter 2 proposes some simple but highly accurate numerical and analytical inductance models for the planar inductor with non-uniform flux and permeability. The proposed inductance model will be used to compare and design different LTCC inductors.

Chapter 3 studies and compares LTCC inductor structures with two different flux path patterns (vertical and lateral) based on the previously proposed inductance model. The lateral

flux structure is revealed as the better choice for low-profile high-current inductor design due to its higher inductance density.

Chapter 4 focuses on the winding ACR loss and core loss modeling for the LTCC inductor, trying to provide some fundamental information and a model to help optimize the low-profile LTCC inductor structure. Here, a FEA simulation is adopt to study the winding ACR. FEA 3D and 2D models are established and compared for these LTCC planar inductors. Based on the FEA simulation results, several ACR closed-from formulas are also proposed to help perform design optimization for these planar inductors. The proposed analytical core loss model considers the impact of non-sinusoid flux and DC flux.

Chapter 5 first compares different LTCC lateral flux inductor structures in a systematic way. This comparison considers inductor volume, winding loss and core loss. Then, a design method is proposed to help optimize the performance of a low-profile LTCC lateral flux inductor. A 1.5MHz, 5V to 1.2V, 15A 3D integrated buck converter with a low-profile lateral flux LTCC inductor substrate is designed and fabricated. This converter can have around 300W/in^3 power density and 87% efficiency.

Chapter 6 proposes some low-profile LTCC lateral flux coupled inductor structures to help further increasing the power density of the integrated POL. A comparison with previous vertical flux coupled inductors shows that the lateral flux coupled inductor can reduce core thickness to half of the value of the vertical flux coupled inductor thickness. As a result, a 1.5MHz, 5V to 1.2V, 40A integrated POL with LTCC lateral flux coupled inductor can achieve power density as high as 700W/in^3.

Chapter 7 provides a summary of the dissertation, and proposes some future works.

Chapter 2. Inductance Modeling for Low-Profile LTCC Inductor with Non-uniform Flux Distribution

2.1 Low-Profile LTCC Inductor with Non-uniform Flux Distribution

2.1.1 Overview and Classification of Low-Profile Inductor Structure: Vertical flux and Lateral Flux Structures

Due to the high aspect ratio, it is not easy to design a low-profile integrated inductor substrate that works as well as a discrete inductor. In order to improve the performance of low-profile inductor substrate, People have tried many different structures. Some low-profile inductors with spiral coil have been reported by [21][36][43][53][54]. Figure 2.1 shows a silicon integrated pot-core inductor with spiral winding [36]. In this inductor, copper is electroplated into through-wafer silicon trenches, resulting in thick copper windings (200~500 μm). The magnetic cores are electroplated on both sides of the silicon substrate to cover the copper windings, and through-wafer magnetic vias are used to close the magnetic path. Powder permalloy NiFe are used as magnetic material. The powder permalloy can be fabricated by using high-current-density electroplating.

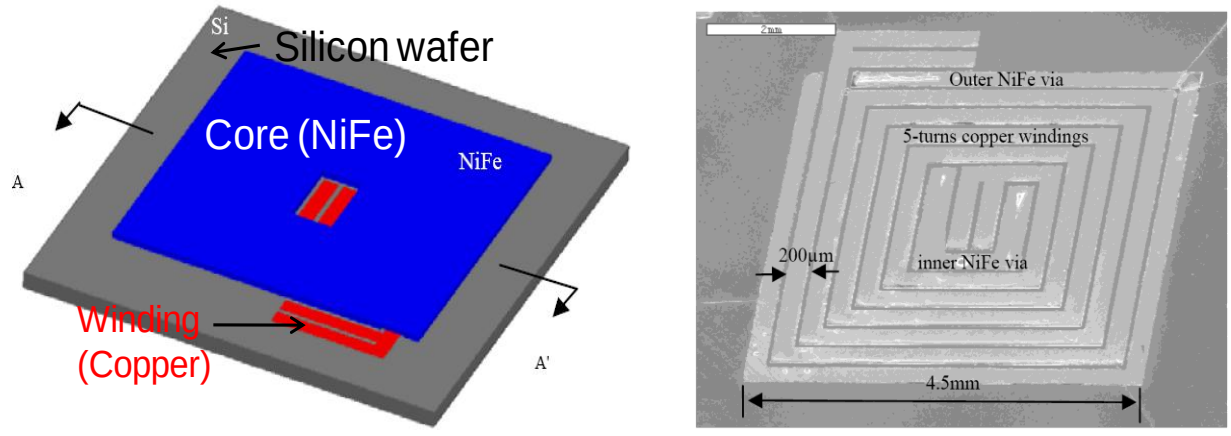

Figure 2.1 Silicon integrated pot-core inductor with spiral winding [36]

[39] reports a low-profile inductor design with a meander coil, which is shown in Figure 2.2. The core material used for this inductor is LTCC ferrite green tape. The material used for winding is silver/platinum (Ag/Pt) paste. First, the LTCC ferrite tapes are cut into rectangles and several layers of the rectangular LTCC ferrite tapes are laminated to form the top, middle, and bottom main layers. The Ag/Pt conductor paste is wiped into the slot of middle lay to build inductor winding. After that, the tapes are laminated using a hydraulic lab press. Finally, the structure is sintered in a normal atmosphere with around 900^{o}C. [55][56] report some low-profile inductor designs with toroidal coil.

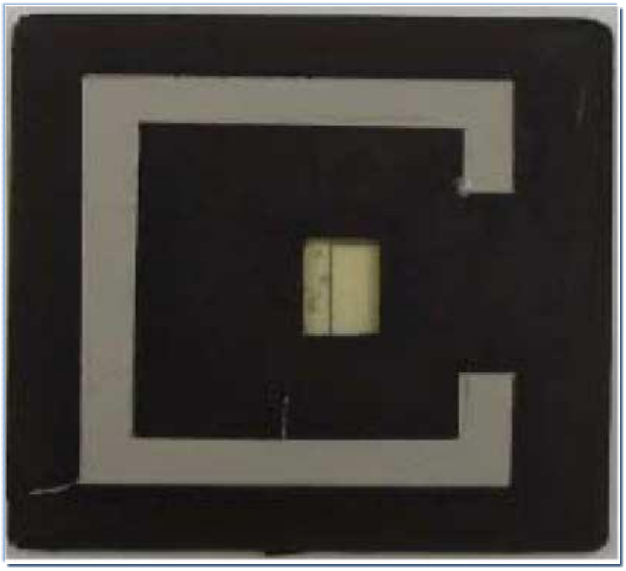

Figure 2.2 Low-profile LTCC inductor with a meander winding [39]

Figure 2.3 shows the LTCC inductor with toroidal winding reported by [55]. In this inductor, soft magnetic NiCuZn ferrite layer is combined with Au and Ag thick film conductors. The maximum number of toroidal coil windings of this inductor is limited by the number of inner vias. The total inductor thickness is on 0.4mm. [57] reports a PCB integrated low-profile inductor with toroidal core and one turn winding structure as shown in Figure 2.4. In this case, the electroplated CoNiFe material is used as core material. 5 laminations are formed on each of

the PCB layers; the thickness of each lamination is about one skin depth of the magnetic material. A single-turned winding is formed by threading a wire through the board, or by filling very large copper plated through-holes.

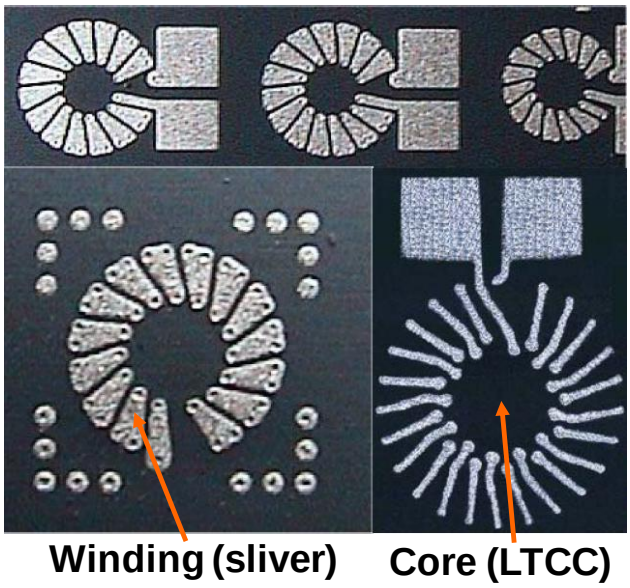

Figure 2.3 LTCC inductor with toroidal winding [55]

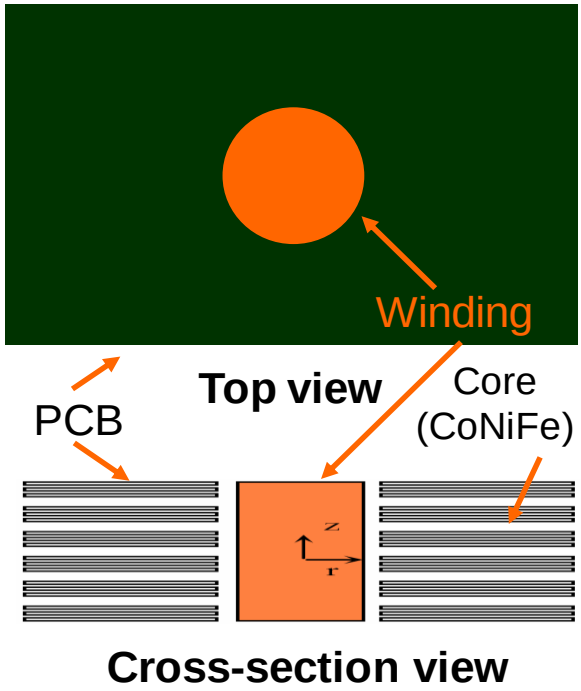

Figure 2.4 PCB integrated low-profile inductor with toroidal core and one turn winding structure [57]

In terms of the flux path pattern, these different structures can be classified into two types. One is a vertical flux structure like a structure with spiral or meander coil, another is a lateral flux structure, like a structure with a toroidal coil and the structure with one turn winding shown in Figure 2.4. The vertical flux pattern means the magnetic flux path plane is perpendicular with the substrate. The lateral flux pattern means the magnetic flux path plane is parallel with the substrate. Figure 2.5 shows the basic cells of these two different inductor structures. Commonly, embedded rectangular winding is used for a vertical flux inductor structure to help reducing inductor profile. For the lateral flux inductor structure, cylindrical winding can always be used to minimize the magnetic path length.

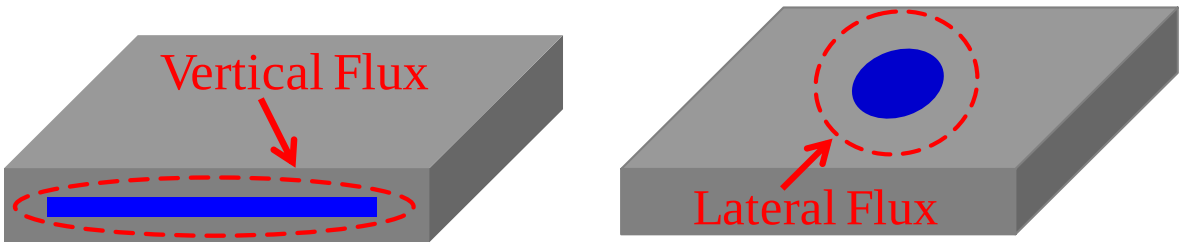

Figure 2.5 Basic cells of planar inductor structures: (a) vertical flux structure, (b) lateral flux structure

As we all known, with a given winding cross-section area, the cylindrical winding will give the shortest magnetic path length. If the core thickness is limited to a certain value, sometimes the cylindrical winding can no longer be used. As an alternative, the rectangular winding with a higher aspect ratio must to be used to allow the passage of a certain current, which may decrease the energy density due to the increasing in the magnetic path length. FEA 3D simulation results of vertical flux inductor structures with different core thicknesses and winding shape but with the same excitation current, core volume and winding cross-section area are shown in Figure 2.6(a) and Figure 2.6(b). The simulation results show that the average energy density of a thick core with cylindrical winding is higher than that of a thin core with

rectangular winding. However, the vertical flux structure in Figure 2.6(a) can be cut into four pieces and laid down to be combined as a new inductor structure with lateral flux pattern, as shown in Figure 2.6(c). With this lateral flux structure, even though the core thickness is reduced, the cylinder winding still can be used, so the average energy density is kept the same as the previous thicker core vertical flux structure. In other words, the lateral flux structure may have high inductance density than vertical flux structure, which is good for reducing inductor size. According to the survey results introduced in chapter1, it can be known that the LTCC technology is one of the promising candidates for high current integrated POL. So, the next section will propose some LTCC inductor with lateral flux structure.

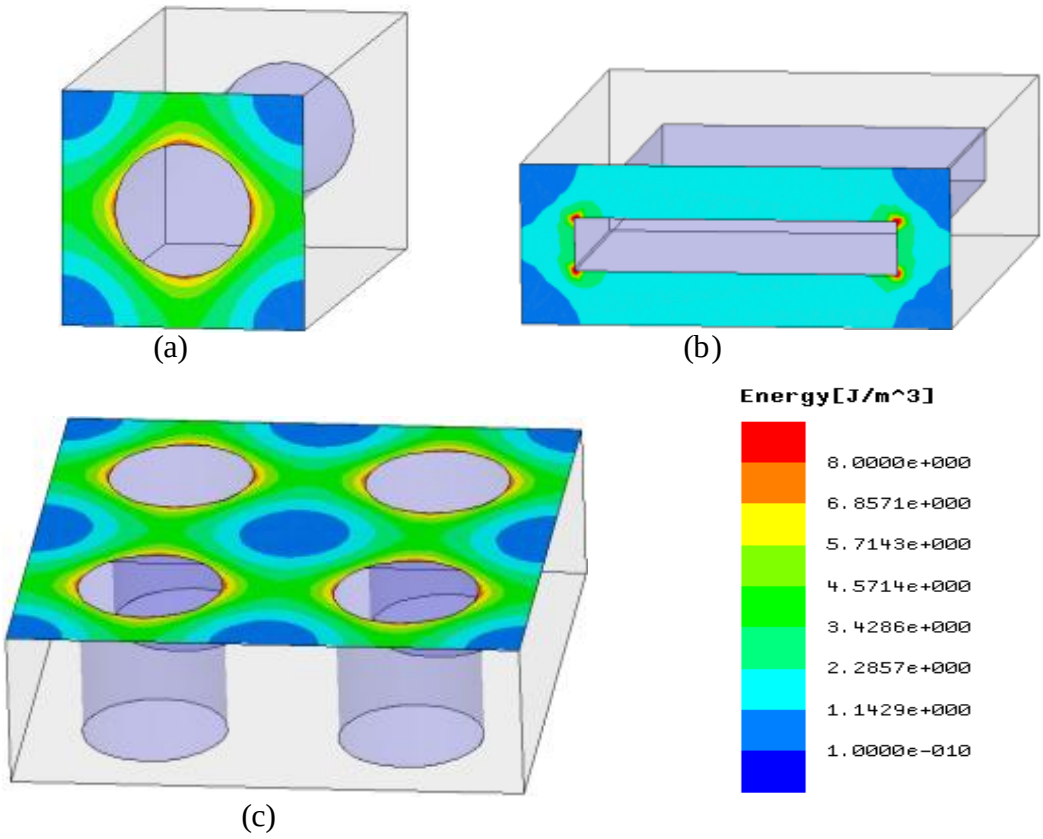

Figure 2.6 FEA 3D simulation results of different inductor structures: (a) vertical flux structure with round shape winding, (b) vertical flux structure with rectangular shape winding, (c) lateral flux structure with round shape winding

2.1.2 Proposed LTCC Inductor with Lateral Flux Structure

There are many different structures that can be used to design a low-profile LTCC lateral flux inductor. One way is connecting many unit cells of the lateral flux inductor in series, as shown in Figure 2.7(a). In this structure, the flux of each unit cell has very little coupling. Because there is only one vertical winding in each unit cell, this structure is defined as the "*N*=1" structure. Figure 2.7(c) is the circuit model for this structure, ignoring the very weak coupling between each unit cell.

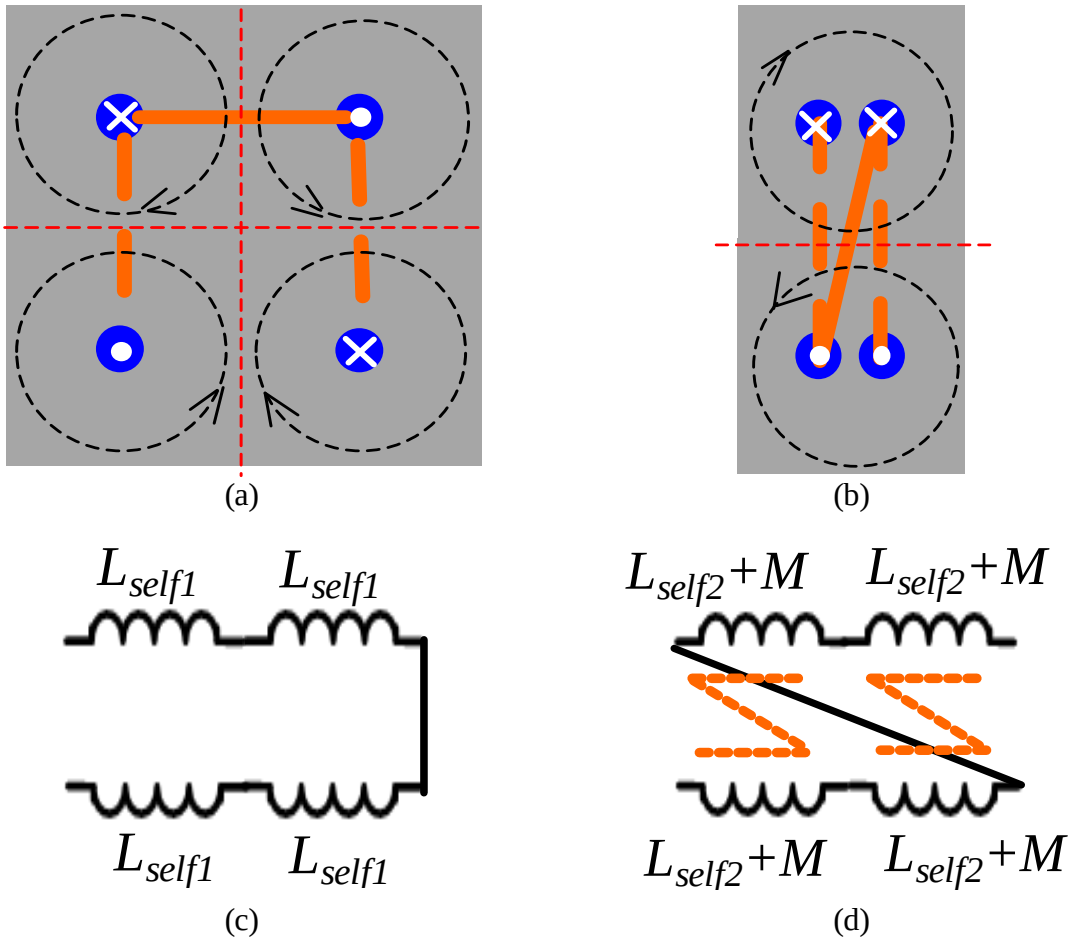

Figure 2.7 Lateral flux inductor structures and their circuit models: (a) Single-turn structure (*N*=1), (b) Two-turn structure (*N*=2), (c) Circuit model for "*N*=1" structure, (d) Circuit model for "*N*=2" structure

The inductance density of the "*N*=1" structure is the same as the inductance density of a unit cell:

$$L\_Density_{N=1} = \frac{4 \cdot L_{self1}}{4 \cdot V_1} = \frac{L_{self1}}{V_1} \tag{2.1}$$

where $L\_Denisty_{N=1}$ is the inductance density of the "*N*=1" inductor, L_{self1} is the self inductance of the "*N*=1" unit cell, and V_1 is the inductor volume of the "*N*=1" unit cell.

Another structure can be made by moving two windings that have the same current direction very closer to each other to introduce flux coupling, as shown in Figure 2.7(b). This new structure merges 4 unit cells into 2 unit cells, but there are two vertical windings in each new unit cell, so this structure is defined as the "*N*=2" structure. Figure 2.7(d) is the circuit model for this structure. The inductance density of the "*N*=2" structure can be calculated as:

$$L\_Density_{N=2} = \frac{4(L_{self2} + M)}{2 \cdot V_2} = 2(1+\alpha)\frac{L_{self2}}{V_2} \tag{2.2}$$

where $L\_Denisty_{N=2}$ is the inductance density of the "*N*=2" inductor, L_{self2} is the self-inductance of one vertical winging in the "*N*=2" unit cell, *M* is the mutual inductance, α is the coupling coefficient, and V_2 is the inductor volume of the "*N*=2" unit cell.

If the impact of the additional vertical winding on magnetic flux path can be ignored, the difference between L_{self1} and L_{self2} will be determined only by the permeability of the core. If we further assume that the permeability of the core material is constant, the L_{self2} will equal L_{self1}. As a result:

$$L\_Density_{N=2} = 2(1+\alpha)L\_Density_{N=1} \tag{2.3}$$

If the two adjacent vertical windings are close enough to provide very strong coupling (α=1), the $L\_Density_{N=2}$ can be increase to four times of $L\_Density_{N=1}$. Following the same methodology,

more windings can be located closer to further increase inductance density, such as an "*N*=3" structure. The inductance density of an "*N*=n" structure is:

$$L\_Density_{N=\mathrm{n}} = n(1+(n-1)\alpha)L\_Density_{N=1} \approx n^2 \cdot L\_Density_{N=1} \qquad (2.4)$$

where $L\_Denisty_{N=\mathrm{n}}$ is the inductance density of the "*N*=n" inductor.

This ideal case analysis result for an embedded-winding planar inductor matches with the analysis result for the conventional multi-turn discrete inductor, whose inductance is proportional to the n^2 (n is the turn number). Actually, this winding-coupled lateral flux planar inductor structure can be looked at as an extension of the multi-turn discrete inductor structure. With a discrete core structure, the following two assumptions can usually both be satisfied:

1) Because the magnetic flux path is confined by the discrete core, it will not be impacted by increasing the number of winding turns.

2) Because there is usually an air gap in the discrete inductor, the effective permeability is almost constant with different number of winding turns.

However, in reality, the above two assumptions cannot be satisfied for this lateral flux inductor with embedded winding and an LTCC core. Firstly, the permeability of LTCC magnetic core will decrease when the magnetic field increases. For example, in the "*N*=2" structure, because there are two close vertical windings with the same current direction, the magnetic field is higher than in the "*N*=1" structure, which decreases the permeability of the core. As a result, the L_{self2} will be smaller than L_{self1}, so even with perfect coupling (α=1), the inductance density of the "*N*=2" structure cannot be increased to four times that of the "*N*=1" structure. Secondly, unlike the discrete inductor, because the winding is embedded in the core in this structure, if the number of coupled windings is further increased, the impact on the magnetic flux path cannot be ignored, and in fact the flux path will change from a circle to an ellipse with longer length. As a

result, the increase in inductance density of this lateral flux LTCC planar inductor by coupling the flux will not be as much as the multi-turn discrete inductor case. In order to compare the inductance density between vertical flux structure and lateral structure, some inductance models are required to calculate inductance accurately for different structures.

Figure 2.9 shows the FEA simulation results for the flux distribution in a LTCC lateral flux inductor unit cell, which is shown in Figure 2.8. The B-H curve of this LTCC material is also shown in Figure 2.9, from which it can be seen that both flux and permeability distribution are very non-uniform in this LTCC lateral flux unit cell. So, the traditional inductance calculation method for discrete inductor, which assumes flux is uniform, cannot be used directly. Actually, the flux distribution of planar inductor with vertical flux structure is also very non-uniform. The FEA simulation results for vertical flux structure can be seen in Figure 2.6(a) and Figure 2.6(b). So, how to calculate inductance for planar inductor with non-uniform flux distribution is the common and fundamental modeling problem for different planar inductor structures. In this chapter, two methods will be introduced to calculate inductance for these planar inductors with non-uniform flux distribution. One is numerical inductance model, which is based on FEA simulation; another one is Analytical Inductance Model.

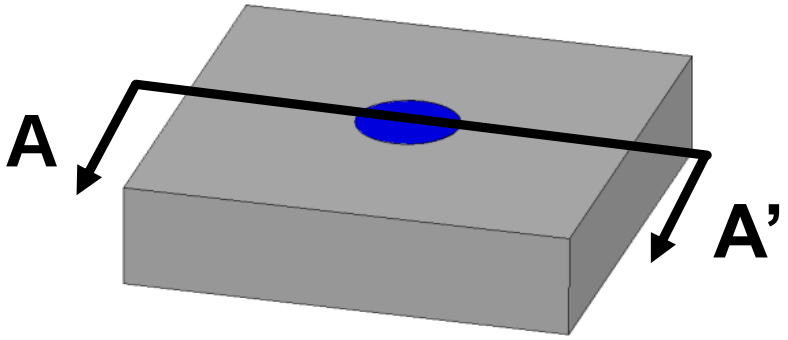

Figure 2.8 Lateral flux inductor unit cell

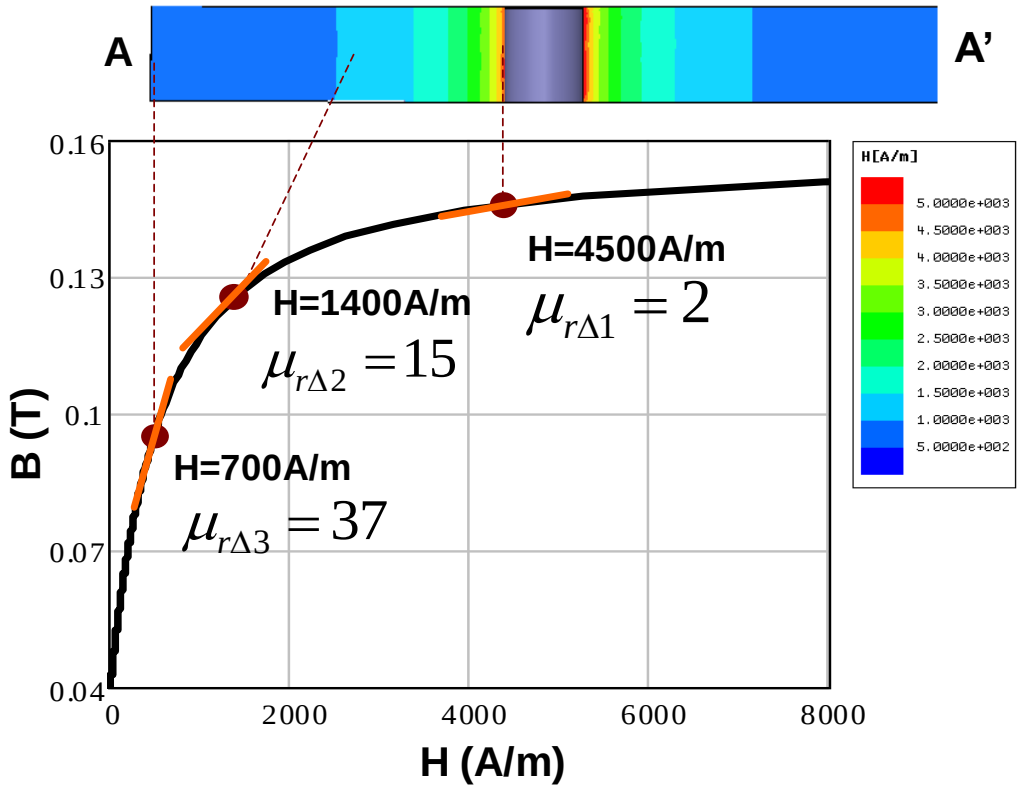

Figure 2.9 FEA simulation results for the flux distribution in a LTCC lateral flux inductor unit cell

2.2 Numerical Inductance Model (FEA Simulation) for LTCC Inductor with Non-uniform Flux Distribution

2.2.1 Introduction of FEA simulation

In today's industry and academia, computer aided tools have been more and more involved in the magnetic component design. FEA method is one of the most popular numerical techniques for solving electromagnetic problems. The basic principle behind FEA is that it breaks up the problems into many tetrahedral elements. The accuracy of this numerical technique has been well proved. So, some numerical models (FEA models) based on Maxwell 3D and 2D (Maxwell software is developed by Ansoft, which is used to solve Maxwell's differential equations for electromagnetic problems.) are proposed and discussed in this section for calculating inductance of planar inductor with non-uniform flux and permeability.

With magneto-static solver, the system computes the static magnetic field in two steps. First, a conduction simulation is performed to compute the current density. Then, the magneto-static field solver computes the magnetic field using Ampere's Law and the Maxwell's equation:

$$\nabla \times H = J \tag{2.5}$$

$$\nabla \cdot B = 0 \tag{2.6}$$

After computing static magnetic field, the energy stored in a static magnetic field can be calculated by

$$U = \frac{1}{2}\int_V H \cdot B dV = \frac{1}{2} L \cdot I^2 \tag{2.7}$$

So, inductance can be calculate by

$$L = \frac{1}{I^2}\int_V H \cdot B dV = \frac{1}{I^2}\int_V H \cdot (H \cdot \mu_0 \cdot \mu_r) dV \tag{2.8}$$

2.2.2 Numerical Inductance Model (FEA Simulation) for LTCC Inductor with Non-uniform Flux Distribution

Because the planar inductor discussed here also has non-linear permeability, the B-H curve should be used to define core material instead of a constant relative permeability. Figure 2.10 shows the B-H curve of LTCC ferrite 40011 from ESL®. By performing curve fitting, this B-H curve can be modeled as:

$$B = 0.1 \cdot \left(\frac{a + b \cdot H + c \cdot H^2}{1 + d \cdot H + e \cdot H^2} \right)^x \tag{2.9}$$

where a=0.094, b=1.7e-3, c=5.6e-6, d=2.3e-3, e=2.3e-6, and x=0.5. The unit for flux density *B* is mT; and the unit for magnetic field strength *H* is Oersteds.

The permeability of magnetic core is determined by magnetic field inside the core. Normally, the DC pre-magnetization field is much larger than the AC flux field of an inductor for POL application. So, after ignoring the AC flux impact on the permeability, the magneto-static solver of Maxwell can be used to calculate inductance for these planar inductors.

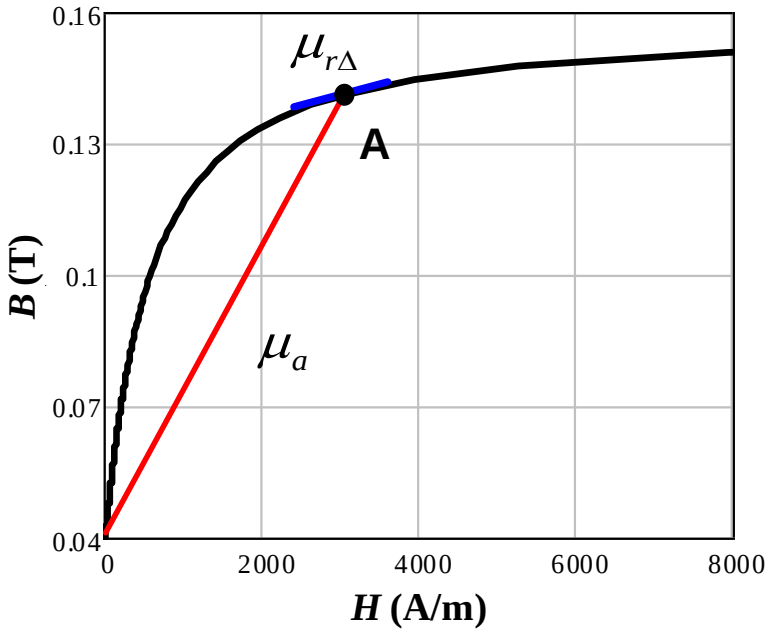

Figure 2.10 B-H curve of ESL®'s LTCC ferrite 40011

The relative permeability, which is used to calculate inductance is calculated based on the computing results of static magnetic field and the B-H curve of core material. Using ESL®'s LTCC ferrite 40011 as an example (the B-H curve is shown in Figure 2.10), assume the value of static magnetic field of a planar inductor core is on point A on the B-H curve. Then, the magneto-static solver will use amplitude permeability to calculate inductance. The amplitude permeability is the slope of line between point A and origin point of B-H curve. As a result, this inductance value only represents the stored DC energy in this inductor. However, for POL

application, the inductance value needs to represent the AC energy excursion, which can be used to predict inductor current ripple. So the incremental permeability rather than amplitude permeability should be used to calculate inductance. The incremental permeability is the slope of point A's tangent. Unfortunately, the magneto-static solver cannot calculate incremental permeability directly. So, a two step magneto-static simulation is introduced to calculate inductance of planar inductor. Figure 2.11 shows the concept of this two step method. First, the inductor is excited by a given DC current I_{DC}. After computing static magnetic field, the Flux linkage can be calculated. The result of this flux linkage is notated as ψ_1. Then, the inductor is excited by given DC current I_{DC} plus a small perturbation Δi. After computing static magnetic field, the Flux linkage is calculated as ψ_2.After these two steps, the inductance of this inductor can be calculated as:

$$L = \frac{\Delta\psi}{\Delta i} = \frac{\psi_2 - \psi_1}{\Delta i} \tag{2.10}$$

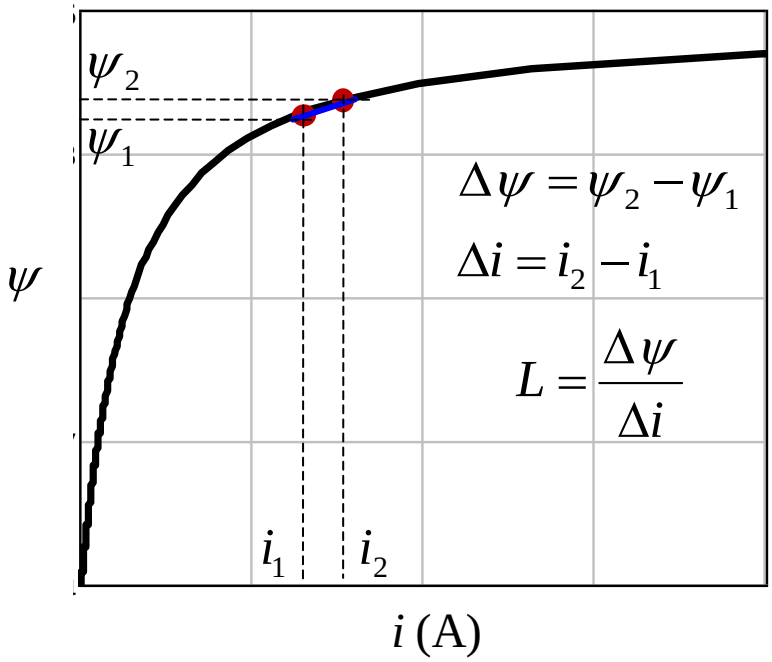

Figure 2.11 Concept of two-step simulation method for calculating inductance

This two step FEA magnetostatic simulation can be either use with Maxwell 3D or 2D model. With 3D model, magneto-static solver computes static magnetic field within the condition much closer to real case, but it is very time consuming. With 2D model, the inductor structure is simplified as a 2D structure by only using the cross-section plane to represent the inductor (Figure 2.12 shows the 3D and 2D simulation models for a vertical flux inductor). By using 2D model, the simulation time will be dramatically reduced, but the accuracy of computed static magnetic field will also be reduced due to the ignoring of surface winding. Figure 2.13 shows the inductance simulation results for LTCC vertical flux planar inductors with both 3D and 2D model. From Figure 2.13, it can be seen that the FEA simulation results of inductance with 2D model is almost the same as the results of 3D model.

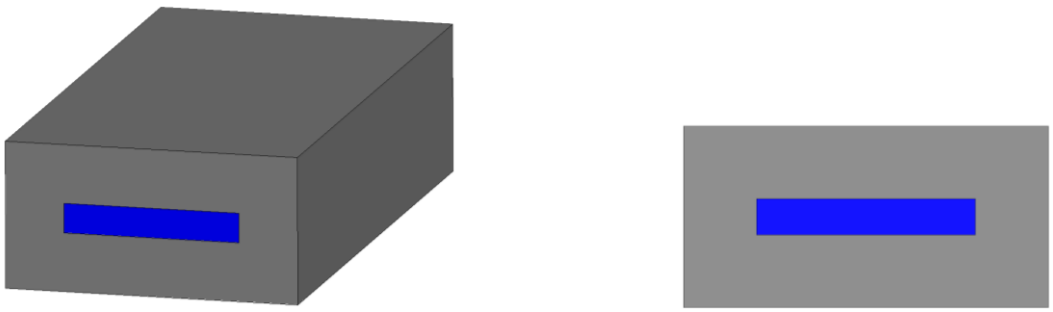

(a) (b)

Figure 2.12 Simulation model for vertical flux planar inductor: a) 3D, b) 2D

The single-turn lateral flux planar inductor structures (N=1) is used as an examples to illustrate the FEA models for lateral flux inductors with non-uniform flux distribution. First, just as previous study for vertical flux structure, a 3D model for lateral flux structure is built as shown in Figure 2.14. Then, the simulation excitation is defined on the two via surfaces as current i_1 and i_2; these two currents have the same value but opposite direction. Also like the two step simulation for vertical flux structure, there are two simulation steps. At the first step, both i_1 and i_2 are equal to I_{DC}; at the second step, both i_1 and i_2 are equal to $I_D+\Delta i$.

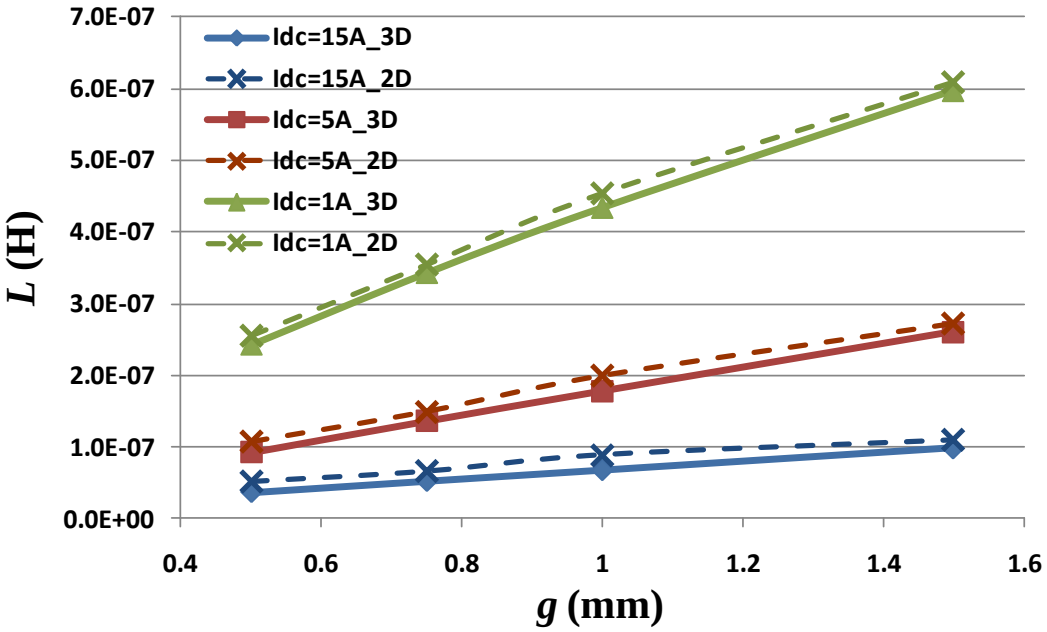

Figure 2.13 Inductance FEA simulation results for LTCC vertical flux planar inductors

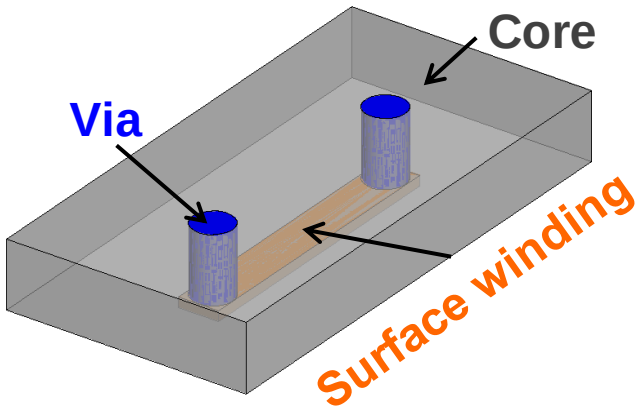

Figure 2.14 FEA 3D model for lateral flux inductor with single-turn structure

Figure 2.15 shows the FEA simulation results of flux line in a single-turn lateral flux inductor. Figure 2.15(a) shows the flux line generated by via; Figure 2.15(b) shows the flux line generated by surface winding. It can be seen that most flux generated by via is constrained inside inductor core due to the high permeability of the core; however, the flux generated by surface

winding is travelling through air to complete the whole path. As a result, the flux generated by via will have higher density than the flux generated by surface winding.

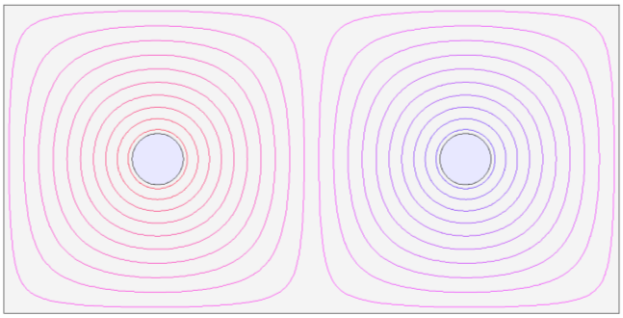

(a)

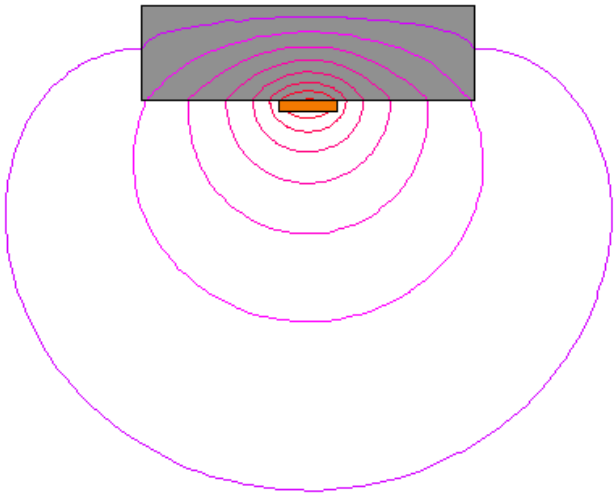

(b)

Figure 2.15 FEA simulation results of flux line in a single-turn lateral flux inductor:(a) flux generated by via only, (b) flux generated by surface winding only

Figure 2.16 shows the FEA simulation results of magnetic field strength H distribution in a single-turn lateral flux inductor. Figure 2.16(a) is the simulation result of flux generated only by via; Figure 2.16(b) is the simulation result of flux generated only by surface winding. It can be known that the magnetic field inside core contributed by surface winding is much smaller than that contributed by via. So, the impact of surface winding on magnetic field inside core can be ignored, which means the surface winding can be removed from previous 3D model.

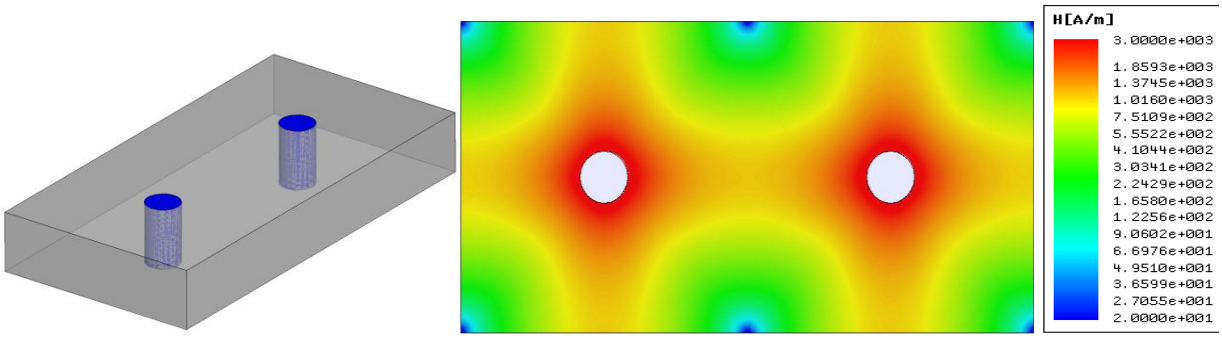

(a)

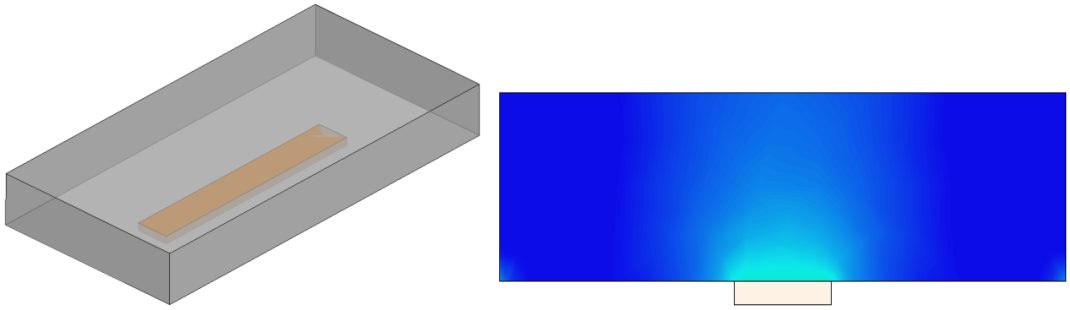

(b)

Figure 2.16 FEA simulation results of magnetic field strength *H* distribution in a single-turn lateral flux inductor: (a) flux generated only by via, (b) flux generated only by surface winding

After removing the surface winding, the 3D model actually can be further simplified to 2D model to help reducing simulation time. Figure 2.17 shows the concept drawing of 2D simulation model for single-turn lateral flux inductor. The two simulation steps are the same as 3D simulation. Figure 2.18 shows the comparison between FEA 3D and 2D simulation results. it can be seen that the FEA simulation results of inductance with 2D model is smaller than with 3D model. The reason is that the flux generated by surface windings of lateral flux inductor is ignored. However, the difference between 2D and 3D results is very small. So, the proposed magneto-static 2D simulation with small perturbation solution is a good solution to calculate inductance of planar inductor with non-uniform flux and permeability due to its fast simulation time and high enough accuracy.

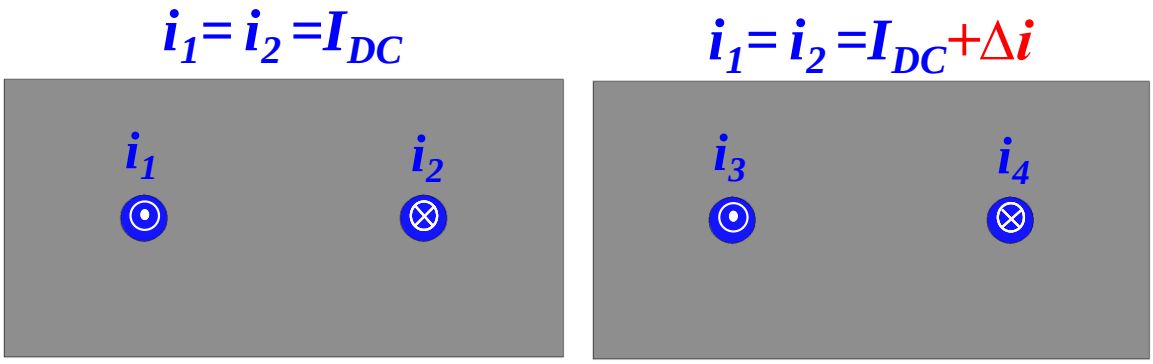

(a) (b)

Figure 2.17 Concept drawing of 2D simulation model for single-turn lateral flux inductor: (a) simulation step 1, (b) simulation step 2

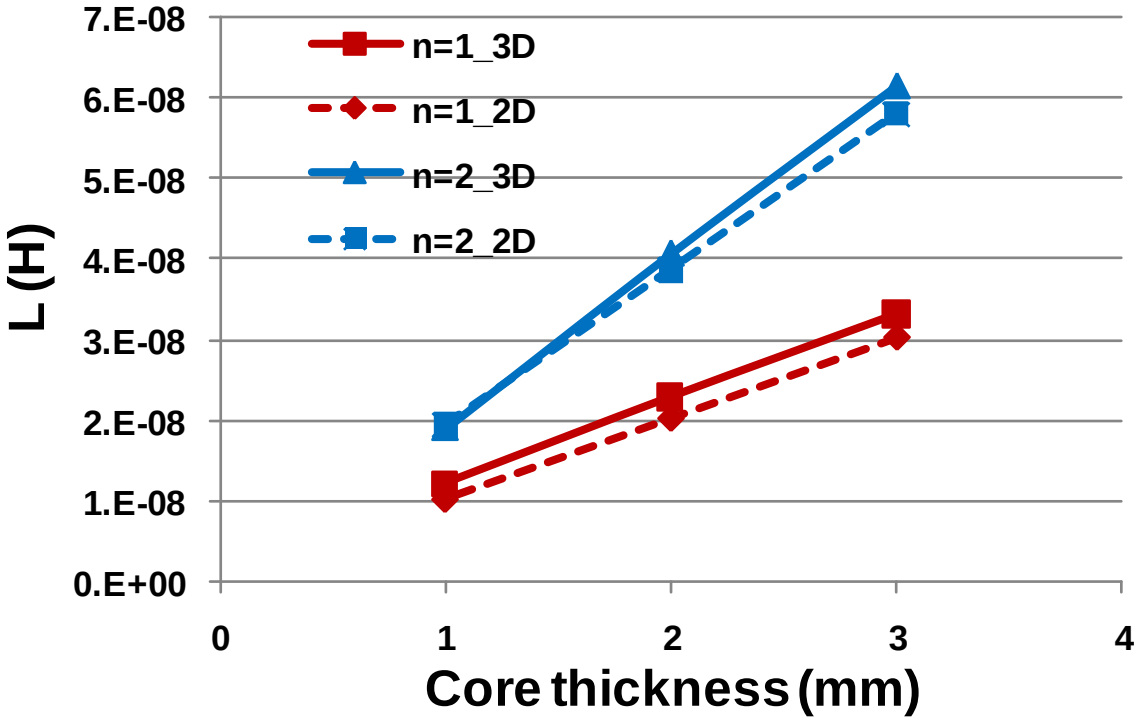

Figure 2.18 Inductance FEA simulation results for LTCC lateral flux planar inductors

2.3 Analytical Inductance Model for LTCC Inductor with Non-uniform Flux Distribution

2.3.1 Overview of Analytical Inductance model for planner Inductor

Commonly, embedded rectangular winding is used for a vertical flux inductor structure, but for a lateral flux inductor structure, cylindrical winding can always be used to minimize the magnetic path length, so the discussion in this section just focuses on these two winding shapes. Figure 2.19 is the FEA 2D simulation result of flux line of planar inductor with round shape and rectangular shape winding. It shows that the most flux lines around the round shape winding can be approximated by a circle, and the most flux lines around the rectangular shape winding can be approximated by an ellipse. Based on this approximation, an inductance calculation method is proposed for round shape winding inductor structure by [58]. Basically, this method assumes that the whole magnetic flux path consists of an infinite number of differential magnetic paths in a circle shape, and that the flux inside these small paths is uniform. The total inductance can be calculated by adding the inductance contributed by each small flux path together. The same methodology was used by [59] to calculate inductance of a rectangular shape winding inductor structure by changing the flux path shape from circle to ellipse. The limitation of these methods is that they all assume the permeability of the magnetic material in all the small magnetic paths are the same. However, for some embedded-winding planar inductor, the magnetic core cannot always be guaranteed to work in the linear range of the B-H curve, so different small magnetic paths will have different permeability values due to the different DC pre-magnetization. In order to achieve more accurate inductance calculation results, the non-linear permeability effect should be considered. So, [60] proposed an empirical model to take into account the variation of permeability by using a curve-fitting method to model the effective permeability of the core with

different load currents. The limitation of this method is that different empirical models should be developed for different inductor structures, which would be very time-consuming.

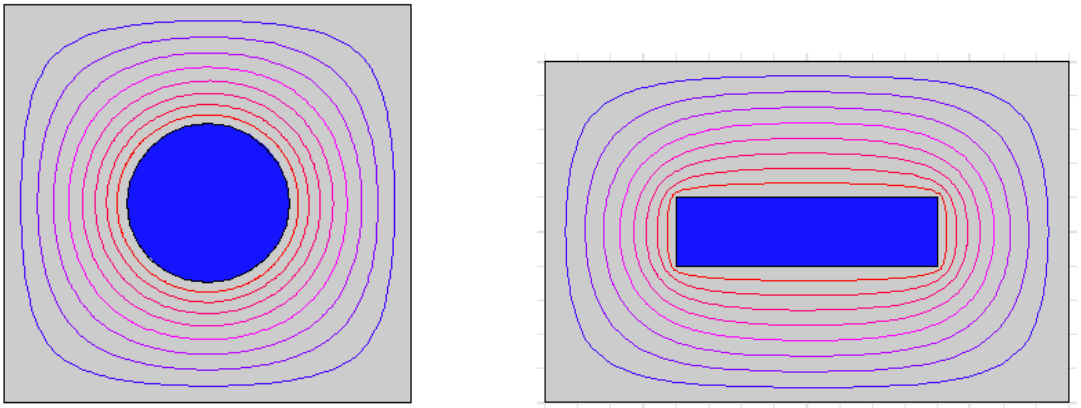

(a) (b)

Figure 2.19 FEA 2D simulation result of flux line pattern for planar inductor (a) with round shape winding, (b) with rectangular shape winding

2.3.2 Analytical Inductance Model for LTCC Inductor with Non-uniform Flux Distribution

In this section, a general analytical inductance model for planar inductor with non-uniform flux and permeability is generated by modifying the method proposed by [58][59]. With this method, the planar inductor is divided into many small concentric rings according to flux path simulation results shown in Figure 2.19 By doing so, the four corners of the rectangular core are ignored. This also can be justified according to flux path simulation results shown in Figure 2.19, which shows that there is very little flux in the four corners. The flux inside each ring is assumed as constant. The permeability of each small ring will be determined according its DC pre-magnetization. Figure 2.20 shows the concept drawing of using this method on a unit cell of lateral flux inductor. r_v is the via radius, r_c is the core radius, r is the radius of each ring core and the Δr is the width of each ring core. If Δr is small enough, flux and permeability both can be assumed as constant in each small ring core, then the flux of each ring core can be calculate as:

$$\Delta\phi(r) = \frac{i \cdot \mu_{r\Delta}(H_{DC}) \cdot h \cdot \Delta r}{2\pi \cdot (r_v + r)} \tag{2.11}$$

where, h is core thickness; $\mu_{r\Delta}(H_{DC})$ is incremental permeability, which is different in different ring and determined by H_{DC}.

Then, the total flux inside core can be calculated by adding the flux of each ring together, which can be done by integration process.

$$\phi_{Total} = \int_0^{r_c - r_v} \Delta\phi(r) = \int_0^{r_c - r_v} \frac{i \cdot \mu_{r\Delta}(H_{DC}) \cdot h \cdot dr}{2\pi \cdot (r_v + r)} \tag{2.12}$$

As a result, the inductance can be calculated as:

$$L = \frac{N \cdot \phi_{Total}}{i} = \int_0^{r_c - r_v} \frac{N \cdot \mu_{r\Delta}(H_{DC}) \cdot h \cdot dr}{2\pi \cdot (r_v + r)} \tag{2.13}$$

where, N is turn number. For this single-turn structure, N=1.

For the LTCC ferrite 40011 provided by ESL, the relationship between incremental permeability and H_{DC} can be defined as:

$$\mu_{r\Delta}(H_{DC}) = 21.77 \cdot e^{-1.067\times10^{-3}\cdot H_{DC}} + 24.22 \cdot e^{-1.57\times10^{-4}\cdot H_{DC}} \tag{2.14}$$

For this lateral flux unit cell, H_{DC} of different ring can be calculated according to ampere law as:

$$H_{DC} = \frac{I_{DC}}{2\pi \cdot (r_v + r)} \tag{2.15}$$

Figure 2.21 shows the inductance calculation results of lateral flux inductor with N=1 structure by using Maxwell 2D model and analytical model. Form Figure 2.23, it can be seen that the results of analytical model can match FEA 2D model very well. There is only some small discrepancy when DC current is very small.

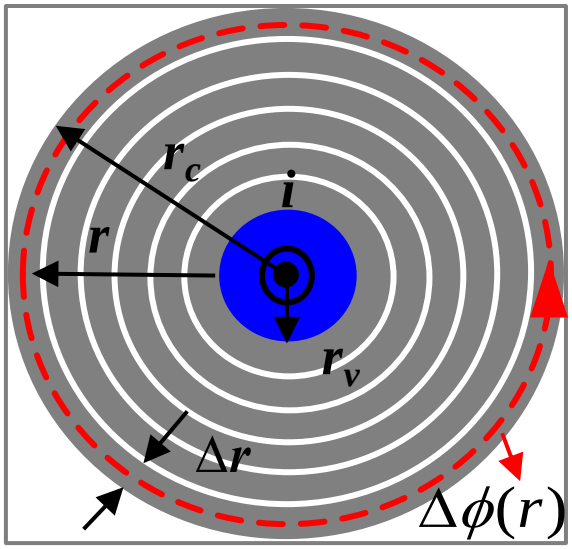

Figure 2.20 Concept drawing of dividing unit cell of lateral flux inductor into many concentric rings

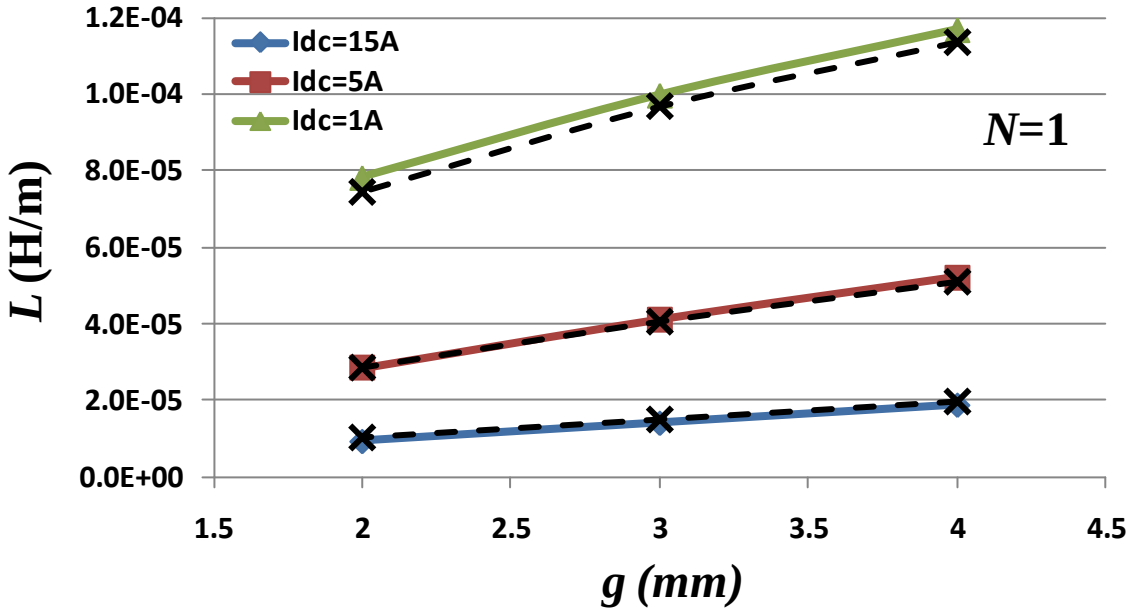

Figure 2.21 Inductance calculation results of lateral flux inductor with *N*=1 structure by using Maxwell 2D model (dash line) and analytical model (solid line)

For lateral flux inductor with *N*=2 structure, the same method can also be applied to calculate inductance. The FEA simulation results of flux path in *N*=2 structure is shown in Figure 2.22. Comparing with *N*=1 structure, the only difference is that the shape of concentric ring is changed from circle to ellipse for *N*=2 structure. The concept drawing about dividing the

half core of a lateral flux N=2 inductor into many ellipse rings is shown in Figure 2.23. With this model, round shape vias are treated as one rectangular winding, which is represented by the dashed rectangular box in Figure 2.23. For this N=2 structure, H_{DC} for different ring core can be calculated according to ampere law as:

$$H_{DC\_N=2} = \frac{2 \cdot I_{DC}}{\sqrt{2} \cdot \pi \cdot \sqrt{\left(2r_v + \frac{d}{2} + r\right)^2 + \left(r_v + r\right)^2}} \tag{2.16}$$

And the inductance of lateral flux inductor with N=2 structure can be calculated as:

$$L_{N=2} = 2\int_0^g \frac{2^2 \cdot \mu_{r\Delta}(H_{DC\_N=2}) \cdot h}{\sqrt{2} \cdot \pi \cdot \sqrt{\left(2r_v + \frac{d}{2} + r\right)^2 + \left(r_v + r\right)^2}} \cdot dr \tag{2.17}$$

where, h is core thickness; $\mu_{r\Delta}(H_{DC})$ is incremental permeability, which is defined by (2.14).

Actually, (2.16) and (2.17) can be modified to be general equations to calculate inductance for lateral flux inductor with any turn number. The general equations for DC flux field intensity and inductance are:

$$H_{DC\_N=n} = \frac{n \cdot I_{DC}}{\sqrt{2} \cdot \pi \cdot \sqrt{\left(n \cdot r_v + \frac{(n-1)d}{2} + r\right)^2 + \left(r_v + r\right)^2}} \tag{2.18}$$

$$L_{N=n} = 2\int_0^g \frac{n^2 \cdot \mu_{r\Delta}(H_{DC\_N=n}) \cdot h}{\sqrt{2} \cdot \pi \cdot \sqrt{\left(n \cdot r_v + \frac{(n-1)d}{2} + r\right)^2 + \left(r_v + r\right)^2}} \cdot dr \tag{2.19}$$

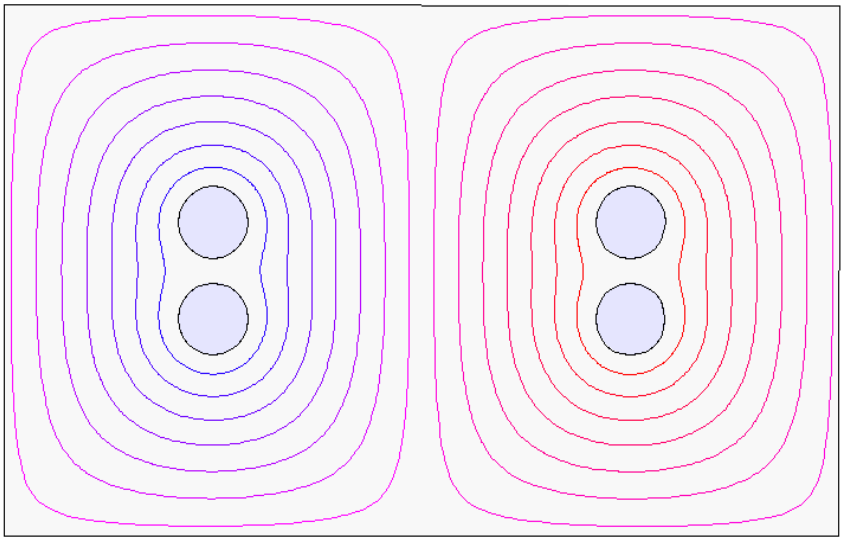

Figure 2.22 FEA simulation results of flux line pattern in lateral flux inductor with *N*=2 structure

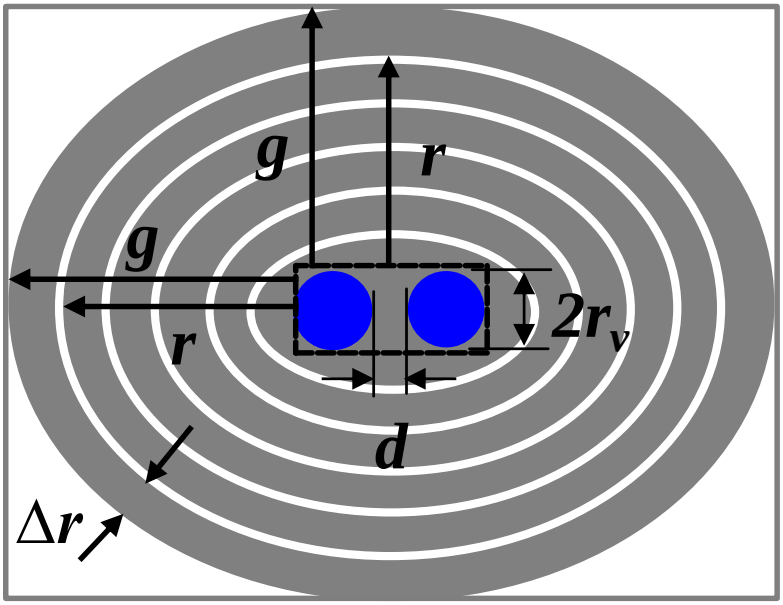

Figure 2.23 Concept drawing of dividing half core of lateral flux *N*=2 inductor into many concentric rings

Figure 2.24 and Figure 2.25 show the inductance calculation results of lateral flux inductor with *N*=2 and *N*=3 structures by using Maxwell 2D model and analytical model. In Figure 2.24 and Figure 2.25, it can be seen that for multi-turn structures, the results of analytical model also can match FEA 2D model very well.

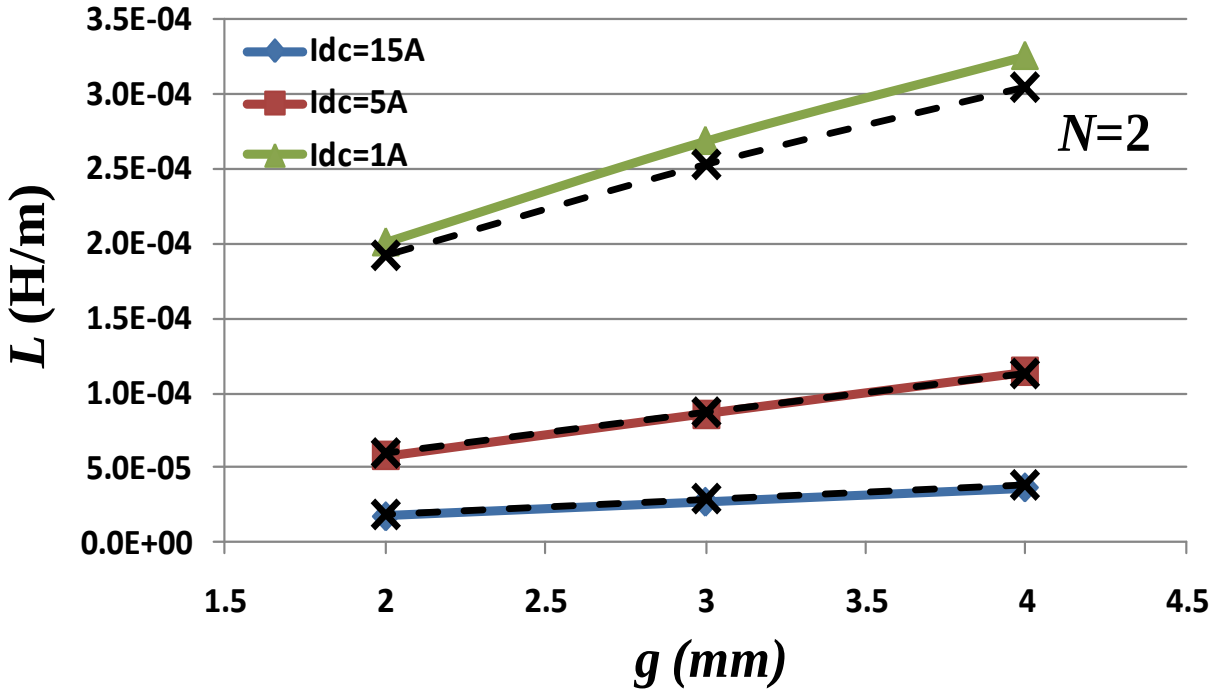

Figure 2.24 Inductance calculation results of lateral flux inductor with *N*=2 structure by using Maxwell 2D model (dash line) and analytical model (solid line)

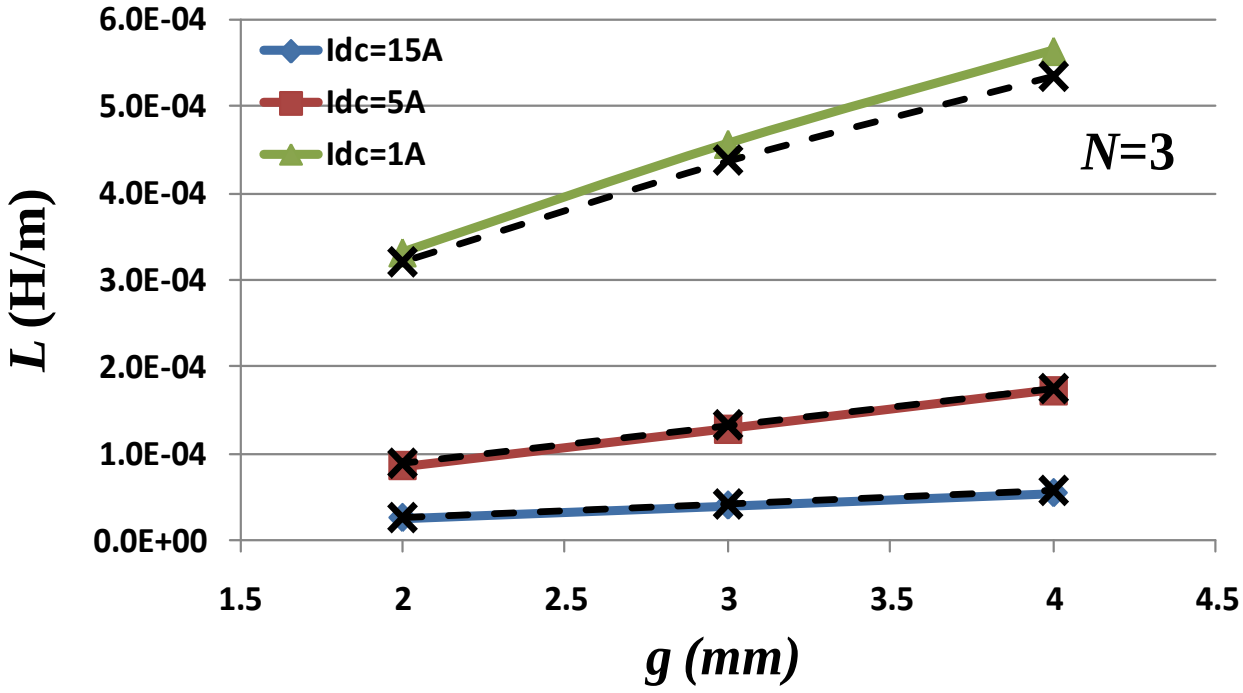

Figure 2.25 Inductance calculation results of lateral flux inductor with *N*=3 structure by using Maxwell 2D model (dash line) and analytical model (solid line)

This analytical inductance model is also can be used to calculate inductance for vertical flux inductor with rectangular winding. The concept drawing about dividing vertical flux inductor with rectangular winding into many ellipse rings is shown in Figure 2.26. The equations for DC flux field intensity and inductance are:

$$H_{DC} = \frac{I_{DC}}{\sqrt{2}\cdot\pi\cdot\sqrt{\left(\frac{w}{2}+r\right)^2+\left(\frac{e}{2}+r\right)^2}} \tag{2.20}$$

$$L = \int_0^g \frac{\mu_{r\Delta}(H_{DC})\cdot l}{\sqrt{2}\cdot\pi\cdot\sqrt{\left(\frac{w}{2}+r\right)^2+\left(\frac{e}{2}+r\right)^2}}\cdot dr \tag{2.21}$$

where, l is inductor length;

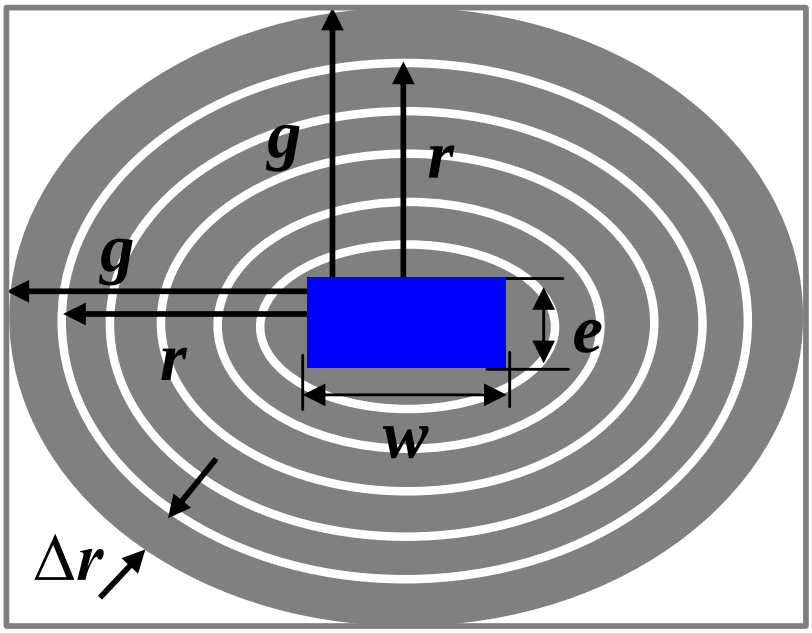

Figure 2.26 Concept drawing of dividing vertical flux inductor into many concentric rings

Figure 2.27 shows the inductance calculation results of vertical flux inductor structures by using Maxwell 2D model and analytical model. It can be seen that the results of analytical model can match FEA 2D model very well.

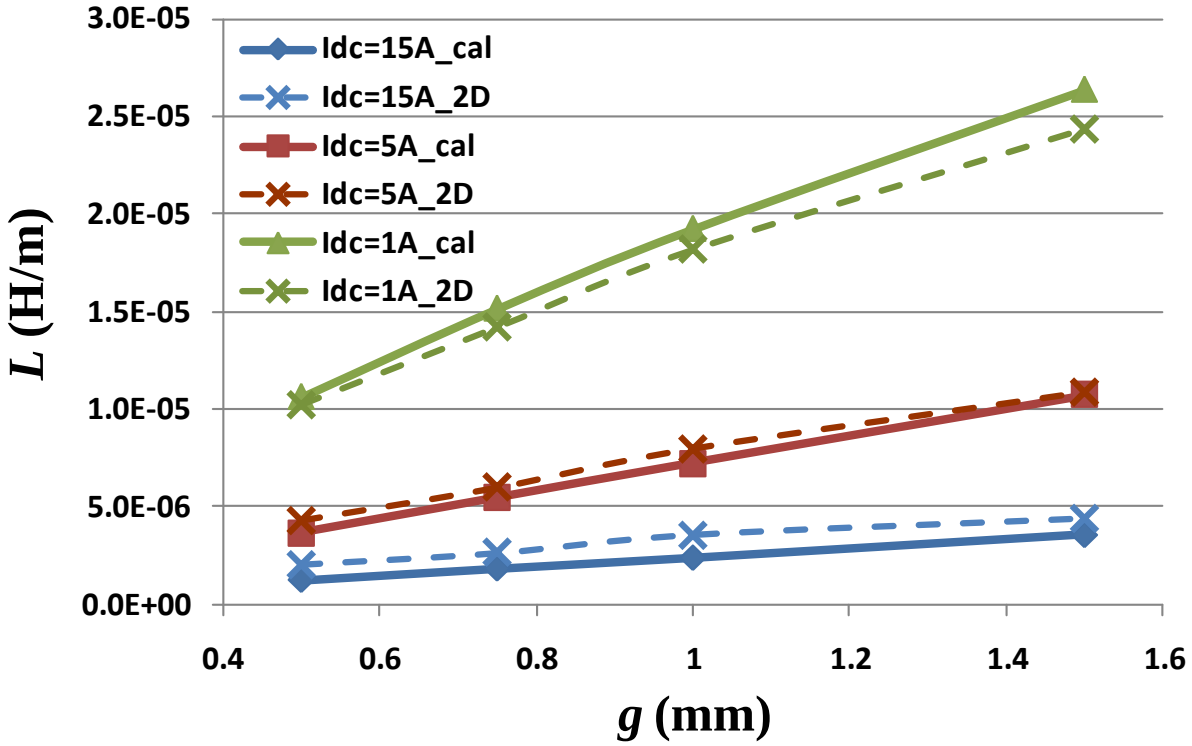

Figure 2.27 Inductance calculation results of vertical flux inductor by using Maxwell 2D model (dash line) and analytical model (solid line)

2.4 Summary

Low-profile planar inductor can be used as substrate for a 3D integrated POL converter to achieve very high power density. However, most planar inductors have non-uniform flux distribution due to high aspect ratio. Some planar inductors, such as low temperature co-fired ceramics (LTCC) inductor even have non-uniform permeability. So, the traditional inductance calculation method, which based on uniform flux and permeability distribution, cannot be used directly for these planar inductors. This chapter proposes some simple but accurate enough

models (includes numerical model and analytical model) to calculate inductance for planar inductors with non-uniform flux and permeability.

For numerical model, a two step magneto-static FEA simulation with small perturbation method is introduced to calculate inductance of planar inductor. 3D and 2D models both are studied and compared. For lateral flux inductor, the FEA simulation result of inductance with 2D model is smaller than that with 3D model. The reason is that the flux generated by surface windings of lateral flux inductor is ignored. However, the difference between 2D and 3D results is very small. So, the proposed magneto-static 2D simulation with small perturbation solution is a good solution to calculate inductance of planar inductor with non-uniform flux and permeability due to its fast simulation time and high enough accuracy.

For Analytical model, the planar inductor is divided into many small concentric rings according to the FEA simulation results. The flux inside each ring is assumed as constant. Then, the flux of each concentric ring can be calculated. The total flux is the sum of the flux inside each ring. Finally, the total inductance can be calculated from the total flux. The calculation results for analytical model can match with FEA 2D simulation very well.

Chapter 3. Inductance Density Comparison between Vertical Flux and Lateral Flux Planar Inductors

In order to design a low-profile inductor substrate with a higher inductance density to achieve a more compact integrated converter, this chapter mainly focuses on the inductance density issue of the low-profile inductor design. By previous proposed analytical inductance models, different LTCC inductor structures with two different flux path patterns (vertical and lateral) are studied and compared.

3.1 Inductance Density of Planar Inductor with Lateral Flux Structure

The inductance density study for planar inductor is based on the analytical inductance models introduced in chapter 2. The basic concept of these models is dividing disc core into many small concentric rings. Inside each concentric ring, both the flux and permeability are assumed as uniform. So, the inductance of each concentric ring can be calculated first, and then the total inductance of planar inductor can be calculated by adding all the ring inductance. Figure 3.1 shows the concept drawing of dividing the lateral flux inductor with single-turn structure into many concentric rings. Where, r_v is the radius of via; g represents core size; r represents the distance between each ring to the via; Δr is the width of each ring. In this example, r_v=0.7mm, Δr=0.1mm, core thickness h=1mm, and g is defined as a variable. The core material is LTCC ferrite 40011 from ESL®. The B-H curve of this magnetic material is in shown if Figure 2.10 in chapter 2. Before studying the inductance density of lateral flux inductor, the magnetic field strength, permeability and inductance for each concentric ring are studied first.

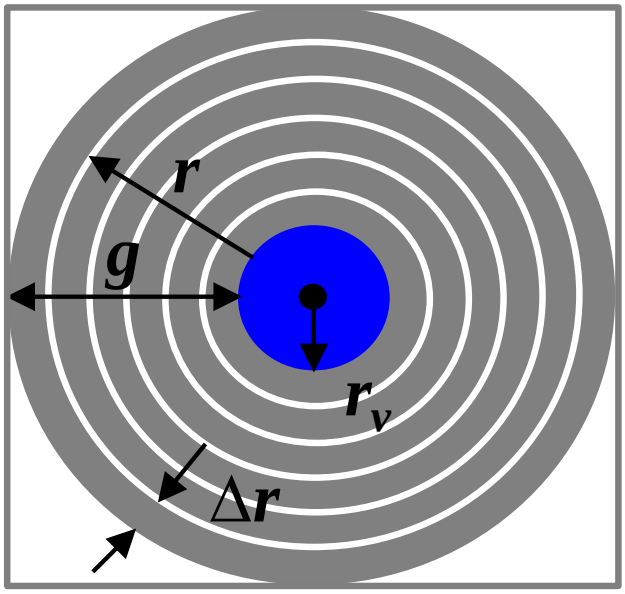

Figure 3.1 Concept of dividing half core of single-turn lateral flux inductor into many concentric rings

According to Ampere law, the magnetic field strength of each ring can be calculated as:

$$H_{DC}(r) = \frac{I_{DC}}{2\pi \cdot (r_v + r)} \tag{3.1}$$

Figure 3.2 shows the H_{DC} value for each concentric ring when inductor current I_{DC}=15A, via radius r_v=0.7mm. Here, r=0mm represents the ring just next to the via; r=4mm represents the ring, whose distance to the via is 4mm; It can be known that from the inner ring to outer ring, the H_{DC} decrease continually. This is because the outer ring has larger magnetic mean path length.

After calculating H_{DC} for each ring, the permeability of each ring can be calculated according to (2.14). Figure 3.3 shows the permeability value for each concentric ring when inductor current is I_{DC}=15A. It can be known that from the inner ring to outer ring, the permeability of the ring core increase continually due to the decreasing of H_{DC}.

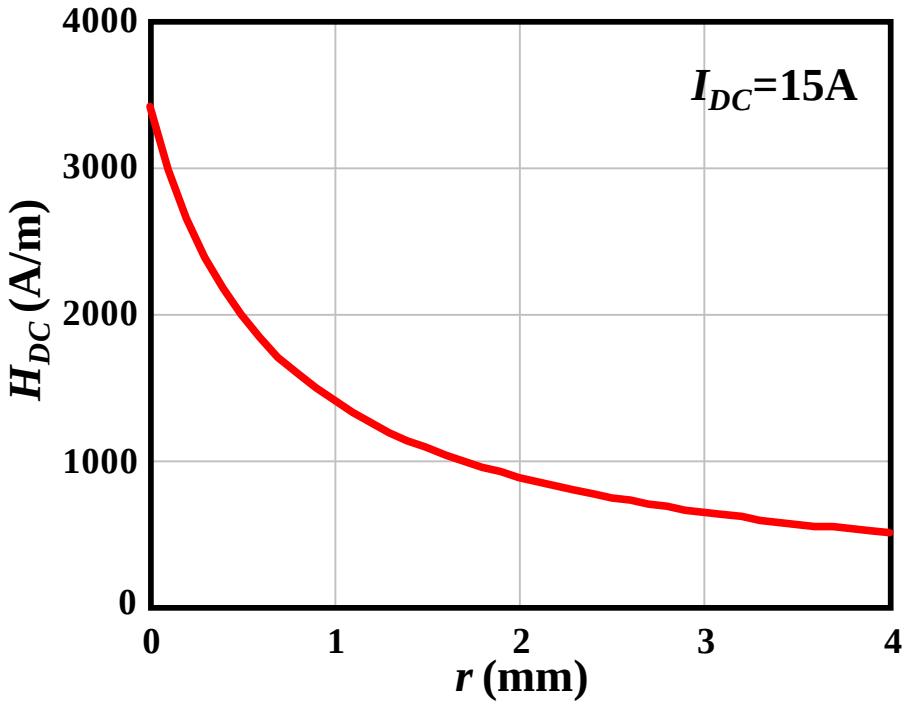

Figure 3.2 H_{DC} value for each concentric ring in a LTCC inductor

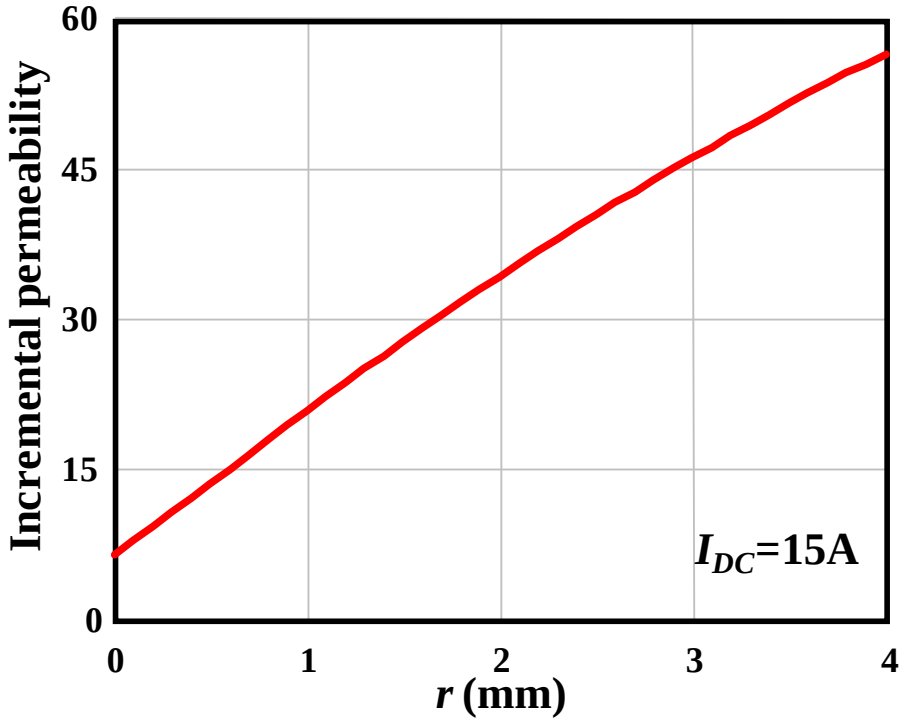

Figure 3.3 Permeability value for each concentric ring in a LTCC inductor

Because both the flux and permeability are assumed as uniform inside each concentric ring, the inductance for each ring can be calculated as:

$$L(r) = \frac{\mu_{r\Delta}(r) \cdot h \cdot \Delta r}{2\pi \cdot (r_v + r)} \tag{3.2}$$

where, h is core thickness.

Figure 3.4 shows the inductance value of each concentric ring when inductor current I_{DC}=15A, via radius r_v=0.7mm. It can be seen that when r is very small, the ring with larger r will have larger inductance. But, when r is larger than some value (in the case, r=2mm), the larger r will give smaller ring inductance. This is because the ring inductance is impacted by two things. One is magnetic mean path length, which is continually reduced when increasing r. Another one is core permeability, which is continually increased when increasing r. When r is small, the core permeability increasing effect dominates the changing of ring inductance, but when r become larger and larger, the magnetic mean path length reducing effect will dominate the changing of ring inductance. From Figure 3.4, it can be known that it is not very efficiency to design this lateral flux inductor with very large core size. Because when the core size is too large, the outer rings don't contribute too much inductance. Actually, the core utilization efficiency can be represented by inductance density.

Figure 3.5 shows the inductance density of the single-turn lateral flux inductor with different core size (represented by parameter g) and different inductor current. In all the cases, via radius r_v=0.7mm. It can be seen that 1) with given via size, there is optimal g value to give maximal inductance density; 2) reducing inductor current will increase inductance density due to larger permeability; 3) the optimal g values for different inductor current cases are almost the same.

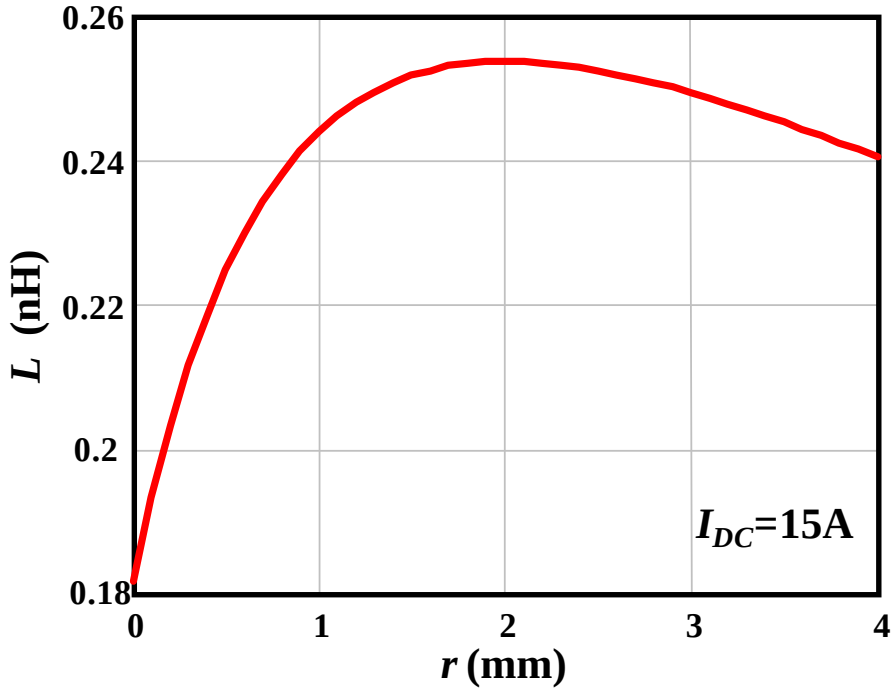

Figure 3.4 Inductance value of each concentric ring in a LTCC inductor

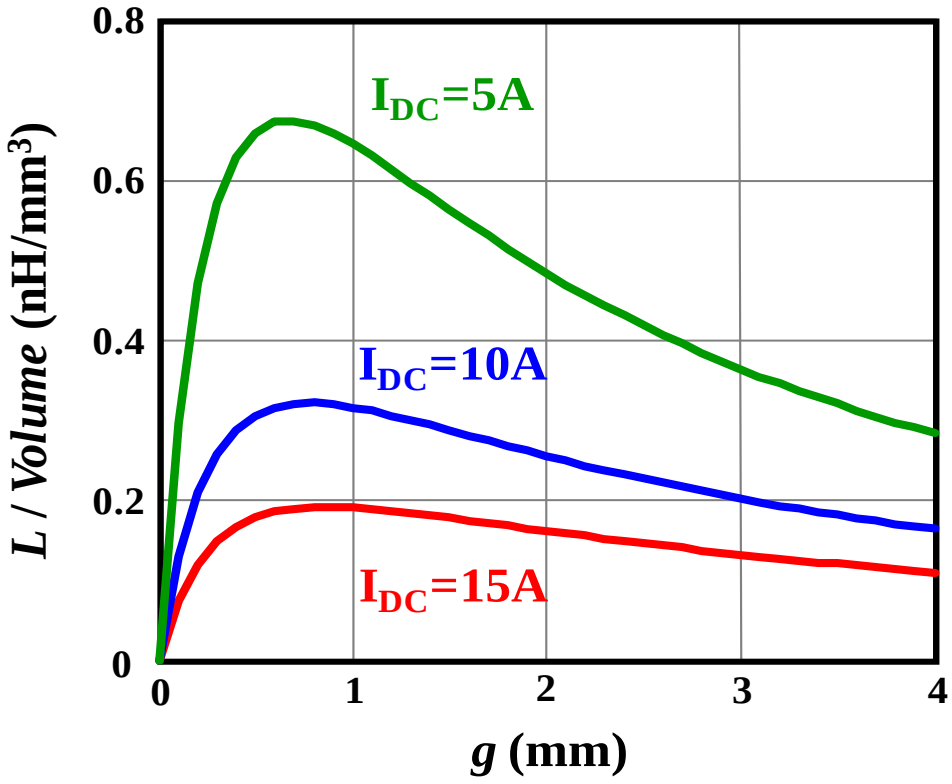

Figure 3.5 Inductance density of the single-turn LTCC lateral flux inductor

Figure 3.6 shows the inductance density curve of the lateral flux inductor defined in Figure 3.1 with a constant permeability (μ_r=200) core and with LTCC core but 0A inductor current. Because the initial permeability of LTCC material is μ_i=200, the inductance density of LTCC core with 0A inductor current is the same as inductance density of constant permeability (μ_r=200) core. There is also an optimal g value to give the maximal inductance density for constant permeability case.

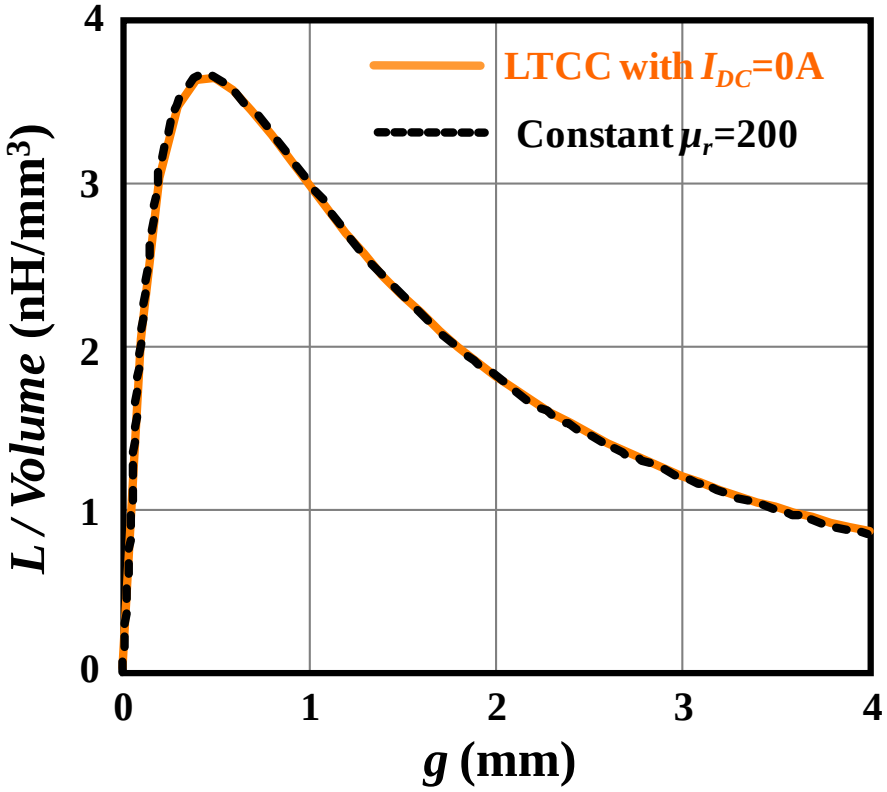

Figure 3.6 Inductance density of the single-turn inductor with constant permeability

Figure 3.7 shows the inductance density curve of lateral flux inductor with constant permeability but different winding cross-section area. Normally, the smaller winding cross-section area is used for smaller inductor DC current. It can be seen that 1) the inductance density is increased when winding cross-section area is reduced; 2) with given winding cross-section area, there is always an optimal g value to give the maximal inductance density.

Based on above analysis, it can be concluded that for lateral flux inductor structure, there is always an optimal *g* value to give the maximal inductance density, no matter with non-linear permeability or constant permeability, with large inductor current or small current.

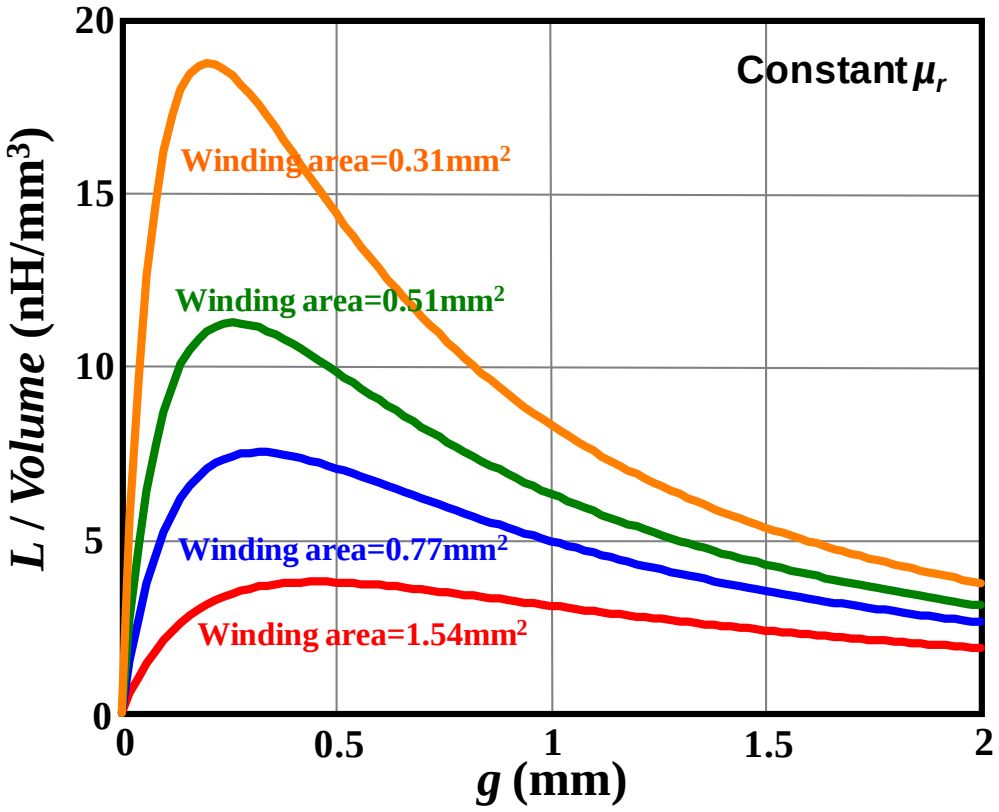

Figure 3.7 Inductance density of lateral flux inductor with constant permeability but different winding cross-section area

Figure 3.8 shows the inductance density curve of the lateral flux inductor with different core thickness *h* and *g* value. It can be known that the core thickness will not impact the inductance density for lateral flux structure. This is because the flux pattern of lateral flux inductor will not be impacted by core thickness. As a result, the lateral flux inductor can be designed with maximal inductance density even with very low profile.

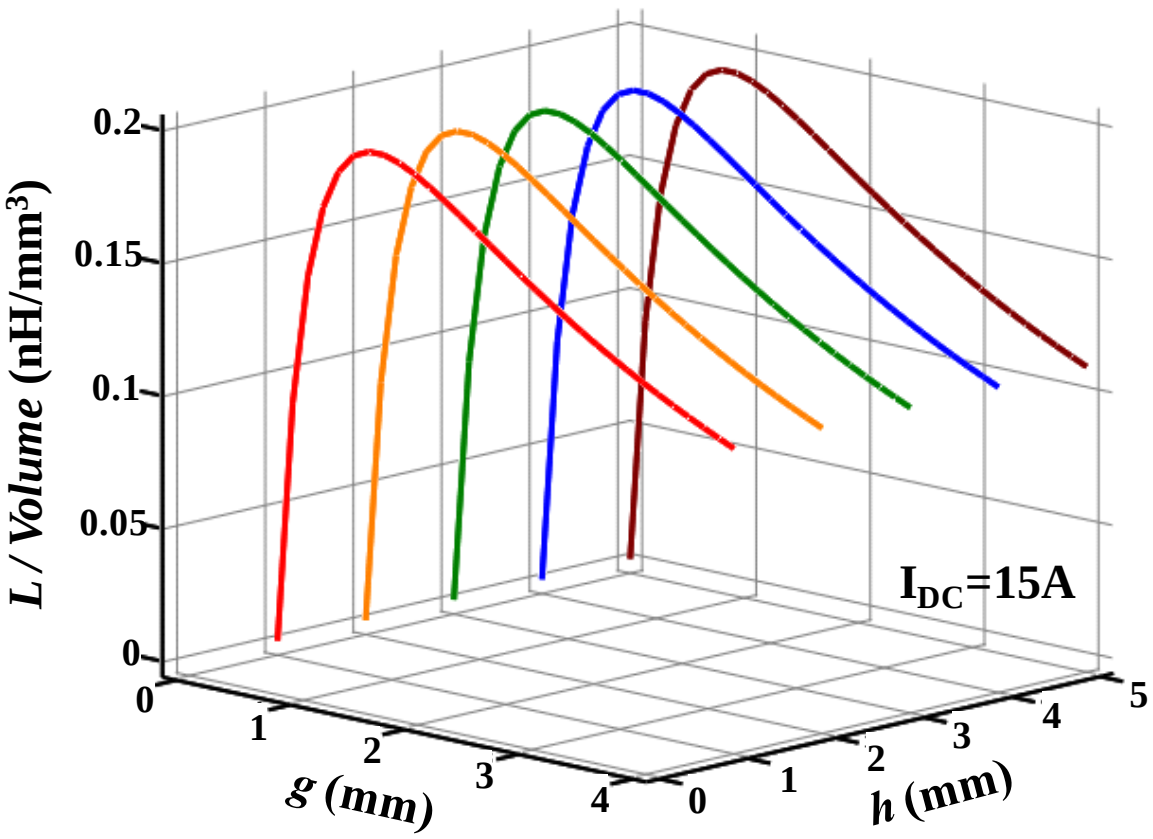

Figure 3.8 Inductance density of the lateral flux inductor with different core thickness

3.2 Inductance Density of Planar Inductor with Vertical Flux Structure

If turn 90 degrees of this lateral flux unit cell, it will becomes a vertical flux unit cell with round shape winding. In this case, core radius will impact both the core thickness and inductance density. As a result, with a given via radius and inductor current, there is only one core thickness that can give the maximum inductance density. For example, Figure 3.5 shows that g= 0.7mm can give the maximum inductance density for 15A inductor current and 0.7mm via radius. So, only 3mm core thickness can give the maximum inductance density for this vertical flux inductor. Actually, in real practice, the vertical flux inductors are usually designed with rectangular winding as shown in Figure 3.9(a). Where, h is core thickness; e is winding thickness; and w is winding width. The inductance density of vertical flux inductor with rectangular winding also

can be calculated according to the concentric ring model introduce in chapter 2. Figure 3.9(b) shows the concept drawing of dividing the vertical flux inductor into many concentric rings. Where, *g* is the distance between core edge and winding edge, and parameter *r* is used to represents the position of each concentric ring.

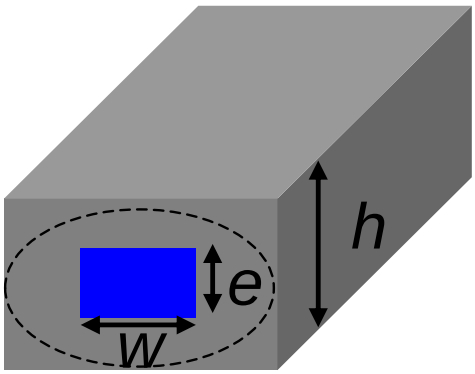

(a)

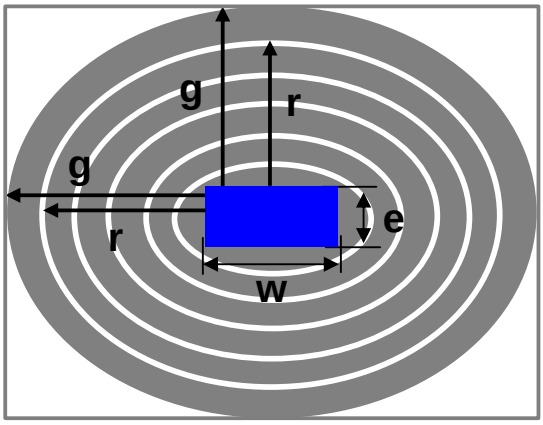

(b)

Figure 3.9 Vertical flux inductors and the concept of dividing its core into many concentric rings: (a) vertical flux structure, (b) concept of dividing its core into many concentric rings

Figure 3.10 shows the inductance density calculation results of vertical flux inductor with different g value and winding shape. In this case, inductor DC current is the same I_{DC}=15A, the winding cross-section area is 1.5mm^2. It can be seen that 1) Comparing with inductor with square shape winding, the inductor with rectangular shape winding has smaller inductance density. The larger winding aspect ratio will cause the smaller inductance density. 2) With given

winding shape, the vertical flux structure also has a optimal *g* value to give maximal inductance density. In this vertical flux structure, the parameter *g* is impacted by core thickness *h*.

$$g = \frac{h - e}{2} \tag{3.3}$$

So, actually the inductance density will be impacted by core thickness.

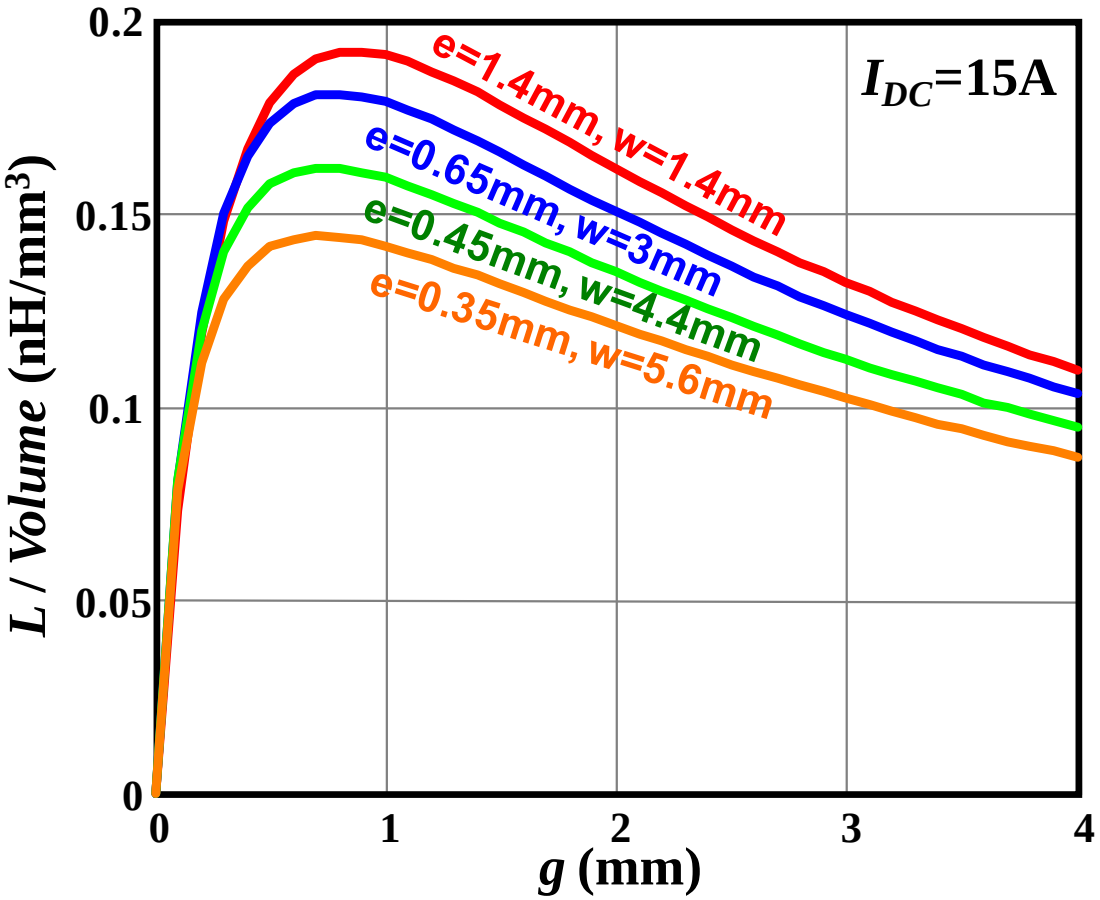

Figure 3.10 Inductance density of vertical flux inductor with different winding shapes

Figure 3.11 shows the inductance density calculation of vertical flux structure with 15A inductor current, 2mm core thickness and 1.5mm^2 winding cross-section area. It shows that for this vertical flux inductor structure there is an optimal *e* value to achieve the maximal inductance density with given core thickness. Too small or too large *e* both will decrease inductance density.

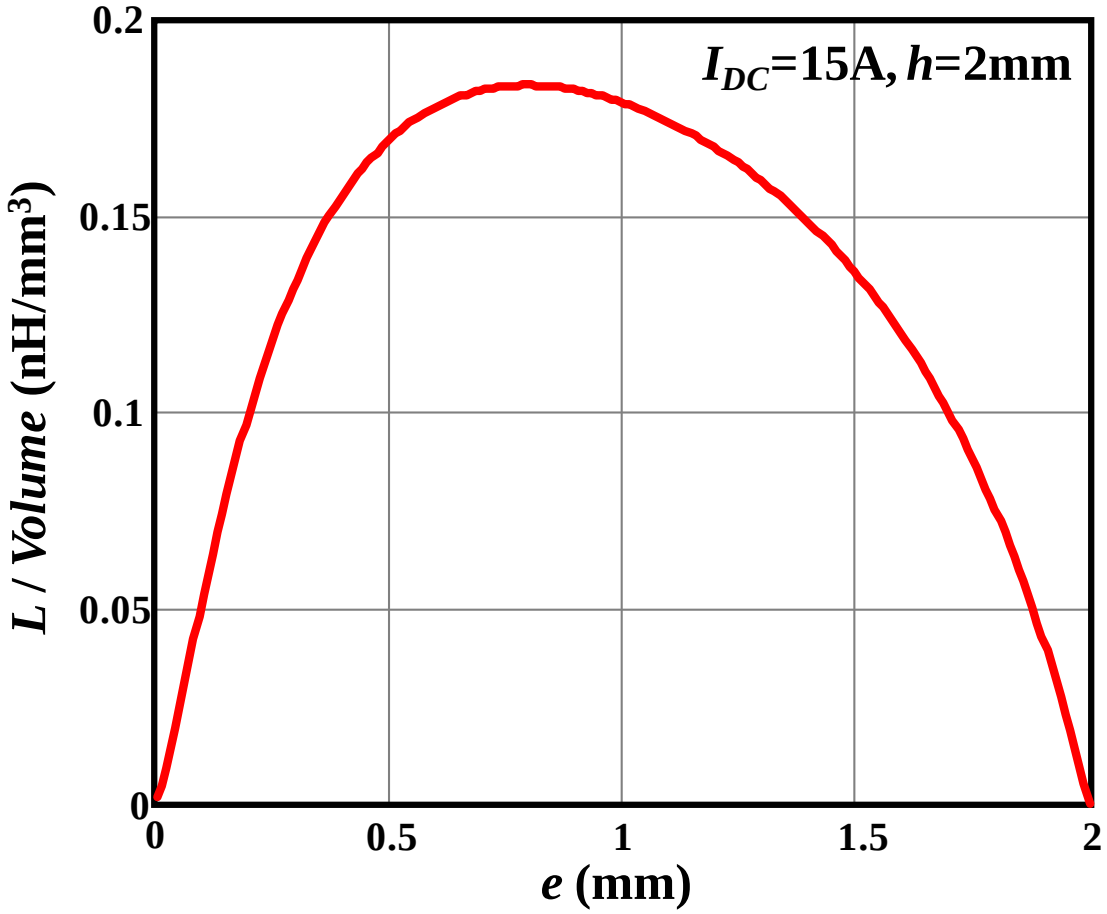

Figure 3.11 Inductance density of vertical flux inductor with given core thickness

Figure 3.12 is inductance density calculation results for vertical flux structure with different core thickness and winding shape. In all the cases, the inductor current I_{DC}=15A, the winding cross-section area is 1.5mm^2. In Figure 3.12, each curve represent one core thickness. It shows that for this vertical flux inductor structure different core thickness h will give different maximal inductance density. Increase core thickness h will increase the maximal inductance density first, but after some value, further increase h will reduce the maximal inductance density. So, there is optimal core thickness h to achieve the highest maximal inductance density. For this I_{DC}=15A case, this optimal core thickness is h=3mm.

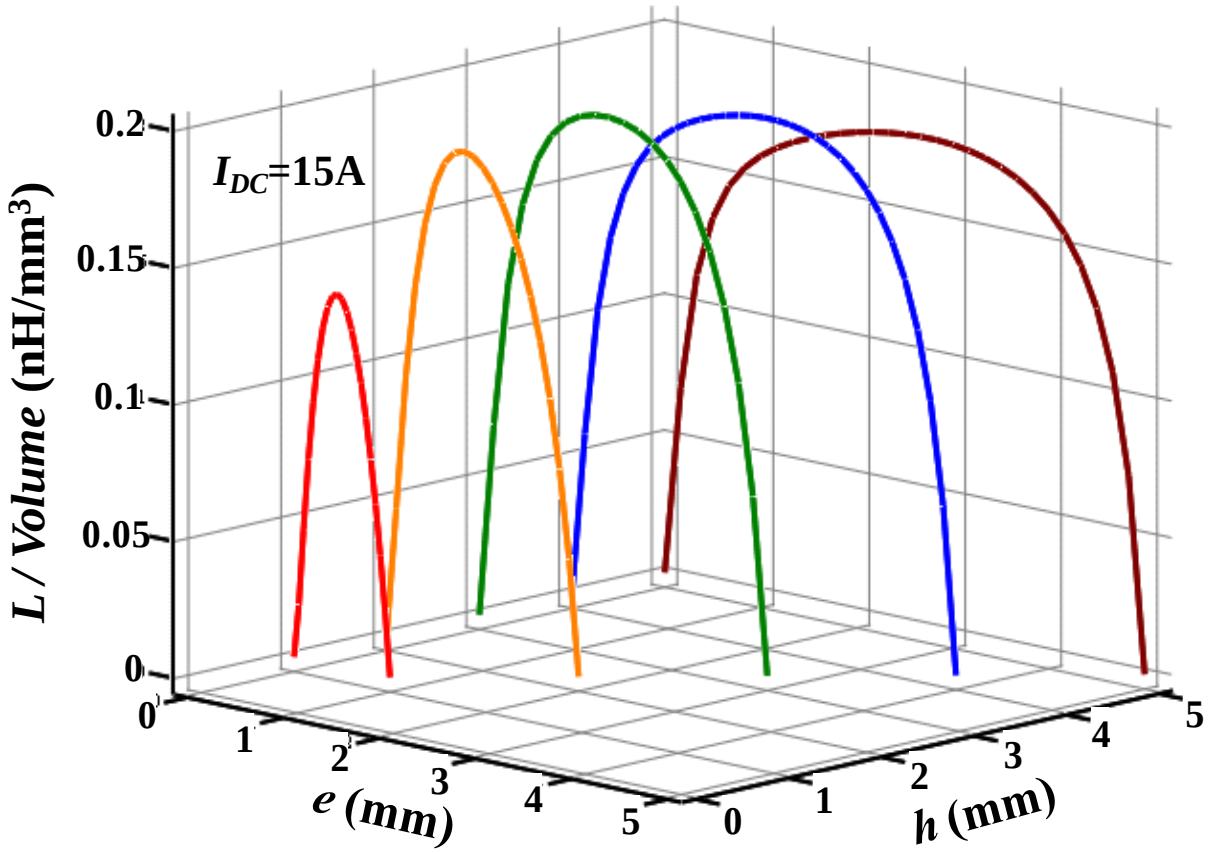

Figure 3.12 Inductance density of vertical flux structure with different core thickness with 15A current

Figure 3.13 shows the inductance density curve for vertical flux inductor with I_{DC}=7.5A. In this case, the winding cross-section area is also reduced to half value of the first case. It can be seen that with this smaller current case, the optimal core thickness changed from previous h=3mm to h=2mm. If the inductor current is further reduced to I_{DC}=3A, and the winding cross-section area is also further reduced to one fifth of the first case, the highest inductance density will change from h=2mm to h=1mm. The inductance density curve with I_{DC}=3A is shown in Figure 3.14

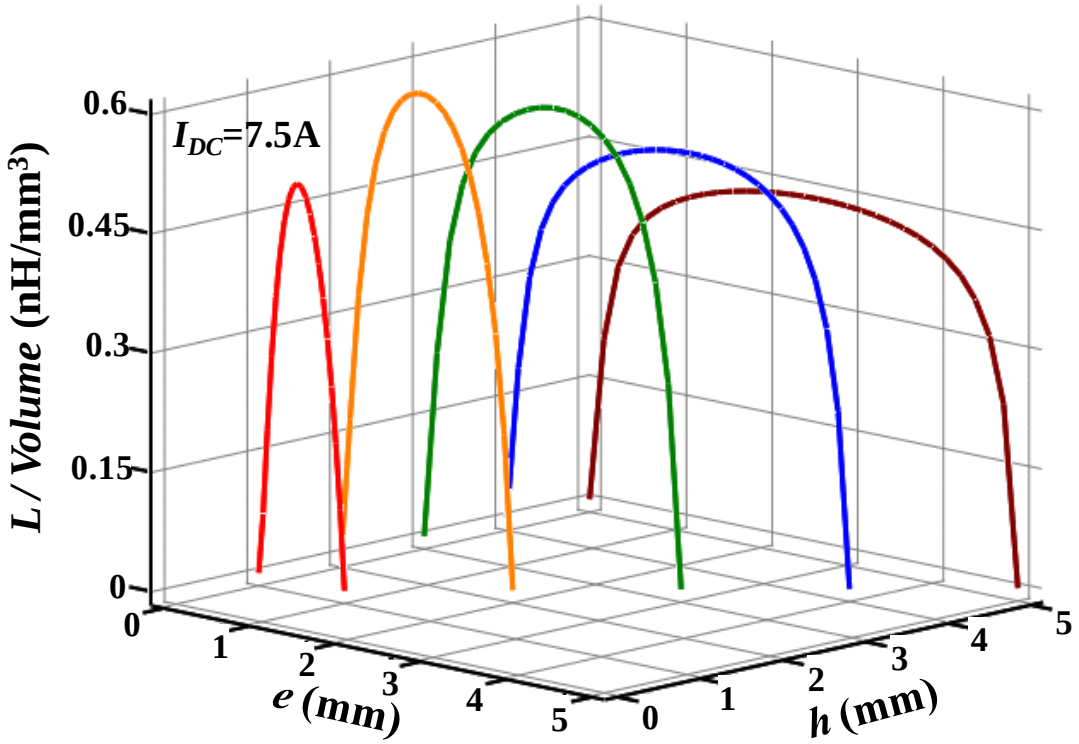

Figure 3.13 Inductance density of vertical flux structure with different core thickness with 7.5A current

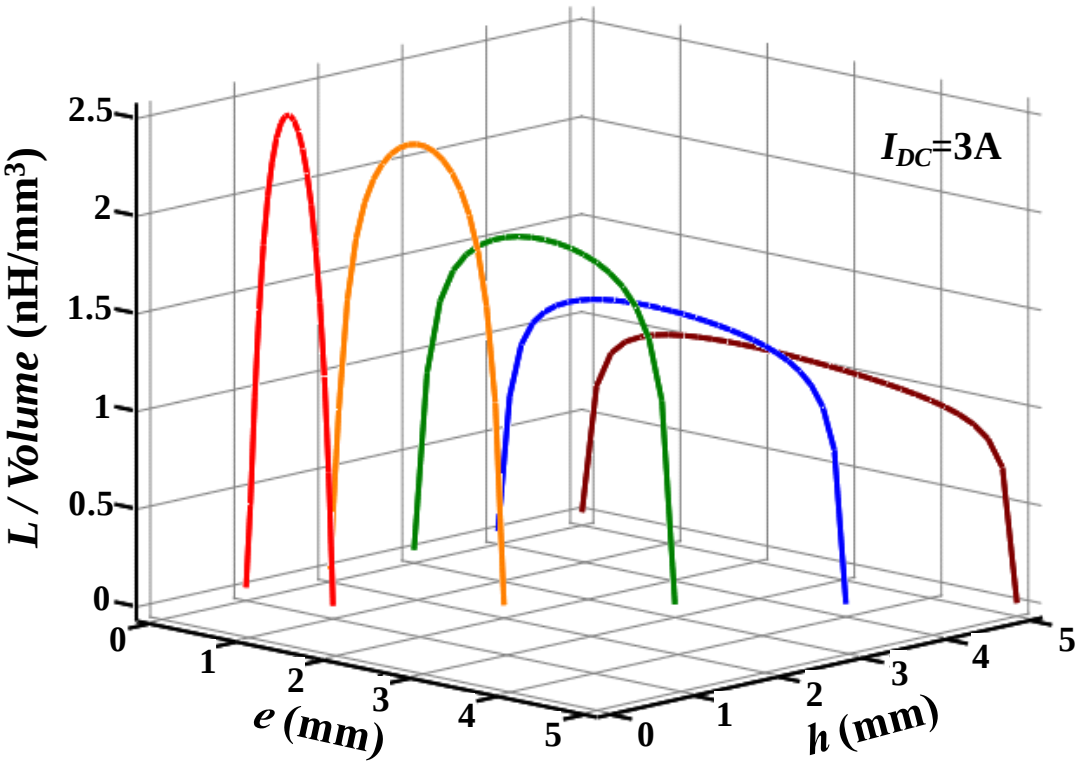

Figure 3.14 Inductance density of vertical flux structure with different core thickness with 3A current

3.3 Inductance Density Comparison between Lateral Flux Structure and Vertical Flux Structure

Figure 3.15 shows the impact of core thickness *h* on maximal inductance density for both vertical flux inductor and lateral flux inductor with 15A inductor current and the same winding cross-section area, which is 1.5 mm^2. It can be seen that the maximal inductance density of lateral flux inductor will not be impacted by core thickness. But the maximal inductance density of vertical flux inductor will be dramatically impacted by core thickness. Too small or too large core thickness both will reduce the maximal inductance density. However, the peak value of vertical flux structure's maximal inductance density is the same as that of lateral flux structure. It shows that if there is no core thickness limitation, the vertical flux structure will have the same inductance density as lateral flux structures. When reducing core thickness, the inductance density of a lateral flux structure will stay constant due to the linear relationship between core thickness and inductance. However, for vertical flux structure, the aspect ratio of the optimal winding will become larger as the core thickness becomes thinner. So, the inductance density of the vertical flux structure will drop as the core thickness decreases.

The inductance density of LTCC lateral flux inductor and LTCC vertical flux inductor both are impacted by inductor current and winding cross-section area. The inductance density comparison results between LTCC lateral flux inductor and vertical flux inductor with smaller inductor current and winding cross-section area are shown in Figure 3.16 and Figure 3.17. For 7.5A inductor current case, the winding cross-section area is reduced to 7.5mm^2; for 3A inductor current case, the winding cross-section area is reduced to 3mm^2. In Figure 3.16 and Figure 3.17, it can be seen that 1) the highest inductance density of vertical flux structure always equals to the maximal inductance density of lateral flux structure; 2) the optimal core thickness value for

vertical flux structure to achieve the highest inductance density is related with inductor current and winding cross-section area. When reducing inductor current and winding cross-section area, the optimal core thickness value will be reduced at the same time. With 7.5A inductor current and 7.5mm^2 winding cross-section area, the optimal core thickness is reduced to *h*=2mm; With 3A inductor current and 3mm^2 winding cross-section area, the optimal core thickness is further reduced to *h*=1.2mm. Although with small inductor current, the vertical flux structure also can be designed with very low profile to achieve the same inductance density as lateral flux structure, there only one choice of core thickness for vertical flux structure. So, the design of vertical flux structure doesn't have too much flexibility comparing with lateral flux structure, whose inductance density will not be impacted by core thickness. Therefore, generally speaking it is better to use lateral flux structure when designing a LTCC low-profile inductor.

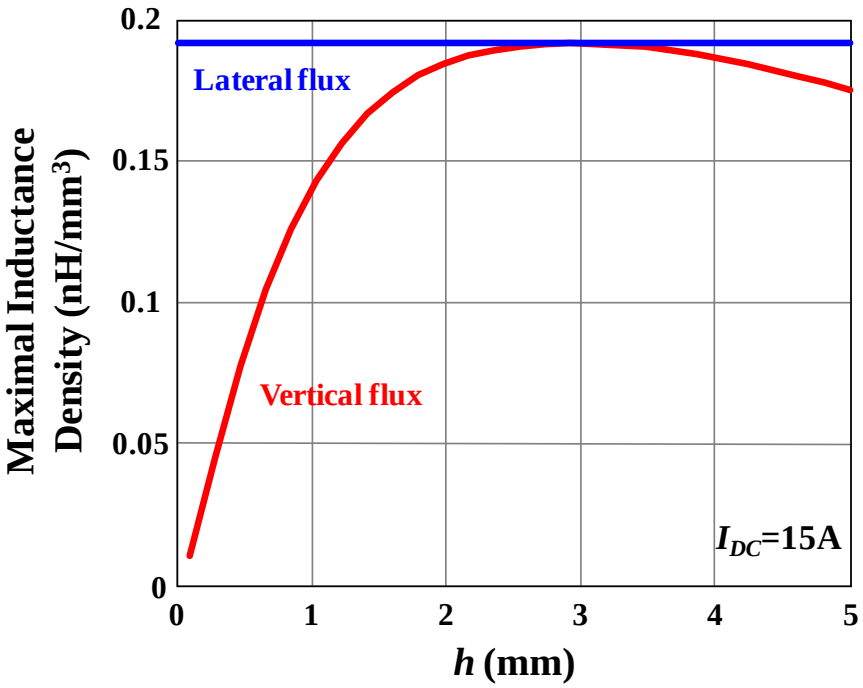

Figure 3.15 Maximal inductance density of vertical flux inductor and lateral flux inductor with 15A inductor current

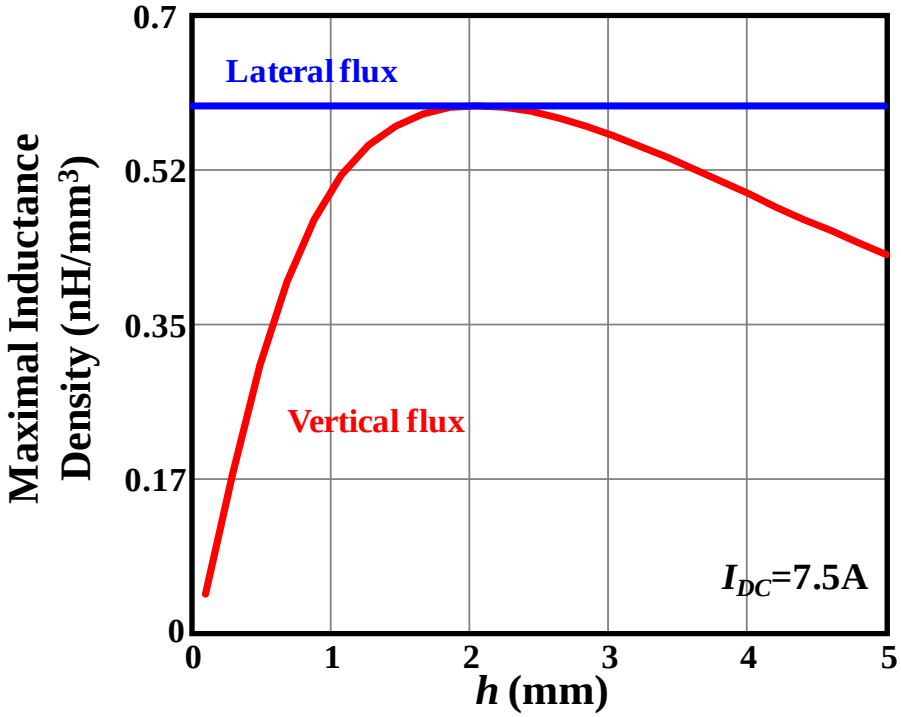

Figure 3.16 Maximal inductance density of vertical flux inductor and lateral flux inductor with 7.5A inductor current

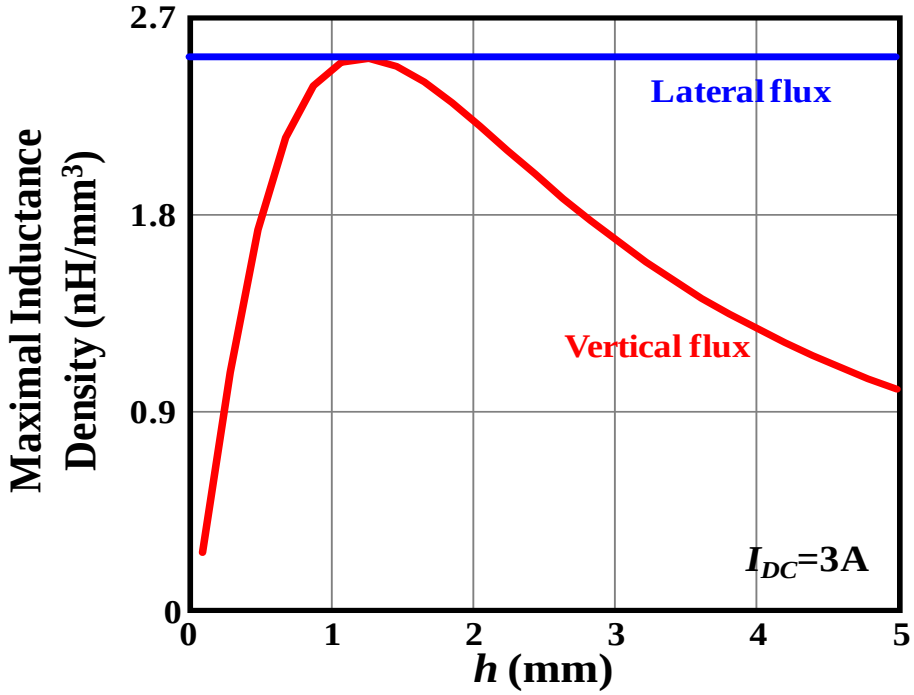

Figure 3.17 Maximal inductance density of vertical flux inductor and lateral flux inductor with 3A inductor current

Figure 3.18 shows the impact of core thickness *h* on maximal inductance density for both vertical flux inductor and lateral flux inductor with constant permeability μ_r=200. It can be seen that with constant permeability core material, 1) the maximal inductance density of vertical flux structure and lateral flux structure are also the same. 2) Just like with LTCC ferrite, which has non-linear permeability, the lateral flux structure has constant inductance density; but the vertical flux structure only can achieve maximal inductance with one particular core thickness. 3) inductor with smaller winding cross-section area has larger inductance density for both lateral flux structure and vertical flux structure. 4) the optimal core thickness for vertical flux structure to achieve the highest inductance density is also related with winding cross-section area. When reducing winding cross-section area, the optimal core thickness value will be reduced at the same time. In this case, the optimal core thickness is reduced from 2.2mm to 1 mm when reducing winding cross-section area from 1.54mm^2 to 0.31mm^2.

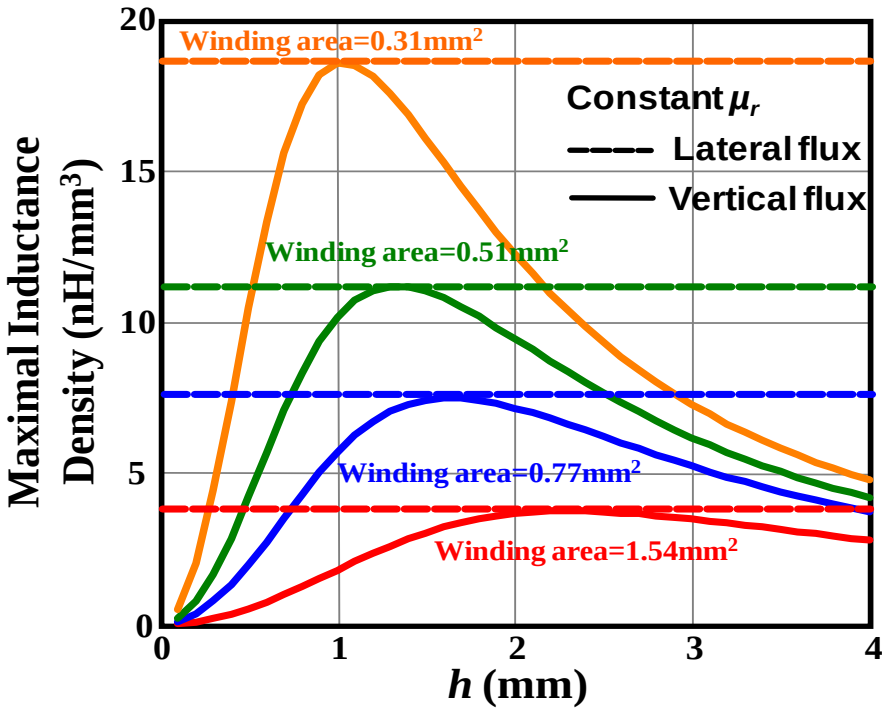

Figure 3.18 Maximal inductance density of vertical flux inductor and lateral flux inductor with constant permeability

3.4 Summary

In this chapter, the inductance density values of different LTCC planar inductors are studied. According to the flux pattern, the LTCC planar inductors are divided into two basic groups. One is with lateral flux structure; another one is with vertical flux structure. The vertical flux type means the magnetic flux path plane is perpendicular with the substrate. The lateral flux type means the magnetic flux path plane is parallel with the substrate. Based on the analytical inductance model proposed in chapter 2, the inductance density values of these two basic structures are compared. For lateral flux structure, the inductor core thickness will not impact the inductance density. So lateral flux inductor can be designed with ultra-low profile but still have very high inductance density. However, for the vertical flux structure, the core thickness will impact the inductance density a lot. With given inductor current and winding cross-section area, there is only one particular core thickness for vertical flux structure to have the same maximal inductance density as lateral flux structure. As a result, the lateral flux structure has much more design flexibility; and it is superior to vertical flux structure for low-profile inductor design from inductance density point of view. This conclusion is not only valid for LTCC planar inductor, which has very non-linear permeability, but also valid for planar inductor with other core material, which has constant permeability.

Chapter 4. Loss Modeling for Low-Profile Planar Inductor with Non-uniform Flux Distribution

In order to optimize the low-profile LTCC inductor design for high-frequency applications, the winding ACR loss and core loss both need to be studied. This chapter focuses on the winding ACR loss issue, trying to provide some fundamental knowledge and a model to help optimize the low-profile LTCC inductor structure proposed in chapter 2

4.1 Overview of Inductor Winding Loss Modeling

In the past 40 years, many efforts [61]–[66] have been made to derive expressions allowing for an accurate representation of the frequency behavior of transformer or inductor winding ACR. However, most effort has been focused on modeling the winding ACR for a conventional discrete transformer and inductor, such as a transformer and inductor with an EE core. In order to analytically calculate the ACR of transformer windings, a one-dimensional field solution is performed by both Dowel1 [61] and Perry [64], and their solutions are adopted by several other authors. The major assumptions that are necessary for the one-dimensional field solution are:

1) The magnetic flux in the transformer winding space is parallel to the core leg. In other words, the core material must have high permeability and no gap in the core.

2) The conductor layers can be modeled as continuous conductor foils, which fill the full core-window breadth.

However, the LTCC ferrite is not a high-permeability material. Its initial permeability is around 200. It will drop to only 50 when applying a 1000A/m H field. Furthermore, the winding structure of the low-profile inductor also cannot be modeled as a continuous conductor foil. In [66], a parametric study of losses is used to identify inductor winding ACR. This approach is

also used in [67] and [68] to analyze other winding loss problems. Numerical simulation is used to do the parametric study, and then some closed-form approximations are generated based on simulation results to calculate the winding ACR.

Here, we will also adopt this methodology to study the winding ACR for a low-profile LTCC inductor. A 3D finite-element analysis (FEA) model and a 2D FEA model are established and compared for these LTCC planar inductors. Based on FEA simulation results, several ACR closed-from formulas are also proposed in this paper to help design optimization for these planar inductors. There are additional issues that are not considered in this paper. One assumption of this paper is that we consider the reliability of finite-element analysis (FEA) to be well-established for high-frequency winding loss prediction. Because FEA is based on applying well-established numerical methods (for electromagnetic problems, it based on the solution of Maxwell's equations), it is very close to a real case. Since 1985, FEA has been successfully used for windings loss predictions. Many papers report some good results about the consistency of FEA results with experimental measurements [69]–[72].

4.2 Numerical Winding ACR Model (FEA simulation) for Planar Inductor

In this section, the FEA simulation for winding ACR of LTCC lateral flux planar inductors is discussed. The Ansoft Maxwell is used to do eddy current simulation for different planar inductor structures. The two-turn structure (N=2) with a square-shaped via (shown in Figure 4.1) is used as an example to illustrate this study. Figure 4.2 shows the simulation results for AC current distribution inside inductor winding of an N=2 planar inductor. It can be seen that most AC current is distributed on the surface and edge of winding due to the skin effect and the proximity effect. The 3D simulation results for AC current distribution on the top and bottom

surface of via are shown in Figure 4.3(a) and Figure 4.3(b), from which it can be seen that the AC current distributions are almost identical on two surfaces of the via. So, we can assume that the AC current distributions inside the via is uniform in the vertical direction. As a result, the corner effect can be ignored, and a 2D model can be used to study the ACR of the via. Figure 4.3(c) shows the 2D simulation results for AC current distribution in the inductor vias, which has very little difference from the 3D simulation results.

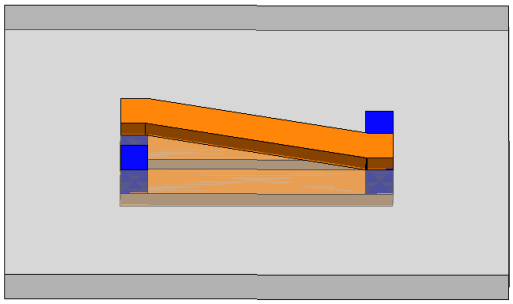

Figure 4.1 LTCC two-turn inductor (*N*=2) with square-shaped via

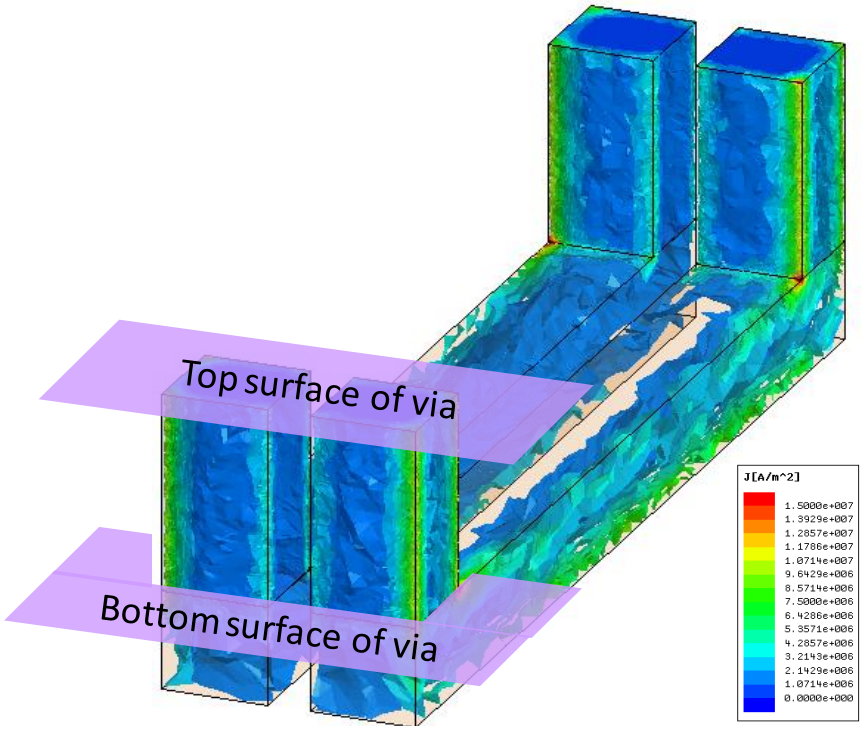

Figure 4.2 FEA 3D simulation result for AC current distribution inside winding of a two-turn inductor

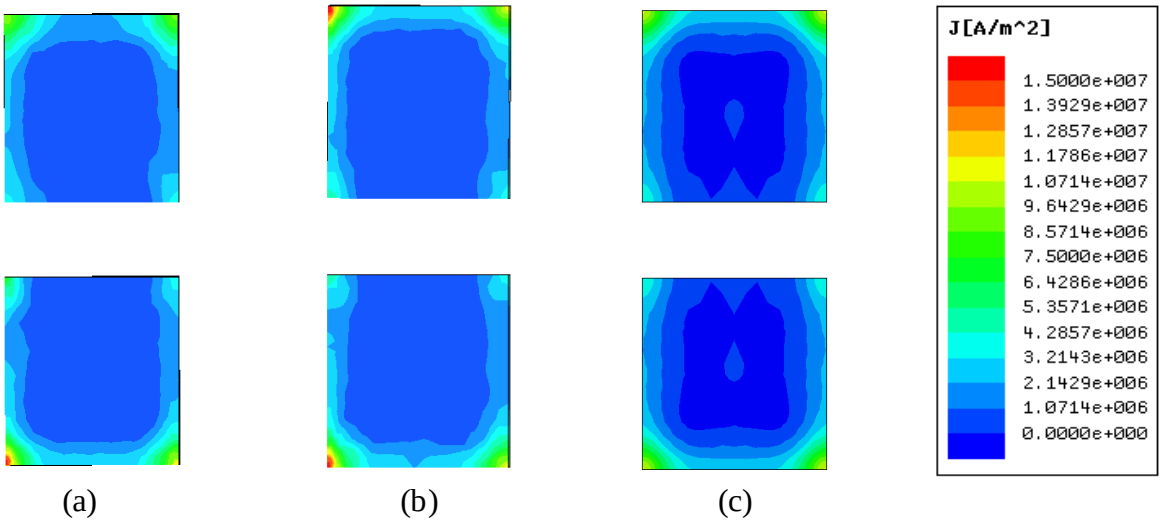

(a) (b) (c)

Figure 4.3 FEA simulation results for AC current distribution in inductor vias (a) 3D simulation result on top surface of via, (b) 3D simulation result on bottom surface of via, (c) 2D simulation result

Because the magnetic core next to the inductor via will impact the AC current distribution inside the via, the magnetic core needs to be defined accurately in the FEA model. Figure 4.4 shows the top view of H distribution on this planar inductor with LTCC core material. (The surface windings are removed). It can be seen that the flux of this LTCC inductor has very non-uniform distribution. The H values of three different core locations point 1, point 2, and point 3 are given in Figure 4.4, where point 1 represents the core area between two vias. Point 2 and point 3 can represent other core areas closed to the inductor via just except the area represented by point 1. So, basically, these three points can represent all the core area closed to inductor via. The *H* value and the incremental permeability of the core in these three points are shown in the B-H curve of ESL®'s LTCC ferrite 40011 in Figure 4.5. Because point 2 and point 3 both are very close to the inductor via, they have a very large *H* value. The core materials in these two locations are both almost saturated, and the incremental permeability is dropped to 6. Because there is very little flux in the area between the two vias, which is represented by point 1, the permeability of core material at point 1 is 200, which is the initial permeability of this LTCC

material. In conclusion, for this multi-turn planar inductor structure, the core material around the inductor via can be simply divided into two parts. The first part is the area between the two vias, which has very high permeability. The second part is the remaining area, which has lower permeability. Figure 4.6(a) shows this simplified 2D simulation model with two permeability values and its simulation results of AC current distribution in the via.

In order to further simply this problem, a 2D simulation model with single permeability is used to compare with this two-permeability model. With this single permeability model, the core material between the vias is also assigned the same permeability as the core around the via. This further simplified 2D simulation model with single permeability and its simulation results of AC current distribution in via are shown in Figure 4.6(b). From Figure 4.6, it can be seen that the simulation results for AC current distribution with these two models are almost the same. The simulation results of via ACR with these two models are also shown in Figure 4.7, which shows that these two models have almost the same ACR results from 1MHz to 6MHz. As a result, the further simplified single permeability model can be used to study the via ACR.

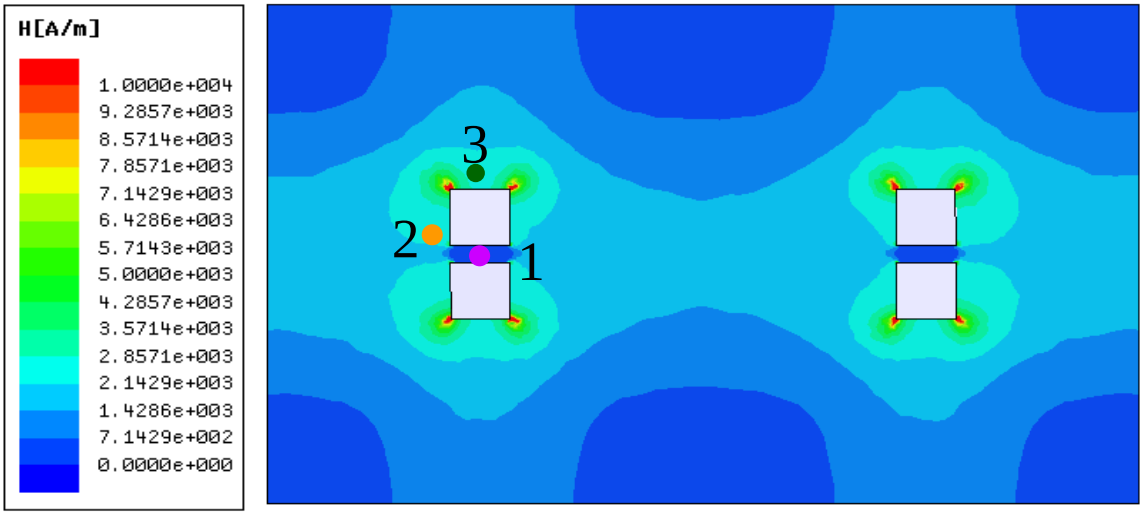

Figure 4.4 Top view of *H* distribution on LTCC inductor with two-turn structure

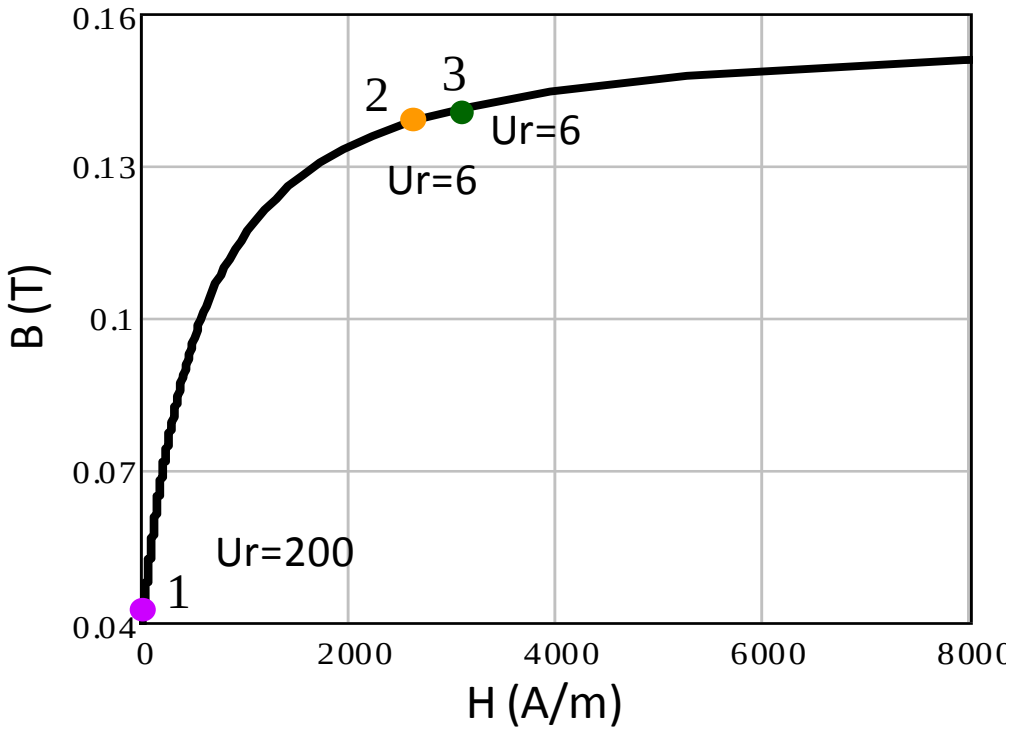

Figure 4.5 ***H*** **value and incremental permeability value of three points shown in Figure 3.4**

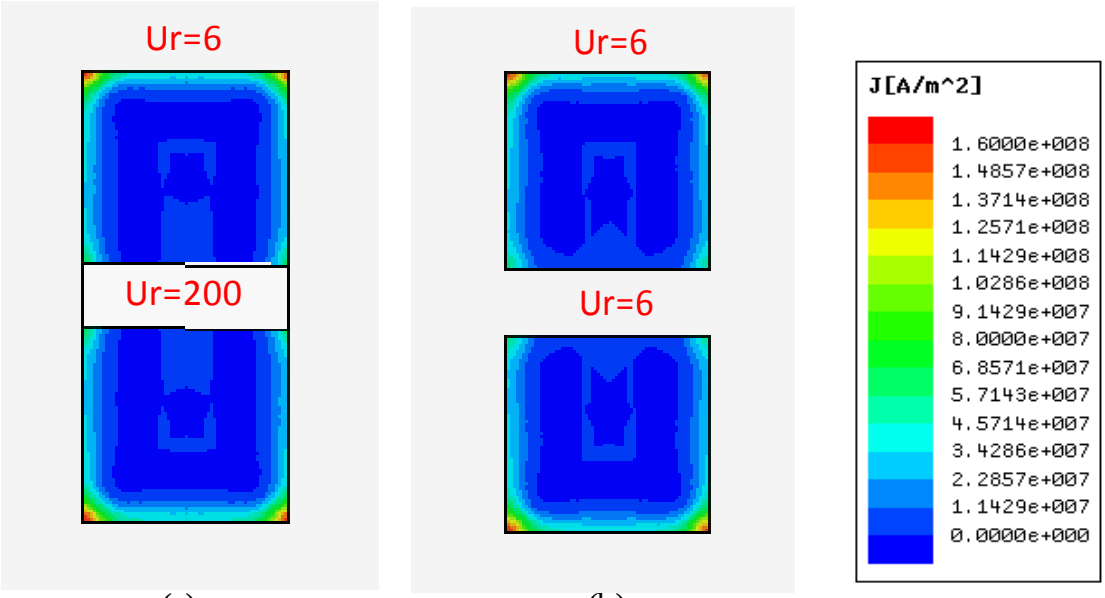

(a) (b)

Figure 4.6 FEA 2D simulation results of AC current distribution in via (a) with two-permeability model, (b) with single-permeability model

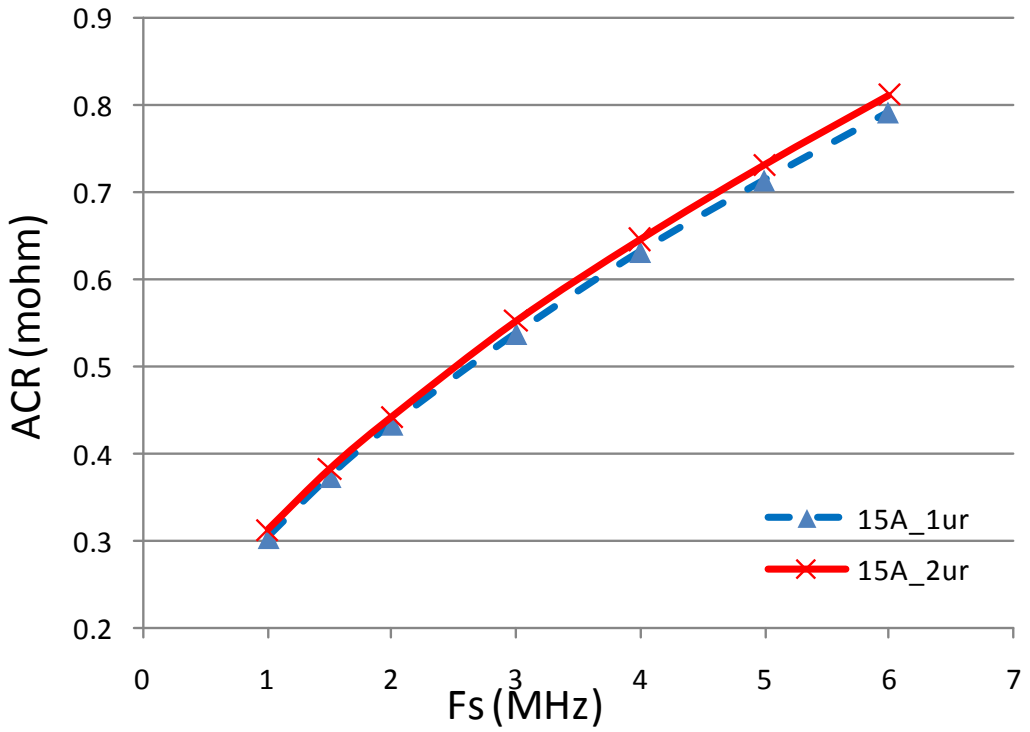

Figure 4.7 FEA 2D simulation results of via ACR

Because of the non-linear B-H curve of LTCC ferrite, the LTCC core will have a different permeability value when the inductor current is changed. Figure 4.8 shows the FEA 2D simulation results of H distribution in the LTCC core with different inductor currents. Figure 4.9 shows the simulation results of the via ACR with different inductor currents using the single-permeability model. From Figure 4.9, it can be seen that although different inductor currents will cause different H values and different incremental permeability, they will not have too much impact on via ACR. So, in this via ACR simulation, there is no need to run the simulation using different permeabilities. In other words, the ACR simulation results of one particular inductor current can be used to predict the via ACR loss for different inductor currents. Figure 4.10 shows the comparison results for via ACR with different via shapes. In this comparison, a two-turn structure is used as an example; the cross-section area and length for all vias are the same: cross-section area=1.5mm^2, length=2mm. Figure 4.10 illustrates that the round via can have a smaller

ACR than the square via. As a result, the round via will be used in the real inductor design. All the model analyses for the square via are also valid for the round via.

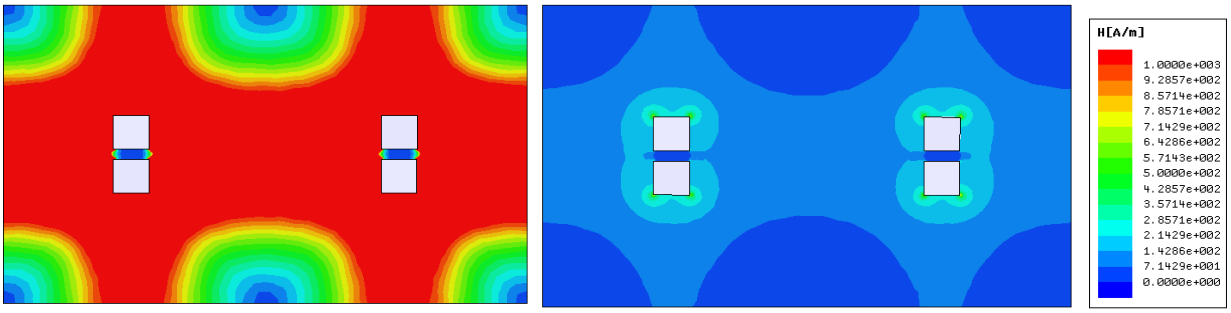

(a) (b)

Figure 4.8 FEA 2D simulation results of *H* distribution in the LTCC core: (a) with 15A inductor current, (b) with 1A inductor current

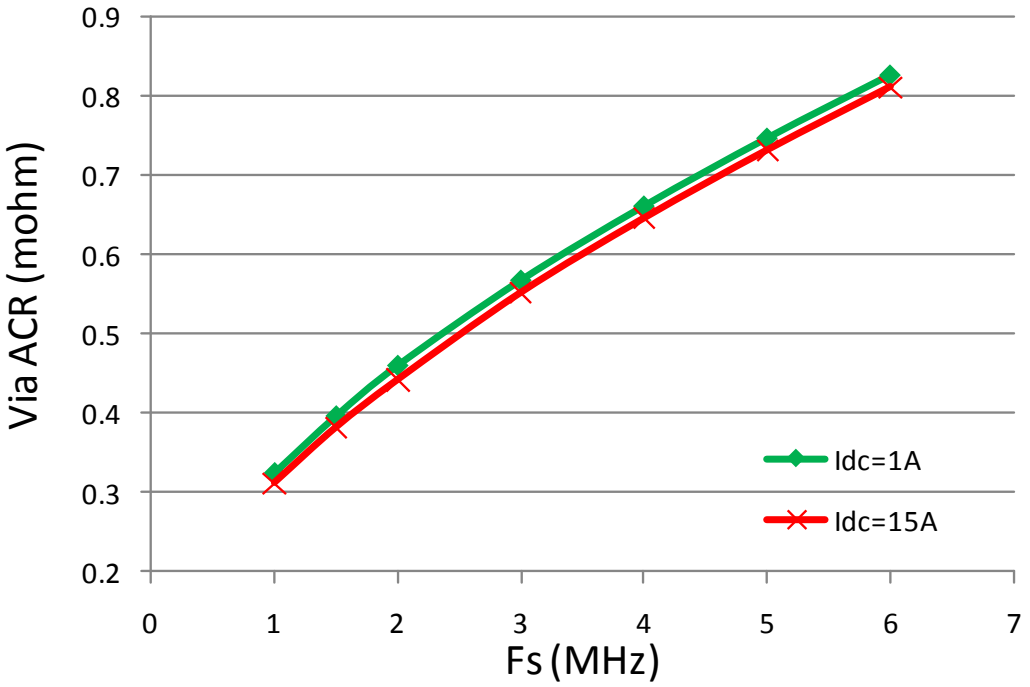

Figure 4.9 FEA 2D simulation results of via ACR with different inductor current by using single permeability model

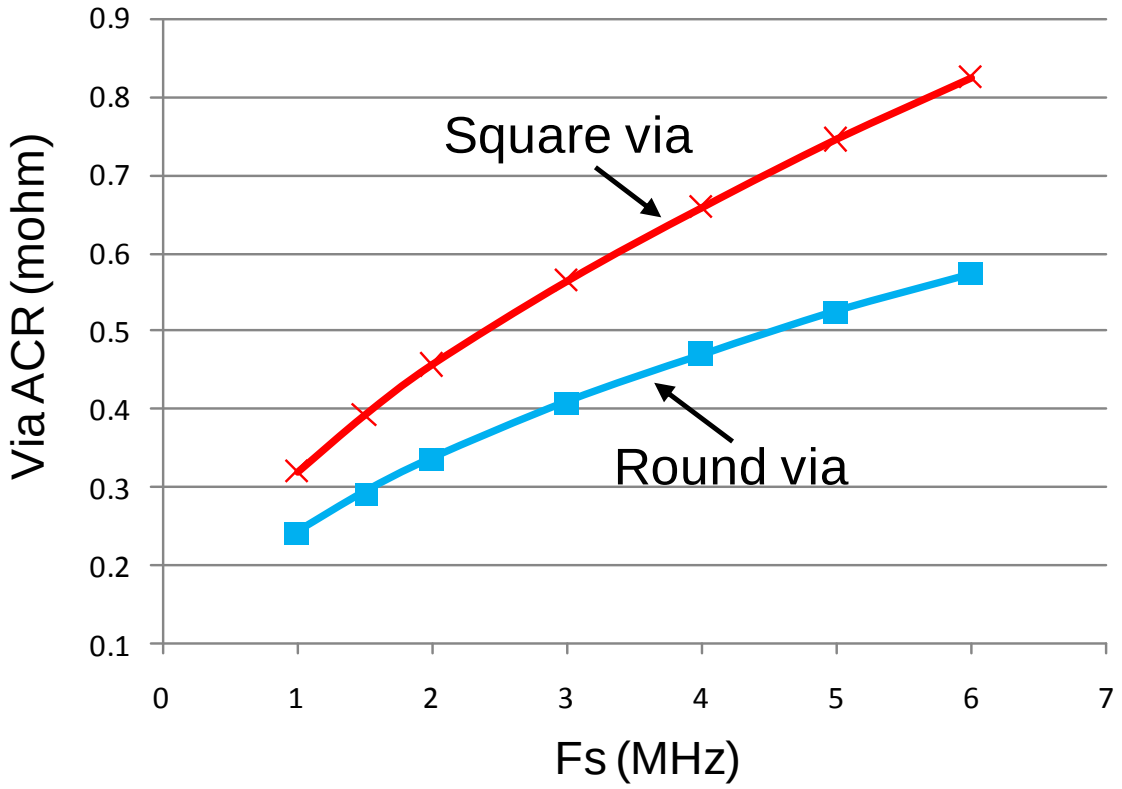

Figure 4.10 FEA 2D simulation results of via ACR for *N*=2 inductor with via cross-section area=1.5mm2, via length=2mm

Figure 4.11 shows the FEA 2D simulation results of the round via ACR with different inductor structures and frequencies. In these simulations, the cross-section area of the via is 1mm^2. The vertical axis of Figure 4.11 is the ratio between the average via ACR and via DCR. Because the ACR is calculated from total ohm loss, as discussed in the previous section, this ACR value is an equivalent parameter to represent the ACR loss. Here, it is defined as the average via ACR. From Figure 4.11, it can be seen that increasing turn number *N* will increase the ratio between average ACR and DCR. This is because the proximity effect will become more sever when increasing turn number *N*.

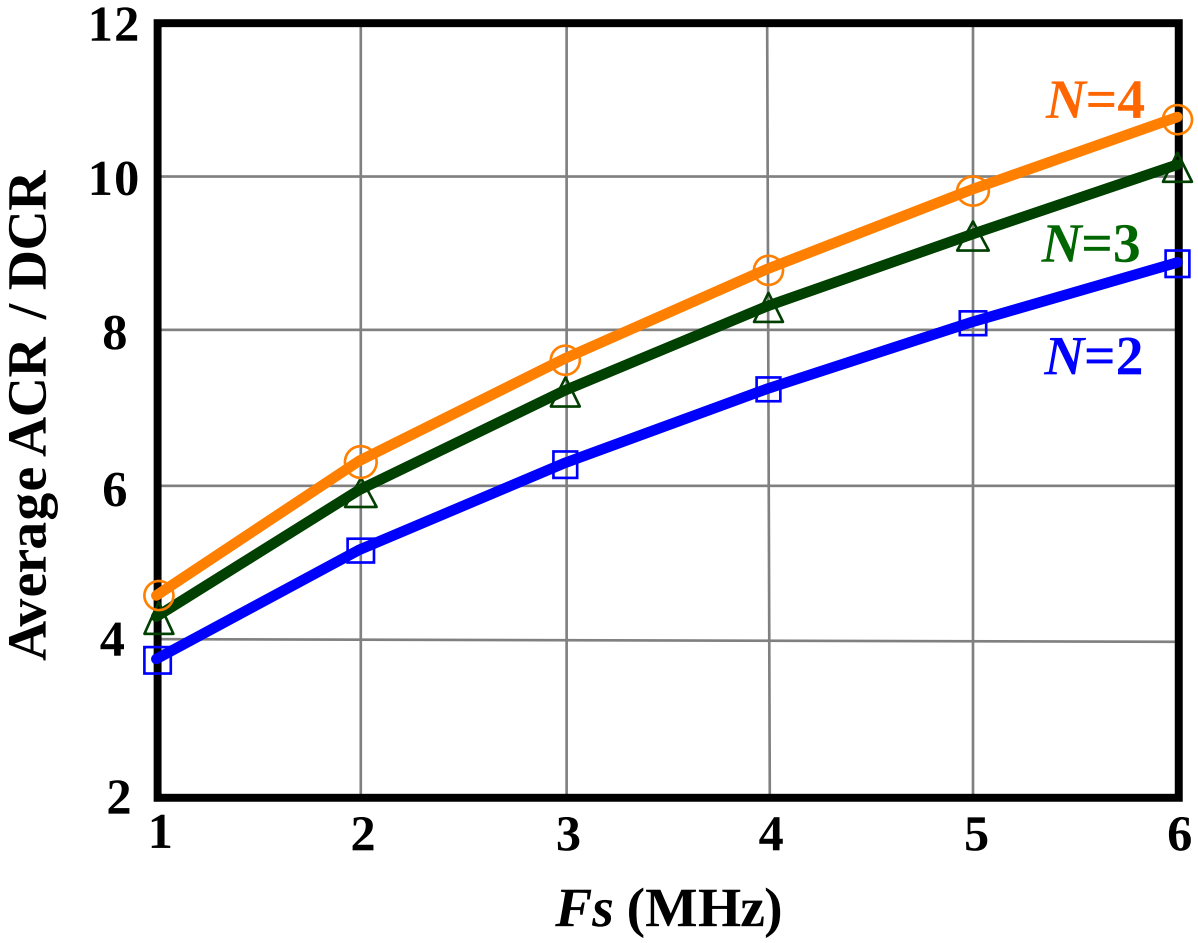

Figure 4.11 FEA 2D simulation results of via ACR/DCR ratio with different inductors

Figure 4.12(a) shows the 3D simulation results for AC current distribution inside the surface winding of an N=2 planar inductor. In Figure 4.12(a), three different positions are chosen to show AC current distribution. Position A is in the middle of surface winding. Positions B and C are both at the corner of the surface winding. Figure 4.12(b) shows the 2D simulation results of the AC current distribution in the surface winding. It can be seen that the 3D result of AC current distribution at position A is almost the same as the 2D simulation result. Position B and C are in the corner area of the surface winding, so the AC current distribution at position B and C are not exactly the same as at position A due to the direction change of the current flow at these

areas. However, the difference between the 3D results of AC current distribution at these corner areas (at position B and C) and the 3D results at position A are very small in this case. As a result, the corner effect is ignored in this study, and the 2D simulation model is used to study the AC current distribution in the whole surface winding. Unlike the inductor via, which is symmetrically surrounded by the core, the surface winding has only one side in contact with the core material. Hence the AC current distribution in the surface winding will be impacted by the permeability of the core material.

Figure 4.13 shows the 2D simulation results of AC current distribution in the surface winding with different inductor currents, which will cause different levels of permeability of the inductor core. The 2D simulation results of the surface winding ACR are shown in Figure 4.14, which shows that surface winding ACR will be changed when inductor current is changed. A smaller inductor current will cause larger winding ACR due to the larger permeability of the inductor core. As a result, when study surface winding ACR, the relationship between the core permeability and inductor current should be considered in FEA 2D model.

The FEA simulation results of the ratio between surface winding ACR and DCR for N=2 LTCC inductor with 15A DC current are shown in Figure 4.15. Here, three surface windings with different aspect ratio are compared. In these three cases the winding cross-section area all equals to 1.5mm^2 and core permeability equals to 20. In Figure 3.15 it can be seen that surface winding with higher aspect ratio has smaller winding ACR.

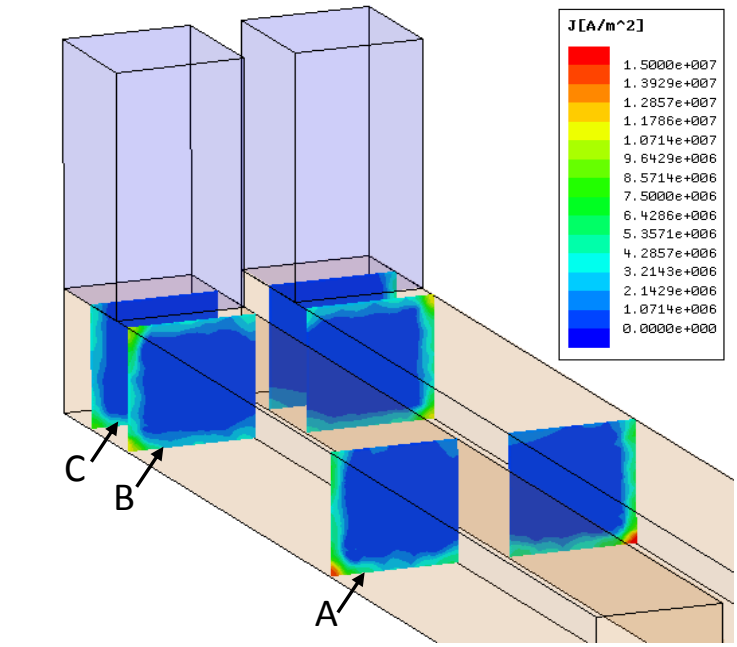

(a)

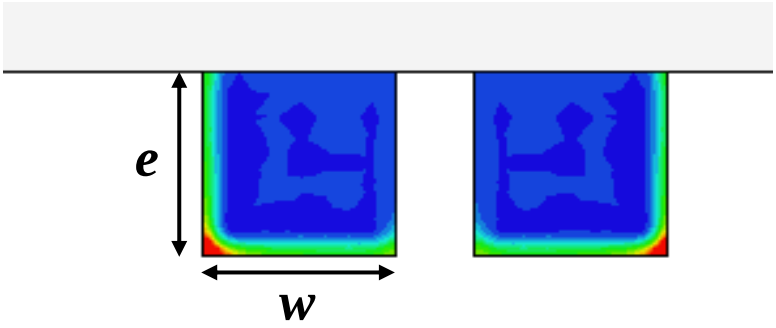

(b)

Figure 4.12 FEA simulation results for AC current distribution inside surface winding of a two-turn inductor: (a) 3D simulation result, (b) 2D simulation result

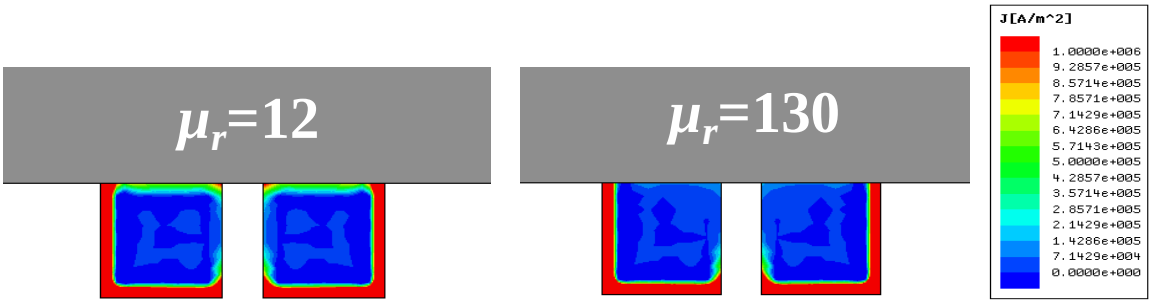

(a) (b)

Figure 4.13 FEA 2D simulation results of AC current distribution in surface winding: (a) with 15A inductor current, (b) with 1A inductor current

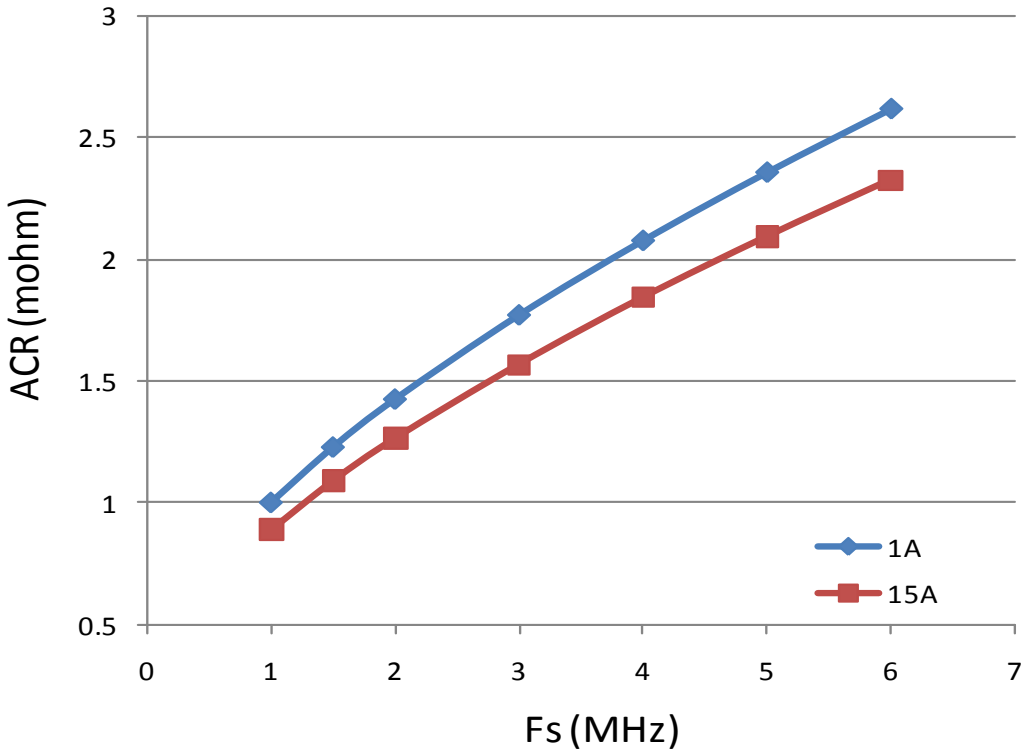

Figure 4.14 FEA 2D simulation results of surface winding ACR with different inductor currents

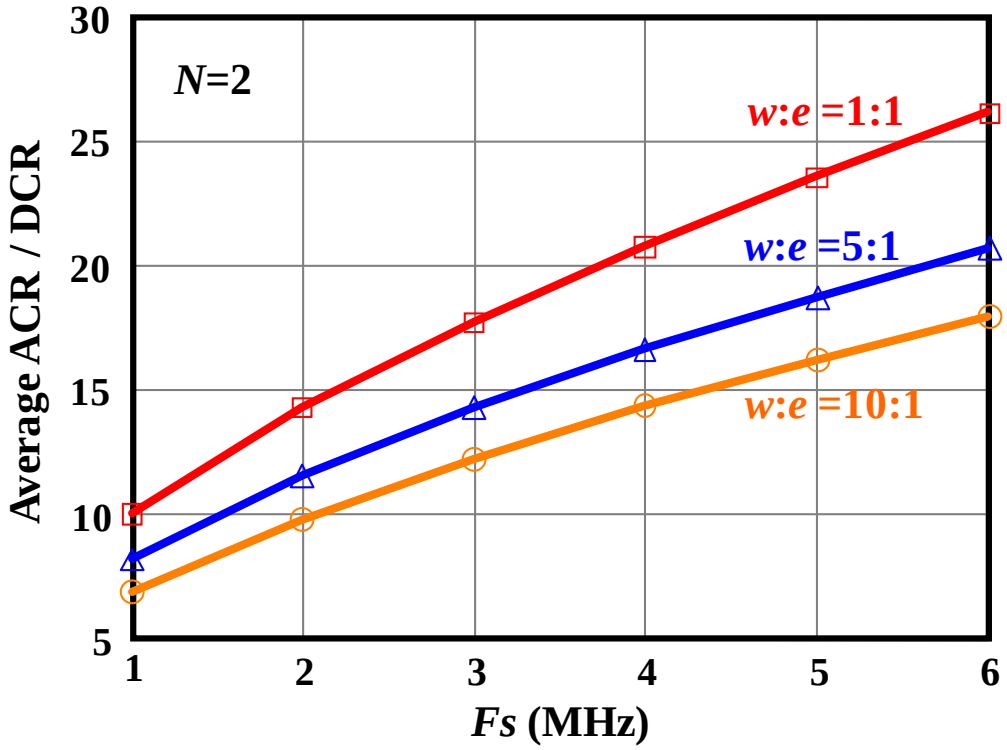

Figure 4.15 FEA 2D simulation results of surface winding ACR/DCR ratio

4.3 Analytical Winding ACR Model for Planar Inductor

Because FEA simulation is not a closed-from solution, it is still a trial-and-error design process. Although the FEA 2D simulation can give quite accurate results with an acceptable simulation time for a given inductor structure, it still will be very time consuming when used to optimize different inductor designs. In order to simplify the design optimization process, several closed-from formulas of ACR for these planar inductors are also proposed.

First, the simplest case via ACR with a one-turn structure is studied. For this case, the AC current distribution is only impacted by the skin effect. Thus if the via radius r_v is much larger than skin depth δ, the AC current can be simply assumed to be uniformly distributed in the outer layer of depth δ. The skin depth δ is defined as

$$\delta = \frac{1}{\sqrt{\pi \cdot f_S \cdot \mu \cdot \sigma}} \tag{4.1}$$

where μ is the permeability of the via; σ is the conductivity of the via; and f_s is the frequency. The ACR and DCR for the round via can then be calculated by

$$ACR = \frac{h}{\sigma \cdot 2\pi \cdot r_v \cdot \delta} \tag{4.2}$$

$$DCR = \frac{h}{\sigma \cdot \pi \cdot r_v^2} \tag{4.3}$$

where h is the via length.

The ratio between the via ACR and DCR for the N=1 case is

$$R_{N=1} = \frac{\sqrt{\mu\sigma}}{2} (\pi r_v^{\,2})^{0.5} f_S^{0.5} \tag{4.4}$$

For an LTCC planar inductor, silver paste is used to build the via. The permeability and conductivity of this silver paste are: $\mu_{Ag} = 4\pi \cdot 10^{-7}$, $\sigma_{Ag} = 2.5 \cdot 10^{7} S/m$.

The calculation results of this closed-from approximation for *N*=1 case are shown as the dashed line in Figure 4.16, which shows that this closed-form approximation can match the FEA simulation very well for the *N*=1 case. Actually, after a little bit of modification, this closed-from approximation also can be used for the multi-turn case. The only thing that needs to be modified is the index of the switching frequency. The general equation for the ratio between the via average ACR and DCR of these LTCC planar inductor structures is

$$R_{N=n} = \frac{\sqrt{\mu\sigma}}{2}(\pi r_v^{\,2})^{0.5} f^{x} \tag{4.5}$$

where x=0.5 when *N*=1; x=0.517 when *N*=2; x=0.526 when *N*=3; and x=0.530 when *N*=4.

The calculation results of the ratio between the via ACR and DCR for the multi-turn structure are also shown in Figure 4.16. It can be seen that this closed-form approximation can match the FEA simulation very well for all cases. The closed-form approximation for the ratio between the average ACR and DCR of the surface winding is extended from the previous closed-form approximation for the via.

$$R_{N=n} = 0.7\sqrt{\mu\sigma}A^{0.5} f^{y} \cdot f_1(w,e) \cdot f_2(\mu_{r\_core}, w, e) \tag{4.6}$$

where y=0.517 when *N*=2; y=0.534 when *N*=3; and y=0.542 when *N*=4. w is the width of the surface winding; e is the thickness of the surface winding; μ_{r_core} is the permeability of the inductor core; and $f_1(w,e)$ represents the impact of the surface winding shape on the ACR. It is curve-fitted as:

$$f_1(w,e) = (\frac{w}{e})^{-(6\cdot 10^{-3}\cdot\frac{w}{e}+0.175)} \tag{4.7}$$

$f_2(\mu_{r\_core}, w, e)$ represents the impact of the core permeability on the ACR. It is modeled as:

$$f_2(\mu_{r\_core}, w, e) = (18.5\cdot 10^{-3}\frac{w}{e} + 0.91)\cdot \mu_{r\_core}^{0.057} \tag{4.8}$$

For an LTCC planar inductor, a copper sheet is used to the build surface winding. The permeability and conductivity of copper are: $\mu_{Cu} = 4\pi\cdot 10^{-7}$, $\sigma_{Cu} = 5.8\cdot 10^{7}\, S/m$.

The calculation and FEA simulation results of the ratio between the surface winding ACR and DCR for *N*=2 LTCC inductor with 15A DC current are shown in Figure 4.17. It can be seen that the proposed closed-form equation can predict surface winding ACR very well.

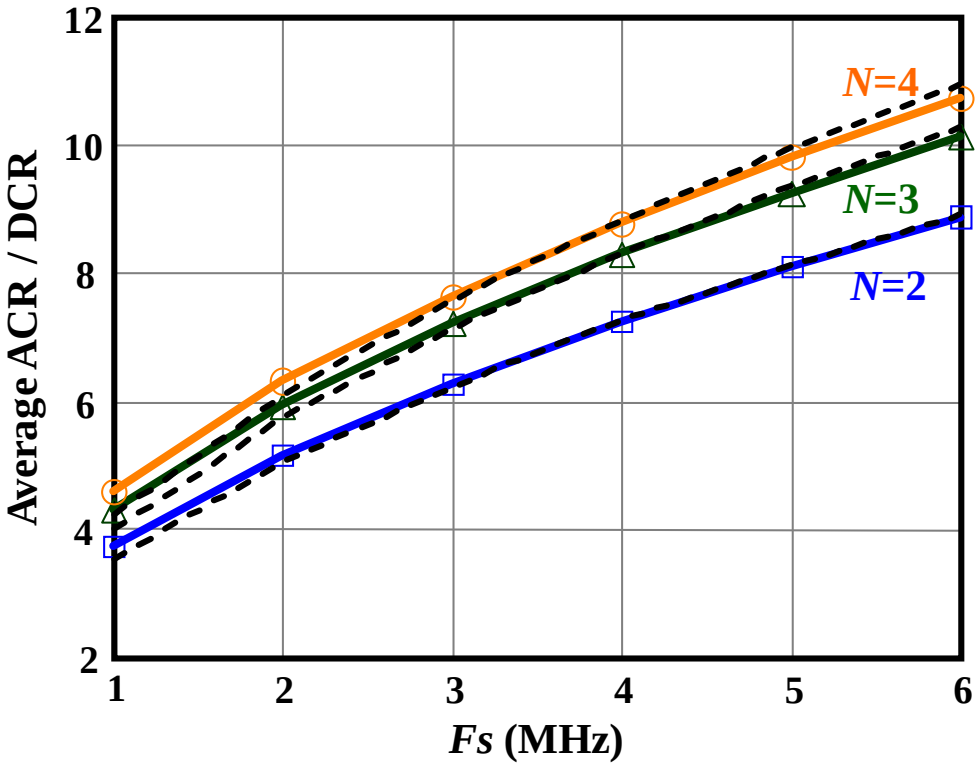

Figure 4.16 Via ACR/DCR ratio with different inductors. Solid color line: FEA 2D simulation results; Black dash line: calculation results

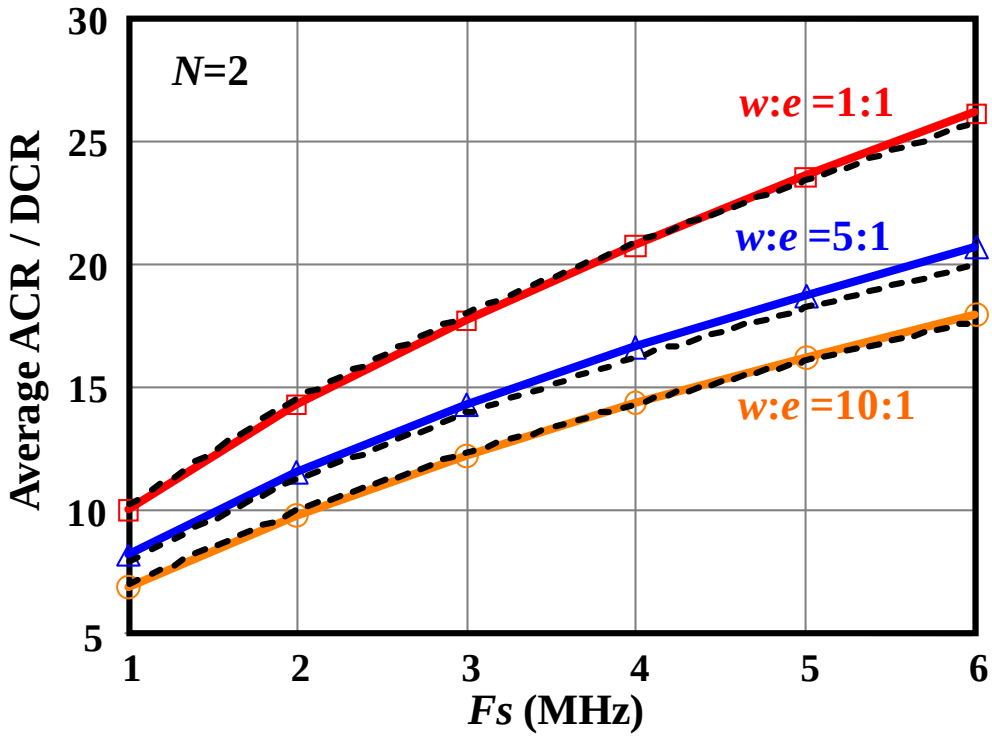

Figure 4.17 Surface winding ACR/DCR ratios. Solid colored lines: FEA 2D simulation results; Black dashed lines: calculation results

The AC resistance loss of different LTCC lateral flux inductors can be studied based on the proposed simulation model and closed-form equation. First, the Fourier analysis is used to analyze the inductor current to acquire different frequency components; then, the ACR loss contributed by different frequency components of the inductor current is calculated based on the Fourier analysis results and ACR calculation results; finally, the total ACR loss is calculated by summing the ACR loss contributed by each frequency component. The fundamental component and second harmonic contribute most of the ACR loss. Hence in the following calculation only these two components are included. Because the buck circuit is widely used for POL converters, a buck circuit with V_{in}=5V, V_o=1.2V, I_o=15A is used as an example to compare the performance of different LTCC lateral flux inductors. For the winding ACR calculation, two switching

frequencies (1.5MHz and 3 MHz) are chosen as examples. In this comparison, the via radius is r_v=0.6mm; the core thickness h=2mm; the surface winding dimension is w=1.5mm, e=0.4mm. For 1.5MHz frequency, the LTCC inductor is design as L=300nH; for 3MHz frequency, the inductance is reduced to L=150nH. The ratio between inductor winding DCR loss and converter output power is shown in Figure. 4.18. With a given frequency, inductor core thickness h and turn number N, the g value can be calculated to satisfy the inductance requirement. Because the winding DCR is only impacted by the g value, there is only one set of curves in Figure 4.18 for different frequencies. Each curve represents one structure. For a frequency of 1.5MHz, there are three dots on the curves to represent three designs with different turn number. For a frequency of 3MHz, there are another three dots on the curves to represent another three designs with different turns numbers. Because the inductors have a smaller size with 3MHz operation frequency, 3MHz inductor designs have a smaller g value.

In Figure 4.18, it can be seen that 1) increasing turn number N will increase the winding DCR loss; 2) increasing the frequency will reduce the winding DCR loss due to a smaller inductor size. The ratio between inductor winding ACR loss and converter output power is shown in Figure 4.19. Because winding ACR is impacted by frequency, there are two sets of curves in Figure 4.19. The solid line is the winding ACR loss curve for 1.5MHz; the dashed line is the winding ACR curve for 3MHz. It can be seen that 1) increasing the turns number N will also increase the winding ACR loss; 2) Increasing the frequency will increase the ACR loss with a given g value; and 3) Because increasing the frequency will also reduce the g value (inductor size), the total ACR loss is almost constant with different frequencies. Considering Figure 4.18 and Figure 4.19 together, it can be concluded that increasing the frequency can reduce both inductor size and winding loss.

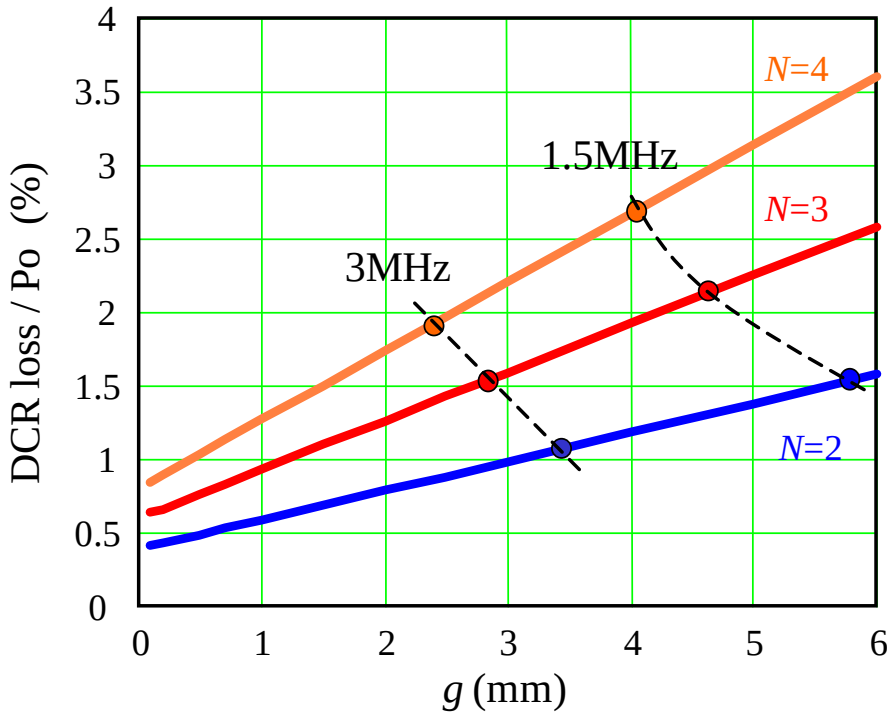

Figure 4.18 Ratio between inductor winding DCR loss and buck converter output power

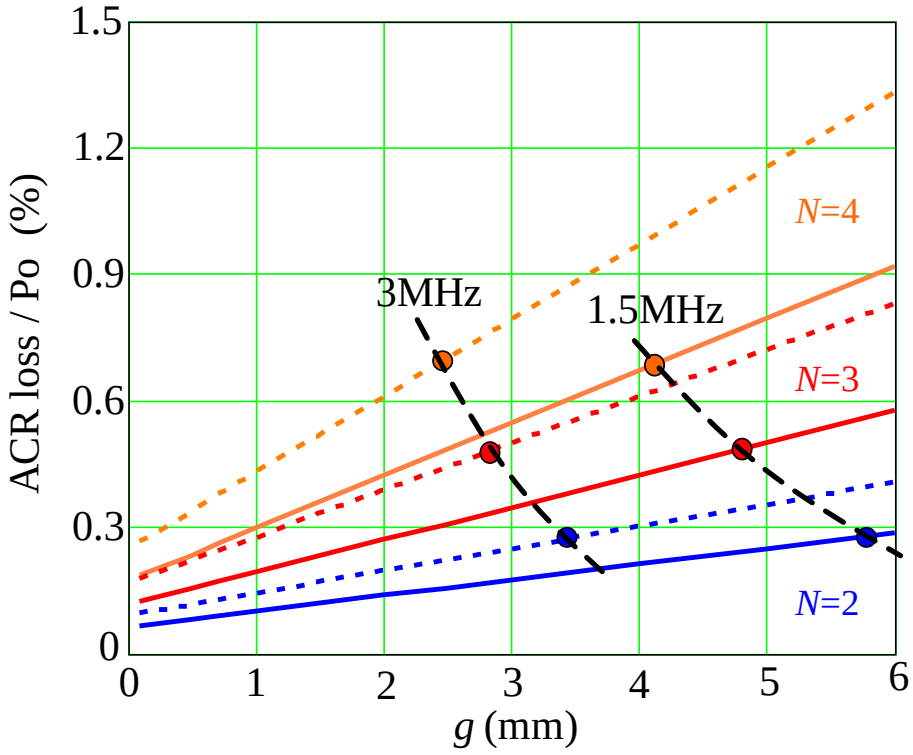

Figure 4.19 Ratio between inductor winding ACR loss and Buck converter output power

4.4 Analytical Core Loss Model for Planar Inductor with Non-uniform Flux Distribution

The concentric ring method also can be used to calculate core loss for LTCC lateral flux inductor with non-uniform flux distribution. Figure 4.20 shows the concept drawing of this concentric ring method for the half-core of a lateral flux inductor. For a single-turn structure, the concentric rings are round; for a multi-turn structure, the concentric rings are elliptical. Because magnetic flux can be assumed to be uniform in each thin ring, the conventional core loss model can be used to calculate core loss of each ring. Then the total core loss is the sum of core loss of each ring.

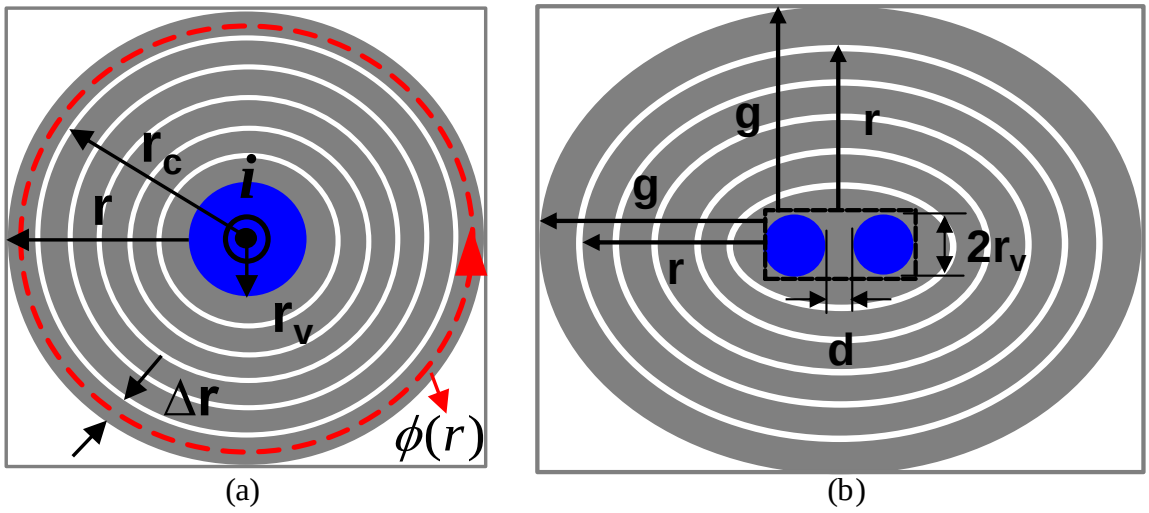

(a) (b)

Figure 4.20 Concept drawing for dividing half core of lateral flux inductors into many concentric rings: (a) single-turn structure, (b) two-turn structure

In the past, many core loss calculation methods have been developed for magnetic components with uniform flux distribution. They can be divided into physically-based models and empirical-based models. Based on physical phenomena, many physically-based core loss models have been studied [73]-[78]. However, most physically-based models require additional

data of the core material well beyond what is typically available in manufacturers' data sheets. One well-known empirical equation to calculate core losses is the Steinmetz equation [79]:

$$P_v = k \cdot f^{\alpha} \cdot \widehat{B}^{\beta} \tag{4.9}$$

where P_v is the core loss per volume; f is the magnetization frequency; $\hat{B}$ is the peak flux density; and k, α and β are coefficients that are determined by experimental measurement.

The major limitation of the Steinmetz equation is that it is only valid for sinusoidal excitation. So, it is not very accurate to use it for inductor core loss prediction in power electronic applications, which normally have non-sinusoidal excitation with DC flux bias. Recently, several core loss models were developed to address arbitrary waveforms based on the Steinmetz equation: 1) the "modified Steinmetz equation" (MSE) [80][81]; 2) the "generalized Steinmetz equation" (GSE) [82], and 3) another model similar to the MSE and GSE that was developed in [83]. All of these models are proven to be accurate within a certain region for core loss calculation with non-sinusoidal excitation. Because MSE also can be used to calculate core loss when the excitation has a DC flux bias, it can be used to calculate inductor core loss for power electronic applications.

Here, MSE is used to calculate the core loss for each concentric ring of an LTCC planar inductor. Without the DC flux bias, the general formula for MSE is

$$P_v = k \cdot f_{eq}^{\alpha-1} \cdot \widehat{B}^{\beta} \cdot f \tag{4.10}$$

where k, α and β are the same coefficients used in the Steinmetz equation; and f_{eq} is an equivalent frequency, defined as

$$f_{eq} = \frac{1}{2\widehat{B}^2\pi^2}\int_0^T \left(\frac{dB}{dt}\right)^2 dt \tag{4.11}$$

In order to determine the coefficients k, α and β (Steinmetz coefficients) for LTCC ferrite, the core loss density of LTCC ferrite with sinusoid excitation is measured. The measurement technology was introduced in [84]. Figure 4.21 shows the core loss measurement results of ESL®'s LTCC ferrite. In these measurements, three different LTCC ferrite tapes are used. LTCC ferrite 4010, whose initial permeability is μ_i=50; LTCC ferrite 4011, whose initial permeability is μ_i=200; and LTCC ferrite 4012, whose initial permeability is μ_i=500. In Figure 4.21, it can be seen that the LTCC ferrite 4010 has the similar core loss density as NiZn ferrite 4F1. LTCC ferrite tapes 4011 and 4012 both have higher core loss density than LTCC ferrite 4010. These two materials can be used for 1.5MHz and 3MHz, but they are not good for 5MHz. The Steinmetz coefficients of these materials are listed in Table 4.1. With these coefficients, the unit for frequency is Hz; the unit for B is T; and the unit for P_v is kW/m^3.

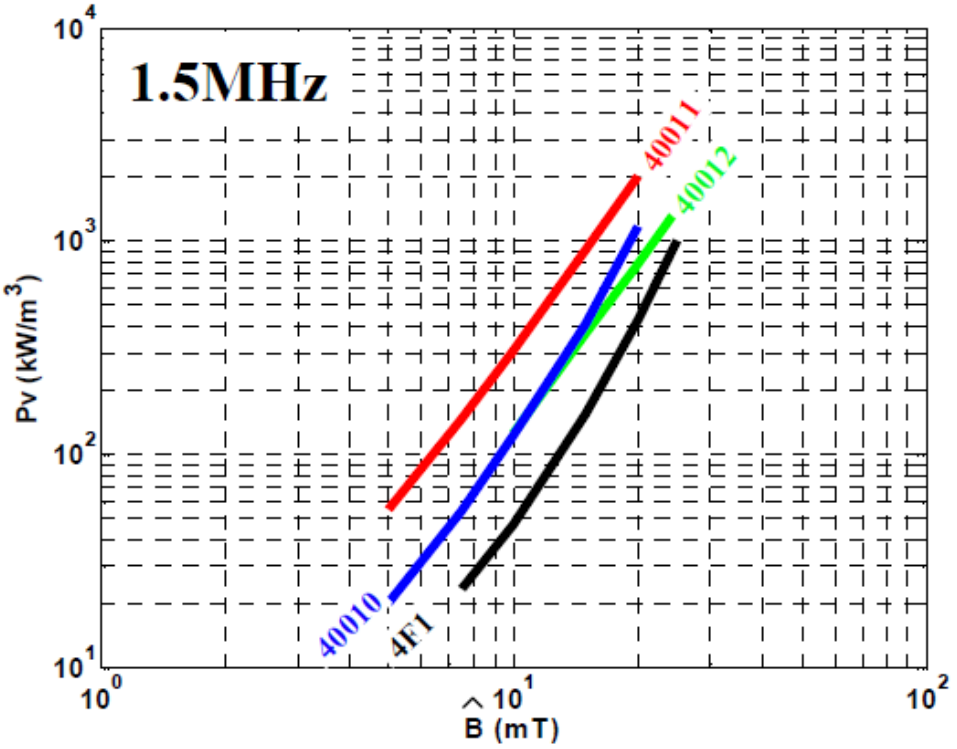

(a)

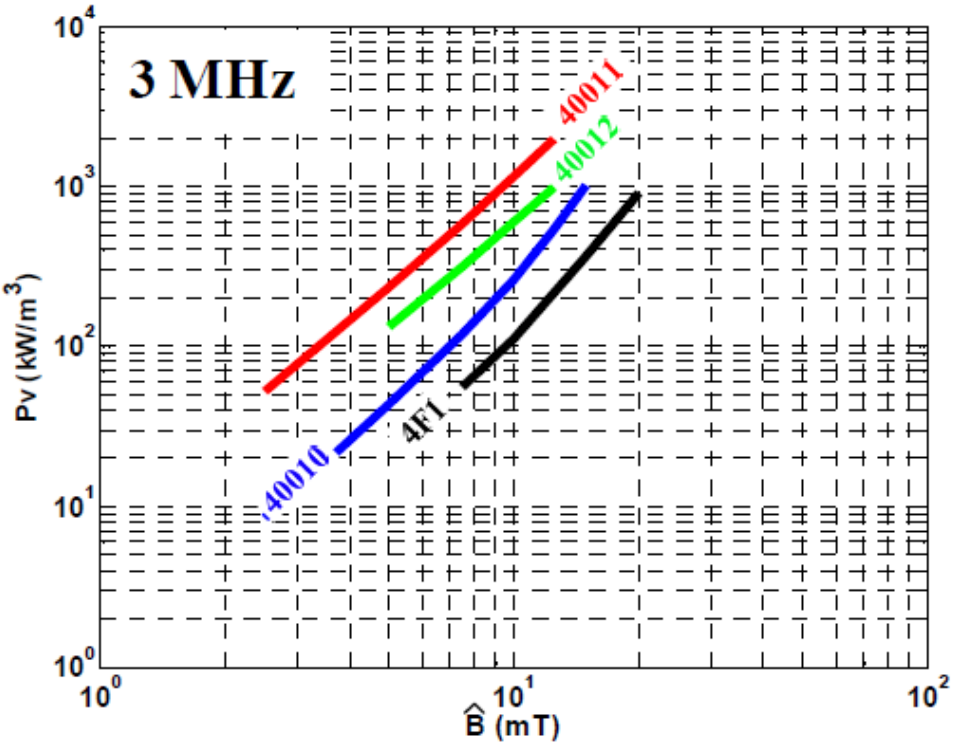

(b)

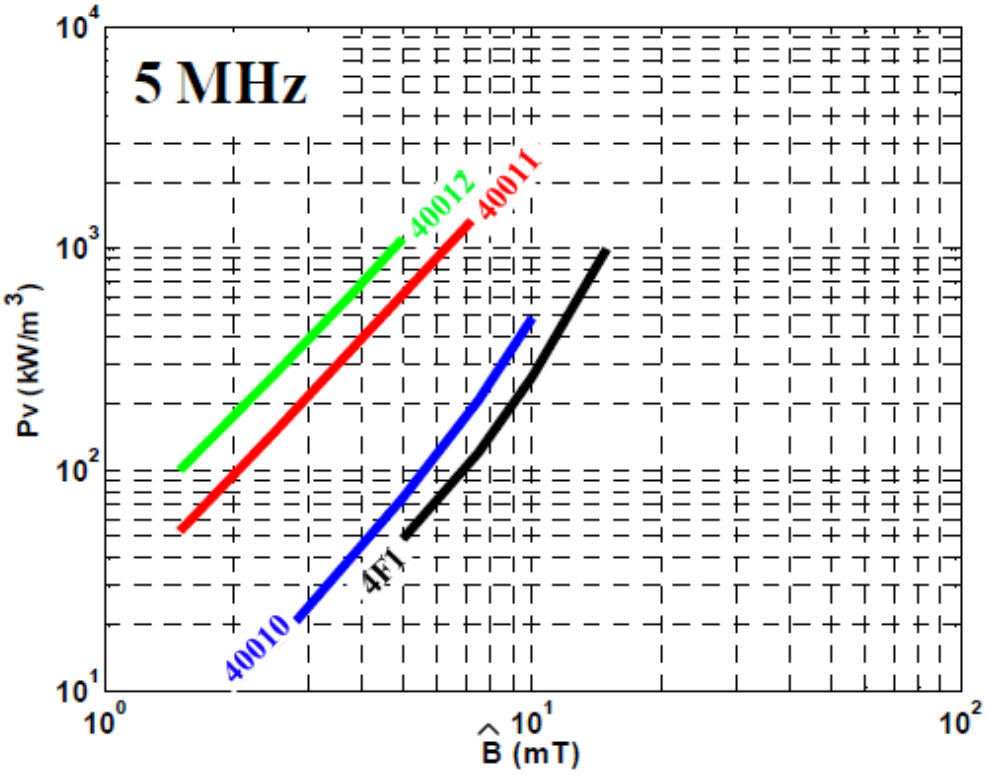

(c)

Figure 4.21 Core loss measurement results of ESL®'s LTCC ferrite: (a) 1.5 MHz, (b) 3 MHz, (c) 5 MHz

Table. 4.1 Steinmetz coefficients of LTCC ferrite

	k	α	β
LTCC ferrite 4010	3.99	1.113	2.673
LTCC ferrite 4011	1.91E-5	1.905	2.271
LTCC ferrite 4012	7.38E-11	2.662	2.082

The equivalent frequency f_{eq} is related with the waveform of excitation. The excitation for the output inductor of a buck converter is rectangular AC voltage with DC current, so the flux inside the inductor core has both AC and DC components, and the AC flux is in triangular form. Figure 4.22 shows the concept drawing for this non-sinusoidal flux. In Figure 4.22, D is the duty cycle of the buck converter. If MSE is used to calculate the core loss for the Buck inductor, the equivalent frequency f_{eq} can be simplified as

$$f_{eq} = \frac{1}{2\hat{B}^2\pi^2}\int_0^T \left(\frac{dB}{dt}\right)^2 dt = \frac{2\cdot f_s}{\pi^2 D(1-D)} \tag{4.12}$$

where f_s is the switching frequency of the buck converter and D is the duty cycle.

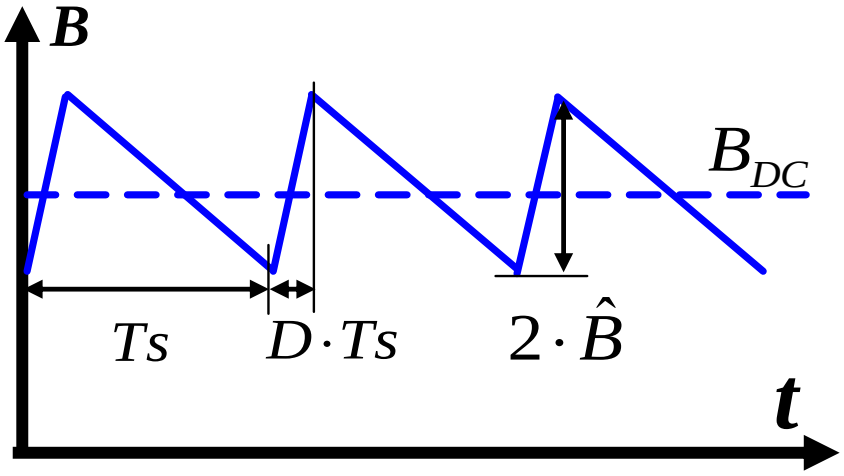

Figure 4.22 Concept drawing of non-sinusoid flux for buck converter inductor

The MSE also can be used to calculate core loss for the condition where the excitation has a DC flux bias. Here, the coefficients k is modified as $K(H_{DC})$ to include the impact of DC flux.

Figure 4.23 shows the measurement results of core loss density for LTCC ferrite with different values of AC flux and DC flux. In this measurement, the AC flux has a sinusoidal waveform. From Figure 4.23, it can be seen that the impact of DC flux on core loss density is independent of AC flux density. Therefore, for this LTCC ferrite, the coefficient k can be modified as a function with DC flux as the only variable. This function is defined as:

$$K(H_{DC}) = k \cdot (a \cdot H_{DC}^5 + b \cdot H_{DC}^4 + c \cdot H_{DC}^3 + d \cdot H_{DC}^2 + e \cdot H_{DC} + 1) \qquad (4.13)$$

where k is the coefficient used in the Steinmetz equation; a = -1.8729e-15, b = 9.5035e-12, c = -1.6711e-8, d = 1.2859e-5, and e = -0.0037.

From (4.13), it can be known that the coefficient K is controlled by H_{DC}. So, the H_{DC} for each ring needs to be calculated first. According to Ampere law, the H_{DC} for each ring can be calculated based on (2.18).

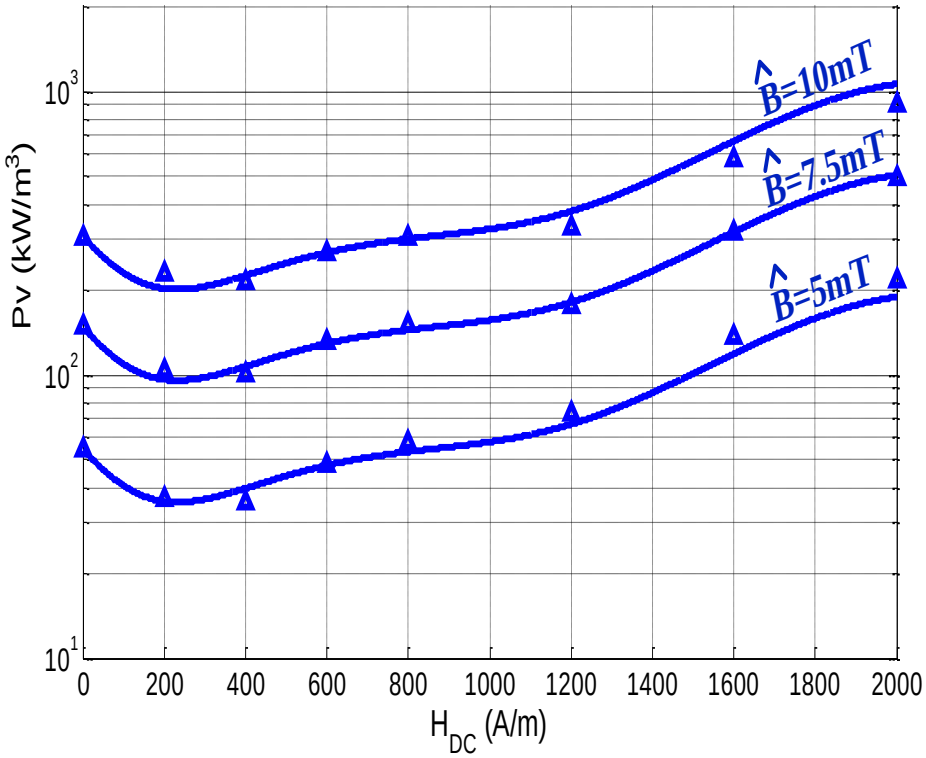

Figure 4.23 Measurement results of core loss density for LTCC ferrite with different AC flux and DC flux

Figure 4.24 shows the calculation results for H_{DC} distribution of a single-turn lateral flux inductor with different DC currents. The x axis parameter r represents the location of the concentric ring, which is defined in Figure 4.20(a). It can be seen that 1) the inner part of the core has a higher H_{DC} than the outer part of the core, and 2) increasing the DC current will increase H_{DC}.

Figure 4.25 shows the calculation results for incremental permeability distribution of single-turn lateral flux inductor with different DC currents based on (2.14) and (2.18). It can be seen that 1) the inner part of the core has smaller incremental permeability than the outer part of the core, and 2) increasing the DC current will reduce the incremental permeability. This is because a higher H_{DC} will cause a lower incremental permeability.

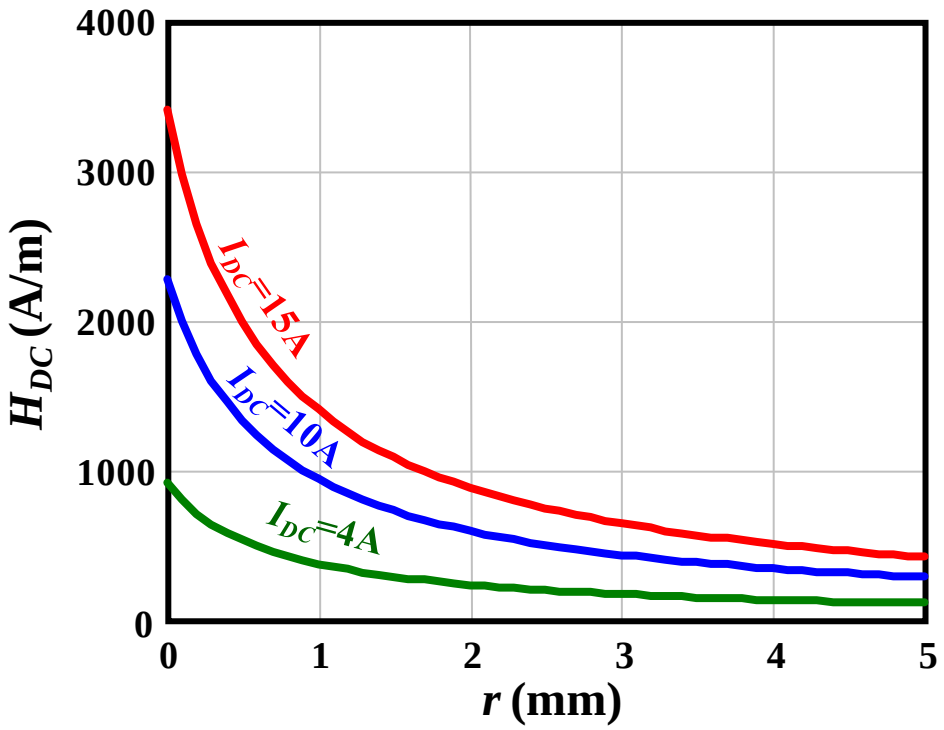

Figure 4.24 H_{DC} distribution of single-turn lateral flux inductor with different DC current

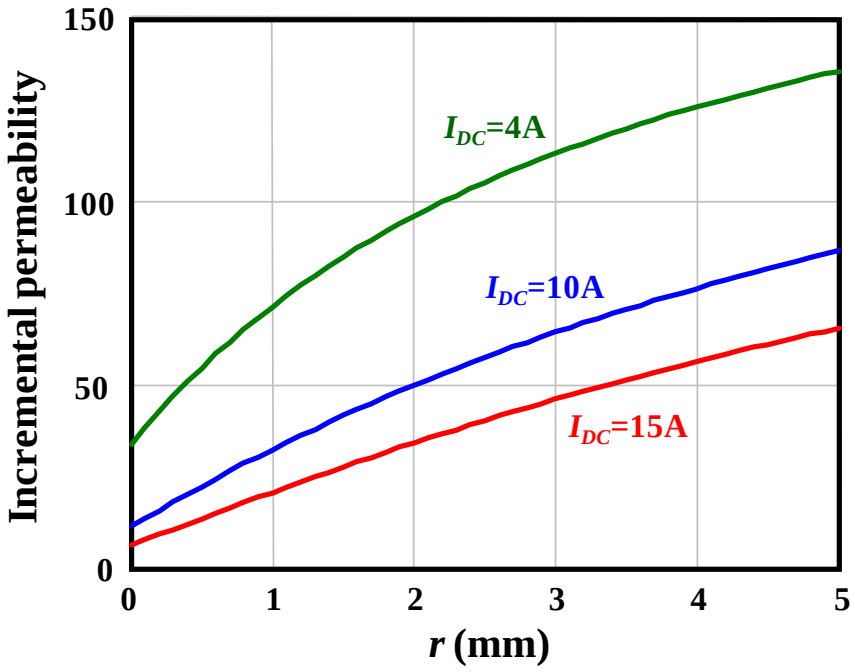

Figure 4.25 Permeability distribution of single-turn lateral flux inductor with different DC current

After calculating the incremental permeability for each ring, the AC flux density for each ring should be calculated as

$$\widehat{B}_{N=n}(r)=\frac{1}{2}\frac{n\cdot i_{AC\_pp}\cdot\mu_{r\Delta}(H_{DC})}{\sqrt{2}\cdot\pi\cdot\sqrt{\left(n\cdot r_v+\frac{(n-1)d}{2}+r\right)^2+\left(r_v+r\right)^2}} \tag{4.14}$$

where $\mu_{r\Delta}(H_{DC})$ is defined by (4); i_{AC_pp} is the peak to peak value of inductor AC current; N is turn number; r_v, r and d are defined in Figure 4.20.

Figure 4.26 shows the calculation results for the amplitude of the AC flux density inside concentric rings based on (4.14). In these cases, the peak-to-peak value of the AC current is always equal to 50% of the DC current. It can be seen that 1) for 15A DC current case, the distribution of AC flux density of each ring is nonlinear; with increasing r, it increases first, then after some point (r=2mm), it begins to drop continually. This is because the inner part of the core has a very high H_{DC} value, which causes the permeability reducing to be very small value. As a

result, the inner core has a very high reluctance and the AC flux is pushed to travel though the outer part of the core. 2) After reducing the DC current to 10A, the permeability of the inner part of the core becomes larger. So, the location for peak B_{AC} is moved from the outside core to the inner core (from r=2mm to r=1mm). 3) After further reducing the DC current to 5A, the reluctance of the inner part of the core will be further reduced, and the AC flux is no longer pushed to outer part of the core. In this case, the peak B_{AC} is located at r=0mm position and increasing r will continually reduce B_{AC}. Figure 4.27 shows the FEA simulation results of AC flux distribution in the unit cell of lateral flux LTCC inductor with different DC current. In this figure, the red color represents the highest flux density; the blue color represents the lowest flux density. It can be seen that the FEA simulation results resemble the calculation results: with a large DC current, the location of maximal AC flux density is at the outer core; with small DC current, the location of maximal AC flux density moves to the inner core.

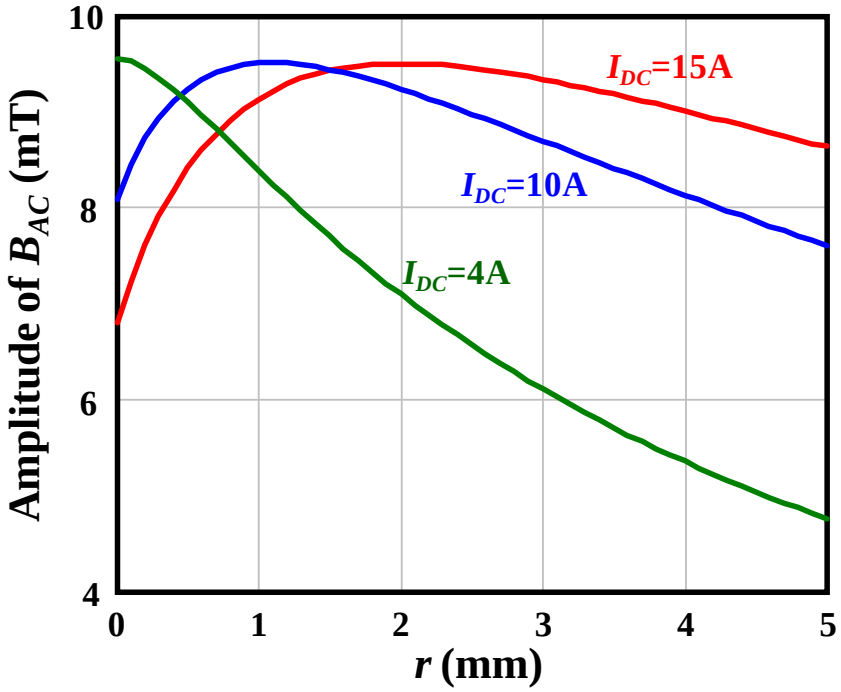

Figure 4.26 AC flux density of concentric rings for single-turn lateral flux inductor

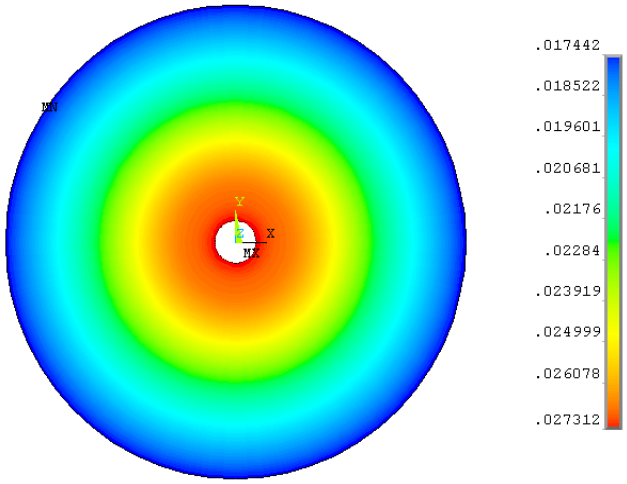

(a)

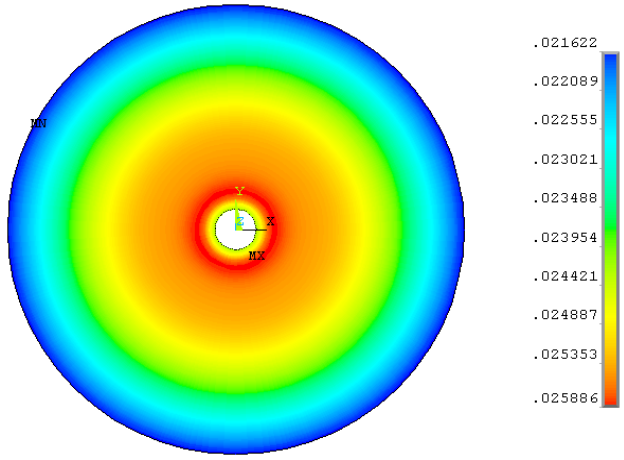

(b)

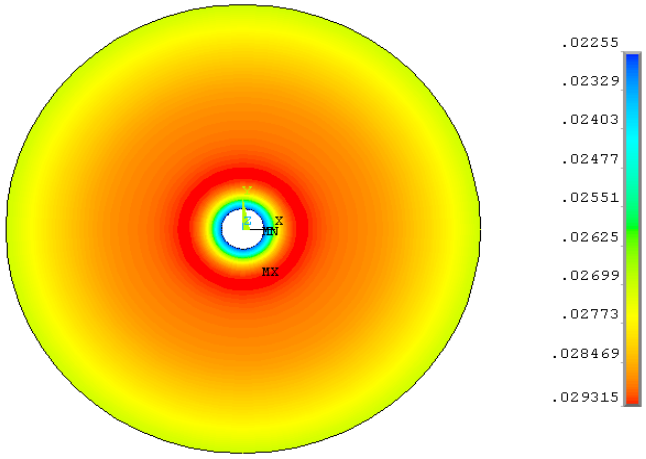

(c)

Figure 4.27 FEA simulation results of AC flux distribution in the unit cell of lateral flux LTCC inductor: (a) I_{DC}=4A, I_{AC}=3A, (b) I_{DC}=7A, I_{AC}=5A, (c) I_{DC}=10A, I_{AC}=8A

After calculating H_{DC} and the AC flux density of each ring, the core loss density of each ring for a LTCC planar inductor with non-uniform flux distribution used in a buck converter can be calculated as:

$$P_v = K(H_{DC}) \cdot \left(\frac{2}{\pi^2 D(1-D)} \right)^{\alpha-1} \cdot \hat{B}^{\beta} \cdot f_s^{\alpha} \tag{4.15}$$

Figure 4.28 shows the core loss density of concentric rings. In these cases, the peak-to-peak value of the AC current is always equal to 50% of the DC current. It can be seen that the core loss density distribution is similar to the AC flux density distribution. 1) With a large DC current (e.g. I_{DC}=15A), from inner core to outer core, the core loss density is increased first, then it will be reduced. 2) Reducing the DC current, the location of the peak core loss density will move to the inner part of the core. 3) With a small DC current(e.g. I_{DC}=4A), from the inner core to the outer core, the core loss density continually be reduced.

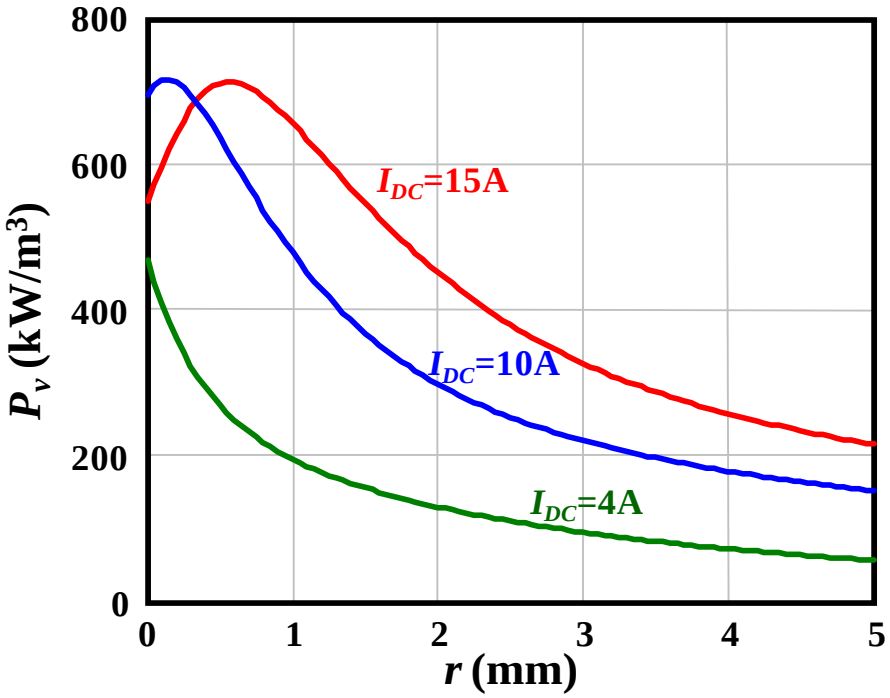

Figure 4.28 Core loss density of concentric rings for single-turn lateral flux inductor

After calculating the core loss density for each ring, the total core loss of the LTCC planar inductor can be calculated by summing all the ring core loss together. This summing process can be done using an integration method. The general core loss equation is:

$$P_{core\_N=n} = 2\int_0^g P_v(r)\cdot h\cdot\left(\sqrt{2}\cdot\pi\cdot\sqrt{\left(n\cdot r_v+\frac{(n-1)d}{2}+r\right)^2+\left(r_v+r\right)^2}\right)\cdot dr \qquad (4.16)$$

In order to verify the proposed analytical core loss model, two LTCC planar inductors are fabricated. One is a single-turn inductor, another one is a three-turn inductor. The dimensions of these two inductors are: for the single-turn structure, r_v=0.65mm, g=3mm, core thickness=2.8mm; for the three-turn structure, r_v=0.65mm, g=3mm, core thickness=2.2mm. Figure 4.29 shows the photos of three-turn inductor. The core loss measurement method is the same as that used in [85]. Table 4.1, Table 4.2 and Table 4.3 show the core loss calculation and measurement results for these LTCC inductors. It can be seen that the calculation results can match measurement results very well, which means the proposed analytical core loss models have very good accuracy.

Figure 4.29 LTCC inductor prototypes for core loss measurement

Table 4.1 Calculation and measurement results for single-turn LTCC inductor with I_{DC}=0A

Excitation	I_{DC}=0A, I_{ac}=0.4A	I_{DC}=0A, I_{ac}=0.6A	I_{DC}=0A, I_{ac}=0.8A
Calculation (mW)	8.2	23.8	51.2
Measurement (mW)	9.54	25.4	53.8

Table 4.2 Calculation and measurement results for single-turn LTCC inductor with I_{DC}=3A

Excitation	I_{DC}=3A, I_{ac}=0.8A	I_{DC}=3A, I_{ac}=1.6A	I_{DC}=3A, I_{ac}=2.4A
Calculation (mW)	3	18.4	53.9
Measurement (mW)	3.8	23	71.4

Table 4.3 Calculation and measurement results for three-turn LTCC inductor with I_{DC}=3A

Excitation	I_{DC}=3A, I_{ac}=0.8A	I_{DC}=3A, I_{ac}=1.6A	I_{DC}=3A, I_{ac}=2.4A
Calculation (mW)	2.72	17	50
Measurement (mW)	3.13	16.6	47.6

4.5 Summary

In this chapter, both the winding loss and the core loss of the LTCC planar inductor are studied and modeled. Because the LTCC planar inductor has very non-uniform flux and permeability distribution, the conventional winding ACR models and core loss models cannot be used. For the winding ACR, first the FEA simulation is used to studied different inductor structures; then some analytical equations are proposed to calculate the winding ACR for an LTCC planar inductor. The proposed analytical equations have very good accuracy from 1MHz to 6MHz. For core loss, some analytical models are also proposed for the LTCC planar inductor with non-uniform flux and permeability distribution. The basic modeling methodology is 1) divide the disc core into many concentric rings; 2) calculate the core loss for each ring; 3) sum all the ring core loss together to get the total core loss. In this proposed core loss model, the modified Steinmetz equation (MSE) is used to calculate core loss for each concentric ring with non-sinusoid excitation and DC flux bias. Several LTCC low-profile planar inductors are fabricated to verify these core loss models. The measurement results show that the proposed core loss models have very good accuracy.

Chapter 5. Comparison and Design of LTCC Inductor Substrate for Integrated Single-Phase POL

Figure 5.1 shows different structures for lateral flux LTCC inductor. Figure 5.1(a) is a single-turn structure; Figure 5.1(b) and Figure 5.1(c) are multi-turn structure: two-turn and three-turn structure. Actually, these multi-turn structures also can be further extended to 4-turn and 5-turn. .In order to optimize the low-profile LTCC lateral flux inductor design, inductance density, inductor core loss and winding loss of these different structures need to be compared. This chapter first compares different LTCC lateral flux inductor structures in a systematical way, which considers inductance density, winding loss and core loss together. After that, a design method is proposed to help optimizing the performance (minimize inductor loss and inductor volume at the same time) of low-profile LTCC lateral flux inductor. Finally, a LTCC lateral flux inductor is designed and fabricated for an integrated POL with 1.5MHz frequency and 15A output current.

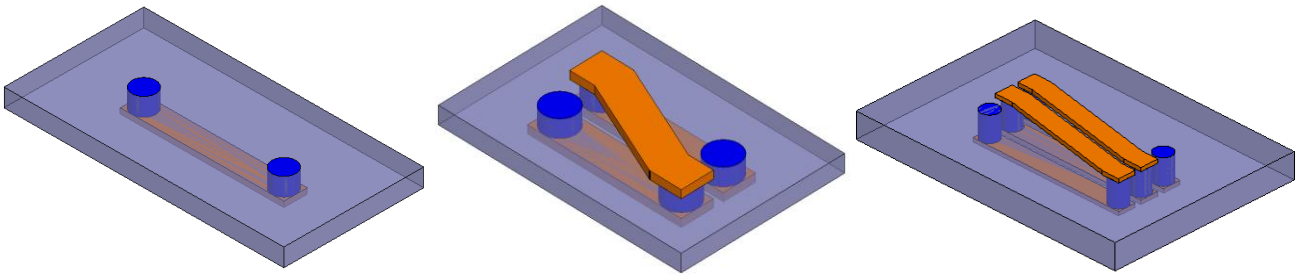

(a) (b) (c)

Figure 5.1 Different structures for lateral flux LTCC inductor: (a) single-turn structure *N*=1, (b) two-turn structure *N*=2, (c) three-turn structure *N*=3

5.1 Comparison between Different Lateral Flux LTCC inductor Structures for High Current Applications

The lateral flux inductor is first studied for high current applications (I_{DC}=15A). The compared performances for different lateral flux inductor include inductance density, core loss and winding loss. In these comparisons, the via radius for all the structures are the same r_v=0.7mm, and the peak to peak value of AC current is 50% of DC current i_{ac_pp}= 7.5A. The inductance density and core loss calculation are based on the analytical model introduced in chapter 2 and chapter 4. These models are based on the concentric ring concept, which means dividing the disc core with non-uniform flux distribution into many concentric rings, which have uniform flux distribution. Figure 5.2 shows the concept drawing about dividing half core of single-turn and two-turn lateral flux inductors into many concentric rings. Where, the parameter g is the distance between via edge and core edge, which represents the core size; the parameter r is used to define each concentric ring, which means the distance between each ring and via edge.

According to the analytical inductance model introduced in chapter 2, the inductance density of LTCC lateral flux inductor with different structures can be calculated and compared. Figure 5.3 shows the inductance density calculation results for lateral flux inductor with multi-turn structures. The inductance density of single-turn structure (N=1) is also shown in Figure 5.3 as reference. Like the single-turn structure, with a given via radius, there is an optimal g value for each multi-turn structure to achieve maximum inductance density. Compared with the single-turn structure (N=1), the multi-turn structures (N>1) have higher inductance density. However, this inductance increasing has some diminishing return.

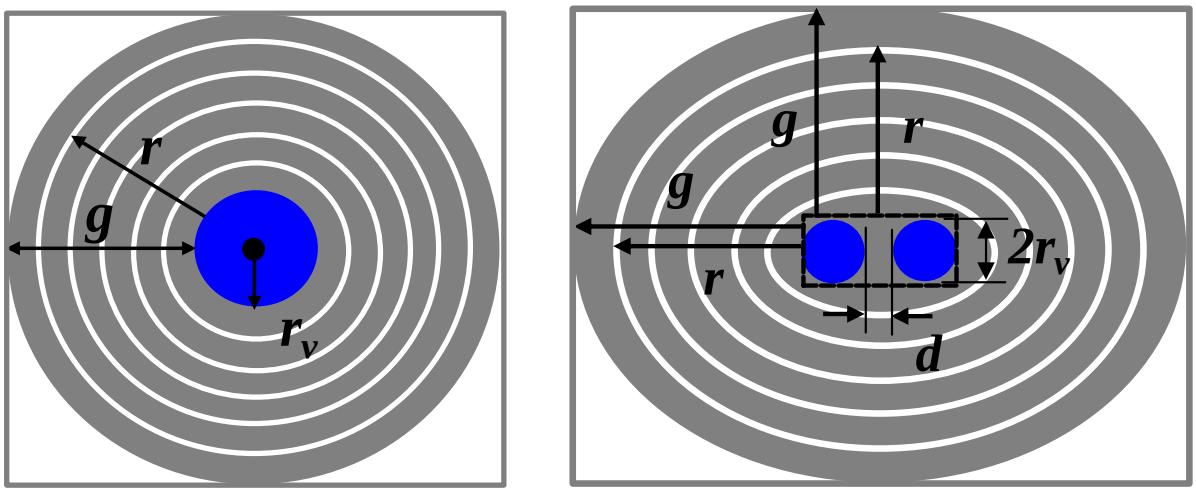

Figure 5.2 Concept drawing about dividing half core of lateral flux inductor into many concentric rings: a) single-turn structure, b) two-turn structure

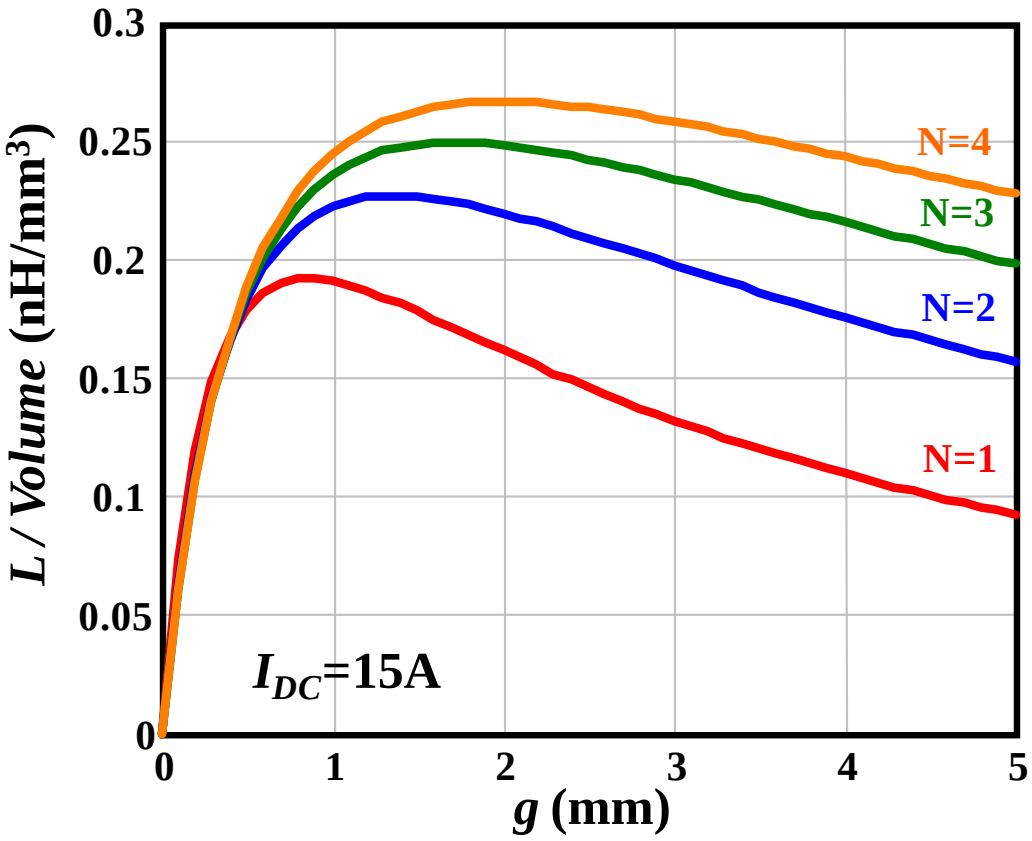

Figure 5.3 Inductance density calculation results for lateral flux inductor

Figure 5.4 shows the H_{DC} distribution of different lateral flux inductor structures. The x axis parameter r represents the location of the concentric ring, which is defined in Figure 5.2. It can be seen that multi-turn structures have higher H_{DC} than single-turn structure. Increasing turn number will increase H_{DC} value through the whole core. As a result, the multi-turn structures will have smaller permeability due to higher H_{DC} value.

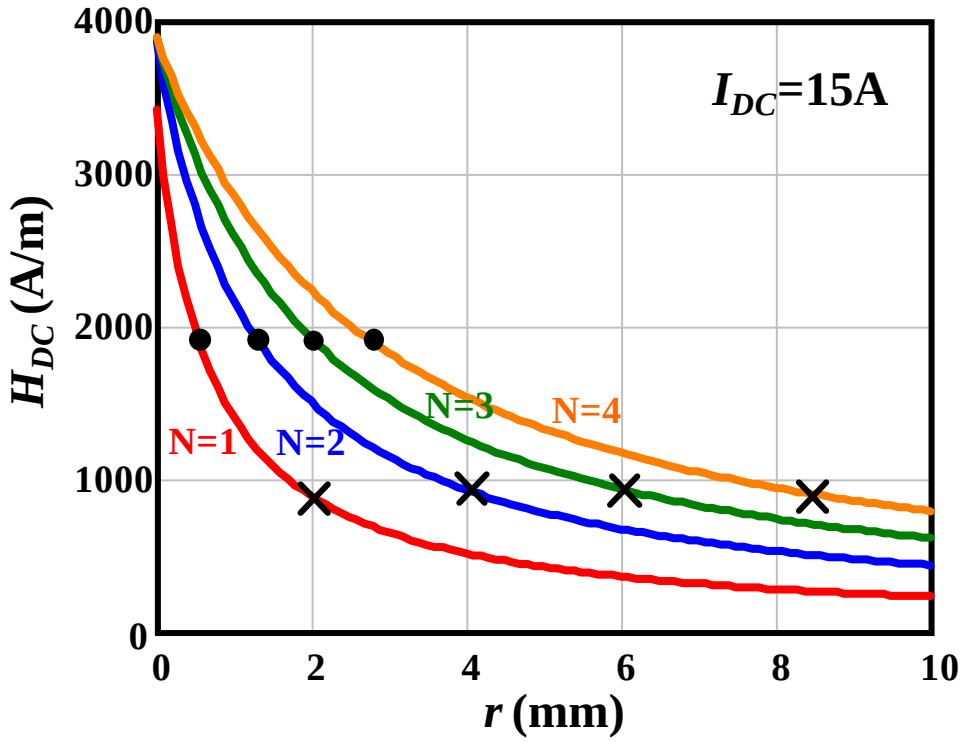

Figure 5.4 H_{DC} distribution of different lateral flux inductor structures

Figure 5.5 shows the incremental permeability distribution of different lateral flux inductor structures. Increasing turn number will reduce incremental permeability due to the increased H_{DC} value. The decreased permeability actually is one of the reasons for the diminishing return of inductance density increasing when increasing turn number. Another reason for diminishing return of inductance density increasing is the increased magnetic path length of concentric ring when increasing turn number. Figure 5.6 shows magnetic mean path length l_m of each ring for lateral flux inductor with different turn number.

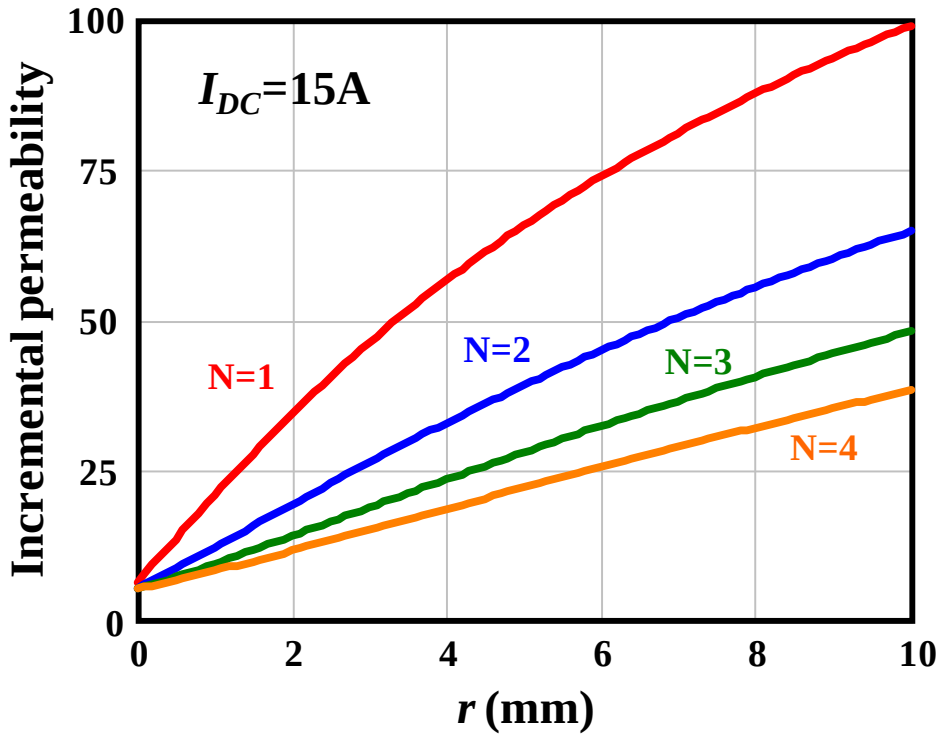

Figure 5.5 Incremental permeability distribution of different lateral flux inductor structures

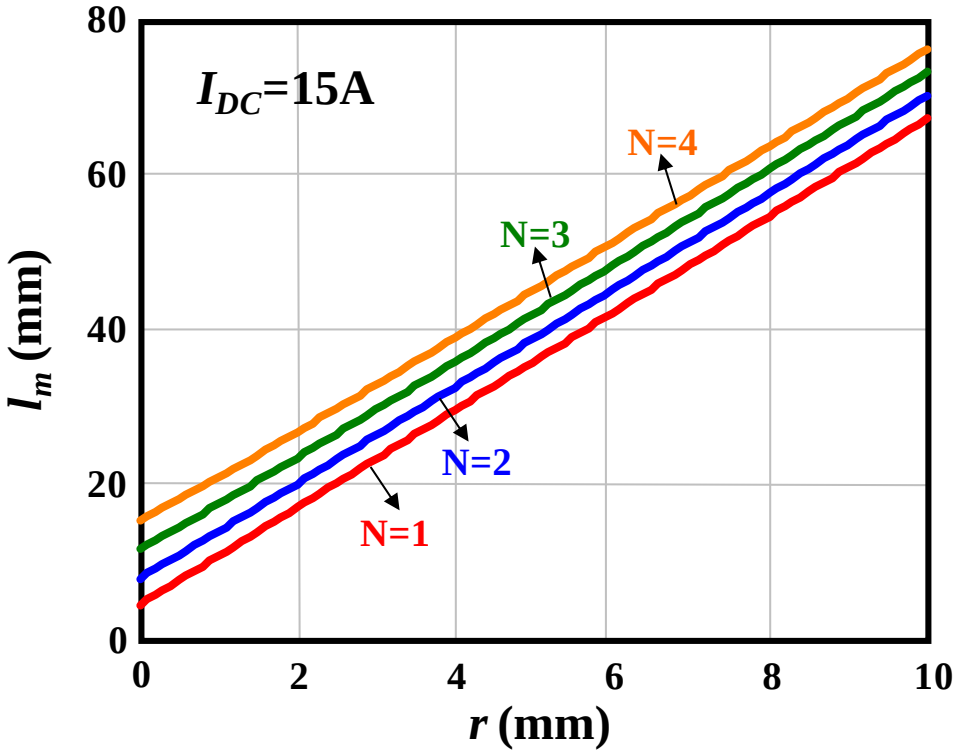

Figure 5.6 Magnetic mean path length l_m of each ring for lateral flux inductor

Figure 5.7 shows the B_{AC} distribution of different lateral flux inductor structures. It can be seen that with give turn number the B_{AC} will increase first and then it will decrease from the center part of the core to the outer part. That is because the inner part of the core has very high H_{DC} value, which causes the permeability reducing to very small value. As a result, the inner core becomes very high reluctance and the AC flux is pushed to travel though outer part of the core. The maximal B_{AC} value is almost the same for lateral flux inductor with different turn number. However, the position of the maximal B_{AC} (marked by cross symbol) will move from inner part to outer part when increasing turn number.

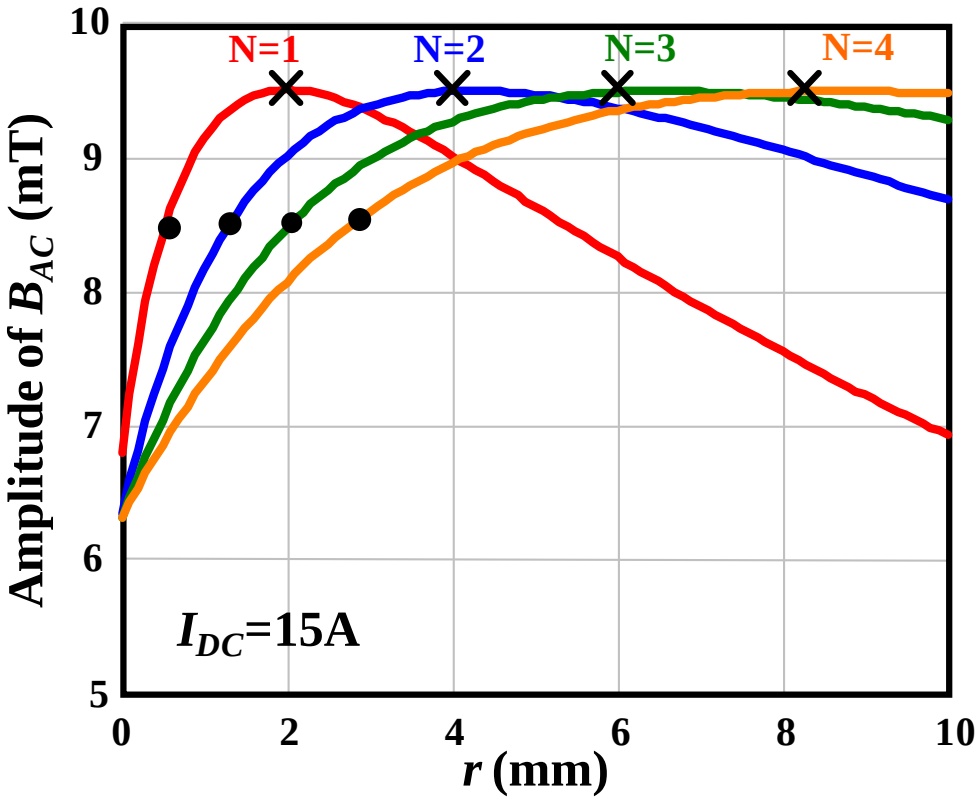

Figure 5.7 B_{AC} distribution of different lateral flux inductor structures

Figure 5.8 shows the core loss density P_v distribution of different lateral flux inductor structures. Just like B_{AC} distribution, from the center part of the core to the outer part, the P_v will increase first, then it will decrease. The locations of maximal P_v are marked by dot symbol. The

maximal P_v locations are also marked by dot symbol in both Figure 5.4 and Figure 5.7 to tell the related H_{DC} and B_{AC} value; and the maximal B_{AC} locations are also marked by cross symbol in both Figure 5.4 and Figure 5.8. From Figure 5.8, it can be seen that the locations for maximal P_v are not the same as the locations for the maximal B_{AC}, it moves to inner core. That is because the P_v is not only impacted by B_{AC} but also impact by H_{DC}; With the same B_{AC}, the higher H_{DC} will cause the higher P_v. Comparing with the maximal B_{AC} location, the maximal P_v location has smaller B_{AC} but higher H_{DC}. So it has higher P_v than maximal B_{AC} location.

Comparing different lateral flux inductor structures, the maximal P_v values are almost the same. Actually, at the maximal P_v location the lateral flux inductor with different turn number also have the same B_{AC} and H_{DC}, which are shown in Figure 5.7 and Figure 5.4. However, the position of the maximal P_v will move from inner part to outer part when increase turn number.

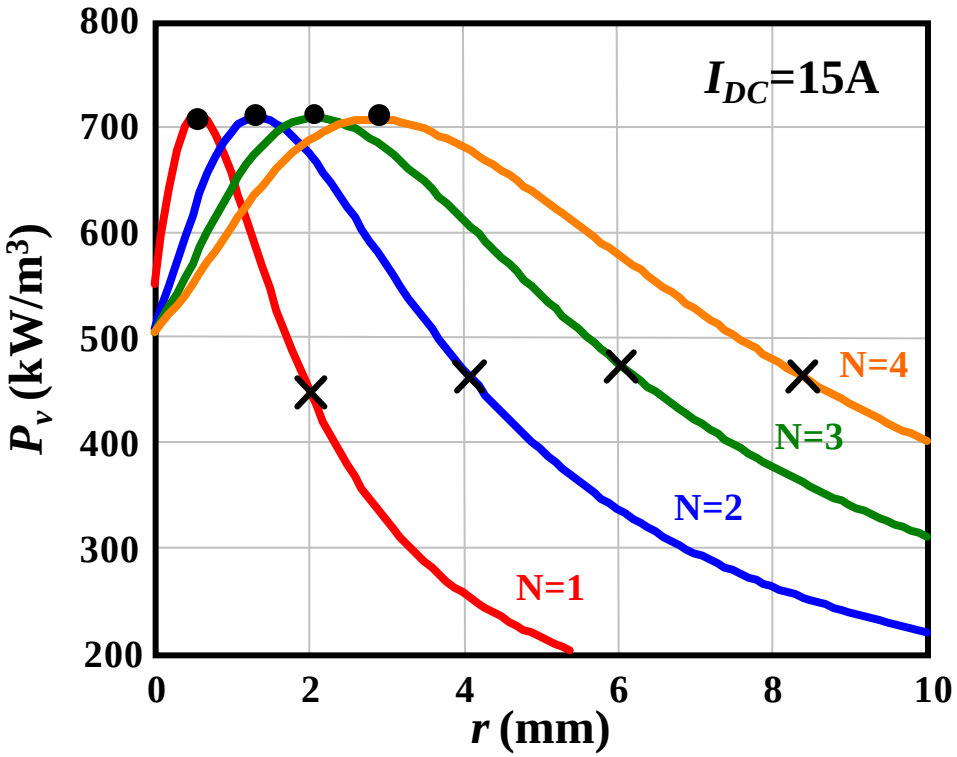

Figure 5.8 Core loss density P_v distribution of different lateral flux inductor structures

In order to compare the core loss aspect for different lateral flux inductor. A quality factor of core loss is defined as:

$$Q_{Core} = \frac{L \cdot 2\pi \cdot F_S}{Core\_Loss} \tag{5.1}$$

Figure 5.9 shows the core loss quality factor for different lateral flux inductors for a buck converter with V_{in}=5V, V_o=1.2V, F_S=1.5MHz and I_{DC}=15A. The inductor AC current is determined by the inductance, which is changed when changing inductor footprint. The unchanged inductor dimensions are via radius r_v=0.7mm and core thickness h=2mm. For given turn number, it can be known that increasing inductor footprint can increase the quality factor of core loss. In other words, the inductance increasing is faster than core loss increasing when increasing inductor footprint. Increasing turn number will also increase quality factor of core loss.

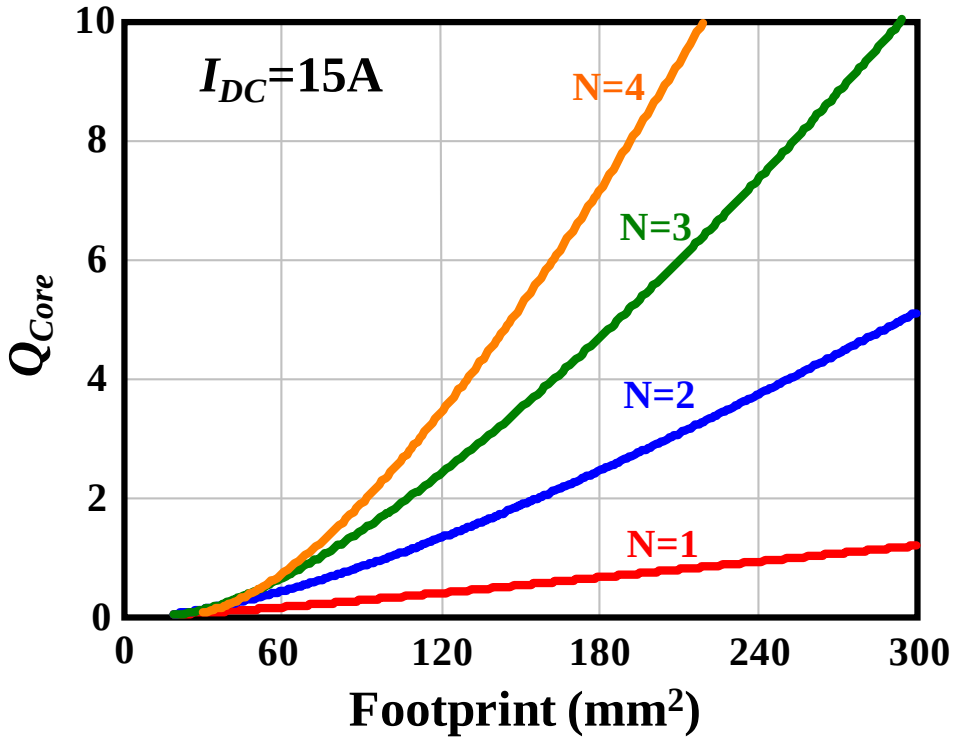

Figure 5.9 core loss quality factor for different lateral flux inductors for a buck converter with V_{in}=5V, V_o=1.2V, F_S=1.5MHz and I_{DC}=15A

In order to compare the winding loss aspect for different lateral flux inductor. A quality factor of winding loss is defined as:

$$Q_{Winding} = \frac{L \cdot 2\pi \cdot F_S}{Winding\_Loss} \tag{5.2}$$

Figure 5.10 shows the winding loss quality factor for different lateral flux inductor for a buck converter with V_{in}=5V, V_o=1.2V, F_S=1.5MHz and I_{DC}=15A. The inductor dimensions are via radius r_v=0.7mm and core thickness h=2mm. It can be seen that increasing inductor footprint also can increase the quality factor of winding loss. However, there is some diminishing return of this increasing, which means that after some footprint, the inductance and winding loss will increase with almost the same rate. Unlike the core loss, increasing turn number will decrease quality factor of winding loss.

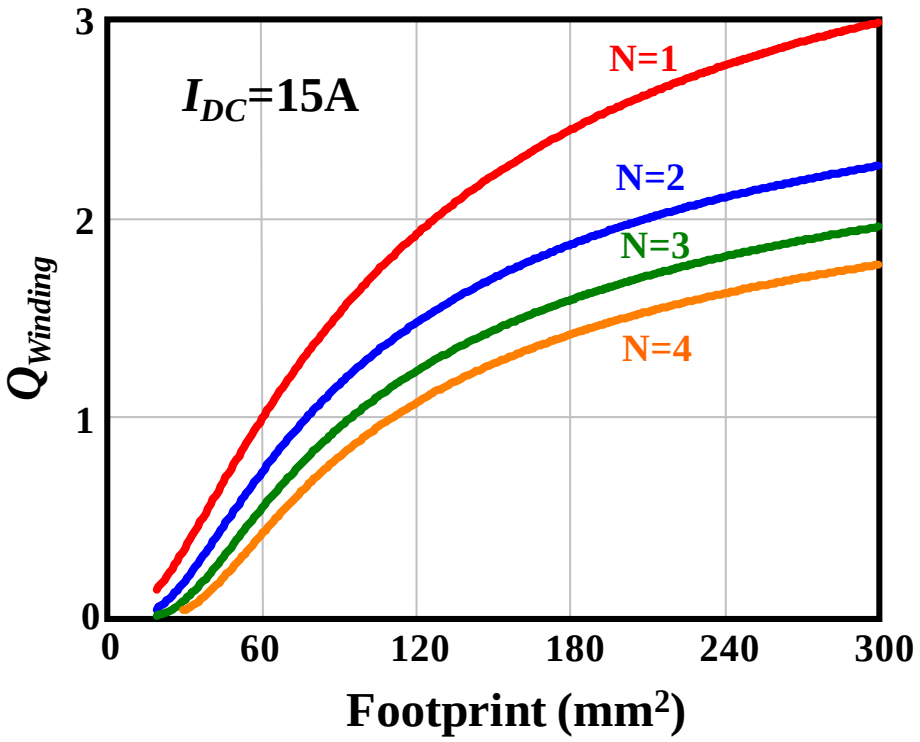

Figure 5.10 Winding loss quality factor for different lateral flux inductor for a buck converter with V_{in}=5V, V_o=1.2V, F_S=1.5MHz and I_{DC}=15A

The quality factor of total loss is defined as:

$$Q_{Total} = \frac{L \cdot 2\pi \cdot F_S}{Core\_Loss + Winding\_Loss} \tag{5.3}$$

Figure 5.11 shows the total loss quality factor for different lateral flux inductor for a buck converter with V_{in}=5V, V_o=1.2V, F_S=1.5MHz and I_{DC}=15A. The inductor dimensions are via radius r_v=0.7mm and core thickness h=2mm. It can be seen that increasing turn number from 1 to 2 and from 2 to 3, the total loss quality factor will be continually increased; but when increase turn number from 3 to 4, the total loss quality factor will not be increased. So, for this 15A case, there is no need to design turn number higher than 3.

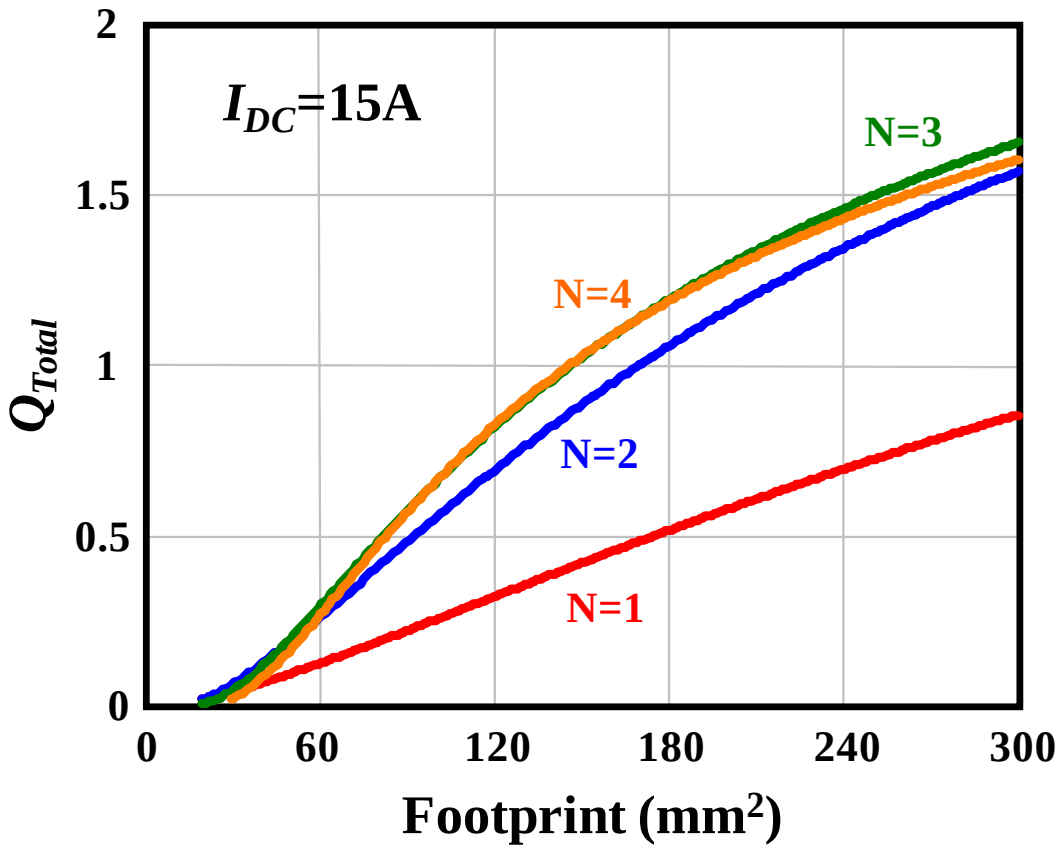

Figure 5.11 Total loss quality factor for different lateral flux inductor for a buck converter with V_{in}=5V, V_o=1.2V, F_S=1.5MHz and I_{DC}=15A

5.2 Comparison between Different Lateral Flux LTCC inductor Structures for Low Current Applications

Previous analysis and comparison is only based on 15A inductor current case. In order to get more general conclusion, different inductor current values need to be studied. Figure 5.12 shows the inductance density of different lateral flux inductors with 10A and 5A inductor current. Comparing with the inductance density of 15A current, it can be known that 1) increasing turn number can always increase inductance density no matter with large current or with small current.; 2) reduce inductor current can increase inductance density.

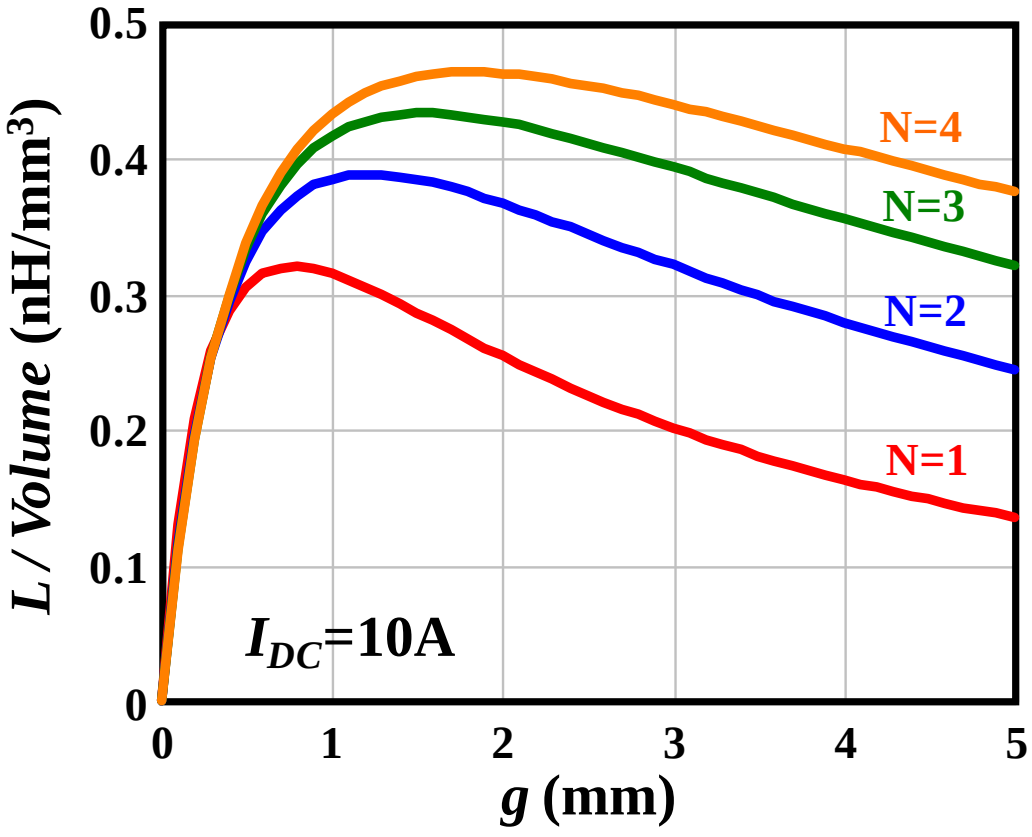

(a)

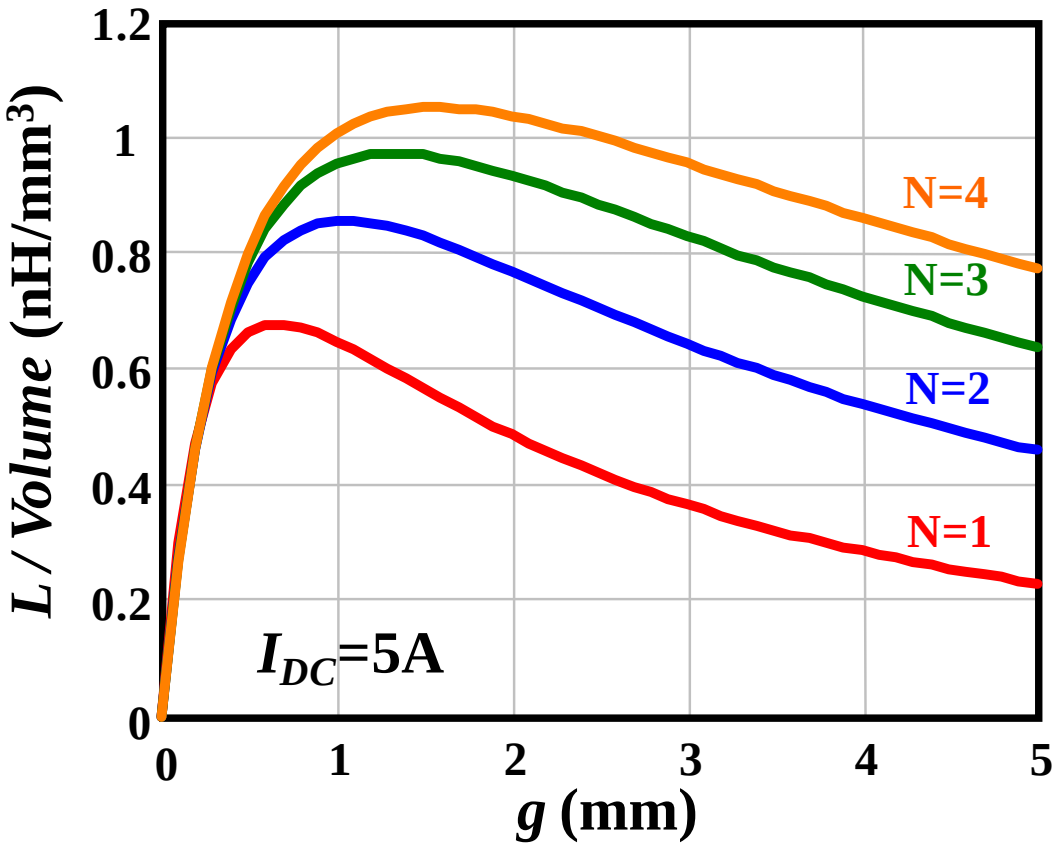

(b)

Figure 5.12 Inductance density of lateral flux inductors with different inductor current (a) 10A, (b) 5A

Figure 5.13 shows the B_{AC} distribution of different lateral flux inductors with 10A and 5A inductor DC current. The inductor AC current is always equal to 50% of the DC current. Comparing with the B_{AC} distribution of 15A DC current, it can be known that 1) the maximal B_{AC} values of different lateral flux inductors are almost the same no matter with high current or low current; 2) The location for maximal B_{AC} will move into inner core when reducing inductor DC current. For I_{DC}=5A case, the maximal B_{AC} position is almost at the most inner core for all the structures. That is because with this small DC current, the H_{DC} value of inner part core is still relative low. As a result, the permeability of inner core is still high enough to make it as low reluctance path for the AC flux.

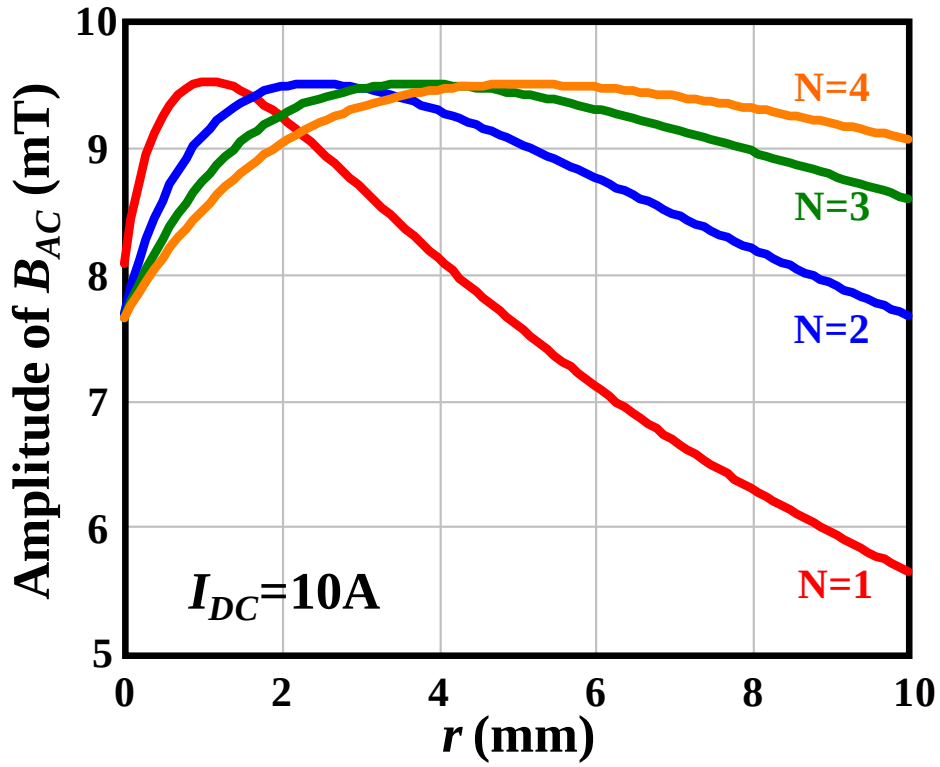

(a)

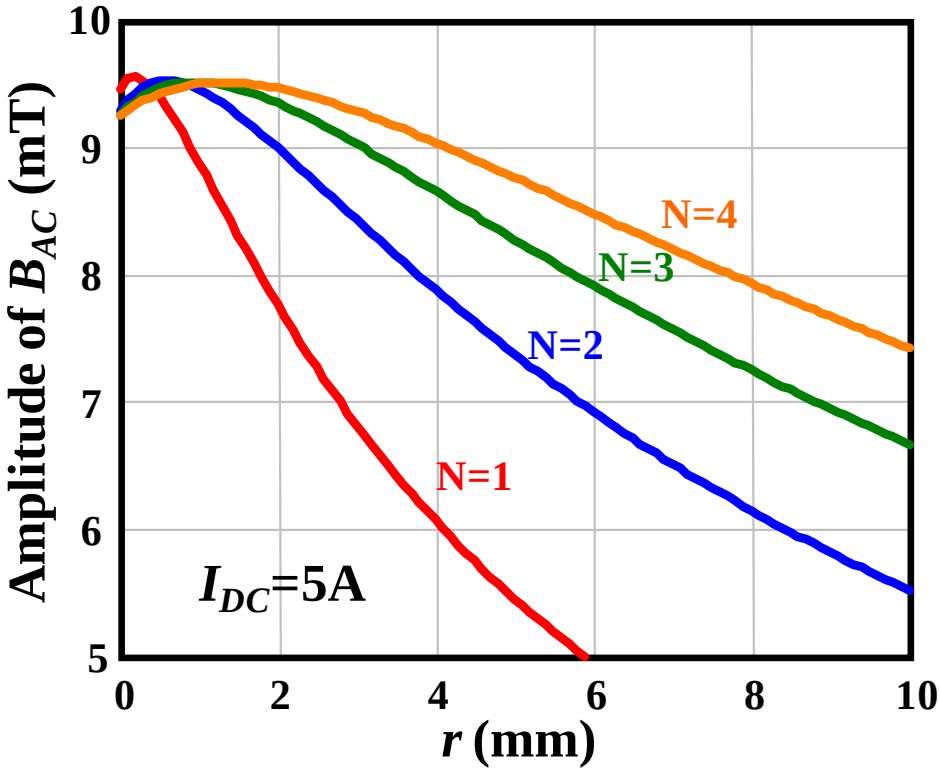

(b)

Figure 5.13 B_{AC} distribution of lateral flux inductors with different inductor current (a) 10A, (b) 5A

Figure 5.14 shows the core loss density P_v distribution of different lateral flux inductors with 10A and 5A inductor DC current. The inductor AC current is always equal to 50% of the DC current. Comparing with the P_v distribution of 15A DC current, it can be known that the location for maximal P_v will move into inner core when reducing inductor DC current. For I_{DC}=5A case, the maximal P_v position is at the most inner core for all the structures. That is because with this small DC current, the maximal B_{AC} position has moved to inner core part.

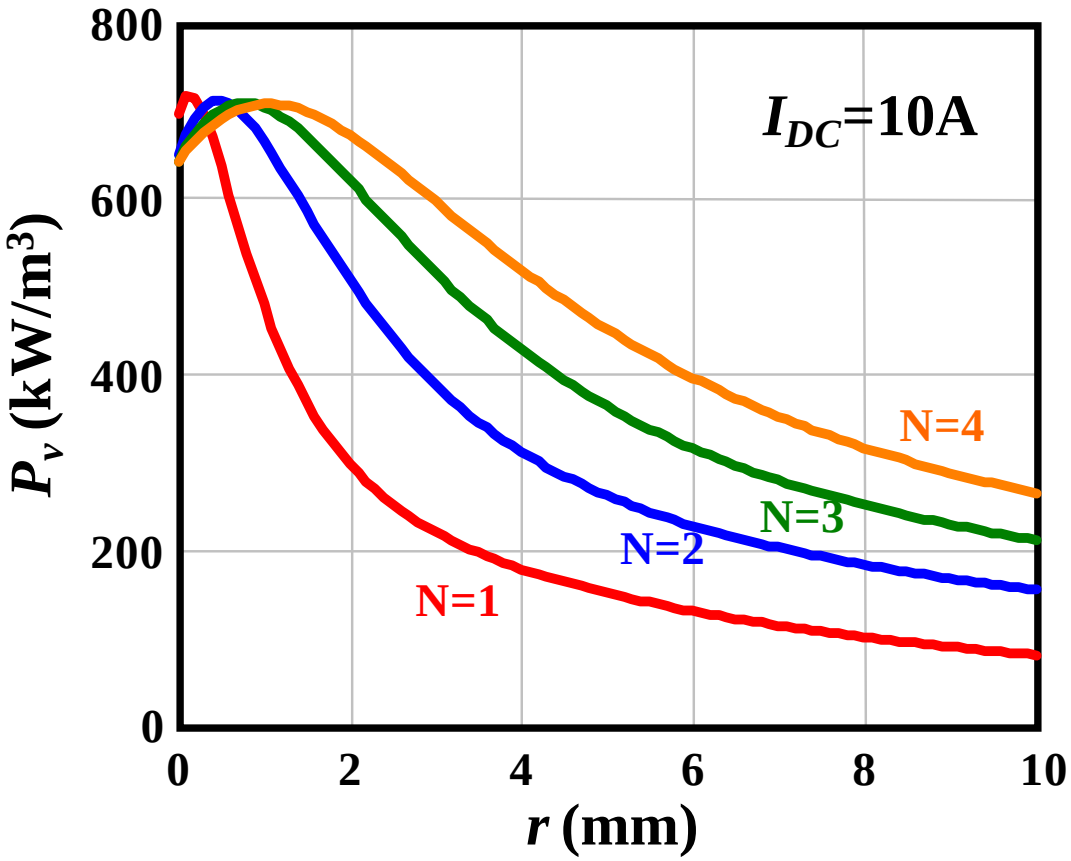

(a)

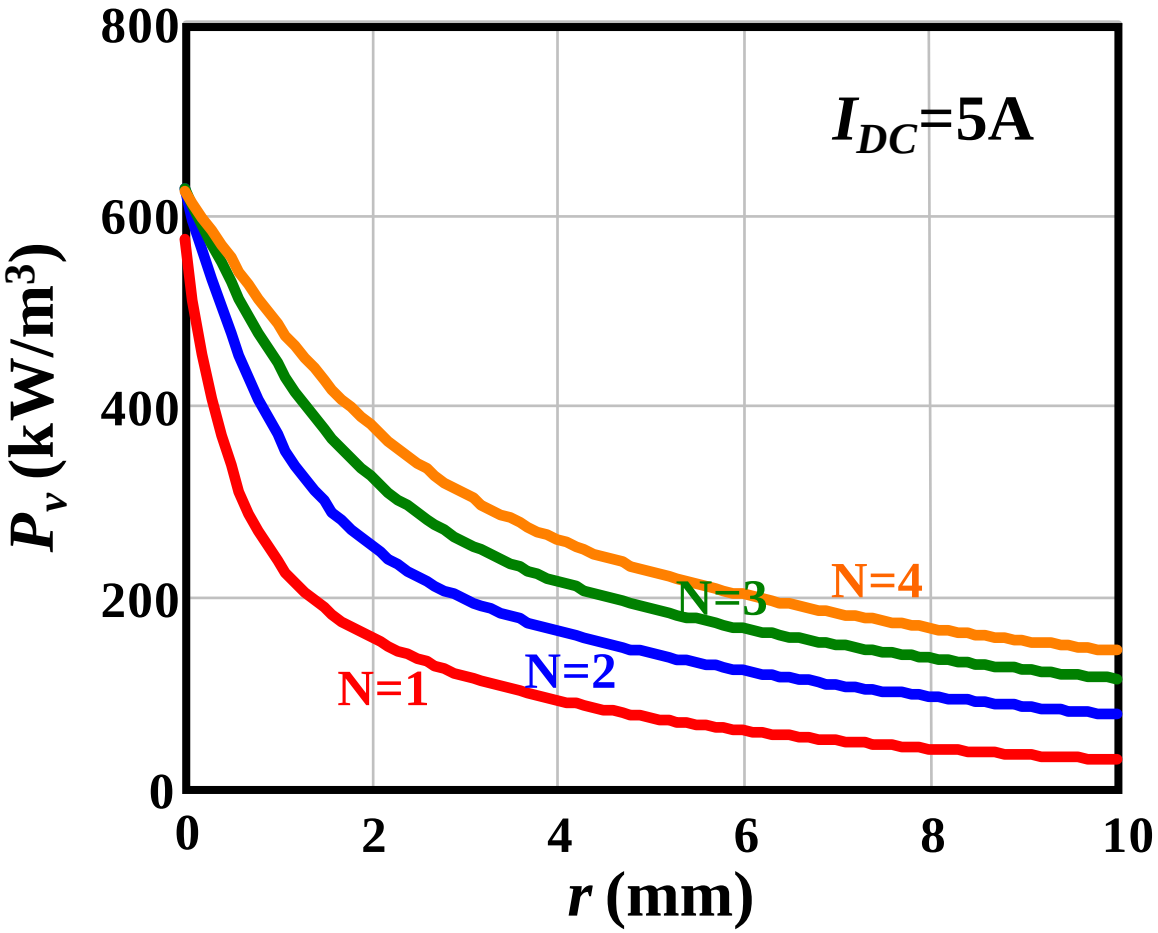

(b)

Figure 5.14 Core loss density P_v distribution of lateral flux inductors with different inductor current (a) 10A, (b) 5A

Figure 5.15 shows the total loss quality factor Q_{Total} of different lateral flux inductors with 10A and 5A inductor DC current. The only changed parameter between Figure 5.15 and Figure 5. 11 is the DC current. Comparing with the Q_{Total} of 15A DC current, it can be known that

1) With given inductor footprint, reducing DC current can increase Q_{Total}. There are three major reasons for the Q_{Total} increasing when reducing DC current. First, the winding DC loss will be reduced due to small DC current. Second, the inductance of these lateral flux inductors will be increased due to permeability increasing caused by reducing DC current. Third, the core loss and

winding AC loss will both be reduced due to smaller inductor current ripple caused by larger inductance.

2) When reducing DC current from 15A to 10A, the Q_{Total} of 4-turn structure becomes larger than that of three-turn structure. Further reducing DC current to 5A, the difference of Q_{Total} between 4-turn and three-turn becomes even larger, which means that for smaller DC current case, the more turn number may be used to improve the performance of LTCC lateral flux inductor.

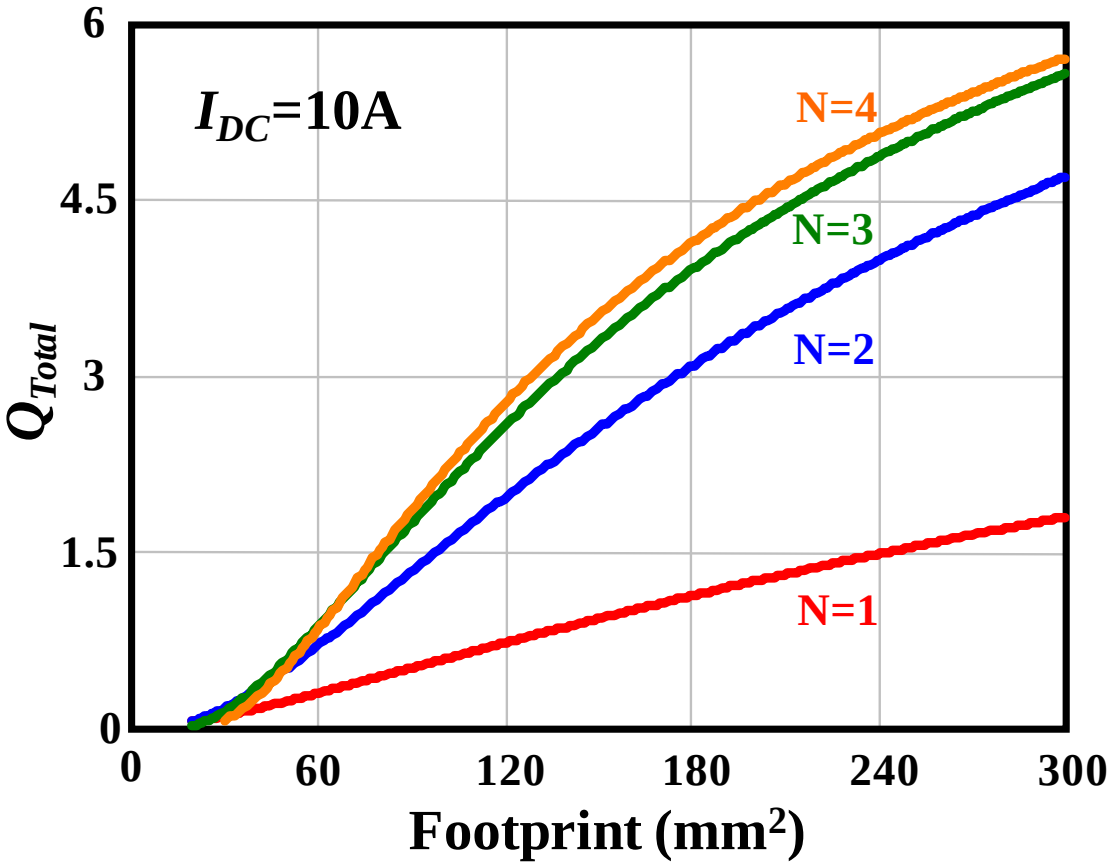

(a)

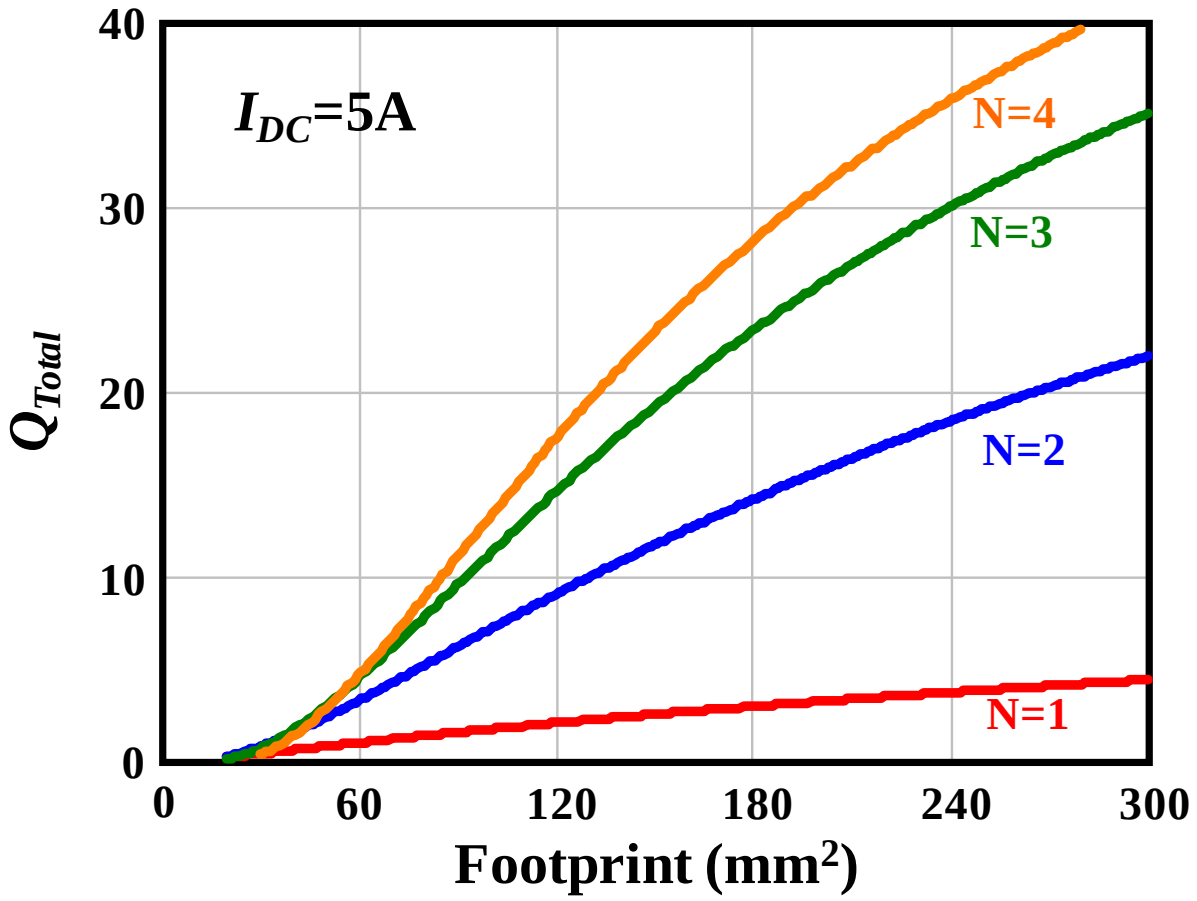

(b)

Figure 5.15 Total loss quality factor Q_{Total} of lateral flux inductors with different DC current (a) 10A, (b) 5A

5.3 LTCC inductor design examples for one-phase integrated POL

In this section, some LTCC inductor substrates are designed for a 1.5MHz, 5V to 1.2V, 15A output current, 3D integrated buck converter. First, a LTCC lateral flux inductor is designed based on proposed optimal design method, which can minimize inductor volume and loss at the same time. Then, a LTCC vertical flux inductor is also designed to compare with LTCC lateral flux inductor. The inductance of lateral flux inductor and vertical flux inductor both are designed as 80nH with 15A inductor current.

From Figure 5.11 it can be known that for lateral flux structure, the 4-turn structure doesn't have too much benefit comparing with three-turn structure with 15A inductor current. So, the lateral flux inductor design only considers single-turn, two-turn and three-turn structures. First the radius of inductor via is chosen as same r_v=0.7mm according to inductor DC current value. Then, the inductance density curve with different g value for different lateral flux structures can be calculated. The results are the same as Figure. 5.3. With given inductance value, the inductor volume can be calculated according to different inductance density. The inductor footprint also can be calculated according to different g based on following equation:

$$\text{Footprint} = (4r_v + 4g) \cdot [N \cdot 2r_v + 2g + (N-1) \cdot d] \tag{5.4}$$

where, N is turn number; g, r_v and d are defined in Figure 5.2

So, with given inductance value L=80nH, Figure 5.3 can be redrawn as Figure 5.16, which shows the impact of inductor footprint on inductor volume. Because footprint and volume both are key parameters for planar inductor, especially for integration applications, Figure 5.16 will be used as one of the design curves for LTCC planar inductor design. From Figure 5.16, it can be known that 1) with given turn number N, there is an optimal inductor footprint to give minimal inductor volume. 2) Increasing turn number can help to reduce inductor volume. Figure 5.17 shows the impact of inductor footprint on core thickness with given inductance L=80nH. It can be seen that 1) increasing footprint will reduce core thickness; 2) increasing turn number will also reduce core thickness.

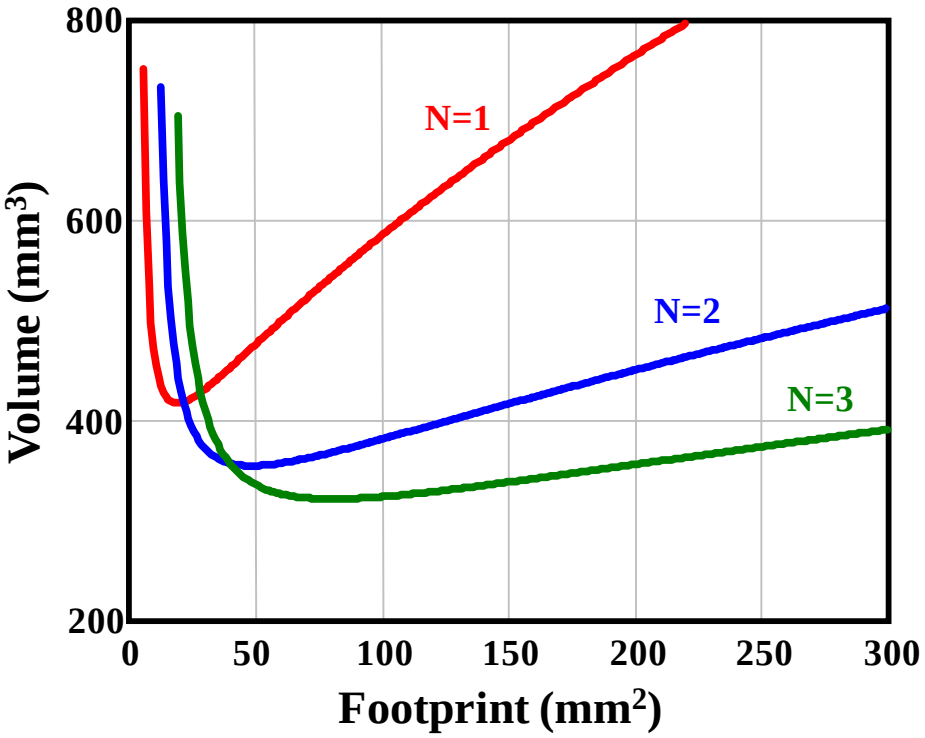

Figure 5.16 Impact of inductor footprint on inductor volume with given inductance value *L*=80nH

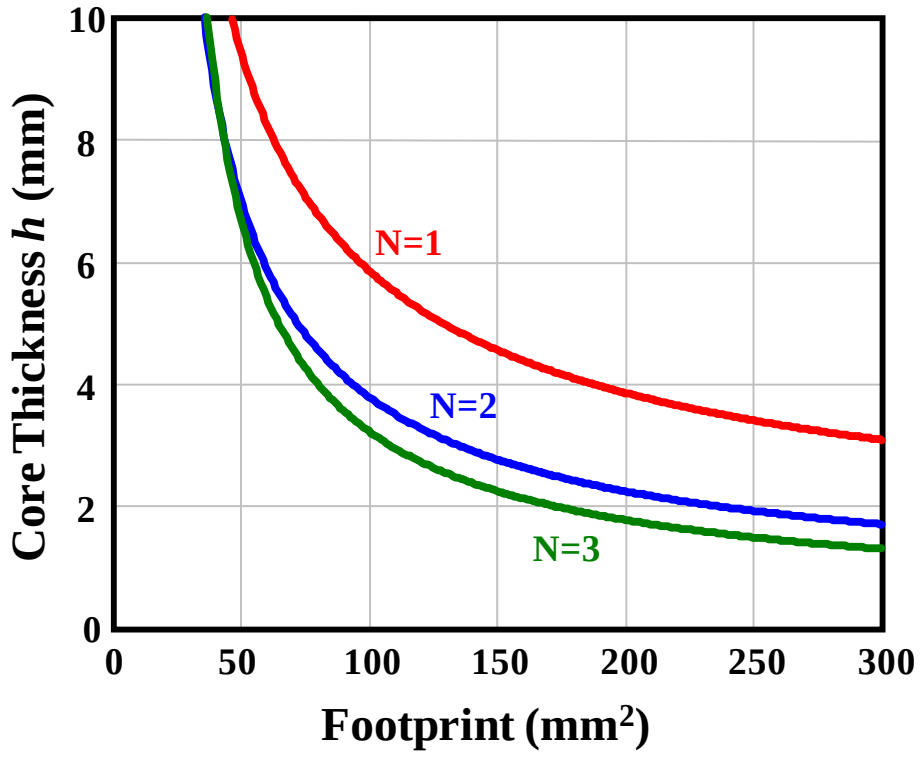

Figure 5.17 Impact of inductor footprint on core thickness with given inductance value *L*=80nH

Besides inductor volume and core thickness, another important parameter for planar inductor is inductor loss, which includes core loss and winding loss. Figure 5.18 shows the impact of parameter g on core loss and winding loss with given inductance L=80nH. The inductor loss calculation is based on the proposed models introduce in chapter 4. From Figure 5.18, it can be seen that 1) there is an optimal g value to give minimal winding loss for different structures; 2) increasing g will increase inductor core loss, but after some point, further increasing g will not impact core loss too much; 3) For single-turn structure, the winding loss is larger than core loss when g is small; but, when g become larger, the core loss will become larger than winding loss; 4) For two-turn and three-turn structures, the winding loss is always larger than core loss.; 5) increasing turn number will increase winging loss but reduce core loss.

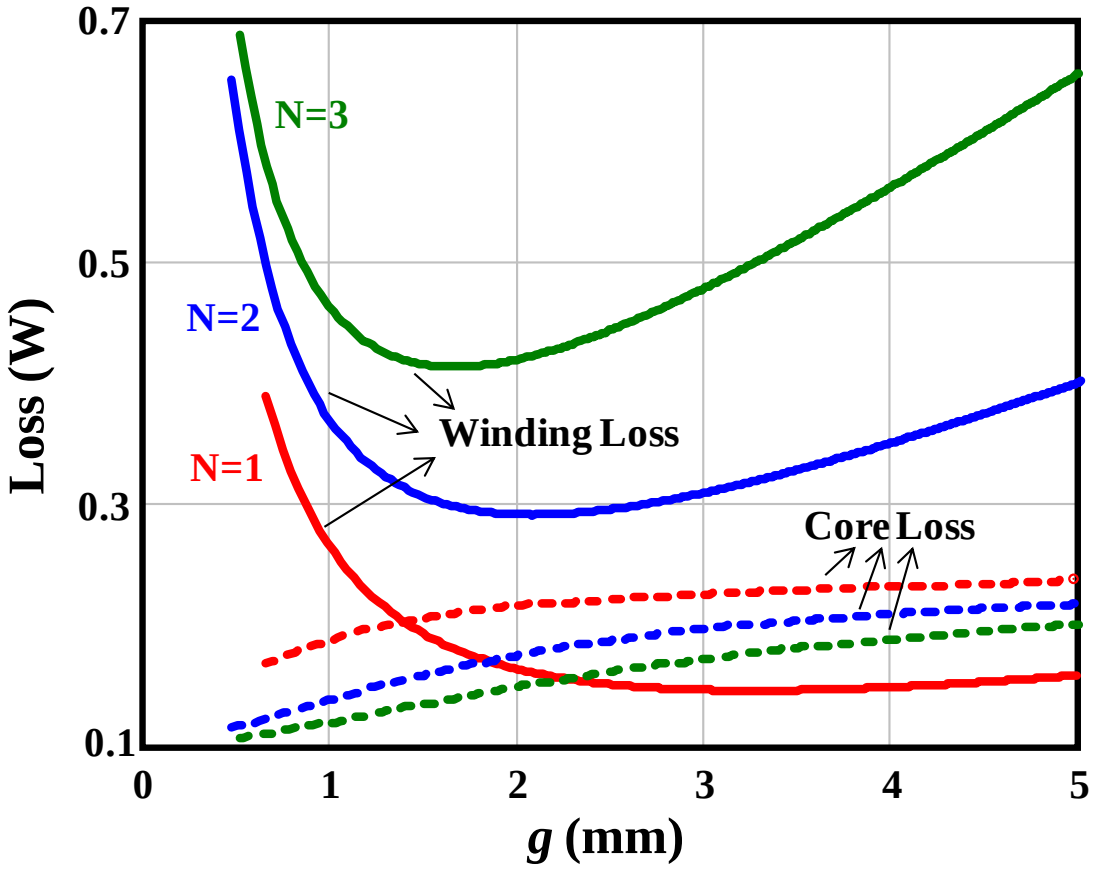

Figure 5.18 Impact of parameter g on core loss and winding loss with given inductance value L=80nH

After combining winding loss and core loss, the impact of parameter g on inductor total loss is shown in Figure. 5.19. It can be seen that 1) there is an optimal g value to give minimal inductor total loss for different structures; 2) increase turn number will increase inductor total loss. After calculating inductor footprint according to different g value, Figure 5.19 can be redrawn as Figure 5.20. This is another design curves for LTCC planar inductor design. After deriving these three sets of design curves shown in Figure 5.16, Figure 5.17 and Figure 5.20, the turn number will be determined first. According to Figure 5.16 and Figure 5.17, it can be seen that for single-turn structure (N=1), the footprint need to be designed between 20mm^2 and 50mm^2 to achieve small inductor volume. But, with this small footprint, the core thickness will be very large (>7mm), which is not practical. So, the single-turn structure is eliminated. According to Figure 5.16 and Figure 5.20, there is a trade-off between two-turn and three-turn structures. The three-turn structure can have smaller volume but larger inductor loss. In order to achieve higher power density for integrated POL, the three-turn structure is chosen. With three-turn structure, there is a footprint region to achieve small inductor volume and loss at the same time. For this particular case, the preferred footprint region should be from 50mm^2 to 200mm^2. Within this footprint range, three-turn lateral flux inductor has almost the same inductor volume and loss. However, according to Figure 5.17, it can be known that different footprint will give different core thickness. Increase inductor footprint from 50mm^2 to 200mm^2, the core thickness will be reduced from 7mm to 1.8mm. For this integrated POL application, it is better to design inductor substrate with lower profile. So, the inductor footprint is chosen as 165mm^2 to achieve 2mm core thickness.

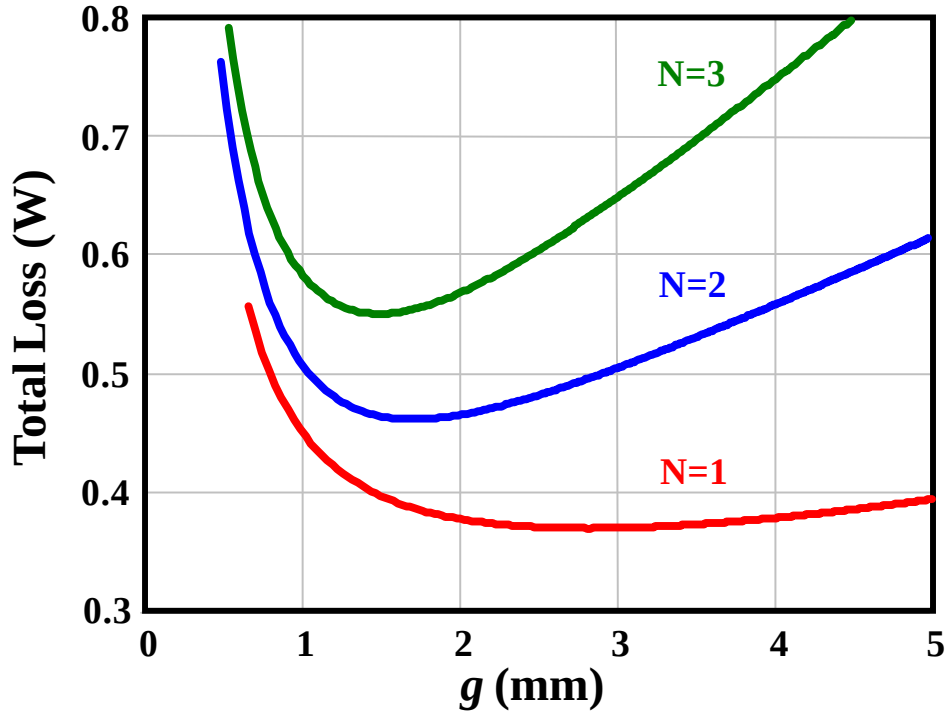

Figure 5.19 Impact of parameter *g* on inductor total loss with given inductance value *L*=80nH

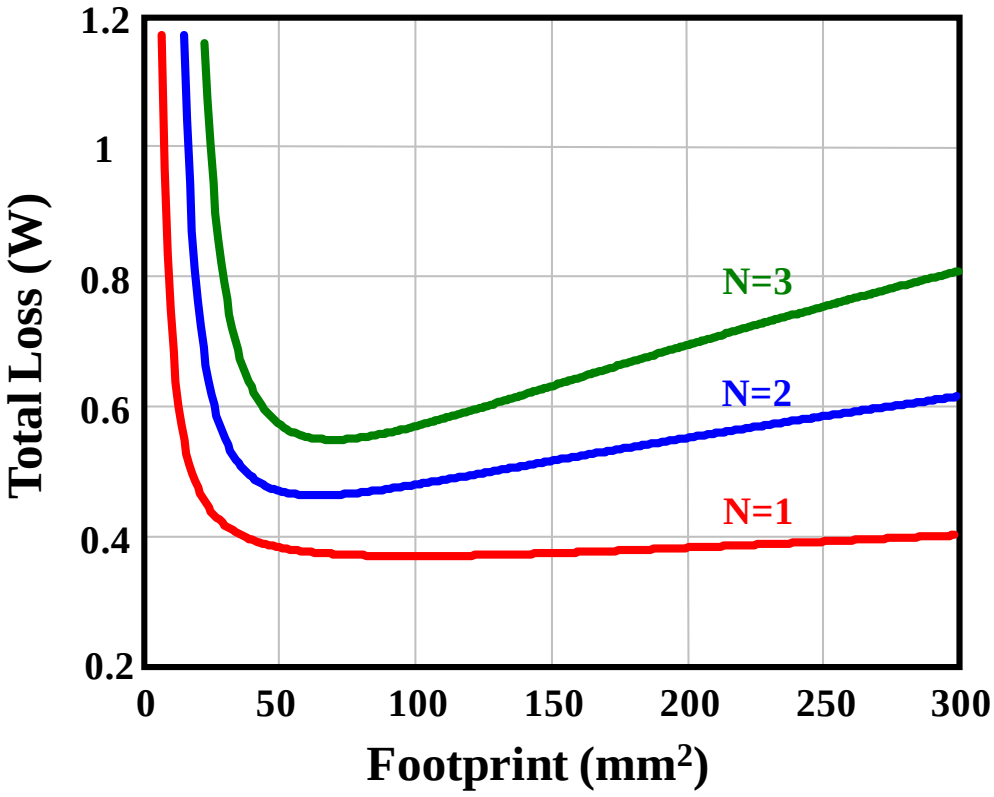

Figure 5.20 Impact of inductor footprint on total loss with given inductance value *L*=80nH

Beside the lateral flux inductor, an LTCC low-profile vertical flux inductor is also designed and fabricated for comparison purpose. The winding cross-section area of this vertical flux inductor is designed to be the same as that of the lateral flux inductor. Figure 5.21 shows the maximal inductance density of the LTCC inductor with different core thickness. It can be known that if the core thickness of this vertical flux inductor is chosen to be 2mm, which is the same as the lateral flux inductor example, this vertical flux inductor almost reaches the maximal inductance density. However, this maximal inductance density of vertical flux structure is still much lower than three-turn lateral flux inductor structure.

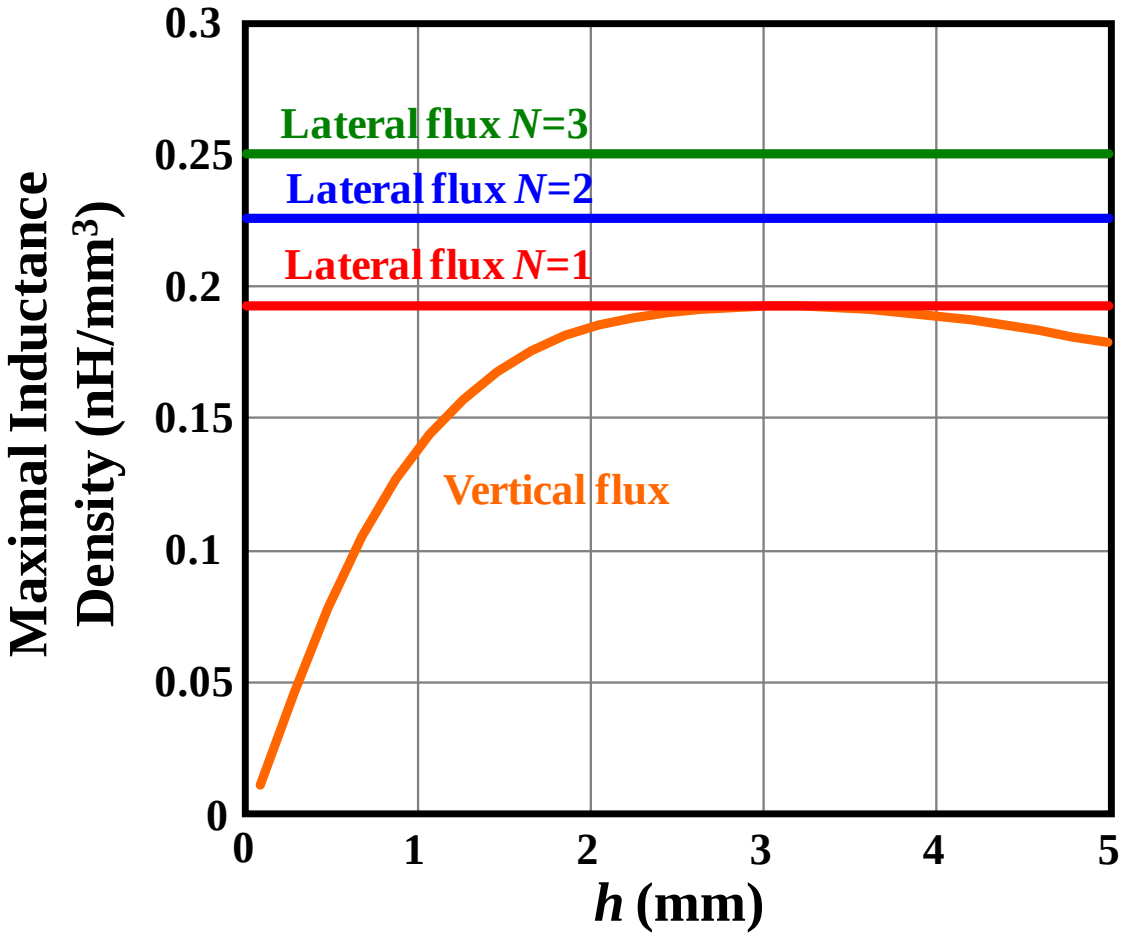

Figure 5.21 Core thickness impact on maximum inductance density for LTCC inductor

Figure 5.22 shows the concept drawing of designed LTCC vertical flux inductor. A U-shaped winding structure is used for this vertical flux structure.

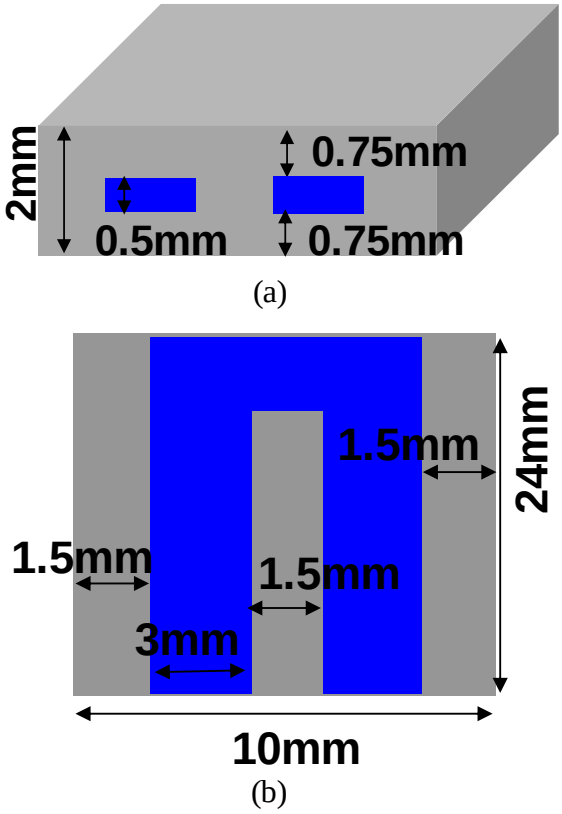

Figure 5.22 Concept drawing of designed LTCC vertical flux inductor: (a) outside view, (a) inside view

The LTCC green tape 40011 provided by ESL is used to fabricate the inductor core for both lateral flux and vertical flux structure. DuPont silver paste 7740 is used to make the embedded-winding for both the lateral flux and vertical flux structures. Copper sheets are used as the surface trace for the lateral flux structure. Figure 5.23 shows the fabrication process for LTCC lateral flux inductor. Step 1): Laminating LTCC green tape to build enough core thickness; Step 2) Making vias by using punching machine or laser; Step 3) Screen printing silver paste into vias; Step 4) sintering core with silver paste with around 900^{o}C and connecting vias by copper sheet after sintering. The temperature profile for sintering in step 4 is shown in Figure 5.24.

Comparing with the fabrication process of vertical flux structure [18], this lateral flux structure has much easier fabrication process.

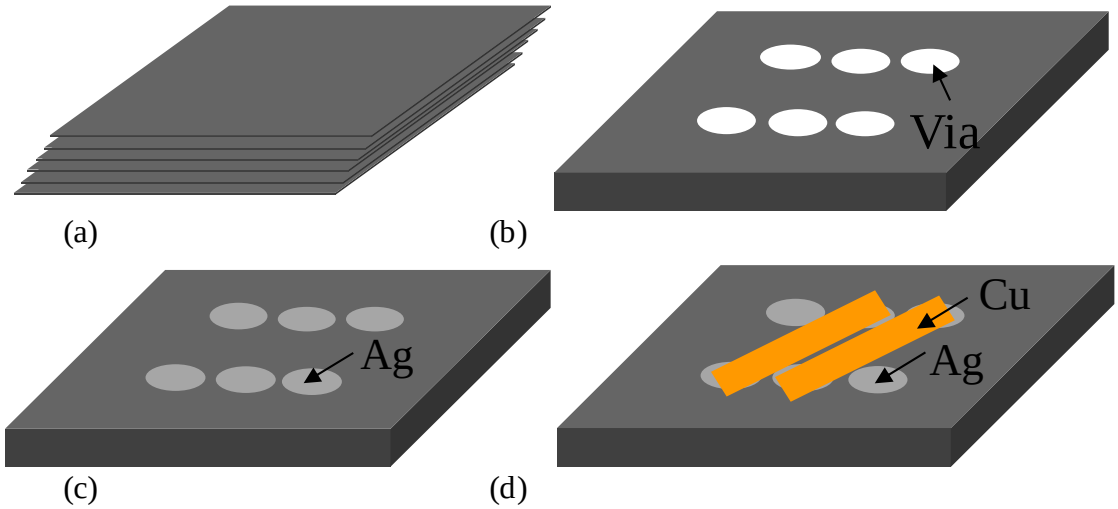

Figure 5.23 Fabrication process for LTCC lateral flux inductor: (a) step 1, (b) step 2, (c) step 3, (d) step 4

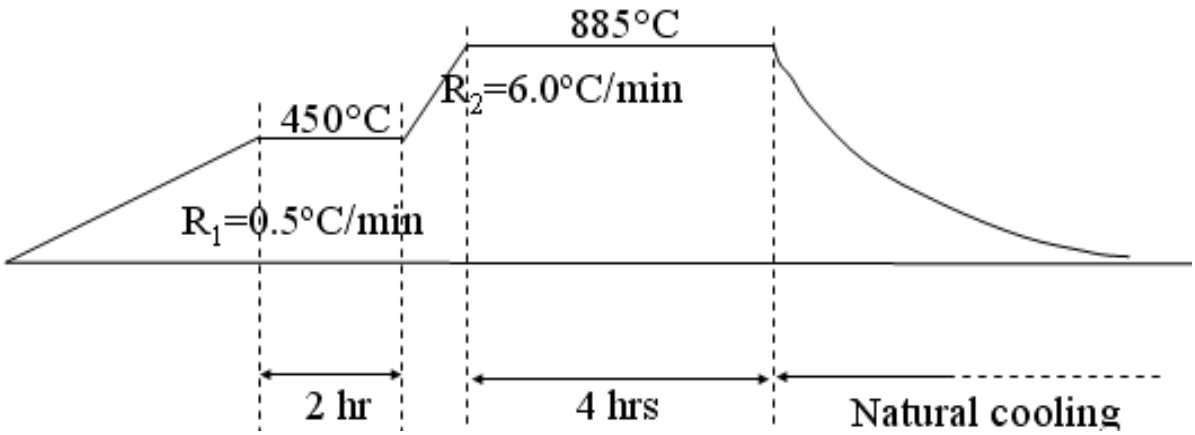

Figure 5.24 Temperature profile for LTCC sintering

The LTCC inductor prototypes are shown in Figure 5.25. The inductance test and calculation results for these two inductor prototypes are shown in Figure 5.26, from which, we can see that the proposed inductance calculation method can predict the real inductance value very well. The lateral flux inductor has around 1.3mΩ DCR and 165mm^2 footprint. The vertical flux inductor has around 1.1mΩ DCR and 240mm^2 footprint. Thus, these two inductors have almost the same winding DCR, but the lateral flux inductor can save around 30% footprint.

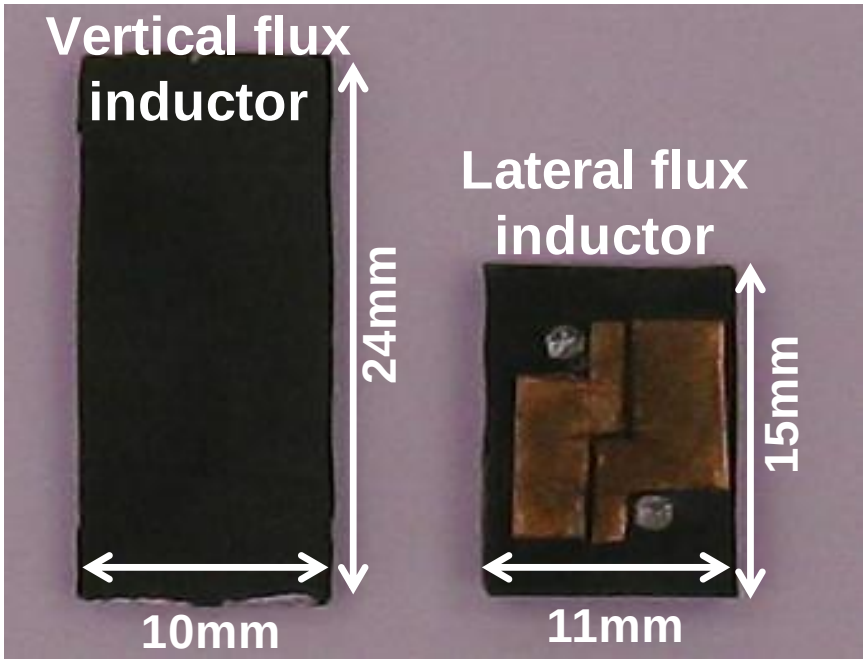

Figure 5.25 LTCC inductor prototypes

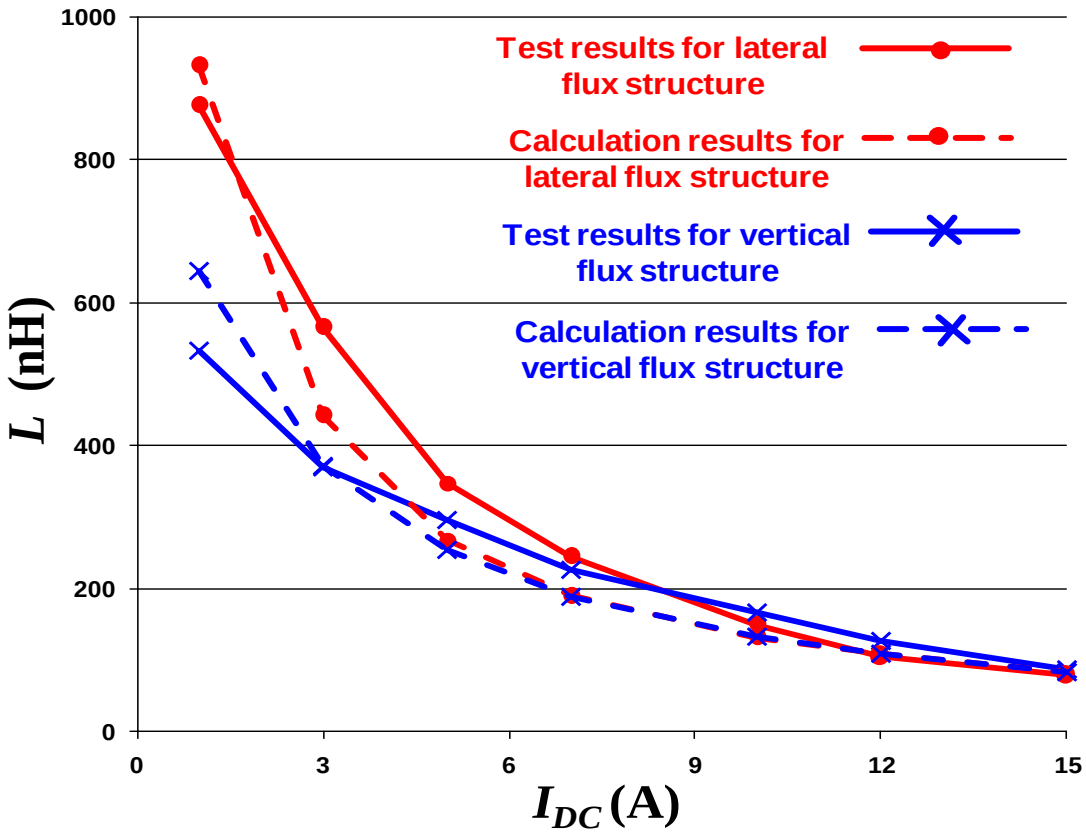

Figure 5.26 Inductance test and calculation results for LTCC inductor prototypes

DBC with two copper layers is used as active layer for this 3D integrated converter. Figure 5.27 shows the layout of this active layer. Two winding traces are built on bottom copper layer of DBC as the surface winding of LTCC inductor substrate. So, in LTCC fabrication, it only need use copper sheet to connect vias on the bottom side of inductor. The output ceramic capacitors are also put at the backside of this active layer to make the height of this converter more even. Bare die MOSFET devices are embedded into the ceramic layer of DBC. The input decoupling capacitor and driver both are put on the top of MOSFET devices to reduce parasitic inductance. By doing so, the switching loss of this integrated POL is reduced comparing with conventional POL, which has larger parasitic inductance. Furthermore, the thermal performance is also improved by embedding MOSFET into DBC layer. The prototype of this 3D integrated converter with LTCC inductor substrate is shown in Figure 5.28.

Figure 5.29 is the efficiency test result for this buck converter with different inductor substrates. This buck converter can have almost the same efficiency with these two inductor prototypes, and around 87% efficiency can be achieved with a 15A load current. The total thickness of this 3D integrated buck converter is around 6mm. If the lateral flux inductor prototype is used as a substrate, the converter footprint will be 165mm^2. So, the 3D integrated converter can achieve around 300W/in^3 power density with the lateral flux inductor substrate.

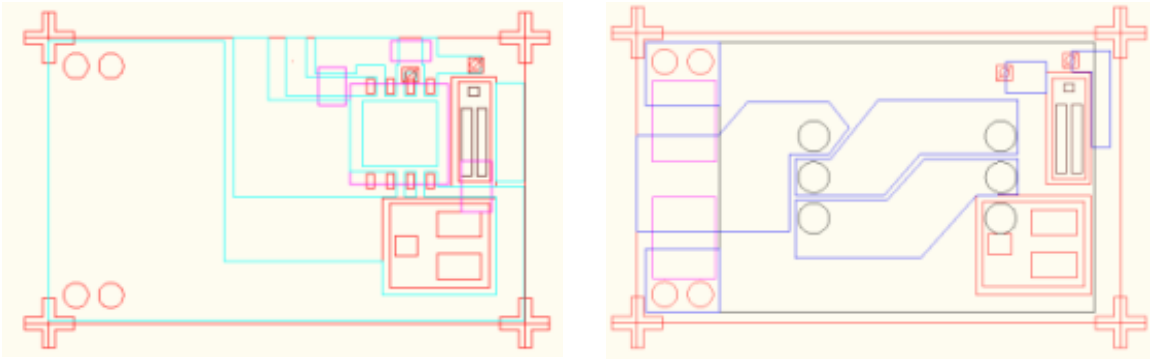

(a) (b)

Figure 5.27 Layout of active layer for 3D integrated POL: (a): top layer, (b) bottom layer

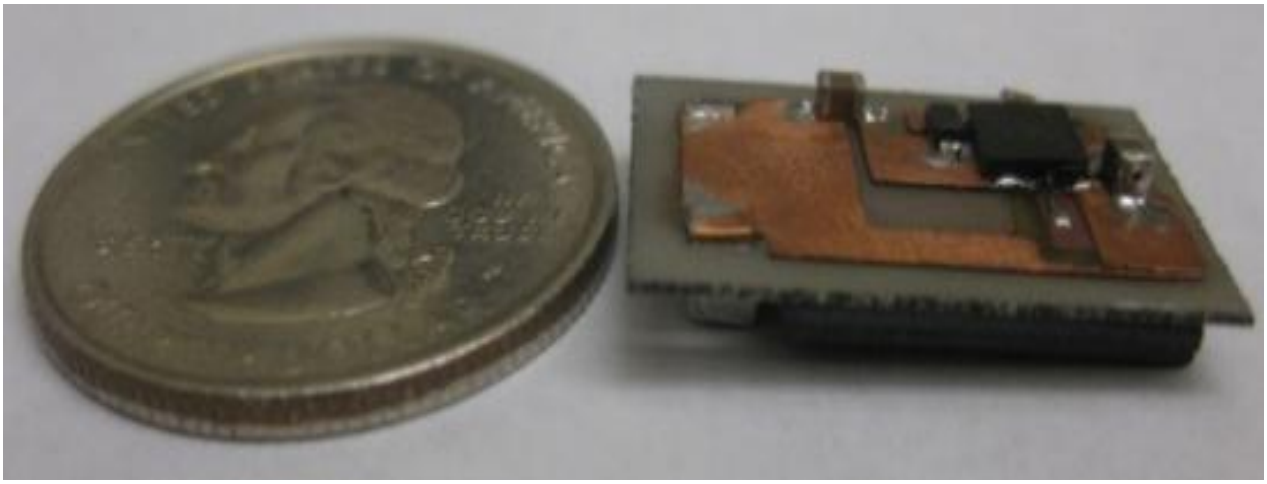

Figure 5.28 3D integrated POL with LTCC inductor substrate

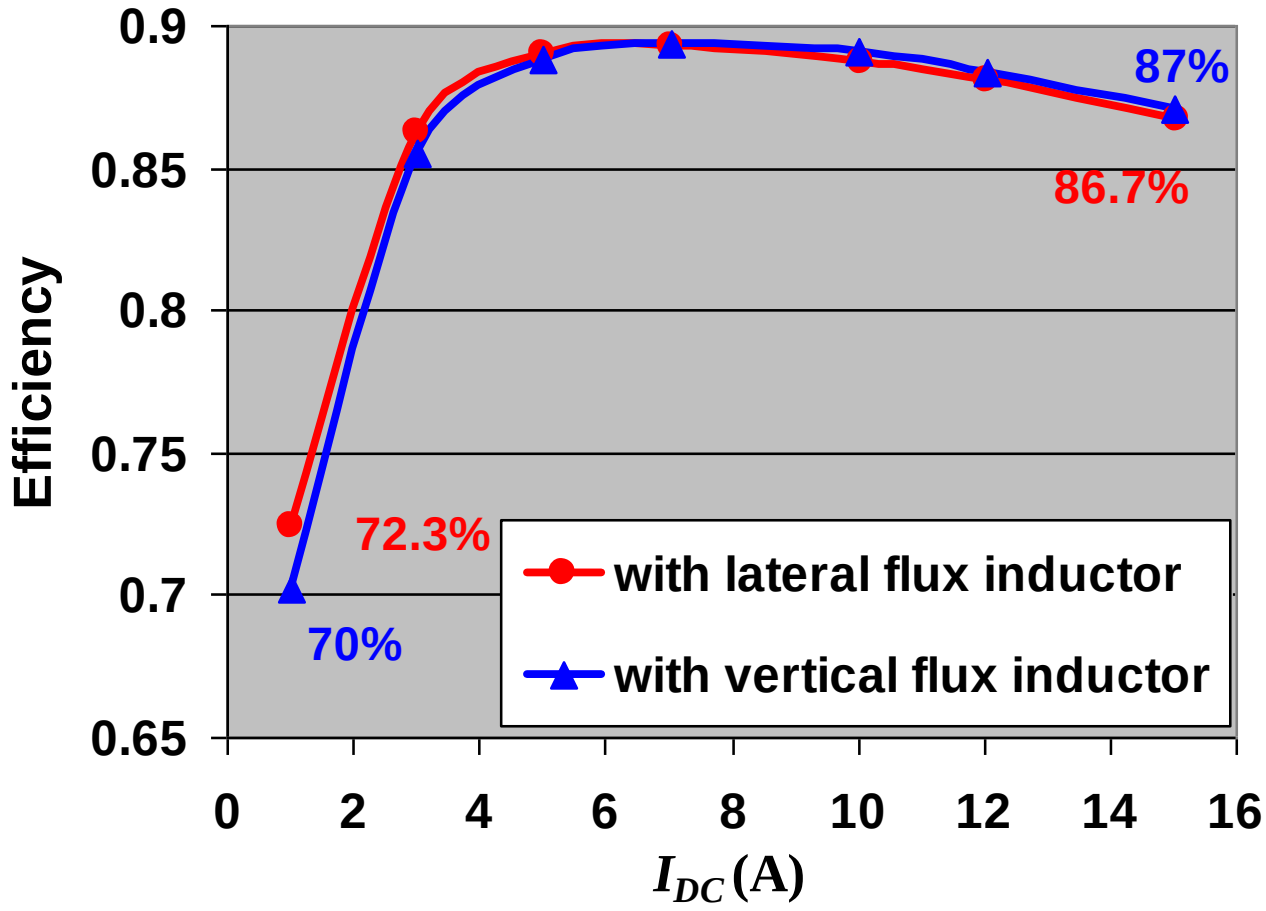

Figure 5.29 Efficiency of 3D integrated buck converter with different inductor substrates

5.4 Summary

In this chapter, different LTCC lateral flux inductors (single-turn and multi-turn structures) are compared first. The inductance density, winding loss, and core loss are all considered in the comparison. Comparing with the single-turn structure, the multi-turn structures have higher inductance density. However, this inductance increasing has some diminishing return. For core loss comparison, the conclusion is that with given core thickness, increasing turn number will increase the quality factor of core loss, which means that with the same inductance, increasing turn number will reduce core loss. However, for winding loss comparison, the conclusion is that with given core thickness, increasing turn number will reduce the quality factor of winding loss, which means that with the same inductance, increasing turn number will increase core loss. With some given core thickness, the total loss quality factor will be increased first when increase turn number but it will start to be reduced after some turn number. This optimal turn number for achieving the maximal total loss quality factor is related with inductor DC current. With large inductor DC current, the optimal turn number is small; with small inductor DC current, the optimal turn number is large. Then, a design method is also proposed for LTCC lateral flux inductor with non-uniform flux distribution. In this design method, inductor volume, core thickness, winding loss, and core loss are all considered. With the help of this design method, the LTCC lateral flux inductor can be optimized to achieve small volume, small loss and low profile at the same time. Several LTCC inductor substrates are also designed and fabricated for 3D integrated POL. comparing with the vertical flux inductor substrate, the lateral flux inductor substrate can save around 30% footprint. A 1.5MHz, 5V to 1.2V, 15A 3D integrated POL converter with LTCC lateral flux inductor substrate is demonstrated with 300W/in^3 power density, which has factor of 3 improvements comparing to today's industry products.

Chapter 6. LTCC Coupled-Inductor for Integrated Two-Phase POL

In chapter 5, a single phase integrated POL with LTCC inductor substrate has been demonstrated with 15A output current and 300W/in^3 power density. In order to further increase the current level and the power density, both the active stage and the passive inductor should be improved. By utilizing two layers of DBC to facilitate the active layer trace layout, the new active stage can be build with the smaller footprint. However, it is very difficult to further reduce the size of LTCC non-coupled inductor. Because the magnetic core should store large dc energy caused by dc current, it is very difficult to design a very small inductor for this high current application. As a result, the inductor is the major bottleneck for further increasing converter power density for high current application. Multi-phase converter with inverse coupled inductor is one possible method to solve this problem. Inverse coupled inductor has DC flux cancelling effect [86][87], so the magnetic core is no longer need to store large dc energy.

6.1 Overview of Coupled-Inductor

In 1998 the inverse coupled inductor was first proposed to use in multi-phase voltage regulator (VR) to improve converter efficiency without suffering transient performance. By using inverse coupled inductors between converter channels as shown in Figure 6.1(a), the converter will have larger equivalent inductances L_{eq1} in steady-state operation and smaller equivalent inductances L_{eq2} in transient response as shown in Figure 6.1(b). Actually, the larger equivalent inductances L_{eq1} is defined as steady-state inductance L_{ss}; and the smaller equivalent inductances L_{eq2} is defined as transient inductance L_{tr}. With these large L_{ss} but small L_{tr}, the

steady-state current ripples can be reduced without compromising the transient response. As a result, the overall efficiency of the converter is improved. Because of the coupling effect, the two inductors on two channels can no longer be considered as two individual inductors. A coupling inductance M between the two inductors can represent the coupling effect. For simplicity, the two inductances built on the same core are considered to be the same ($L_1=L_2=L_{self}$). If the coupling coefficient α in the inverse coupling case is defined to be negative, the coupling inductance M, steady-state inductance L_{ss}, and transient inductance L_{tr} can be calculated as:

$$M = \alpha \cdot L_{self} \tag{6.1}$$

$$L_{ss} = \frac{L_{self}^2 - M^2}{L_{self} + \frac{D}{1-D} M} \tag{6.2}$$

$$L_{tr} = L_{self} + M \tag{6.3}$$

In order to improve converter efficiency without suffering transient speed, the large ratio between steady-state inductance and transient inductance is preferred.

$$\frac{L_{ss}}{L_{tr}} = \frac{1-\alpha}{1+\frac{D}{1-D}\alpha} \tag{6.4}$$

Accord to (6.4), it can be known that the ratio between L_{ss} and L_{tr} is only determined by duty cycle D and coupling coefficient α. Because the duty cycle is determined by converter input and output voltage, only coupling coefficient α can be used to control the ratio between L_{ss} and L_{tr}. Figure 6.2 shows the ratio between L_{ss} and L_{tr} with different α. It can be seen that stronger coupling has larger ratio between L_{ss} and L_{tr}. As a result, previous coupled inductor design for VR application is normally choose α between -0.8 and -0.9.

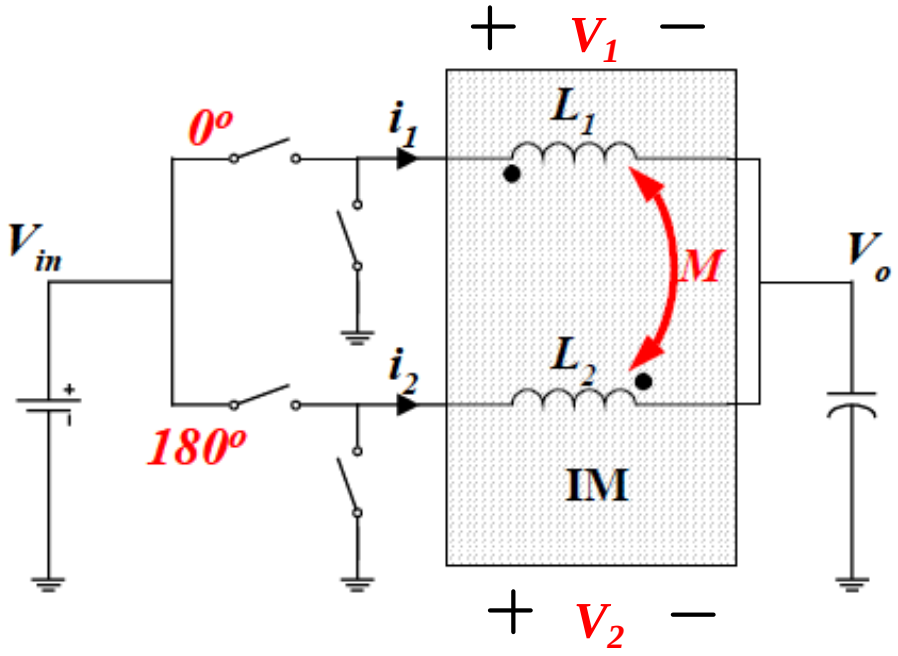

(a)

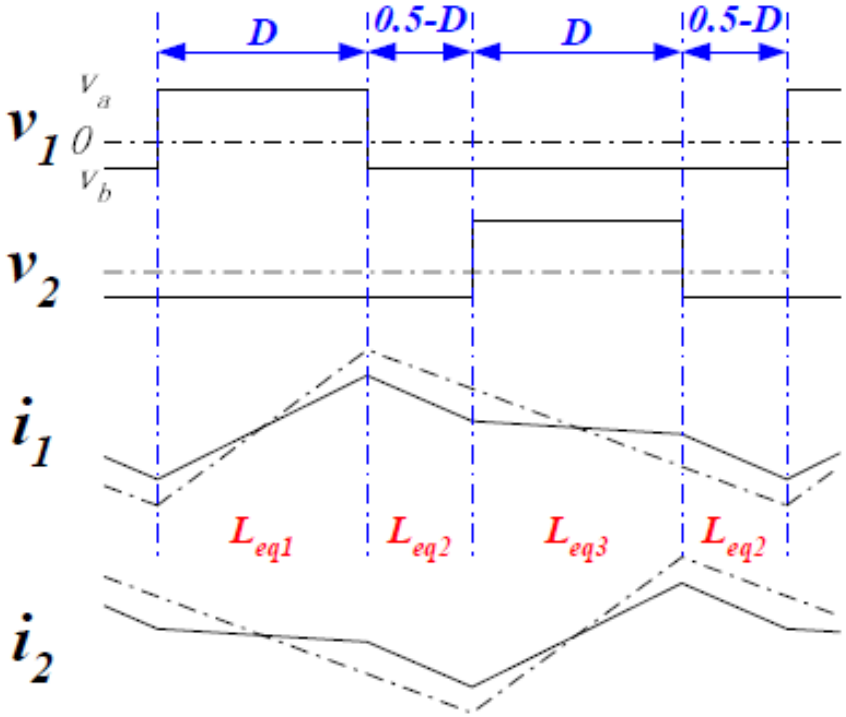

(b)

Figure 6.1 Two-phase buck with inverse coupled inductor: (a) circuit schematic drawing, (b) inductor current waveform and equivalent inductances

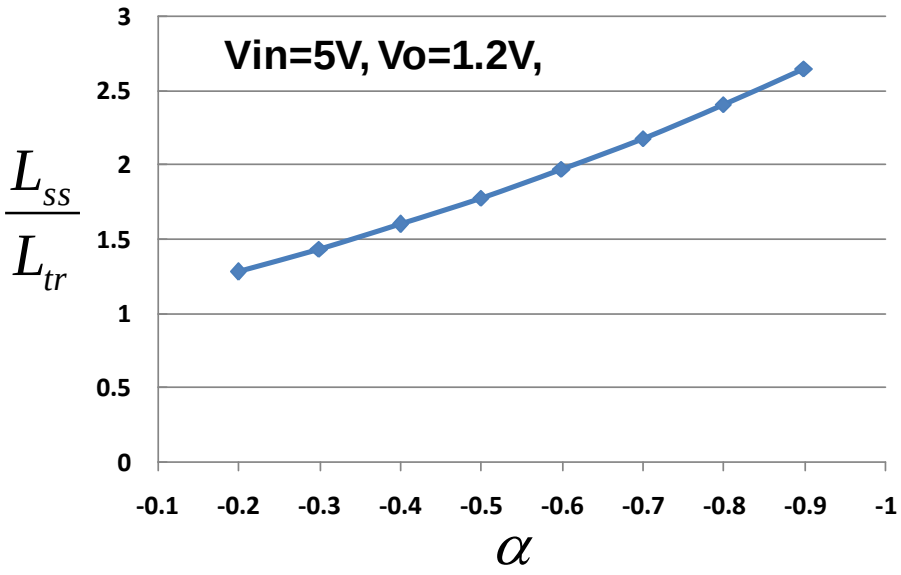

Figure 6.2 Ratio between L_{ss} and L_{tr} with different coupling coefficient α

Figure 6.3 shows the core structure and equivalent magnetic circuit of a discrete inverse coupled inductor. It can be seen that the magnetic fluxes generated by two phase currents cancel each other in the outer legs of the core. This flux cancellation effect will help to reduce coupled inductor size. The coupling coefficient α and dc flux ϕ_{dc} are impacted by reluctance R_{side} and R_{mid}, which are controlled by air gap g_{side} and g_{mid} [87]. α and ϕ_{dc} equations are written in the following

$$\alpha = -\frac{R_{mid}}{R_{side} + R_{mid}} \tag{6.5}$$

$$\phi_{dc} = \frac{N \cdot I_{dc}}{R_{side} + 2R_{mid}} \tag{6.6}$$

where, N is the turn number of coil, I_{dc} is the dc current.

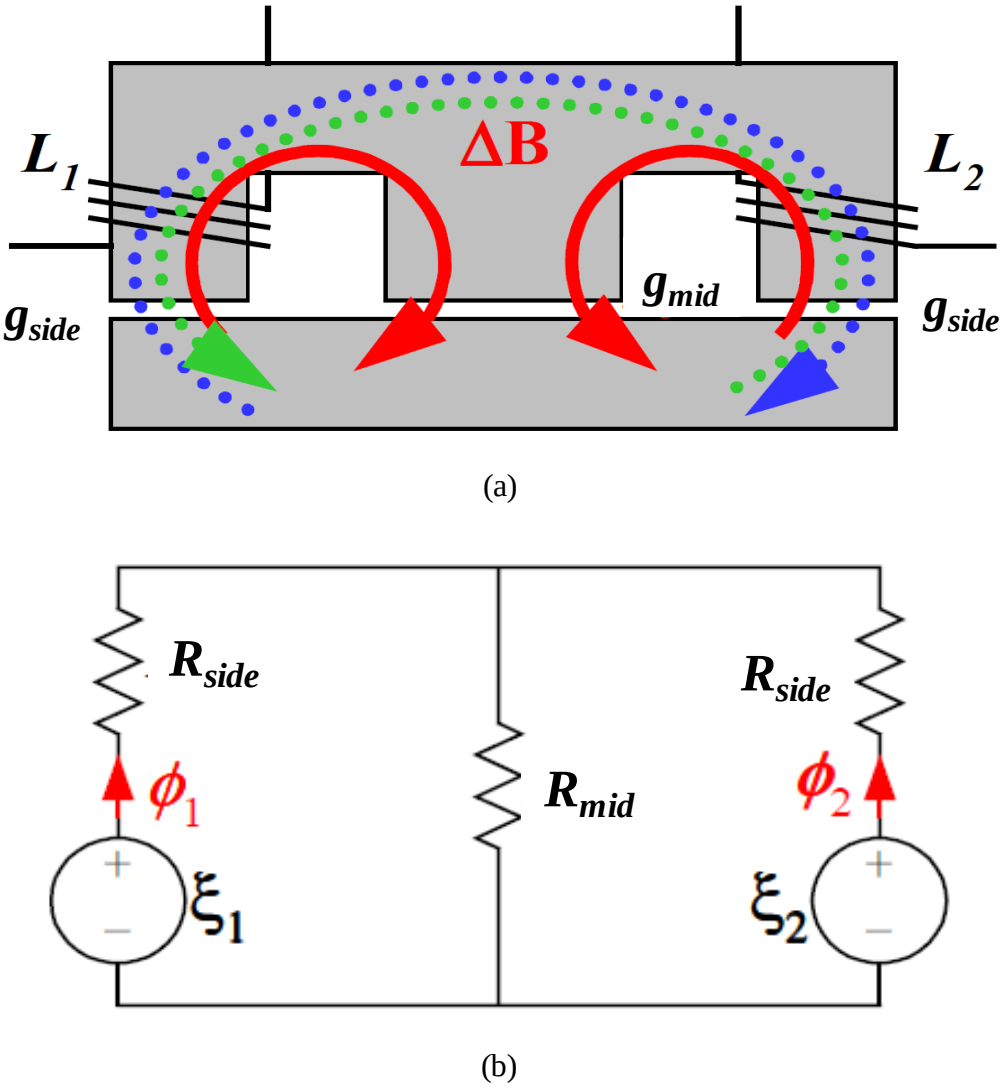

Figure 6.3 Discrete inverse coupled inductor: (a) core structure, (b) equivalent magnetic circuit

In order to further increase current level and power density for integrated POL, [26] proposed some LTCC coupled inductor substrate with vertical flux structure for 3D integrated POL. By using these LTCC vertical flux coupled inductor, the 3D integrated POL can achieve 40A output currant and 500W/in^3 power density. However, these LTCC vertical flux coupled inductors still have some limitations, such as too thick core thickness, complicate fabrication process and easily cracking. In this chapter, some low-profile LTCC coupled inductor with

lateral flux structures are proposed to help increasing power density of integrated POL and avoiding the problems of LTCC vertical flux coupled inductor. By careful designing the lateral flux coupled inductor, the core thickness is reduced to the half value of vertical flux coupled inductor thickness. As a result, the integrated POL with LTCC lateral flux coupled inductor can achieve power density as high as 700W/in^3.

6.2 LTCC Planar Coupled-Inductor for 3D Integration Applications

6.2.1 Vertical Flux LTCC Coupled-Inductor and Its Limitation

Figure 6.4 shows two possible LTCC vertical flux inverse coupled inductor structures: the top-and-bottom-winding coupled inductor structure (structure 1) and the side-by-side-winding coupled inductor structure (structure 2). From Figure 6.4, it can be seen that these LTCC coupled inductor structures don't have any air gap to control coupling. The coupling coefficient can be controlled by controlling dimension *d*. It can be seen that, the winding of structure 1 has larger aspect ratio than that of structure 2 due to the core thickness limitation. As a result, the magnetic mean path length of structure 1 normally is longer than that of structure 2, which means structure 2 is much more possible to have higher inductance density than structure 1.

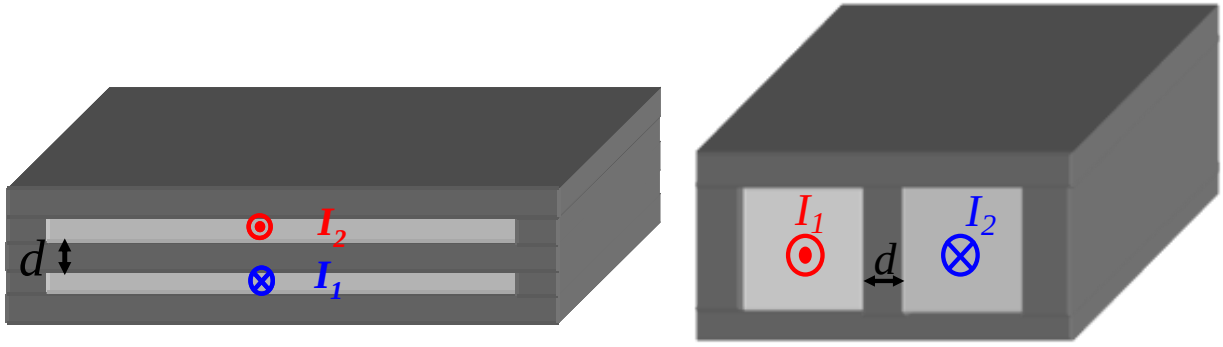

(a) (b)

Figure 6.4 LTCC vertical flux inverse coupled inductor structures:(a) top-and-bottom-winding structure (b) side-by-side-winding structure

Figure 6.5 shows the FEA 2D simulation results of dc flux density for LTCC integrated coupled inductor structure 2 with different *d* value. It can be seen that coupling coefficient is increased when reduces the gap between two inductor winding, which is defined as *d*. So, for this LTCC vertical flux coupled inductor, the parameter *d* can be used to control coupling coefficient. From Figure 6.5, it also can be seen that the dc flux distribution of LTCC integrated coupled inductor structure 2 is uniform in two areas: middle leg area and the other outer part area. So, coupled inductor structure 2 can be roughly divided into these two parts. Each area roughly operates at one B-H curve operating point and has one permeability value. In Figure 6.5, the location A on the LTCC core is used to represent the whole outer part core area. The operation point of location A on B-H curve with different coupling coefficient is shown in Figure 6.6. It can be known that the dc flux density of location A (representing the whole outer part core area) is also reduced when reduces *d* to increase inverse coupling coefficient. This is because the stronger inverse coupling has more dc flux cancellation. As a result, the LTCC core will have larger permeability when coupled inductor has stronger coupling, which is a potential benefit for increasing inductance density.

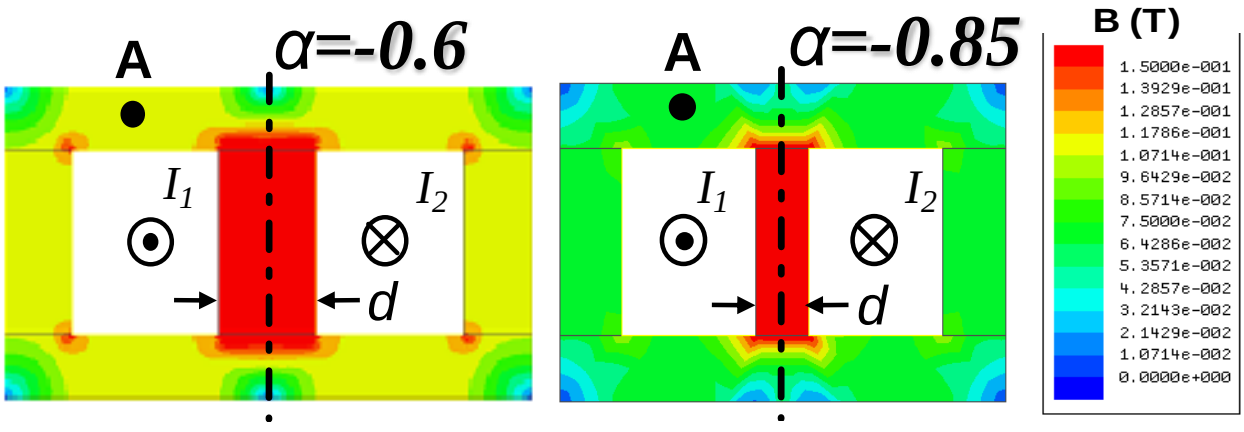

Figure 6.5 FEA 2D simulation results of dc flux density for LTCC integrated coupled inductor structure 2

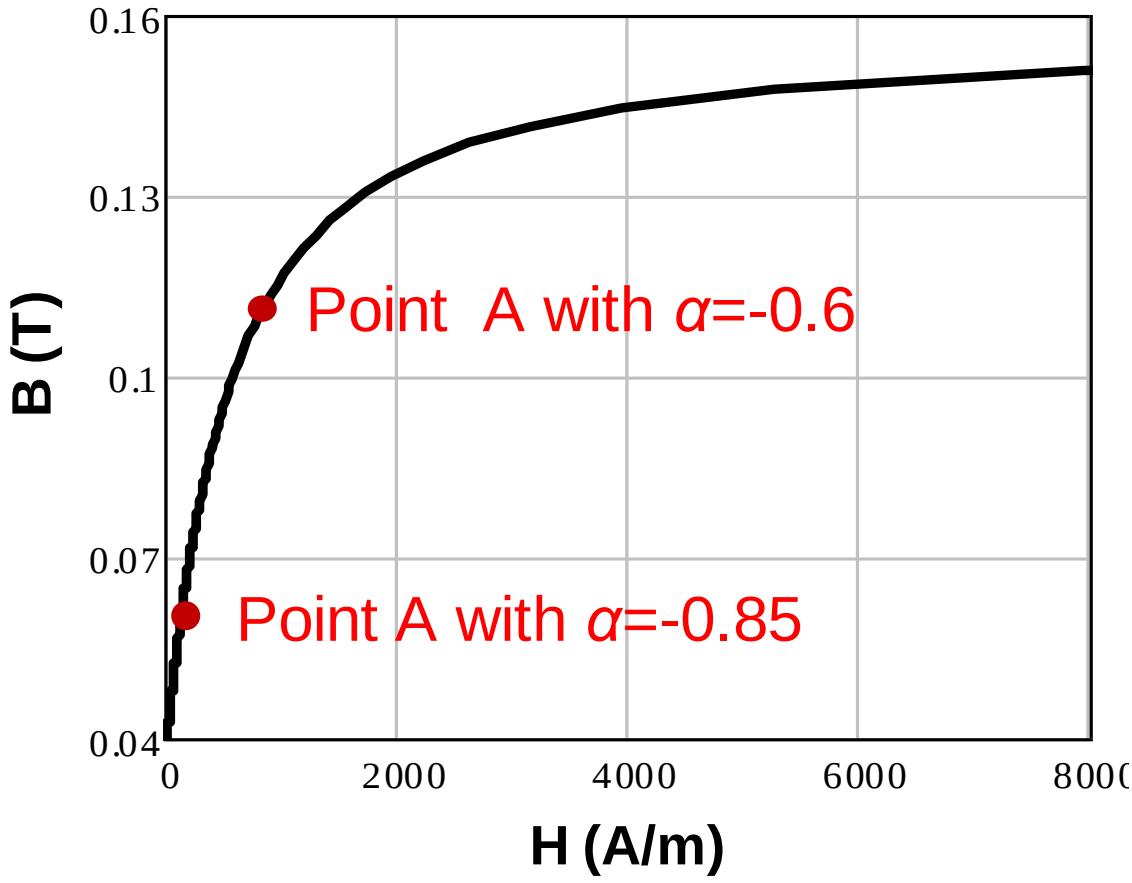

Figure 6.6 The operation point of location A on B-H curve

Figure 6.7 (a) is the prototype of LTCC vertical flux coupled inductor structure 1. Figure 6.7 (b) is the prototype of LTCC vertical flux coupled inductor structure 2. It can be known that the structure 2 can have smaller footprint than structure 1. Figure 6.8 shows some major fabrication steps for low-profile LTCC vertical flux coupled inductor structure 2: 1) laminate LTCC bottom layer; 2) laminate LTCC middle layer with slots; 3) screen print silver paste inside slots to build coils; 4) laminate top LTCC layer; 5) sinter inductor around 900^{o}C.

Actually, the fabrication process for vertical flux structure is not very easy. Several steps need to be taken care very carefully; otherwise, vertical structure is very easy to be cracked during sintering. First, many small holes should be drilled on the surface to help dissipating air

during sintering (see Figure 6.7); Second, the outer leg width w_1 (see Figure 6.8) cannot be designed very small. Figure 6.9 shows the side view for two LTCC vertical flux coupled inductor prototypes with different w_1 value. It can be seen that there is very serious cracking with smaller w_1. In order to avoid this cracking, the w_1 value need be increased to 2mm at least, which will increase inductor footprint.

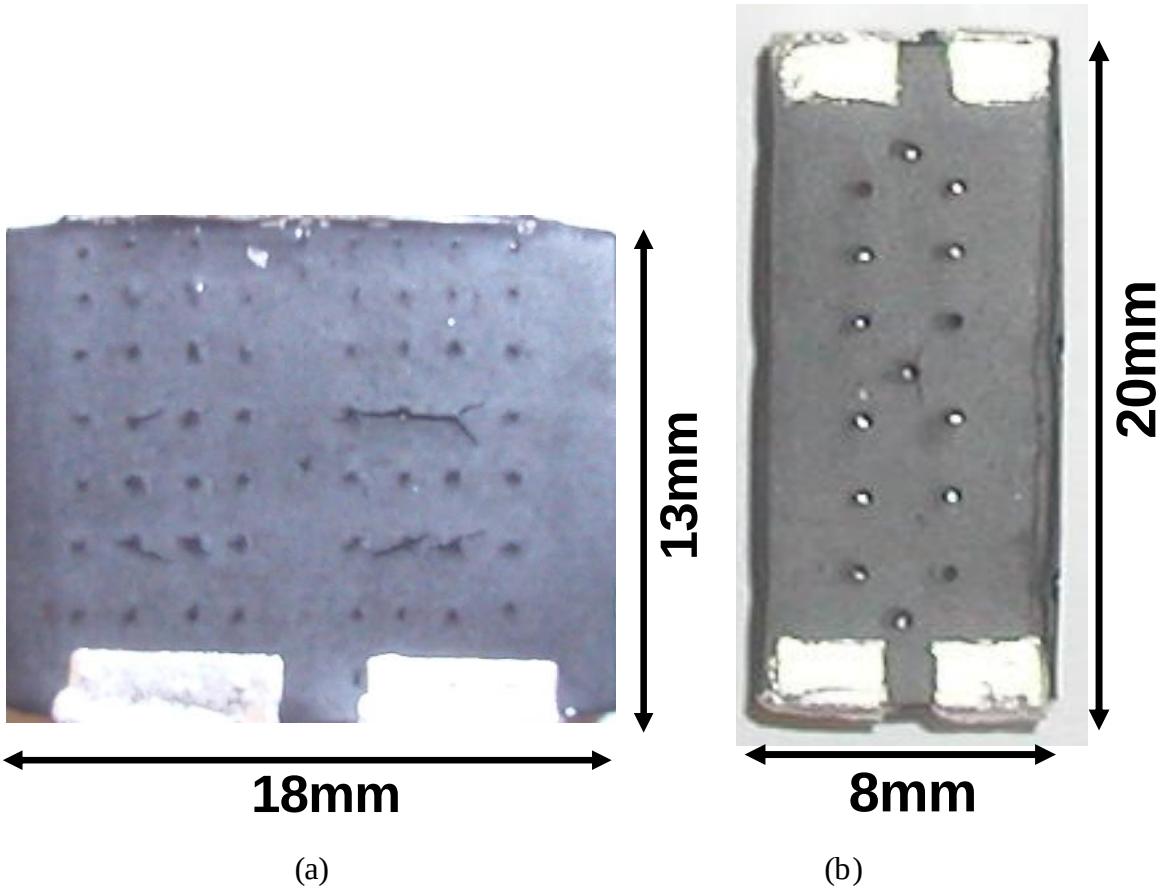

Figure 6.7 The prototype of LTCC vertical flux coupled inductors: (a)top-and-bottom-winding structure, (b)side-by-side-winding structure

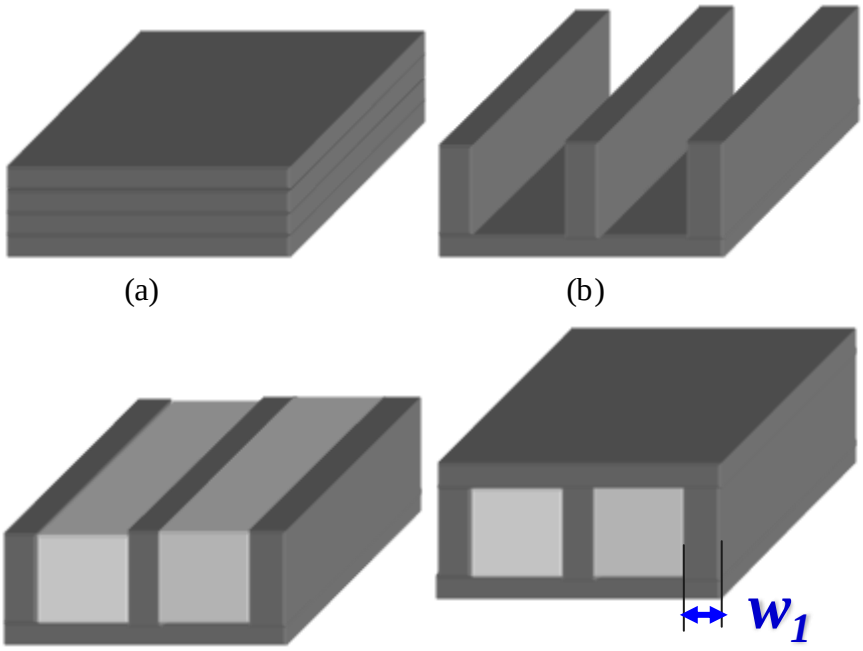

Figure 6.8 Major fabrication steps for low-profile LTCC vertical flux coupled inductor structure 2:(a) step 1, b) step 2, c) step 3, d) step 4

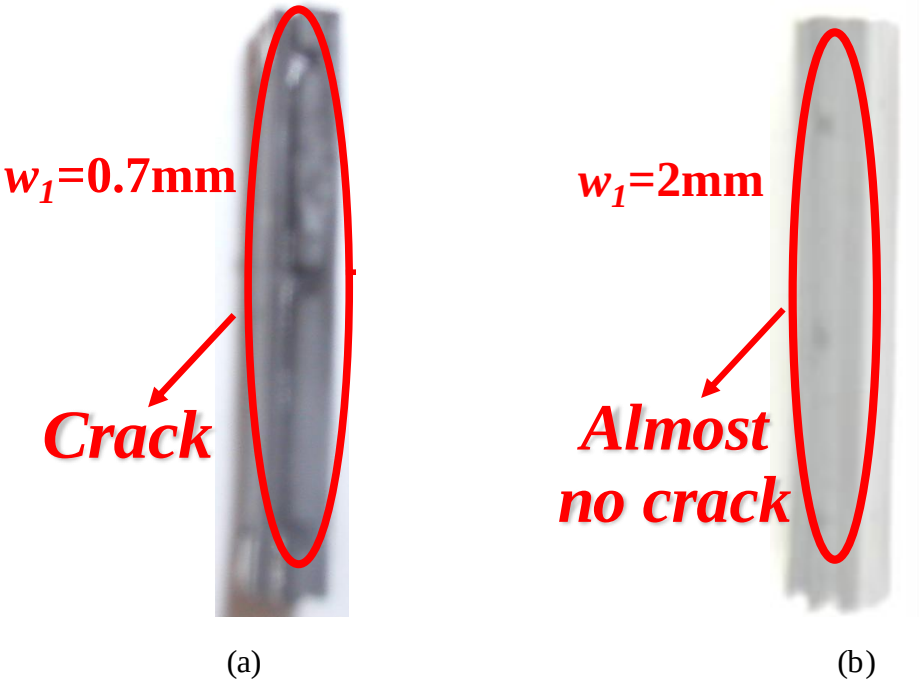

Figure 6.9 Side view for two LTCC vertical flux coupled inductor prototypes with different w_1 value: (a) w_1=0.7mm, (b) w_2=2mm

Besides the complicate fabrication process, another drawback of vertical flux coupled inductor is the core thickness cannot be designed to be very thin. The core thickness of the LTCC vertical flux coupled inductor prototypes shown in Figure 6.7 (b) is 3.4mm, which is not very good for 3D integration. The reason for this thick core design is mainly because that it is not easy to get strong coupling with thin core structure for vertical flux coupled inductor. Figure 6.10 shows the core structure and equivalent magnetic circuit for vertical flux coupled inductor with different core thickness. Where, the R_c, R_1, and R_2 represent magnetic reluctance for each core part. The coupling coefficient is impacted by these reluctances as:

$$|\alpha| = \frac{R_C}{R + R_C} = \frac{1}{\frac{R}{R_C} + 1} \tag{6.7}$$

where, $R = 2R_1 + R_2$

From Figure 6.10 it can be known that reducing core thickness t will reduce R_c but increase R. As a result, it will reduce coupling coefficient. In order to reduce the impact of core thickness on coupling coefficient, the vertical flux structure can turn 90 degree to become a lateral flux structure. Figure 6.11 shows the core structure and equivalent magnetic circuit for a lateral flux coupled inductor with different core thickness. From Figure 6.11 it can be known that reducing core thickness t will reduce R_c and R together, even with the same ratio. As a result, the core thickness will not impact coupling coefficient a lot with lateral flux coupled structure. So, the lateral flux coupled inductor can be designed with very low profile without suffering coupling coefficient.

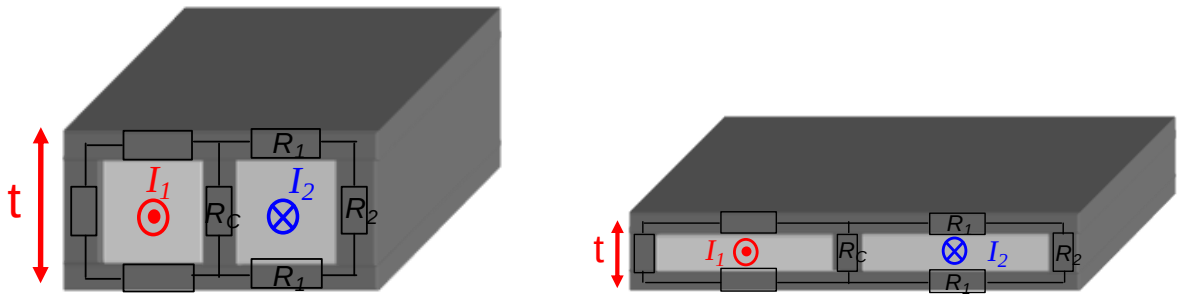

(a) (b)

Figure 6.10 Core structure and equivalent magnetic circuit for vertical flux coupled inductor with different core thickness: (a) thick core, (b) thin core

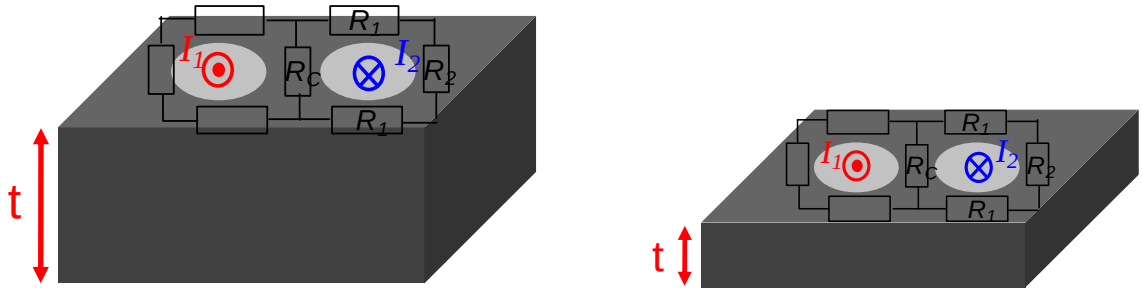

(a) (b)

Figure 6.11 Core structure and equivalent magnetic circuit for lateral flux coupled inductor with different core thickness: (a) thick core, (b) thin core

6.2.2 Lateral Flux LTCC Coupled-Inductor

Figure 6.12 shows top view of 3 different lateral flux inverse coupled inductor structures. The blue dots represent the embedded coils; the solid lines represent the top surface windings; the dash lines represent the bottom surface windings. Figure 6.12(a) is a single-turn lateral flux structure for each inductor. Figure 6.12(b), (c) and (d) all are two-turn lateral flux structure for each inductor. Coupling coefficient of these lateral flux structures all can be controlled by controlling dimension *d*. Inductor structure 1 with two-turn coil (N=2) is the extension of inductor structure 1 with single-turn coil (N=1). Actually, the two-turn coil structure can be further extended to any number turn structures, such as three-turn coil (N=3) and 4-turn coil

(*N*=4) structures. With this structure, all the flux of one inductor has some coupling effect with the flux of another inductor. This is the key difference between structure 1 and structure 2, which only has coupled flux in the middle part. The flux around coil vias on the two sides of structure 2 is not coupled. So, there is no dc flux cancellation effect on the two sides of structure 2, which is not good for high inductance density design. For structure 3, it has interleaved coils between two inductors. The interleaved coils may help increasing coupling between two inductors, but it will reduce the coupling between coils inside the each inductor, which will reduce self inductance. So, the structure 3 is not very suitable for coupled inductor but it is a good candidate for transformer design. So, lateral flux coupled inductor structure 1 is chosen for further study and discussion.

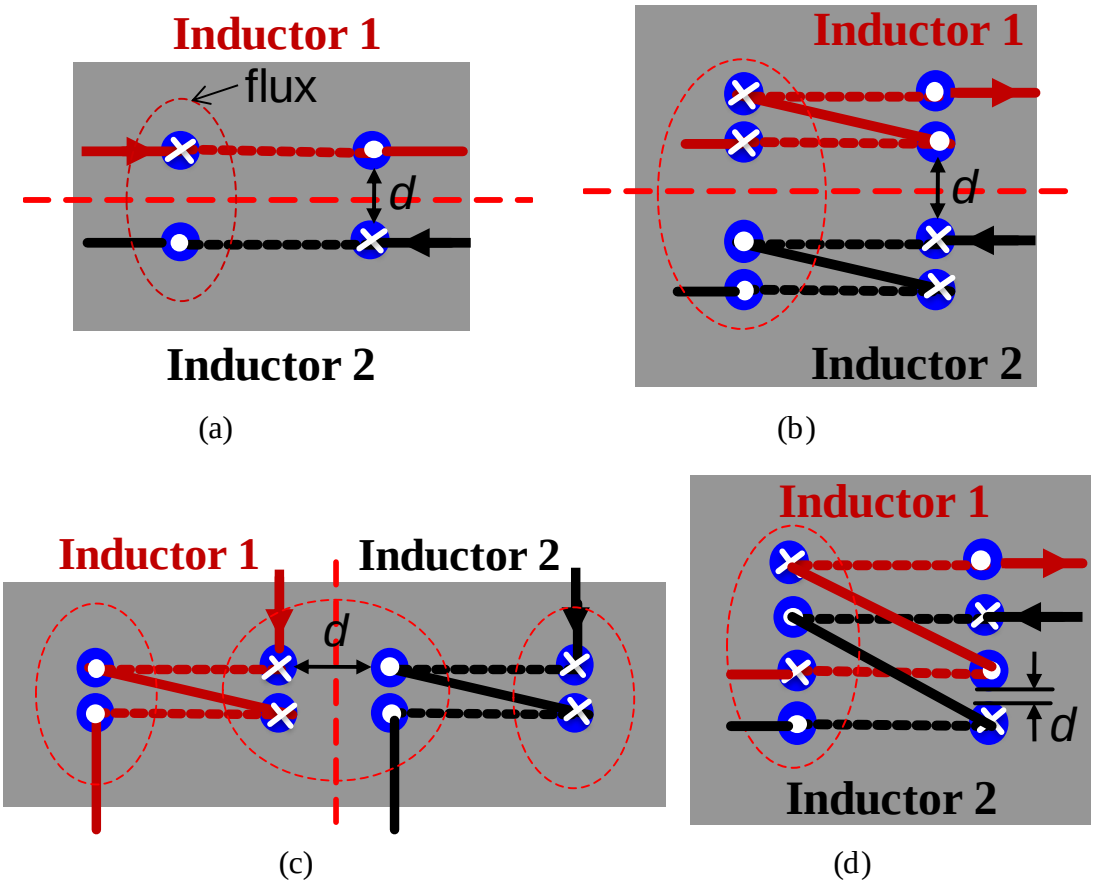

Figure 6.12 Top view of 3 different lateral flux inverse coupled inductor structures: (a) structure 1 with *N*=1, (b) structure 1 with *N*=2, (c) structure 2, (d) Structure 3

Figure 6.13 shows the FEA 2D simulation results of DC flux density for LTCC lateral flux coupled inductor structure 1 with two-turn coil. It can be seen that 1) for lateral flux coupled inductor, the DC flux density also will be reduced when increasing coupling coefficient by reducing *d*. 2) the flux distribution of LTCC lateral coupled inductor is very non-uniform. So, it is very difficult to build a reluctance model to help designing lateral flux coupled inductor. As a result, Maxwell FEA simulation is used to help designing this LTCC lateral flux coupled inductor.

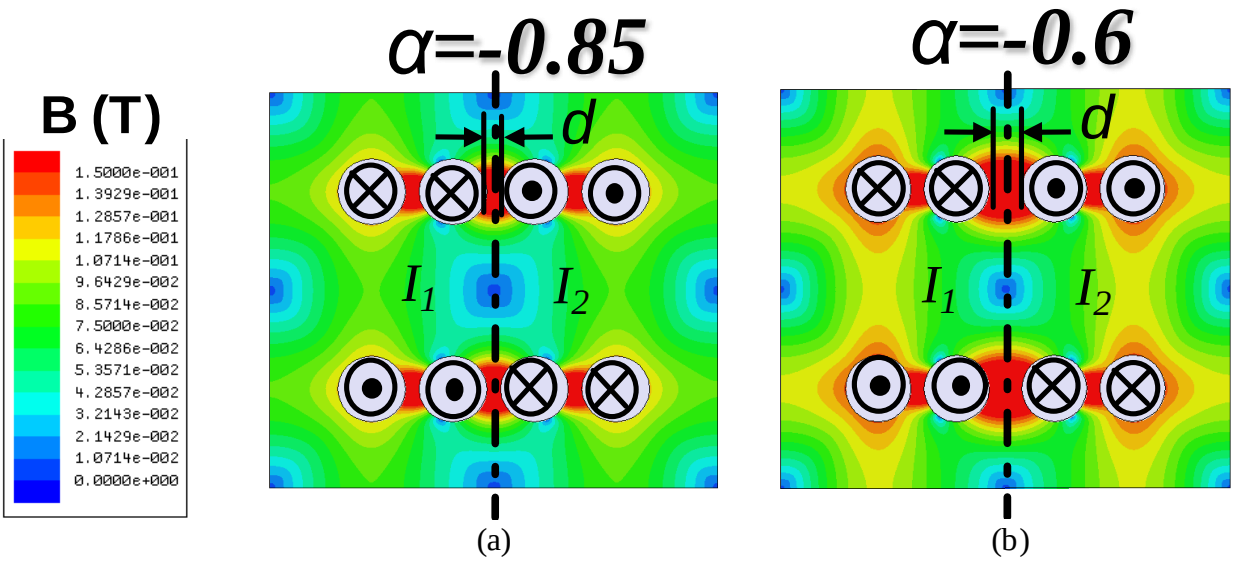

Figure 6.13 FEA 2D simulation results of DC flux density for LTCC lateral flux coupled inductor structure 1 with two-turn coil: (a) *d*=0.4mm, (b) *d*=1mm

6.3 Numerical Inductance Model (FEA Simulation) for LTCC Coupled-Inductor

The LTCC lateral flux coupled inductors are used as an example to illustrate the FEA simulation method. Figure 6.14 shows the FEA 3D model for these lateral flux coupled inductors. Blue cylinders represent via filled with silver; Yellow bars represent the two copper

windings on the bottom surface. Ansoft®'s Maxwell 12 is used to do simulation. In this FEA simulation, there are two things need to be considered at the beginning:

1) The impact of AC current ripple on inductor coupling. The inductor current has AC ripple, which has non-uniform distribution in via and surface winding. These non-uniform distributed AC current will impact the coupling between two inductors.

2) The non-linear B-H curve of LTCC ferrite material.

In order to consider the impact of AC current, it is better to use eddy current solver to simulate this coupled inductor. However, the eddy current solver doesn't support material with non-linear B-H curve. The magneto static solver can support non-linear B-H curve, but it only simulate with DC current. After comparing two simulation solvers, the magneto static solver is chosen to do simulation. The reason is that although the non-uniform distributed AC current will impact coupling effect, its impact is not very huge. Figure 6.15 shows the FEA simulation results of self inductance L_{self}, mutual inductance M and transient inductance L_{tr} with two simulation solver for lateral flux coupled inductor with constant permeability. In these simulations, the via radius r_v=0.6mm, core thickness h=2mm, d=0.4mm, g=4mm, the relative permeability of core is μ_r=100. The eddy current solver is simulated with 1MHz, 3MHz and 5MHz AC current. It can be known that the difference between eddy current simulation results and magneto static simulation results are very small. So, for 1MHz-5MHz application, the impact of non-uniform distributed AC current on coupling effect can be ignored and the magneto static simulation can be used to study coupled inductor.

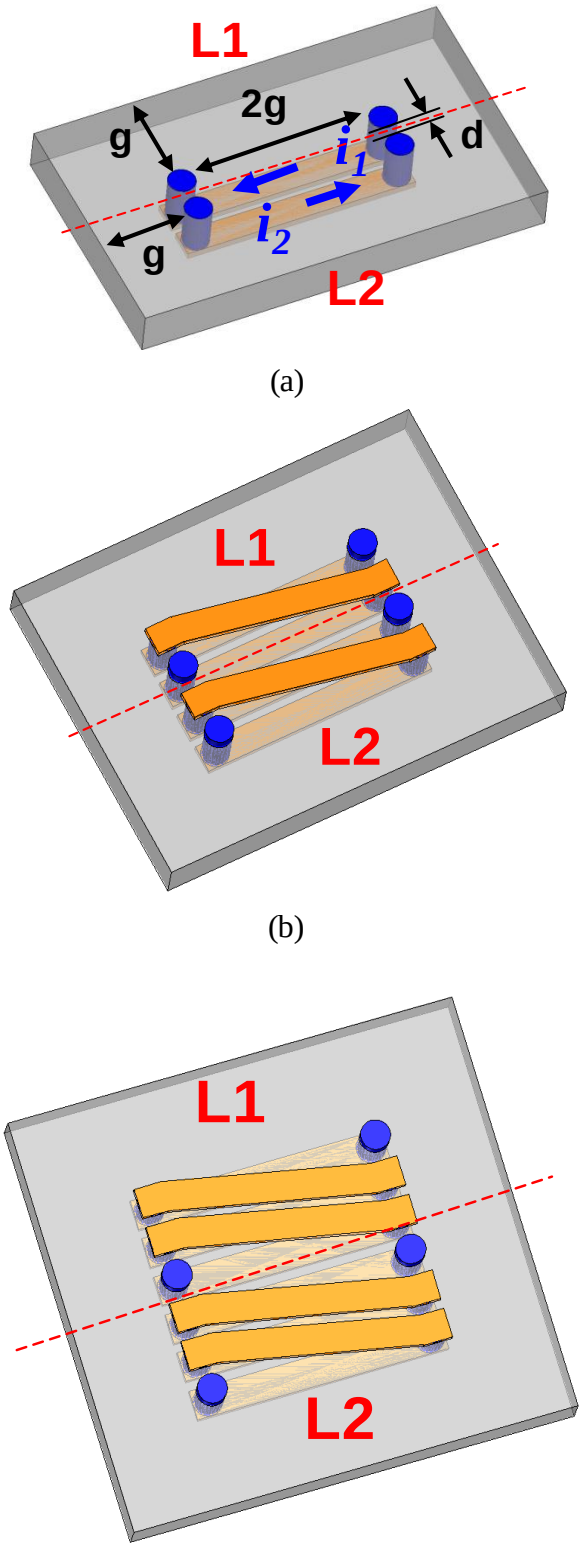

Figure 6.14 FEA 3D models for lateral flux coupled inductors: (a) single-turn structure, (b) two-turn structure, (c) three-turn structure

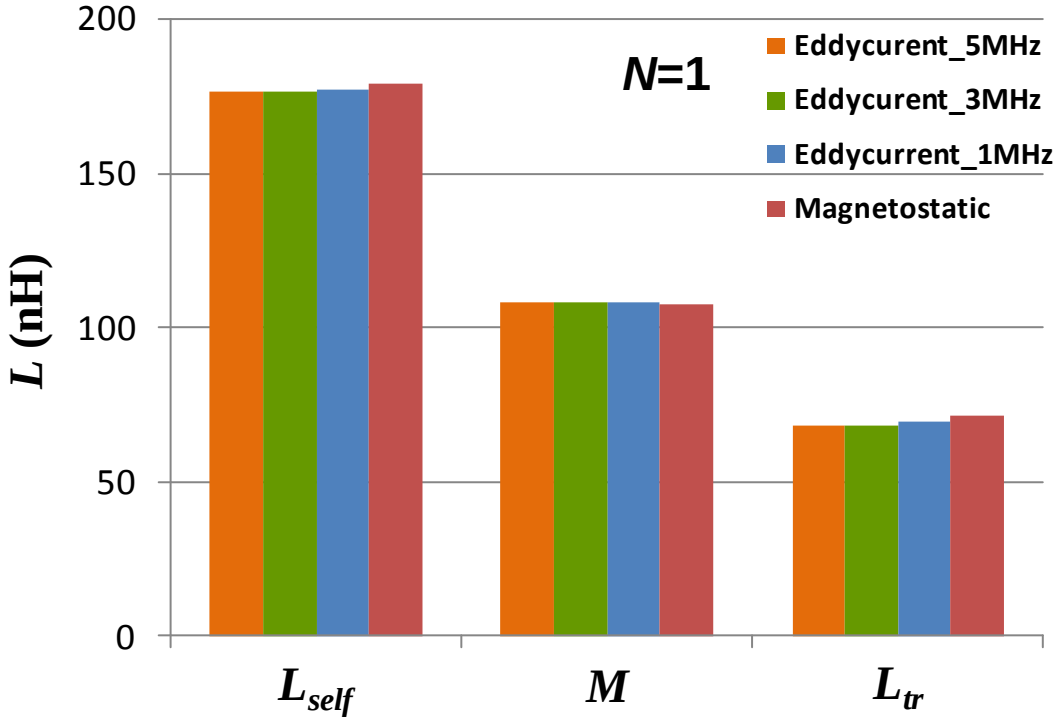
N=1
Eddycurent_5MHz
Eddycurent_3MHz
Eddycurrent_1MHz
Magnetostatic
L (nH)
200
150
100
50
0
L_{self}
M
L_{tr}

(a)

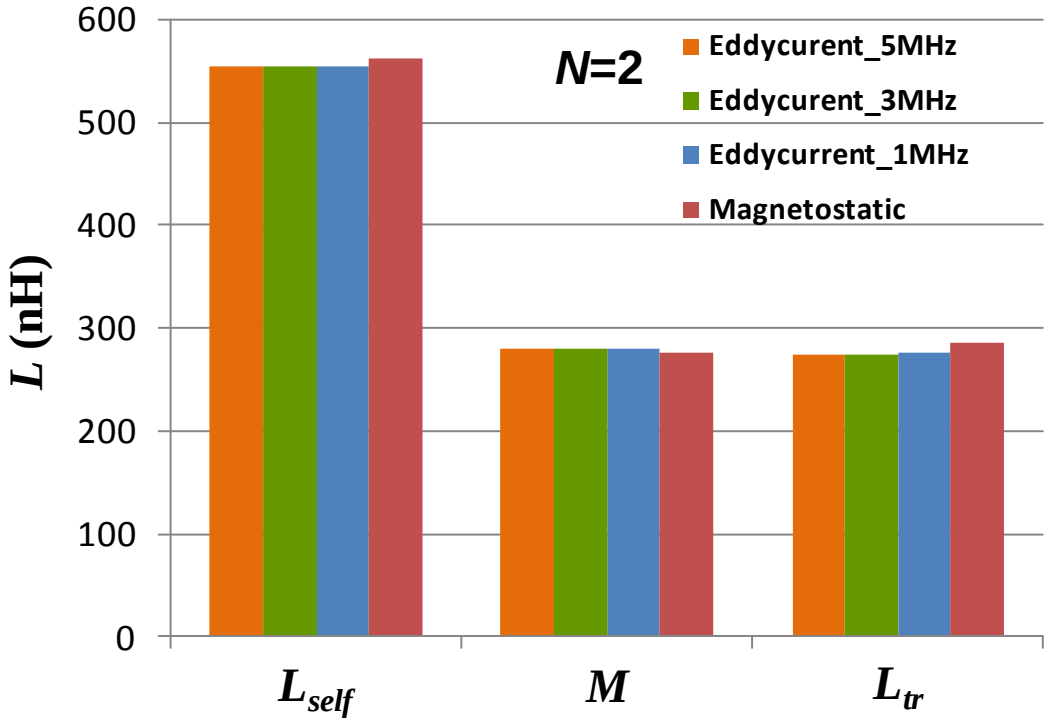
N=2
Eddycurent_5MHz
Eddycurent_3MHz
Eddycurrent_1MHz
Magnetostatic
L (nH)
600
500
400
300
200
100
0
L_{self}
M
L_{tr}

(b)

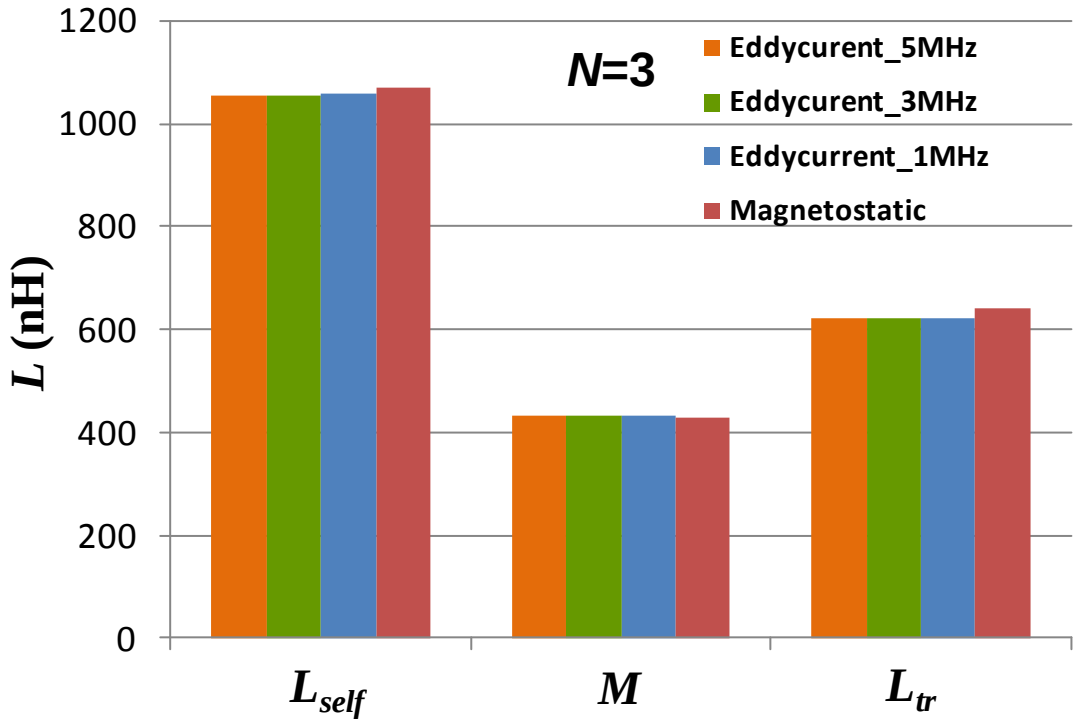

(c)

Figure 6.15 FEA 3D simulation results of inductance for lateral flux coupled inductors: (a) single-turn structure, (b) two-turn structure, (c) three-turn structure

Because LTCC ferrite has non-linear B-H curve, the FEA simulation for LTCC coupled inductor also need two steps just like FEA simulation for LTCC non-coupled inductor. First, the two coils of coupled inductor are both excited by DC current as $i_1=i_2=I_{DC}$. After computing static magnetic field, the Flux linkage can be calculated. The result of this flux linkage of i_1 is notated as ψ_{11} and flux linkage of i_2 is notated as ψ_{21}. Then, one coil of the coupled inductor is excited by given DC current I_{DC} plus a small perturbation Δi, but another coil still excited by given DC current I_{DC}. So $i_1= I_{DC}+\Delta i$ and $i_2=I_{DC}$ After computing static magnetic field again, the flux linkage of i_1 is notated as ψ_{12} and flux linkage of i_2 is notated as ψ_{22}. After these two steps, the self inductance and mutual inductance of this inductor can be calculated as:

$$L_{self} = \frac{\Delta\psi_1}{\Delta i_1} = \frac{\psi_{12} - \psi_{11}}{\Delta i_1} \tag{6.8}$$

$$M = \frac{\Delta\psi_2}{\Delta i_1} = \frac{\psi_{22} - \psi_{21}}{\Delta i_1} \tag{6.9}$$

This two steps magneto static FEA simulation can be used for both 3D and 2D model. The 2D model for lateral flux single-turn coupled inductor is shown in Figure 6.16. Comparing with the 3D model shown in Figure 6.14(a), the 2D model ignores the surface winding.

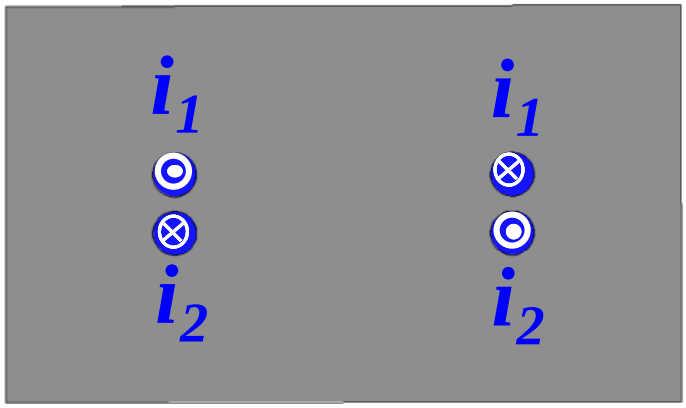

Figure 6.16 FEA 2D model for lateral flux single-turn coupled inductor

Figure 6.17 shows the FEA simulation results of self inductance L_{self} and mutual inductance M with 3D magneto static and 2D magneto static simulation for lateral flux single-turn coupled inductor. In these simulations, the via radius r_v=0.6mm, core thickness h=2mm, d=0.4m, I_{DC}=20A. It can be known that for single-turn structure the difference between 3D simulation results and 2D simulation results are very small.

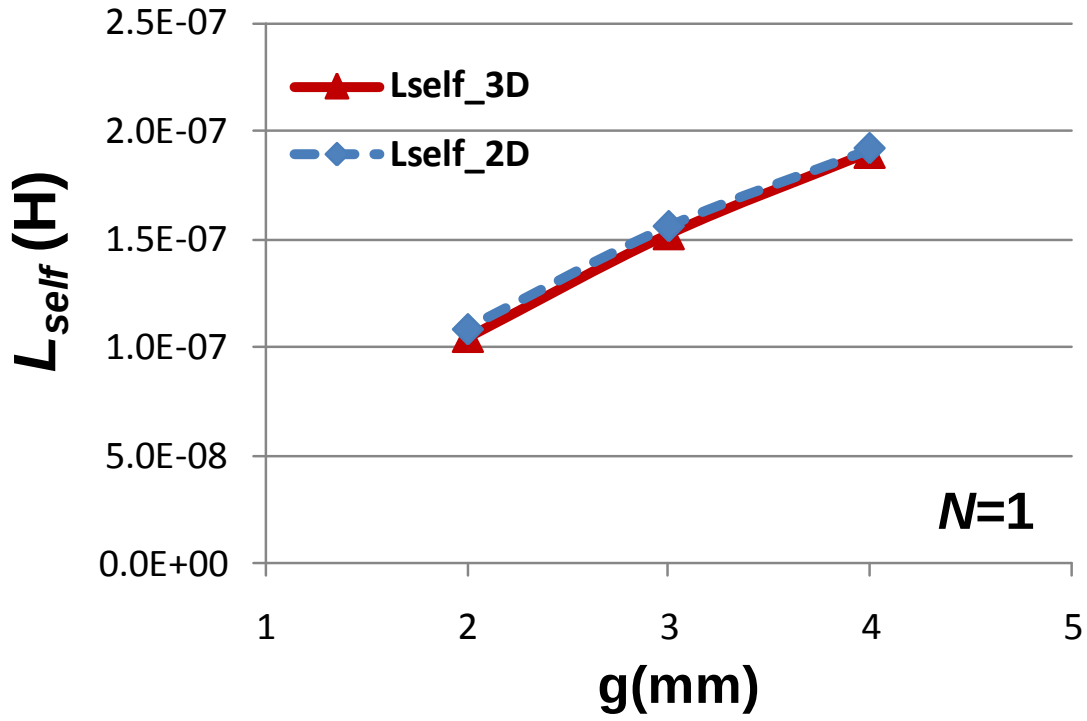

(a)

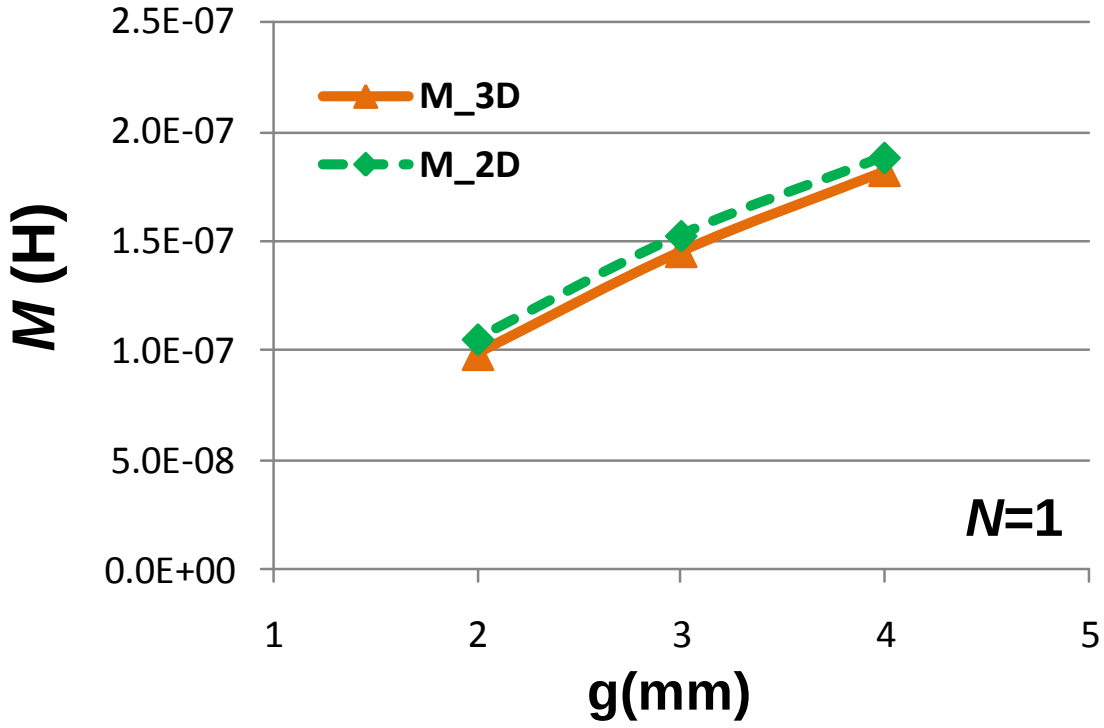

(b)

Figure 6.17 Magneto static 3D and 2D simulation results of inductance for lateral flux single-turn coupled inductor: (a) self inductance L_{self}, (b) mutual inductance M

6.4 Basic Study for LTCC Lateral Flux Coupled Inductor

Figure 6.18 shows the simulation results of coupling coefficient with different dimension of LTCC lateral flux single-turn coupled inductor. In these simulations, via radius r_v=1mm, core thickness h=1mm, I_{DC}=20A. It can be seen that, just like LTCC vertical flux coupled inductor, when increasing d, the coupling coefficient of lateral flux coupled inductor will decrease. Besides the dimension d, the dimension g also will impact coupling coefficient. Increasing g will increase coupling coefficient. However, in real design, g normally is much larger than d, so dimension g can be used to control the footprint first. Then, with given g value, dimension d can be used to control the coupling coefficient. The relationship between g and inductor footprint of structure 4 is shown in the following

$$Footprint = (4 \cdot g + 4 \cdot r_v) \cdot (2 \cdot g + 8 \cdot r_v + d) \approx (4 \cdot g + 4 \cdot r_v) \cdot (2 \cdot g + 8 \cdot r_v) \quad (6.10)$$

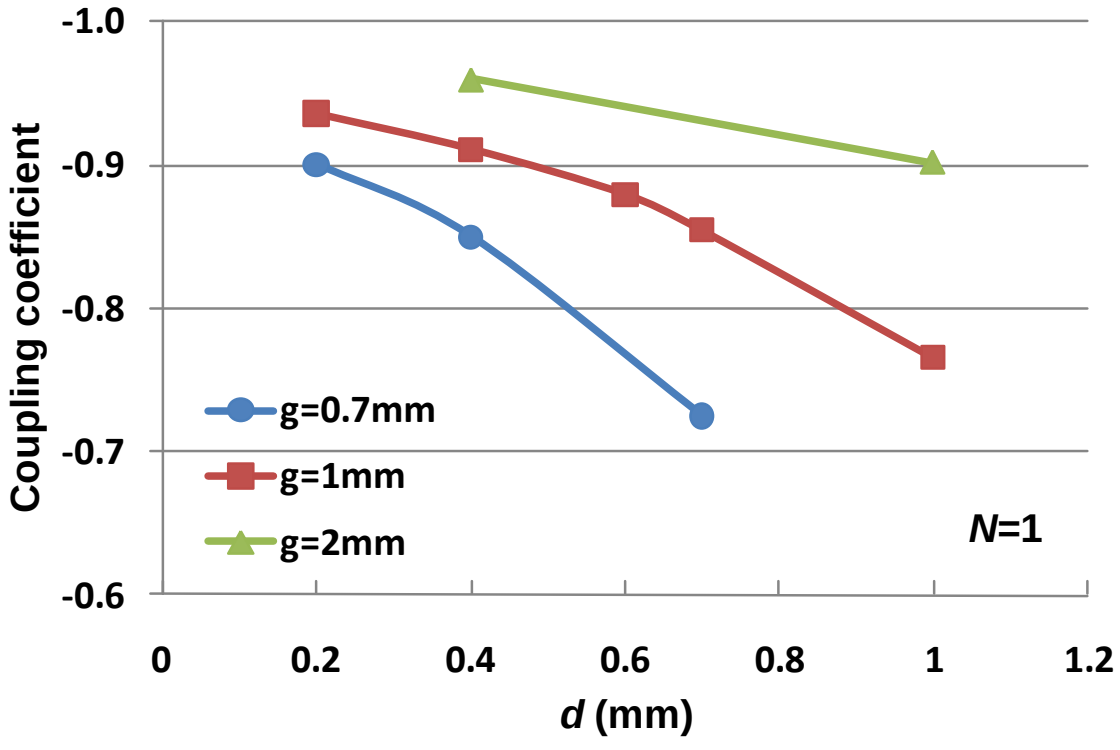

Figure 6.18 FEA simulation results of coupling coefficient for LTCC lateral flux single-turn coupled inductor

In Figure 6.14, the via of lateral flux coupled inductors is designed as round shape. Actually, the via also can be designed as square or rectangular shape. Figure 6.19 shows the half core of single-turn lateral flux coupled inductors with different via shape but the same via cross-section area. Figure 6.20 shows the FEA 2D simulation results of steady state inductance *Lss* density for these lateral flux coupled inductor structures. In these simulations, via cross-section area is 3mm^2, core thickness h=1mm, g=0.7mm, I_{DC}=20A. For rectangular via case 1, w=2mm, e=1.5mm. For rectangular via case 2, w=1.5mm, e=2mm. Different d values are used to give different coupling coefficients. The L_{ss} calculation is based on (6.2), and the duty cycle is D=0.24. It can be seen that among these different via shapes, the round shape can give the highest L_{ss} density to help reducing the size of coupled inductor. So, the round shape via is chosen for lateral flux coupled inductor design. The following studies are all based in round shape via.

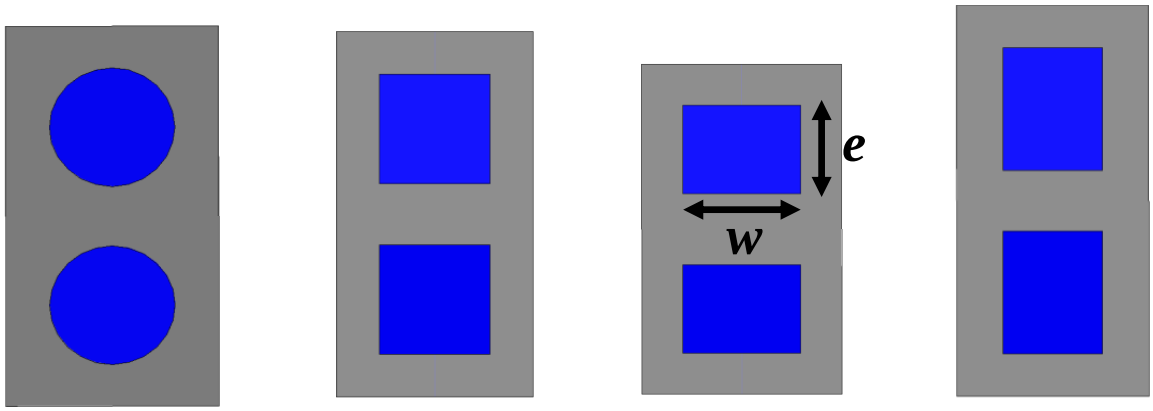

Figure 6.19 Half core of single-turn lateral flux coupled inductors with different via shape: (a) round-shape via, (a) square-shape via, (c) rectangular-shape via case 1, (d) rectangular-shape via case 2

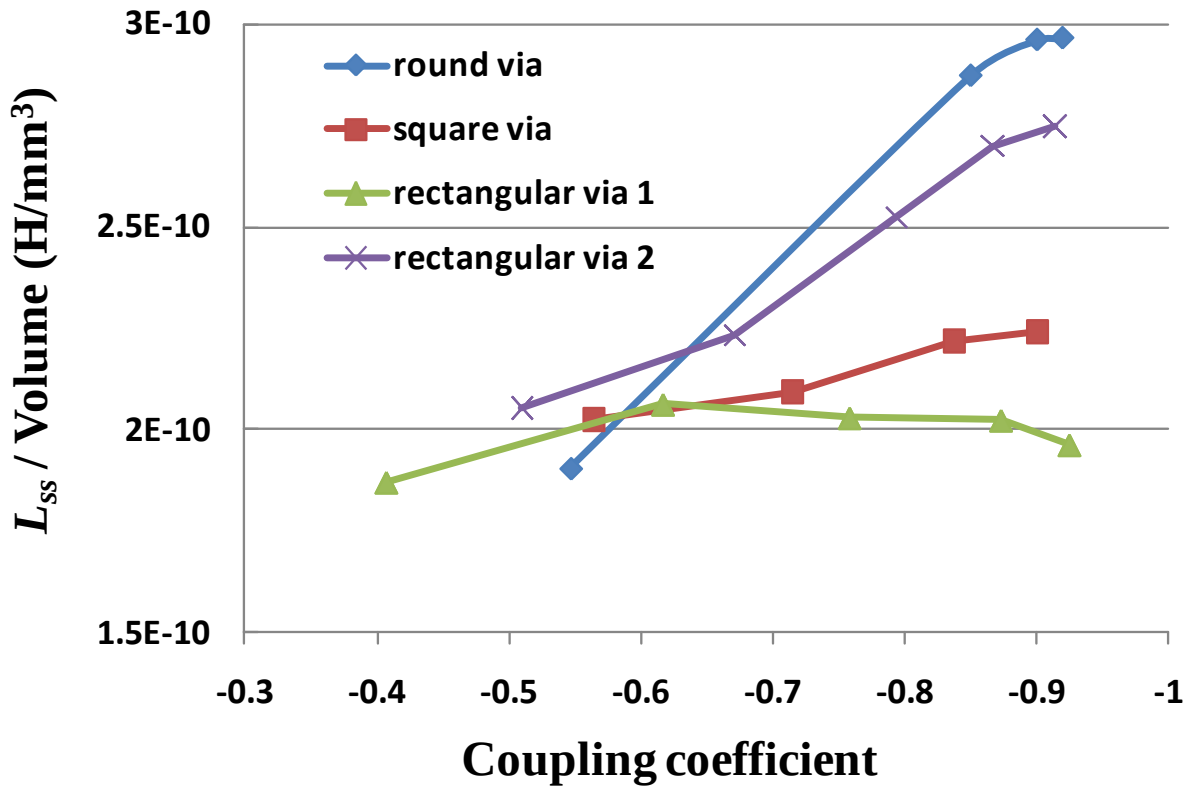

Figure 6.20 FEA 2D simulation results of steady state inductance *Lss* density for lateral flux coupled inductor structures shown in Figure 6.21

Figure 6.21 shows the FEA simulation results of steady state inductance L_{ss} density for lateral flux single-turn coupled inductor structure. In these simulations, the via radius r_v=1mm, core thickness h=1mm, g=1mm, I_{DC}=20A. Different d values are used to give different coupling coefficients. The L_{ss} calculation is based on (6.2), and the duty cycle is D=0.24. With given g value, there is an optimal coupling coefficient α to give the maximal L_{ss} density. The basic reason for these inverse-U shape curves is that increasing α can increase DC flux cancelling effect to help increasing permeability, but if α is increased to be too large, the coupled inductor will work more like a transformer, which is not very efficient for storing energy. As a result, there is an optimal α value to give the maximal *Lss* inductance density.

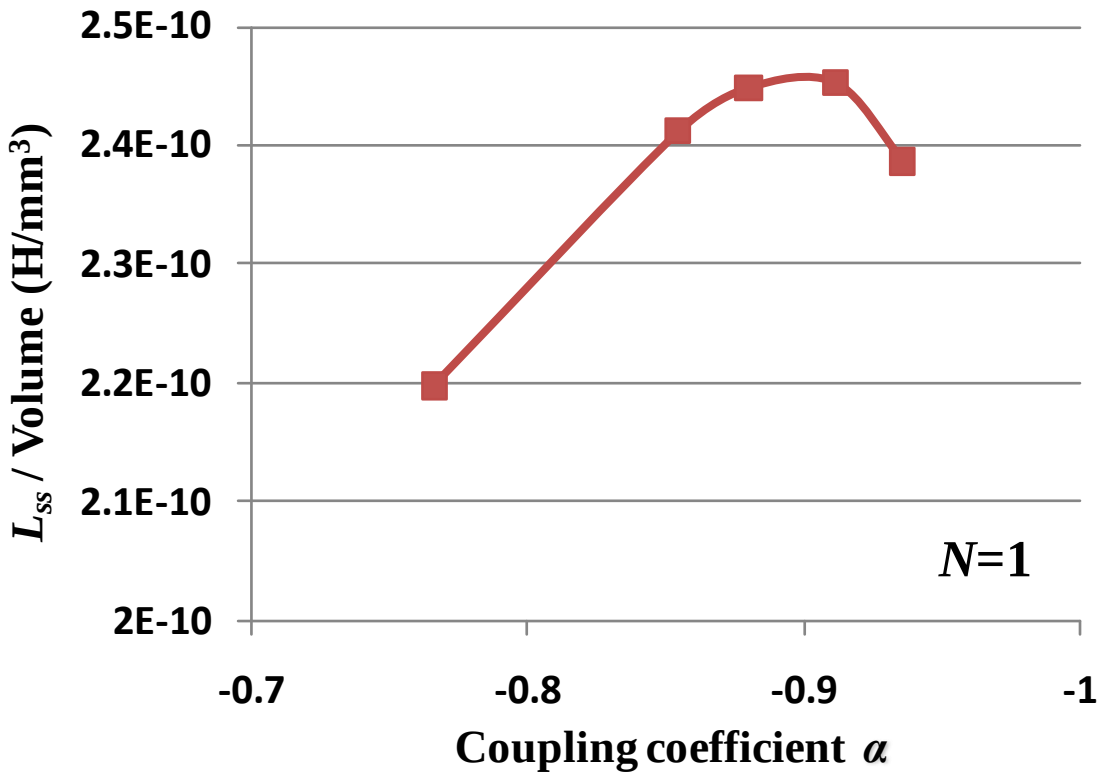

Figure 6.21 FEA simulation results of steady state inductance *Lss* density for lateral flux single-turn coupled inductor with different coupling coefficient

Figure 6.22 shows the FEA simulation results of steady state inductance L_{ss} density for lateral flux coupled inductor with different turn number. In these simulations, the via radius r_v=1mm, core thickness h=1mm, I_{DC}=20A. The L_{ss} calculation is based on (6.2), and the duty cycle is D=0.24.

It can be seen that 1) there is also an optimal coupling coefficient α to give the maximal L_{ss} density for lateral flux multi-turn coupled inductors. 2) Increasing turn-number from 1 to 2 can dramatically increasing L_{ss} density, but further increase turn number from 2 to 3 will not increase L_{ss} density too much. As a result the two-turn structure is chosen to design LTCC lateral flux coupled inductor substrate for a 3D integrated POL converter.

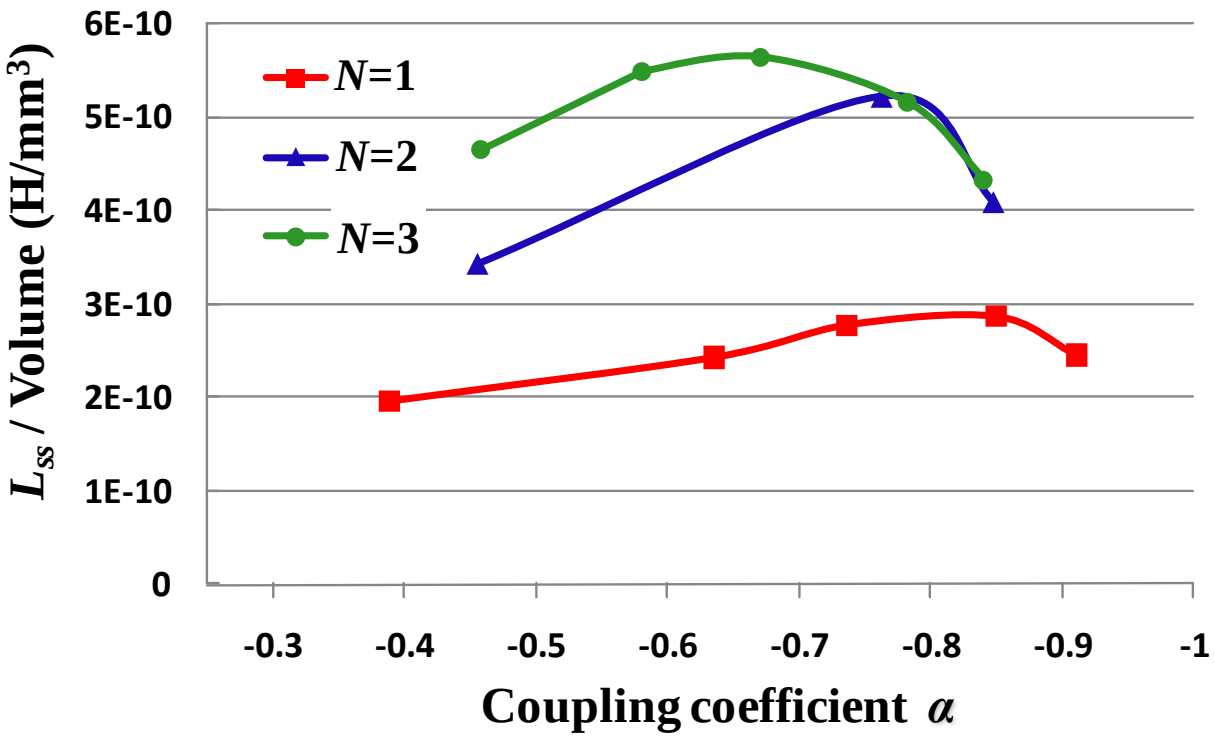

Figure 6.22 FEA simulation results of steady state inductance L_{ss} density for lateral flux coupled inductor with different turn number

6.5 Lateral Flux LTCC Coupled-Inductor Design Example for Two-phase Integrated POL

In order to verify previous analysis and simulation results, a low-profile LTCC lateral flux coupled inductors is designed and fabricated. This low-profile inductor works as the substrate for an integrated 1.5MHz, 5V to 1.2V, 40A two-phase buck converter. The converter integration concept and fabrication process are the same as [88]. This coupled inductor substrates is designed based on given steady state inductance (L_{ss}=68nH with I_L=20A) and footprint (FP=160mm^2), which are determined by converter active layer design. The two-turn structure is used for this lateral flux coupled inductor design.

There are also 5 major design steps:

1) Determine winding cross-section area according to inductor current;

2) Calculate g value according to given footprint;

3) Select α value according to the simulation results of relationship between steady state inductance density and α;

4) Determine d value according to the simulation results of relationship between α and d;

5) Calculate core thickness according to given steady state inductance.

For this particular example: L_{ss}=68nH, inductor footprint FP=160mm^2, inductor current =20A, the radius of coil via is chosen as r_v=1mm; then, according to (6.10), g can be calculated as g=2mm. Then the steady state inductance L_{ss} density can be simulated with different coupling coefficient. The simulation result is shown in Figure 6.23. It can be seen that the maximal steady state inductance density can be achieved when α=-0.6. However, α=-0.8 is also another good choice, because with this case the steady state inductance density is just a little bit lower, but the coupling coefficient is higher. Because the footprint of this coupled inductor has been predetermined, the L_{ss} density actually represents the inductor core thickness. Larger L_{ss} density will give thinner core thickness h.

$$h = \frac{2 \cdot L_{ss}}{L_{ss\_density} \cdot FP} \tag{6.11}$$

where, FP is the total footprint of coupled inductor. Because there are two inductors, the L_{ss} should timed by factor 2.

Figure 6.24 shows the impact of coupling coefficient on core thickness. It can be known that for α=-0.6, the core thickness h is around 1.5mm; for α=-0.8, the core thickness h is only increased to around 1.7mm. So, α=-0.8 case is chosen to be fabricated for a 2-phase POL.

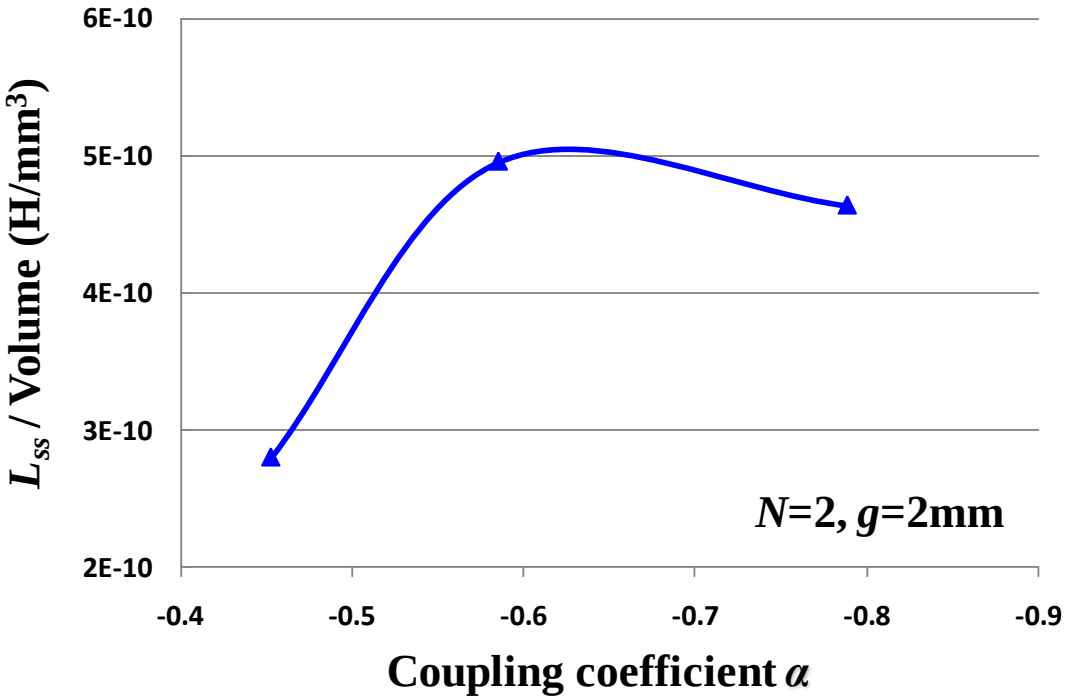

Figure 6.23 Impact of coupling coefficient on steady state inductance density for two-turn structure with given inductor footprint

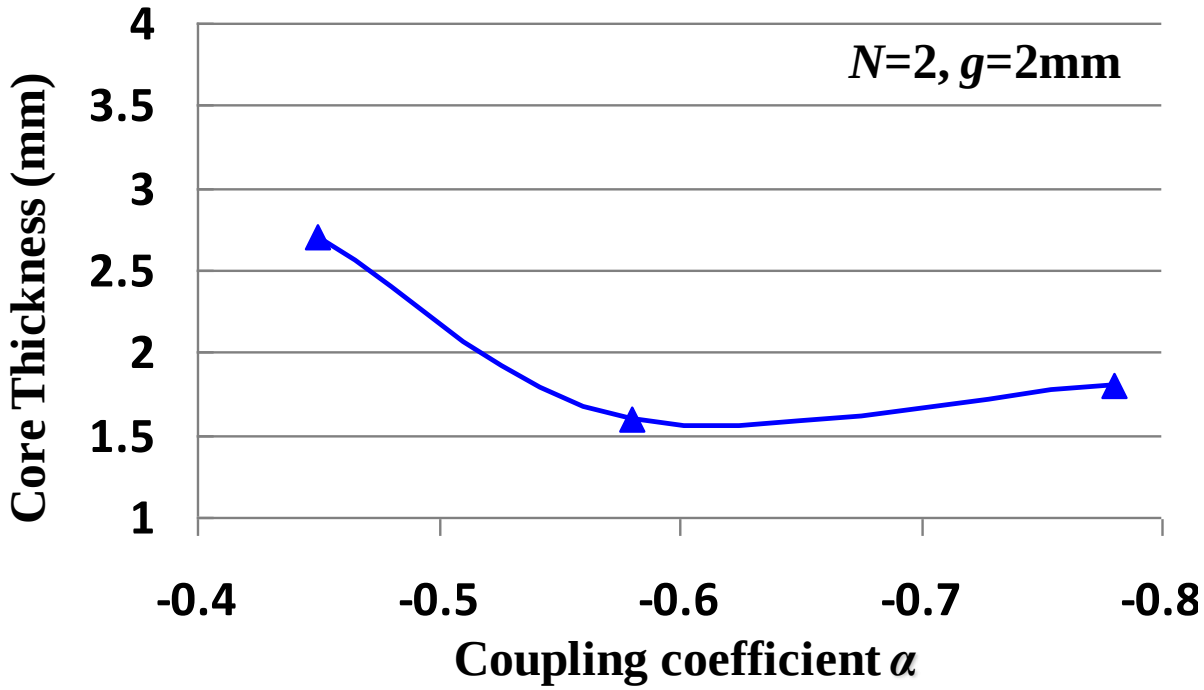

Figure 6.24 Impact of coupling coefficient on core thickness for *N*=2 structure with given inductor footprint

The fabrication process for LTCC coupled inductor is almost the same as fabrication process for LTCC non-coupled inductor. Figure 6.25 shows some major fabrication steps for LTCC lateral flux coupled inductor: 1) laminate whole LTCC core; 2) build vias on LTCC core; 3) screen print silver paste inside vias to build coils; 4) sinter this structure around 900^{o}C; 5) connect via coils by using copper trace. Figure 6.26 shows the photo of fabricated lateral flux coupled inductor. Comparing with vertical flux structure, the lateral flux structure has easier fabrication process. First, the lamination process is reduced to only once; second, silver paste coils have more exposure area, which is good for air dissipating during sintering.

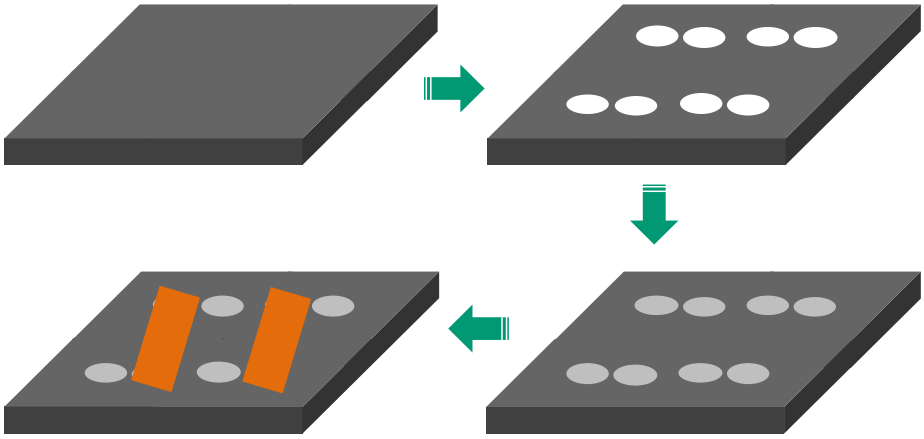

Figure 6.25 Major fabrication steps for LTCC lateral flux coupled inductor

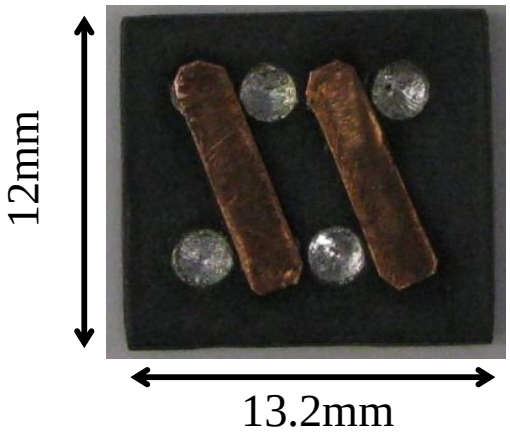

Figure 6.26 Lateral flux coupled inductor prototype

Figure 6.27 shows the test results of inductor current and device drain to source voltage for a 2-phase buck converter with this lateral flux coupled inductor prototype. From Figure 6.27, it can be seen that the inductor current ripple is smaller at light load condition (I_L=0A) comparing with that at heavy load condition (I_L=20A), which means the inductance of this LTCC coupled inductor becomes larger when DC current becomes smaller. This is because the B-H curve of this LTCC material is very non-linear. So, different DC current will cause different permeability due to different saturation condition. According to the inductor current waveform, the L_{ss} and L_{tr} of this coupled inductor can be calculated [2]. Figure 6.28 shows the steady state inductance with different phase current. It can be seen that the vertical flux and lateral flux coupled inductors have almost the same steady state inductance curve. Both of them have around 70nH-80nH steady state inductance with 20A phase current. And both of them have nonlinear inductance due to the nonlinear B-H curve. At light load condition, these LTCC coupled inductors can achieve steady state inductance as high as 400nH, which is very good for increasing light load efficiency.

Table 6.1 is the comparison results between lateral flux coupled inductor and vertical flux coupled inductor prototypes. It can be seen that the lateral flux and vertical flux coupled inductor has almost the same steady state inductance, transient inductance and footprint. The core thickness of lateral flux structure is only half of that of vertical flux structure. However, the coil DCR of lateral flux structure is larger than that of vertical flux structure due to the more complex coil structure. Fig. 17 shows the integrated buck converter with LTCC coupled inductor substrate. With vertical flux coupled inductor this converter can have power density as high as 500W/in^3; with lateral flux coupled inductor the power density of this converter can be further increased to 700W/in^3.

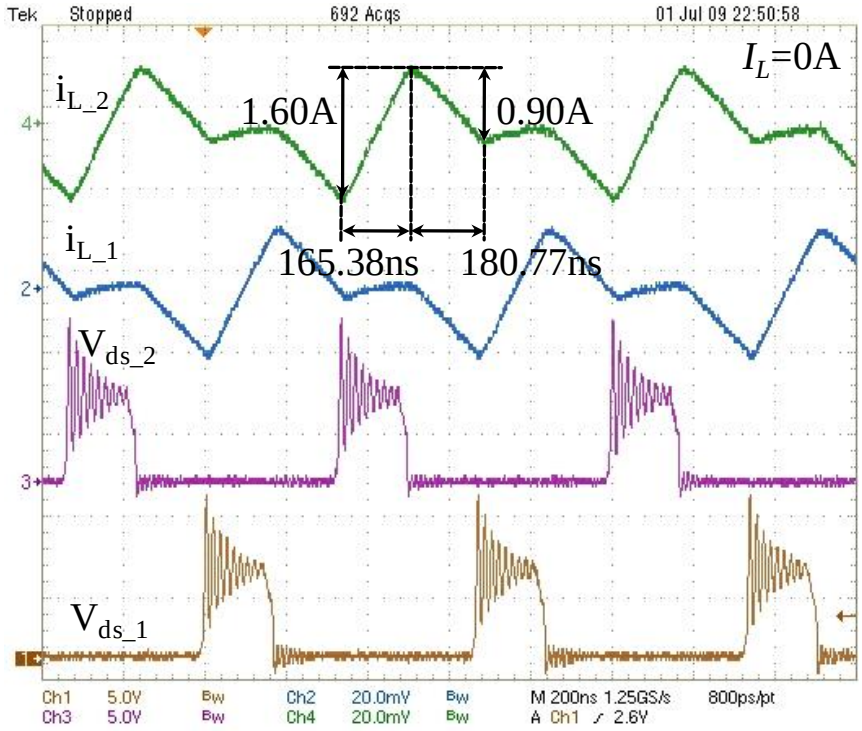

(a)

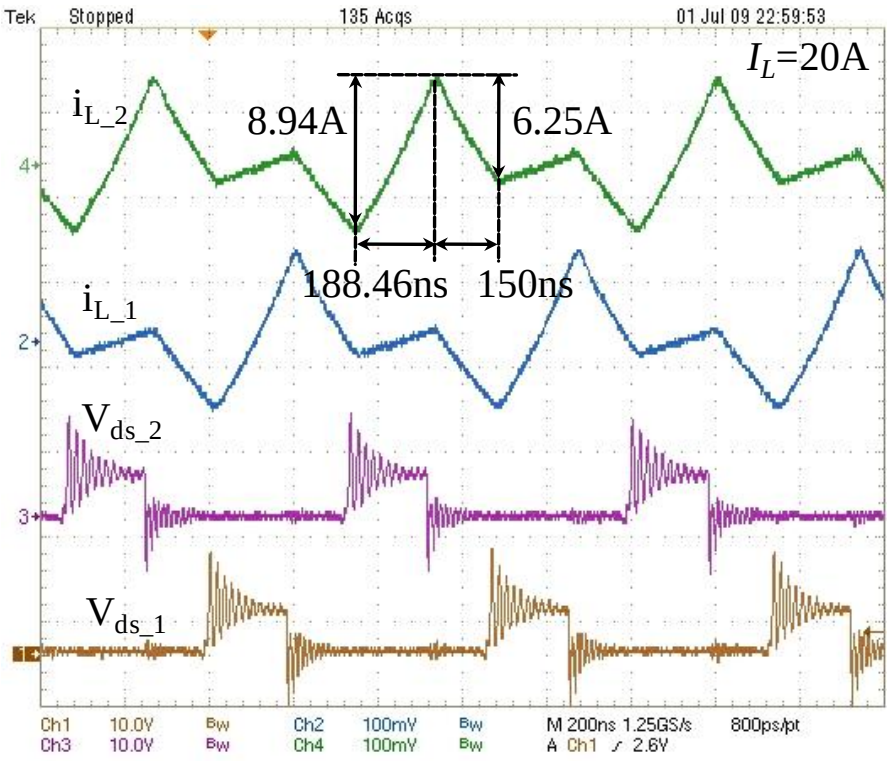

(b)

Figure 6.27 Test results of inductor current and device drain to source voltage for a 2-phase buck converter with lateral flux coupled inductor:(a) inductor current I_L=0A, (b) inductor current I_L=20A

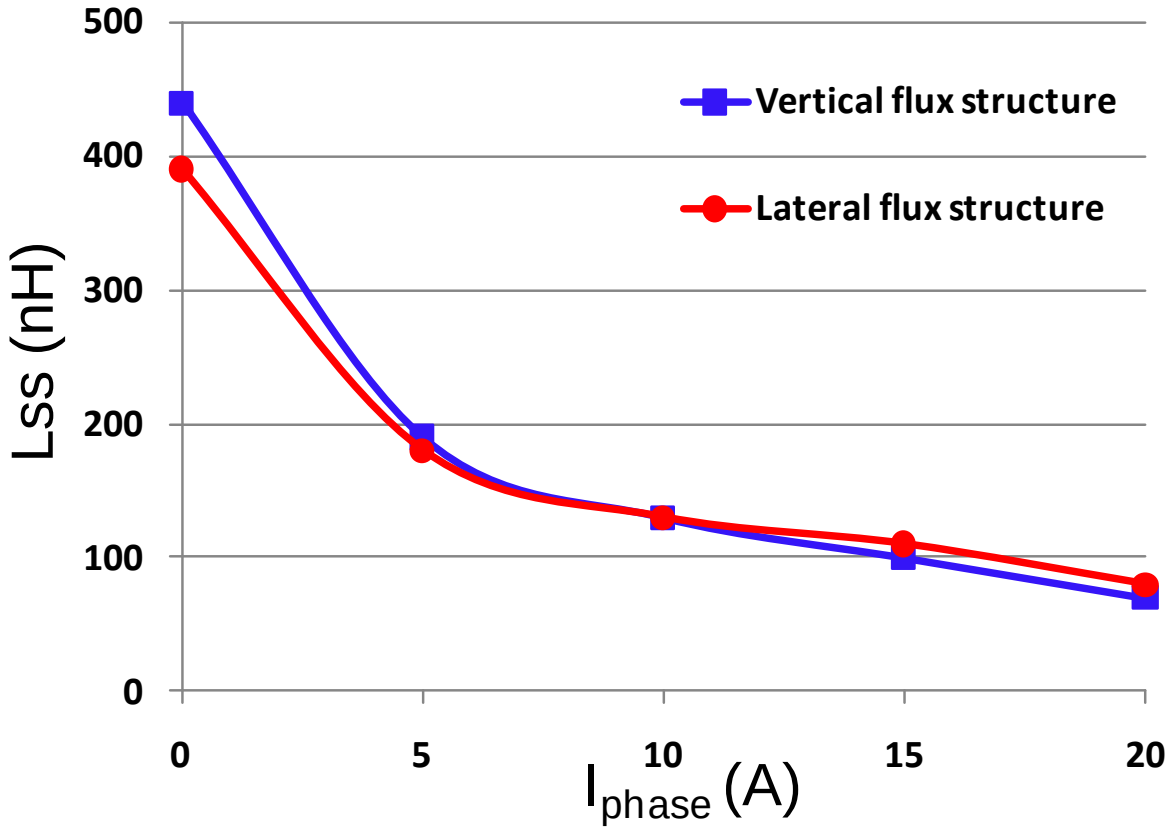

Figure 6.28 Steady state inductance of LTCC coupled inductor prototypes

Table 6.1 Test results of low-profile coupled inductor

Coupled inductor	Footprint	Core thickness	*Lss* (I_L=20A)	*Ltr* (I_L=20A)	Coil DCR
Lateral flux	158mm^2	1.8mm	80nH	29nH	0.6m
Vertical flux	160mm^2	3.4mm	70nH	28nH	0.4m

6.6 Summary

In this chapter, LTCC lateral flux coupled inductor structure is proposed to further increase power density of 3D integrated POL converter. In order to study this LTCC lateral flux coupled inductor, A FEA simulation model is established first. Then, different LTCC lateral flux coupled inductors are studied and compared. The two-turn structure is revealed as the best design choice

for 40A applications from inductance density point of view. After that, a LTCC lateral flux coupled inductor is designed and fabricated for a 40A 3D integrated POL. Comparing with previous vertical flux coupled inductor prototype, the lateral flux coupled inductor prototype has the same inductance and footprint, but only half the core thickness. The fabrication process for lateral flux coupled inductor is also much simple than vertical flux coupled inductor. A 1.5MHz, 5V to 1.2V, 40A output current, 3D integrated POL converter with LTCC lateral flux coupled inductor substrate is demonstrated with 700W/in^3 power density, which has a factor of 7 improvements comparing to today's industry POL products in the same current level.

Chapter 7. Conclusions and Future Work

7.1 Conclusions

Today, every microprocessor is powered with a Voltage Regulator (VR), which is also known as a high current Point-of-Load converter (POL). These circuits are mostly constructed using discrete components, and populated on the motherboard. With this solution, the passive components such as inductors and capacitors are bulky. They occupy a considerable footprint on the motherboard. The problem is exacerbated with the current trend of reducing the size of all forms of portable computing equipment from laptop to netbook, increasing functionalities of PDA and smart phones. In order to solve this problem, a high power density POL needs to be developed. An integration solution was recently proposed to incorporate passive components, especially magnetic components, with active components in order to realize the needed power density for the POL. Today's discrete VR only has around 100W/in^3 power density. The 3D integration concept is widely used for low current integrated POL. With this solution, a very low profile planar inductor is built as a substrate for the active components of the POL. By doing so, the POL footprint can be dramatically saved, and the available space is also fully utilized. This 3D integrated POL can achieve 300-1000W/in^3 power density, however, with considerably less current. This might address the needs of small hand-held equipment such as PDA and Smart phone type of applications. It does not, however, meet the needs for such applications as netbook, laptop, desk-top and server applications where tens and hundreds of amperes are needed. So, although the high density integrated POL has been demonstrated at low current level, magnetic integration is still one of the toughest barriers for improving power density, especially for high current POL.

In order to alleviate the intense thirst from the computing and telecom industry for high power density POL, the 3D integration concept needs be extended from low current applications to high current applications. The key technology for 3D integration is the low-profile planar inductor design. Before this research, there was no general methodology to analyze and design a low-profile planar inductor due to its non-uniform flux distribution, which is totally different as a conventional bulky inductor. A Low Temperature Co-fired Ceramic (LTCC) inductor is one of the most promising candidates for 3D integration for high current applications. For the LTCC inductor, besides the non-uniform flux, it also has non-linear permeability, which makes this problem even more complicated. This research focuses on penetrating modeling and design barriers for planar magnetic to develop high current 3D integrated POL with a power density dramatically higher than today's industry products in the same current level.

In the beginning, a general analysis method is proposed to classify different low-profile inductor structures into two types according to their flux path pattern. One is a vertical flux type; another one is a lateral flux type. The vertical flux type means that the magnetic flux path plane is perpendicular with the substrate. The lateral flux type means that the magnetic flux path plane is parallel with the substrate. This analysis method allows us to compare different inductor structures in a more general way to reveal the essential difference between them. After a very thorough study, it shows that a lateral flux structure is superior to a vertical flux structure for low-profile high-current inductor design from an inductance density point of view, which contradicts conventional thinking. This conclusion is not only valid for the LTCC planar inductor, which has very non-linear permeability, but is also valid for the planar inductor with other core material, which has constant permeability.

Next, some inductance and loss models for a planar lateral flux inductor with a non-uniform flux are also developed. With the help of these models, different LTCC lateral flux inductor structures (single-turn structure and multi-turn structures) are compared systematically. In this comparison, the inductance density, winding loss and core loss are all considered. The proposed modeling methodology is a valuable extension of previous uniform flux inductor modeling, and can be used to solve other modeling problems, such as non-uniform flux transformer modeling.

After that, a design method is proposed for the LTCC lateral flux inductor with non-uniform flux distribution. In this design method, inductor volume, core thickness, winding loss, core loss are all considered, which has not been achieved in previous conventional inductor design methods. With the help of this design method, the LTCC lateral flux inductor can be optimized to achieve small volume, small loss and low profile at the same time. Several LTCC inductor substrates are also designed and fabricated for the 3D integrated POL. Comparing the vertical flux inductor substrate with the lateral flux inductor substrate, we can see a savings of 30% on the footprint, and a much simpler fabrication process. A 1.5MHz, 5V to 1.2V, 15A 3D integrated POL converter with LTCC lateral flux inductor substrate is demonstrated with 300W/in^3 power density, which has a factor of 3 improvements when compared to today's industry products.

Furthermore, the LTCC lateral flux coupled inductor is proposed to further increase power density of the 3D integrated POL converter. Due to the DC flux cancelling effect, the size of LTCC planar coupled inductor can be dramatically reduced to only 50% of the LTCC planar non-coupled inductor. Compared to previous vertical flux coupled inductor prototypes, a lateral flux coupled inductor prototype is demonstrated to have a 50% core thickness reduction. A

1.5MHz, 5V to 1.2V, 40A 3D integrated POL converter with LTCC lateral flux coupled inductor substrate is demonstrated with 700W/in^3 power density, which has a factor of 7 improvements when compared to today's industry POL products in the same current level.

In conclusion, this research not only overcame some major academia problems about analysis and design for planar magnetic components, but also made significant contributions to the industry by successfully scaling the integrated POL from today's 1W-5W case to a 40W case. This level of integration would significantly save the cost, and valuable motherboard real estate for other critical functions, which may enable the next technological innovation for the whole computing and telecom industry.

7.2 Future Work

The lateral flux planar inductor substrate built with LTCC ferrite shows promise for 3D integration for high current applications. Following this research there are still some remaining works can be done which are related to this dissertation:

1. With the emerging Gallium-Nitride (GaN) based power transistors, the switching frequency of a Point-of-Load (POL) converter can be pushed to several Mega-hertz. So, the LTCC lateral flux inductor design should be extend from today's 1.5MHz to as high as 5 MHz to help further increase converter power density.

2. The core loss modeling for these planar inductors with non-uniform flux distribution can be combined with FEA simulation. By doing so, first, more accurate result can be achieved; furthermore, it can predict core loss for planar inductor with any structure, which even has very non-uniform flux distribution, such as LTCC coupled inductor.

3. The LTCC inductor substrate concept can also be extended to LTCC transformer to help designing high density integrated off-line converters.

4. The LTCC technology can also be used to integrate capacitor, and furthermore, to integrate magnetic and capacitor as one passive component.

References

[1] Xunwei Zhou, Pit-Leong Wong, Peng Xu, Fred C. Lee, Alex Q. Huang, "Investigation of Candidate VRM Topologies for Future Microprocessors," IEEE Transactions on Power Electronics, Nov 2000, pp. 1172 - 1182.

[2] Peng Xu, "Multiphase Voltage Regulator Modules with Magnetic Integration to Power Microprocessors", Ph.D. Dissertation, Virginia Tech 2002.

[3] Kaiwei Yao, "High-Frequency and High-Performance VRM Design for the Next Generations of Processors", Ph.D. Dissertation, Virginia Tech 2004.

[4] Jinghai Zhou, "High Frequency, High Current Density Voltage Regulators", Ph.D. Dissertation, Virginia Tech 2005.

[5] D12S36A datasheet. www.deltaww.com

[6] FB6831J application note. www.fujielectric.com

[7] LM3218 datasheet. www.national.com

[8] EN5396 application note. www. enpirion.com

[9] LT4601 datasheet. www. linear.com

[10] GaNpowIR™ datasheet. www.irf. com

[11] Y. Ren, M. Xu, J. Zhou and Fred C. Lee, "Analytical Loss Model of Power MOSFET", IEEE Transactions On Power Electronics, VOL.21, No. 2, Mar 2006, pp.310-319.

[12] Yucheng Ying, "Device selection criteria----based on loss modeling and Figure of Merit", Thesis of Master of Science in Electrical Engineering of Virginia Tech, 2008.

[13] RJK0305DPB datasheet. www.renesas.com

[14] Parul Dhagat, Student, Satish Prabhakaran, and Charles R. Sullivan, "Comparison of magnetic materials for V-groove inductors in optimized high-frequency DC-DC converters." IEEE Transactions on Magnetics, vol. 40, no. 4, pp. 2008-2010, July 2004.

[15] Cheng, K.W.E.; Tang, C.Y.; Cheng, D.K.W.; Wu, H.; Ho, Y.L.; Lu, Y ,"Investigation of polymer bonded magnetic materials for power conversion" Hong Kong Polytechnic University, PESC 2002, pp. 1254 - 1259.

[16] Kelly, S.; Collins, C.; Duffy, M.; Rhen, F.M.F.; Roy, S "Core Materials for High Frequency VRM Inductors", PESC 2007, pp.1767 - 1772

[17] Robert Hahn, Steffen Krumbholz, Herbert Reichl, "Low profile power inductors based on ferromagnetic LTCC technology", in proc. Electronic Components and Technology Conference, 2006, pp. 528-533.

[18] Michele Lim, "Low Temperature Co-fired Ceramics Technology for Power Magnetics Integration", PhD. Dissertation, 2008.11

[19] M. Mu, Yipeng Su, Qiang Li, David Gilham, Fred C. Lee, "Magnetic Characterization of Low Temperature Co-fired Ceramic (LTCC) Ferrite Materials for High Frequency Power Converters" CPES Conference, 2011.

[20] T. O'Donnell, N. Wang, R. Meere, F. Rhen, S. Roy, D. O'Sullivan, C. O'Mathuna, "Microfabricated inductors for 20 MHz Dc-Dc converters", Applied Power Electronics Conference and Exposition, 2008, pp. 689-693.

[21] Eberhard Waffenschmidt, Bernd Ackermann, and J. A. Ferreira, " Design method and material technologies for passives in printed circuit Board Embedded circuits", IEEE Transactions on Power Electronics, vol. 20, no. 3, pp. 576-584, May 2005.

[22] Arthur Ball, "Thermal and Electrical Considerations for the Design of Highly-Integrated POL Converters", PhD. Dissertation, 2008.11

[23] Rana J. Pratap, Saikat Sarkar, Stephane Pinel, Joy Laskar, and Gary S. May, "Modeling and Optimization of Multilayer LTCC Inductors for RF /Wireless Applications Using Neural Network and Genetic Algorithms", 2004 Electronic Components and Technology Conference, 2004.

[24] Joong-Keun Lee, Chan-Sei Yoo, Hyun-Chul Jung, Woo-Sung Lee; Jong-Kwan Yook, "Design of band pass filter for 900MHz ZigBee application using LTCC high Q inductor" Microwave Conference Proceedings, 2005. APMC 2005. Asia-Pacific Conference Proceedings

[25] Shuwei Yang, Yali Qin; Zhefu Wu, Suming Zhuang, “Design of compact LTCC bandpass filter with high process tolerance using meander line coupled inductor", Ultra-Wideband (ICUWB), 2010 IEEE International Conference on, 2010, pp.1 - 4

[26] Yan Dong, “Investigation of Multiphase Coupled-Inductor Buck Converters in Point-of-Load Applications”, PhD. Dissertation, 2009.7

[27] Magali Brunet, Terence O’Donnell, Laurent Baud, Ningning Wang, Joe O’Brien, Paul McCloskey, and Sean C. O’Mathuna, "Electrical performance of microtransformers for DC-DC converter applications." IEEE Transactions on Magnetics, vol. 38, no. 5, pp. 3174-3176, Sept. 2002.

[28] Srinivasan Iyengar, Trifon M. Liakopoulos and Chong H. Ahn, “A DC/DC boost converter toward fully on-chip integration using new micromachined planar inductors”, in proc. Power Electronics Specialists Conference, 1999, pp. 72-76.

[29] Yasushi Katayama, Satoshi Sugahara, Haruo Nakazawa, Masaharu Edo, “High-Power-Density MHz-Switcing Monolithic DC-DC Converter with Thin-Film Inductor.” , in proc. Power Electronics Specialists Conference, 2000, pp. 1485-1490.

[30] Sullivan, C. R. and S. R. Sanders, "Design of microfabricated transformers and inductors for high-frequency power conversion." IEEE Transactions on Power Electronics, vol. 11, no. 2, pp. 228-238, Mar. 1996.

[31] T. O'Donnell, N. Wang, M. Brunet, S. Roy, A. Connell, J. Power, C. O’Mathuna, P. McCloskey, “Thin film micro-transformers for future power conversion”, Applied Power Electronics Conference and Exposition, 2004, pp. 939-944.

[32] Masato Mino, Toshiaki Yachi, Akio Tago, Keiichi Yanagisawa, and Kazuhiko Sakakibara, "A new planar microtransformer for use in micro-switching converters." IEEE Transactions on Magnetics, vol. 28, no. 4, pp. 1969-1973, July 1992.

[33] Eui-Jung Yun, Myunghee Jung, Chae Il Cheon, and Hyoung Gin Nam, “Microfabrication and characteristics of low-power high-performance magnetic thin-film transformers." IEEE Transactions on Magnetics, vol. 40, no. 1, pp. 65-70, Jan. 2004.

[34] Ahn, C. H. and M. G. Allen (1996). "A comparison of two micromachined inductors (bar- and meander-type) for fully integrated boost DC/DC power converters." Power Electronics, IEEE Transactions on 11(2): 239-245.

[35] Toshiro Sato, Hiroshi Tomita, Atsuhito Sawabe, Tetsuo Inoue, Tetsuhiko Mizoguchi, and Masashi Sahashi, “A Magnetic Thin Film Inductor and its Application to a MHz Switching dc-dc Converter”, IEEE Transactions on Magnetics, vol. 30, no. 2, pp. 217-223,Mar. 1994.

[14] Satish Prabhakaran, Charles R. Sullivan, and Kapil Venkatachalam, "Measured electrical performance of V-groove inductors for microprocessor power delivery." IEEE Transactions on Magnetics, vol. 39, no. 5, pp. 3190-3192, Sept. 2003.

[36] Mingliang Wang; Batarseh, I.; Ngo, K.D.T.; Huikai Xie, “Design and Fabrication of Integrated Power Inductor Based on Silicon Molding Technology”, Power Electronics Specialists Conf., 2007, pp. 1612-1618.

[37] Robert Hahn, Steffen Krumbholz, Herbert Reichl, “Low profile power inductors based on ferromagnetic LTCC technology”, in proc. Electronic Components and Technology Conference, 2006, pp. 528-533.

[38] Tsutomu Mikura, Koichi Nakahara, Kota Ikeda, Ken Furukuwa, and Katsuhiko Onitsuka, “New substrate for micro DC-DC converter”, Electronic Components and Technology Conference, 2006, pp. 1326-1330.

[39] Michele H. Lim, Jacobus. D. van Wyk, F. C. Lee, and Khai D. T. Ngo, “A Class of Ceramic-Based Chip Inductors for Hybrid Integration in Power Supplies”, IEEE Transactions on Power Electronics, vol. 23, no. 3, pp. 1556-1564, May 2008.

[40] I. Kowase, T. Sato, K. Yamasawa, Y. Miura, “A planar inductor using Mn-Zn ferrite/polyimide composite thick film for low-Voltage and large-current DC-DC converter”, IEEE Transactions on Magnetics, vol41, no. 10, pp. 3991-3993, Oct. 2005.

[41] A. M. Pernia, M. J. Prieto, J. M. Lopera, J. Reilly, S. S. Linton, C. Quinones, “Thick-film hybrid technology for low output voltage DC/DC converter”, in proc. Industry Applications Conf., 2002, pp. 1315-1322.

[42] Moon, K.W.; Hong, S.H.; Kim, H.J.; Kim, J.;, “A fabrication of DC-DC converter using LTCC NiZnCu ferrite thick films”, in proc. Int. Magnetics Conf., 2005, pp. 1109-1110.

[43] Matthias Ludwig, Maeve Duffy, Terence O’Donnell, Paul McCloskey, and Seán Cian Ó Mathùna, “PCB integrated inductors for low power DC/DC converter”, IEEE Transactions on Power Electronics, vol. 18, no. 4, pp. 937-945, July 2003.

[44] Zhang, Y. E., S. R. Sanders, “In-board magnetics processes”, in proc. Power Electronics Specialists Conference, 1999, pp. 561-567.

[45] Tang, S. C., S. Y. R. Hui, and Henry Shu-Hung Chung, "A low-profile power converter using printed-circuit board (PCB) power transformer with ferrite polymer composite." IEEE Transactions on Power Electronics, vol. 16, no. 4, pp. 493-498, July 2001.

[46] Brett A. Miwa, Leo F. Casey, and Martin F. Schlecht, "Copper-based hybrid fabrication of a 50 W, 5 MHz 40 V-5 V DC/DC converter." IEEE Transactions on Power Electronics, vol. 6, no. 1, pp. 2-10, Jan. 1991.

[47] J. A. Cobos, M. Rascon, L. Alvarez, S. Ollero, M. de Graf and W. Waanders, “Low profile and low output voltage DC/DC converters for on-board power distribution using planar magnetics”, in proc. Industry Applications Conference, 1997, pp. 1153-1158.

[48] A.B. Lostetter, F. Barlow, A. Elshabini, K. Olejniczak, and S. Ang, “Polymer thick film (PTF) and flex technologies for low cost power electronics packaging”, International Workshop on Integrated Power Packaging, IWIPP 2000, pp. 33-40.

[49] T. Fujiwara, "Planar integrated magnetic component with transformer and inductor using multilayer printed wiring board", IEEE Transactions on Magnetics, vol. 34, no. 4, pp. 2051-2053, July 1998.

[50] Meinhardt, M., T. O'Donnell, Henning Schneider, John Flannery, Cian O’Mathuna, Peter Zacharias, and Thomas Krieger, “Miniaturised “Low Profile” module integrated converter for photovoltaic applications with integrated magnetic components”, in proc. Applied Power Electronics Conference, 1999, pp. 305-311.

[51] Lopera J. M. Lopera, Miguel J. Prieto, Alberto M. Pern´ıa, Fernando Nu˜no, Martinus J. M. de Graaf, Jan Willem Waanders, and Lourdes Alvarez Barcia, "Design of integrated magnetic elements using thick-film technology." IEEE Transactions on Power Electronics, vol. 14, no. 3, pp. 408-414, May 1999.

[52] D. C. Hopkins, “Thick-film power hybridization of switchmode power circuits”, in proc. Applied Power Electronics Conference, 1989, pp. 249-255.

[53] T. O'Donnell, N. Wang, R. Meere, F. Rhen, S. Roy, D. O'Sullivan, C. O'Mathuna, “Microfabricated inductors for 20 MHz Dc-Dc converters”, Applied Power Electronics Conference and Exposition, 2008, pp. 689-693.

[54] E. Waffenschmidt, Joep Jacobs “Integrated Design Procedure for Printed Circuit Board Inductors in DC-to-DC Converters”, 2007, pp. 1-10.

[55] Robert Hahn, Steffen Krumbholz, Herbert Reichl, “Low Profile Power Inductors Based on Ferromagnetic LTCC Technology”, Electronic Components and Technology Conference 2006, pp.528-533.

[56] Tsutomu Mikura, Koichi Nakahara, Kota Ikeda, Ken Furukuwa, K. Onitsuka, “New Substrate for Micro DC-DC Converter”, Electronic Components and Technology Conference 2006, pp.1326-1330.

[57] Kelly, S.; Collins, C.; Duffy, M.; Rhen, F.M.F.; Roy, S “Core Materials for High Frequency VRM Inductors”, PESC 2007, pp.1767 - 1772

[58] E. OSEGUEDA, K. D. T. NGO, W. M. POLIVKA, M. M. WALTERS, “Perforrated - Plate Magnetics. Part I: Mode-I Inductor/rransformer” IEEE TRANSACTIONS ON AEROSPACE AND ELECTRONIC SYSTEMS VOL. 31, NO. 3 JULY 1995.

[59] M. J. Prieto, A. M. Pernia, J. M. Lopera, J. A. Martin, F. Nuno, "Design and analysis of thick-film integrated inductors for power converters", IEEE Trans. Industry Applications, Volume 38, Issue 2, March-April 2002, pp. 543 - 552.

[60] Michele H. Lim, Jacobus, D. van Wyk, Khai D. T. Ngo, “Modeling of an LTCC Inductor Capable of Improving Converter Light-Load Efficiency”, APEC 2007, Feb. 2007, pp.85 – 89.

[61] P. L. Dowell, “Effects of eddy currents in transformer windings,” Proc. Inst. Elect. Eng., vol. 113, pp. 1387–1394, Aug. 1966.

[62] P. S. Venkatraman, “Winding eddy current losses in switch mode power transformers due to rectangular wave currents,” in Proc. Powercon 11, sec. A-1. 1984, pp. 1–11.

[63] B. Carsten, “High frequency conductor losses in switch mode magnetics,” in Proc. High-Frequency Power Conversion Conf., May 1986, pp. 155–176.

[64] M. P. Perry, “Multiple layer series connected winding design for minimum losses,” IEEE Trans. Power App. Syst., vol. PAS-98, pp. 116–123, Jan./Feb. 1979.

[65] J. A. Ferreira, “Electromagnetic Modeling of Power Electronic Converters”. Boston, MA: Kluwer, 1989.

[66] Jiankun Hu and Charles R. Sullivan, “AC Resistance of Planar Power Inductors and the Quasidistributed Gap Technique”, IEEE TRANSACTIONS ON POWER ELECTRONICS, VOL. 16, NO. 4, JULY 2001

[67] J. Hu and C. R. Sullivan, “The quasi-distributed gap technique for planar inductors: design guidelines,” in Proc. IEEE Ind. Applicat. Conf., vol. 2, 1997, pp. 1147–1152.

[68] F. Robert, P. Mathys, and J.-P. Schauwers, “A closed-form formula for 2-D ohmic losses calculation in SMPS transformer foils,” in Proc. Appl. Power Electron. Conf. (APEC’99), 1999, p. 199.

[69] A. F. Goldberg, J. G. Kassakian, and M. F. Schlecht, “Finite-element analysis of copper loss in 1–10 MHz transformers,” IEEE Trans. Power Electron., vol. 4, pp. 157–167, Mar. 1989.

[70] L. Ye, G. R. Skutt, R. Wolf, and F. C. Lee, “Improved winding design for planar inductors,” in Proc. 28th Annu. IEEE Power Electron. Spec. Conf. (PESC’97), vol. 2, 1997, pp. 1561–1567.

[71] G. Skutt, F. C. Lee, R. Ridley, and D. Nicol, “Leakage inductance and termination effects in a high-power planar magnetic structure,” in Proc. IEEE Appl. Power Electron. Conf. Expo. (APEC’94), vol. 1, 1994, pp. 295–301.

[72] R. Prieto, J. A. Cobos, O. Garcia, P. Alou, and J. Uceda, “Model of integrated magnetics by means of “double 2D” finite element analysis techniques,” in Proc. 30th Annu. IEEE Power Electron. Spec. Conf., vol. 1, 1999, pp. 598–603.

[73] G. Bertotti, “General properties of power losses in soft ferromagnetic materials”, IEEE Transactions on Magnetics, vol. 24, no. 1, pp. 621-630, 1988.

[74] G. Bertotti, Hysteresis in magnetism: for physicists, materials scientists, and engineers, Academic Press, 1998.

[75] W. Roshen, “Ferrite core loss for power magnetic components design”, IEEE Transactions on Magnetics, vol. 27, no. 6, pp. 4407–15, 1991.

[76] J.-T. Hsu and K.D.T Ngo, “A Hammerstein-based dynamic model for hysteresis phenomenon”, IEEE Transactions on Power Electronics, vol. 12, no. 3, pp. 406–413, 1997.

[77] H. Saotome and Y. Sakaki, “Iron loss analysis of mn-zn ferrite cores”, IEEE Transactions on Magnetics, vol. 33, no. 1, pp. 728–34, 1997.

[78] K. H. Carpenter, “Simple models for dynamic hysteresis which add frequency-dependent losses to static models”, IEEE Transactions on Magnetics, vol. 34, no. 3, pp. 619–22, 1998.

[79] C. P. Steinmetz, “On the law of hysteresis,” Proc. IEEE, vol. 72, pp.196–221 , Feb. 1984.

[80] M. Albach, T. Durbaum, and A. Brockmeyer, “Calculating core losses in transformers for arbitrary magnetizing currents a comparison of different approaches.”, in PESC 96. 27th Annual IEEE Power Electronics Specialists Conference, June 1996, vol. 2, pp. 1463–8.

[81] J. Reinert, A. Brockmeyer, and R.W. De Doncker, “Calculation of losses in ferro- and ferrimagnetic materials based on the modified Steinmetz equation”, in Proceedings of 34th Annual Meeting of the IEEE Industry Applications Society, 1999, pp. 2087–92 vol.3.

[82] Jieli Li, T. Abdallah, and C. R. Sullivan, “Improved calculation of core loss with nonsinusoidal waveforms”, in Conference Record of the 2001 IEEE Industry Applications Conference. 36th IAS Annual Meeting, 2001, pp. 2203–2210.

[83] Jinjun Liu, T.G. Wilson, Jr., R.C. Wong, R. Wunderlich, and F.C. Lee, “A method for inductor core loss estimation in power factor correction applications”, in Proceedings of APEC 2002 - Applied Power Electronics Conference and Exposition, 2002, p. 439.

[84] Mingkai Mu, Qiang Li, David Gilham, Fred C. Lee, Khai D.T. Ngo, " New Core Loss Measurement Method for High Frequency Magnetic Materials", IEEE Energy Conversion Congress & Expo, Sept. 2010.

[85] Mingkai Mu, Fred Lee, "A New High Frequency Inductor Loss Measurement Method", IEEE Energy Conversion Congress & Expo, Sept. 2011.

[86] P. Wong, Q. Wu, P. Xu, B. Yang, and F.C. Lee, “Investigating Coupling inductor in interleaving QSW VRM,” Proc. IEEE APEC conf., 2000, pp.973-978.

[87] P. Wong, “Performance improvement of multi-channel interleaving voltage regulator modules with integrated coupling inductors”, VPI&SU dissertation, Mar., 2001.

[88] Arthur Ball, Michele Lim, David Gilham, Fred C. Lee, “System design of a 3D integrated non-isolated Point Of Load converter”, APEC 2008, pp. 181 - 186.